

**NASA SPACE ENGINEERING RESEARCH CENTER  
FOR UTILIZATION OF LOCAL PLANETARY RESOURCES**

**ORIGINAL CONTAINS  
COLOR ILLUSTRATIONS**

**ANNUAL  
PROGRESS REPORT  
1990-91**

**APR-91**

**Director: T. Triffet, Principal Investigators: K. Ramohalli, J. Lewis**

**THE UNIVERSITY OF ARIZONA**

**4717 E. FT. LOWELL RD./AML  
TUCSON, AZ 85712**

**TELEPHONE: (602) 322-2304 FAX: (602) 326-0938**

# TABLE OF CONTENTS

	Page
Executive Summary.....	iv
Publications.....	viii
 <b>I. PROCESSING OF PROPELLANTS, VOLATILES AND METALS</b>	
 <b>A. Reduction of Lunar Regolith</b>	
Coproduction of Volatiles and Metals from Extraterrestrial Materials.....	IA-15 <sub>1</sub>
J.S. Lewis	
Production of Oxygen from Lunar Ilmenite.....	IA-4 <sub>52</sub>
F. Shadman and Y. Zhao	
Beneficiation of Lunar Ilmenite.....	IA-33 <sub>3</sub>
Joaquin Ruiz	
"Cold" Plasma Processing of Local Planetary Ores for Oxygen and Metallurgically Important Metals.....	IA-36 <sub>54</sub>
D.C. Lynch, D. Bullard, and R. Ortega	
Innovative Techniques for the Production of Energetic Radicals for Lunar Materials Processing Including Photogeneration Via Concentrated Solar Energy.....	IA-47 <sub>55</sub>
D.E. Osborn, D.C. Lynch, and R. Fozzalari	
Oxygen and Iron Production by Electrolytic Smelting of Lunar Soil.....	IA-52 <sub>56</sub>
R.O. Colson and L.A. Haskin	
Experimental Study of the Electrolysis of Silicate Melts.....	IA-63 <sub>57</sub>
R. Keller and K.T. Larimer	
An Investigation of the Thermal Shock Resistance of Lunar Regolith and the Recovery of Hydrogen from Lunar Soil Heated Using Microwave Radiation.....	IA-70 <sub>58</sub>
T.T. Meek	
 <b>B. Reduction of Carbon Dioxide</b>	
Oxygen Plant Breadboard Design, and Techniques for Improving Mission Figure-of-Merit.....	IB-1 <sub>59</sub>
K. Ramohalli	
Thermal Analysis, Optimization and Design of a Martian Oxygen Production Plant.....	IB-9 <sub>510</sub>
V.A. Iyer and K.R. Sridhar	
Issues on the Production and Electrochemical Separation of Oxygen from Carbon Dioxide.....	IB-21 <sub>511</sub>
P. Kaloupis and K.R. Sridhar	
Compression of Martian Atmosphere for Production of Oxygen.....	IB-36 <sub>512</sub>
D.C. Lynch, A.H. Cutler, and P.E. Nolan	
 <b>C. Reduction of Carbonaceous Materials</b>	
Dehydration Kinetics of TALC at 1 Bar.....	IC-1 <sub>513</sub>
J. Ganguly and K. Bose	

## II. PRODUCTION OF STRUCTURAL AND REFRACTORY MATERIALS

Recovery of Precious Metals from Space.....	II-1 514
H. Freiser	
Processing of Glass-Ceramics from Lunar Resources.....	II-15 515
B.D. Fabes and W. H. Poisl	
Development and Mechanical Properties of Structural Materials from Lunar Simulant.....	II-23 516
C.S. Desai	
High Temperature Seals Between Ceramic Separation Membranes and Super-Alloy Housing.....	II-31 517
G. Honea and K.R. Sridhar	

## III. RESOURCE DISCOVERY AND CHARACTERIZATION

Determination of Lunar Ilmenite Abundances from Remotely Sensed Data.....	III-1 518
S.M.Larson, J.R. Johnson, and R.B. Singer	
Continuous Monitoring of the Lunar or Martian Subsurface Using On-Board Pattern Recognition and Neural Processing of Rover Geophysical Data.....	III-7 519
C.E. Glass, R.V. Boyd, and B.K. Sternberg	
Spacewatch Search for Near-Earth Asteroids.....	III-25 520
T.Gehrels	
Compositions of Near-Earth Asteroids.....	III-28 521
L.A. Lebofsky and M.L. Nelson	

## IV. SYSTEM AUTOMATION AND OPTIMIZATION

Development of A Figure-of-Merit for Space Missions.....	IV-1 522
B. Preiss, T. Pan, and K. Ramohalli	
Quantitative Simulation of Extraterrestrial Engineering Devices.....	IV-7 523
A. Arabyan, P.E. Nikraves, and T.L. Vincent	
Modeling Simulation, and Control of an Extraterrestrial Oxygen Production Plant.....	IV-13 524
L. Schooley, F. Cellier, B. Zeigler, A. Doser, and G. Farrenkopf	

## V. DATABASE DEVELOPMENT

Near-Earth Asteroids: Observer Alert Network and Database Analysis.....	V-1 525
D.R. Davis and C.R. Chapman	
The Steward Observatory Asteroid Relational Database.....	V-8 526
M.V. Sykes and E.M. Alvarez del Castillo	

## **SUMMARY OF PROGRESS**



01117 12  
PIA 1

## 1990 SUMMARY OF PROGRESS 1991

This year a broad-based strategy featuring evaluation of several attractive options for Indigenous Space Materials Utilization (ISMU) was implemented. After a detailed examination of various competing technologies, a number of existing projects-- such as those featuring ilmenite processing-- were continued; these are detailed below. Additionally, following the advice of the SERC Advisory Committee, the development of a plant for producing oxygen from carbon dioxide was chosen for a total system demonstration.

This new project resulted from a careful screening of candidate systems for scientific merit, engineering feasibility and significant payback impact on space missions. In addition to its obvious application to the Martian atmosphere, the plant could be used on Earth's moon for extracting oxygen from the carbon dioxide that would be one of the products of carbothermal reduction of ilmenite.

Full system engineering was demonstrated through detailed component selection, computer-aided design, thermochemical calculations, mechanical design, and smart sensor incorporation. A solid state electrolytic cell of zirconium, ordered to specification from a well known manufacturer, constituted the heart of the system. This was installed and operated at SERC in the new Mobile Space Engineering Laboratory (MSEL), using authentically simulated (anaerobic) carbon dioxide, and the oxygen production rate was found to be consistent with cell specifications. Thermal and electrical controls were proven through innovative automated designs involving several engineering departments.

Research on high-temperature seals, alternative cell materials and geometries, catalysis for compactness, autonomous automation, and scale-up continues. Cell design was examined by Professor Sridhar, for possible improvements through the use of other materials with different chemistries and innovative geometries. Several new classes of materials, electrodes and catalysts were investigated. The most promising of these shows almost an order of magnitude improvement in the oxygen production rate while operating at a lower temperature. This demonstration also provided an opportunity to prove the self-contained design and packaging that will be necessary in space missions.

This development is being led technically by Professor Kumar Ramohalli, Principal Investigator for Engineering, who also leads the key Figure-of-Merit development and coordinates the other engineering projects that follow.

Rational selection of processes and plants from a variety of options can only be accomplished after examining overall mission impact. The Figure-of-Merit approach to mission design was created for this purpose. During the year the method was updated and interfaced with a data base. Over eight hundred individual factors, that vary from cryogenic storage to power source and plant mass, are now considered. Results clearly demonstrate the advantages of ISMU over all earth-transported systems in a quantitatively interpretable manner. Of equal significance is the ability to evaluate new component options for systems under consideration.

The continuing ilmenite reduction work of Professor Shadman established that hydrogen reduction is faster and more complete than carbon monoxide reduction. Both of these processes were studied as functions of flow rate and temperature in a series of detailed experiments-- outstanding pioneering research that resulted in several technical publications.

Professor David Lynch demonstrated that one to two orders of magnitude improvement in rates of ilmenite conversion are possible through plasma chlorination. His experimental equipment was completed, and operated consistently for a number of runs. A modification was made that will allow the possibility of driving these reactions by solar radiation is to be evaluated. Professor Lynch also initiated a project on chemical compressors for concentrating extraterrestrial gas feedstocks. The consequent reduction of mechanical complexity should greatly improve reliability.

Propellant storage is also an important ISMU issue. In realistic scenarios high densities are desired for reducing container mass, and off-earth production must exceed use from the start. A low-level effort was also begun by Professor Ramohalli to investigate the most promising high-density propellant combinations, as well as their storage and end-use behavior.

Professor Charles Glass continued his experiments using ground-penetrating radar. The mobile apparatus was operated on a dry river bed near Tucson, varying the frequency of the signal, and thereby the depth of penetration and resolution of detail. It was demonstrated that depths up to nine meters could be mapped, and specific details could then be resolved down to five centimeters. Subsurface cavities are easily detected. Continuous profiling of real-time data using a single neural network was demonstrated, and a large tank (7 ft. in diameter and 7 ft. deep) was constructed and filled with a homogenous medium for verification tests.

Computer animation of a hypothetical extraterrestrial oxygen production plant was produced by Professor Nikraves and his students. The program they devised is flexible and can be easily updated, modified and expanded. A video tape made from its output attracted considerable attention in the media. Additionally, by introducing modern computer graphics to a number of undergraduates, the project proved to have much educational value.

Professor Desai installed a general purpose high-temperature vacuum oven that is being shared by several investigators. Using a simulated lunar soil consisting of ground basalt, typical specimens varying in degree of compaction, temperature-time history, particle size, and metallic additives were made for testing a variety of mechanical properties. The work will continue with more realistic simulants including agglomerates during the coming year.

Professor Fabes began a new project to investigate glass-ceramic and composite production from lunar regolith. Products made locally of such materials-- from heat shields and building blocks to surface coatings for protection, sealing and reflectivity-- will find many applications.

Any conceivable ISMU plant must be highly automated. Professors Schooley, Cellier and Ziegler are developing a control/monitoring/communication system model for such a plant. This year they demonstrated the smart sensor concept, which features distributed intelligence, through temperature control of the electrolytic oxygen cell described above. Remote control of the system located in the MSEL is intended.

SAIC in San Diego, under subcontract to the Center, produced samples of glass fiber embedded (<5%, by mass) composites from simulated lunar soil, as well as a complete hemispherical segment dish. This 14" diameter demonstration piece clearly demonstrates the feasibility of manufacturing low technology solar collectors on site in a non-energy intensive way.

The engineering developments described above were supported and extended by a strong science program. Technical coordination of this program is provided by Professor John Lewis, Principal Investigator for Science, who also leads the achondritic meteorite sample preparation and gaseous carbonyl processing projects described below.

Since lunar soil samples are both limited and very difficult to obtain, simulants must be used for much of the SERC program. Crushed basaltic samples, perhaps with glassy spheres added, can be utilized in some experiments, but not in processing studies where chemical reactions are critical. Professor Lewis determined that a reasonably close match in chemical composition was provided by a certain basaltic achondrite meteorite found in Australia, and was able to obtain several large pieces.

Some of these meteoritic fragments were reduced to the proper particle size distribution and prepared for Professor Ruiz to use in his ilmenite separation studies, prior to working with actual Apollo samples. His experiments with regolith simulants suggest that neither magnetic nor electrostatic separation by conventional rotating-drum techniques can be operated efficiently enough to avoid processing very large amounts of  $\text{Fe}^{3+}$  - free regolith rich in agglutinates. Methods of improving the efficiency are being sought, and the possibility of using crushed basaltic rocks instead of fines is being studied.

Professor Lewis' group also continued to pursue gaseous carbonyl processing as a way to extract and purify ferrous metals from lunar soils. The process lends itself to thin film deposition of such metals at low temperatures and the casting of intricate shapes. Cobalt with a high concentration of platinum-group and precious metals is one of its byproducts. An extensive review of the pertinent literature was completed, planning for critical experiments begun, and the necessary equipment ordered. Experiments carried out by W. Jenkin under this project have shown a promising degree of control over iron metal deposition achieved by varying the carrier gas composition.

Closely related is the research effort led by Professor Freiser to discover an efficient method of recovering platinum-group and other precious and strategic metals from lunar and asteroidal materials, including the complex deposits that form on electrodes during magma electrolysis. A variety of experiments featuring solvent extraction were performed. The results were promising and these are continuing.

Also in support of this program, Professor Ganguly continued his work on volatile release from carbonaceous meteorites, performing systematic experiments on the dehydration of OH-silicate talc. Substantial progress was made on the development of computational tools for modeling the time-temperature kinetics and equilibrium chemistry of carbonaceous chondritic material, aimed toward near future experiments with CM chondrite material and eventual process design.

Under subcontract to SERC, Professor Larry Haskin's research on magma electrolysis, an oxygen recovery process requiring no beneficiation of feedstock, was concentrated in three areas during the year. These were: the measurement of atomic solubilities of metals in silicate melts; electrolysis experiments under various conditions of temperature, container material, electrode configuration, current density, melt configuration, and sample mass (100 to 200 mg)-- measuring the energy required and determining the character of the resulting products; and theoretical assessment of compositional requirements for steady-state operations of an electrolysis cell.

The conditions to optimize oxygen production by this method were defined last year, and the dependence of conductivity on melt composition, as well as the dependence of efficiency on  $\text{FeO}$  concentration, and cathodic/anodic reactions, were studied in detail. Results were judged sufficient to establish feasibility, and a related SERC subcontract was awarded to Dr. Rudolph Keller to begin coordinated tests at near industrial scale. A 7 inch diameter high-temperature furnace was purchased, an appropriate crucible designed and built, and complementary experimentation begun.

The fundamental studies of microwave sintering performed by Professor Thomas Meek, also under a SERC subcontract, complements the engineering research of Professor Desai on possible lunar construction materials. Samples closely approximating actual lunar soil samples in their composition were prepared and tested. Melting occurred first at grain boundaries, requiring much less energy than gross melting to achieve binding, and frequency-sensitive gas emission was observed, suggesting another possible oxygen production technique.

The research conducted by Professor Singer and his students is focussed on lunar resource assessment. By means of a telescope located on a mountain top within the city limits of Tucson, and CCD image processing, dramatic progress was made in locating areas of high  $\text{TiO}_2$  concentration, indicating the presence of substantial ilmenite deposits, on the surface of the full moon. Results can be displayed in a variety of enhanced colors to aid interpretation.

Professor Tom Gehrels achieved remarkable results with his Spacewatch telescope and new 2048 x 2048 CCD asteroid-locating computing system. No less than six new Earth-crossing asteroids were discovered and later verified by others! Orbital transfer calculations for space science and resource return missions are being calculated by Professor Lewis.

Complementary to this research, Professor Larry Lebofsky and Dr. Marcia Nelson continued the application of Hapke theory to the difficult task of characterizing asteroids, especially estimating their water content. Extensive calculations were carried out for the limited number of asteroidal bodies for which reflectance data are available-- arriving, as yet, at no definite conclusions.

Also promising in this regard is the relational asteroid/comet database work supervised by Professor Sykes. The creation of an appropriate file storage format and development of specialized search/sort routines in dBase language made it possible to quickly isolate classes of these bodies (such as all known asteroids that cross within a certain distance of the Earth) and display everything known about them.

Of course, compilation of this database continues; as does further development of the SERC database in dBase format supervised by Dr. Andrew Cutler. Initially, the latter is concentrated on oxygen production references, which were made available on disk during the year, but will be expanded to cover a much wider range of space resource topics in succeeding years.

This brief summary merely illustrates the range of the Center's work during 1990-91. Complete treatments of all the projects noted and the results they obtained during the year may be found in our Annual Progress Report (APR-91). But perhaps it will serve to show the range and highly integrated character of the Center's research and development program-- and to emphasize our stress on demonstrations and full-system engineering, while carrying out a broad mixture of innovative programs in support of cost effective space missions.

Dr. T. Triffet  
Director

## **PUBLICATIONS**

## **SERC/culpr PUBLICATIONS**

The following publications of the Center are available without charge to qualified organizations and may be obtained by written request to the Director.

Those marked with an asterisk are finished products featuring overviews for corporate, government and university management, while those preceded by a dash are designed for the primary purpose of attracting potential students. The remainder contain detailed technical information on research and development projects, and are published in simplified form, with standardized binding and slightly non-uniform format, to permit rapid dissemination of results.

- \* **PB-89** Program Brochure 1988-89
- \* **AER-90** Annual Executive Report 1989-90
- \* **Newsletter** Vol. 1, Nos. 1-4, 1989-90  
Vol. 2, Nos. 1- , 1990-91
  
- **AF-88** Advance Flyer 1987-88
- **CP-88** Center Poster 1987-88
  
- APR-89** Annual Progress Report 1988-89
- APR-90** Annual Progress Report 1989-90
- APR-91** Annual Progress Report 1990-91
  
- First Annual Symposium** on Space Mining  
and Manufacturing 1989
- AIS-89/A** Abstracts
- AIS-89** Proceedings
- Second Annual Symposium** on Resources of  
Near-Earth Space 1990
- AIS-90/A** Abstracts
  
- WR-89/1** Automation of Extraterrestrial  
Sources of Oxygen Production  
Workshop (AESOP) Report 1989
- TM-90/1** Mining Lunar Soils for He-3 1990

# **I. PROCESSING OF PROPELLANTS, VOLATILES AND METALS**

## **A. REDUCTION OF LUNAR REGOLITH**



51-26  
14661  
N91-24366

Coproduction of Volatiles and Metals from Extraterrestrial Materials

J. S. Lewis

Lunar and Planetary Laboratory  
The University of Arizona

AX 800000

Abstract

This report covers two main efforts in support of the general goals of SERC/culpr

1. We continue to investigate processes for the coproduction of metals from extra-terrestrial materials in conjunction with plausible schemes for oxygen extraction. Our principal emphasis has been upon the extraction and purification of iron from the ilmenite reduction process for oxygen, from the cathode metal deposits made in the magma electrolysis process for oxygen, and from native ferrous metal alloys on the Moon and asteroids. All work on the separation and purification of ferrous metals has been focussed upon the gaseous carbonyl process, a scheme that involves only temperatures attainable by passive thermal control.

2. We have begun to explore a variety of schemes, involving the use of several different propulsion options and both propulsive and aerobraking capture at Earth, for return of extraterrestrial resources to Earth orbits.

In addition, we continue to search out new opportunities in space resource utilization. Examples include continuation of work underway on the feasibility of locating Solar Power Satellites in highly eccentric Earth orbit, on the energetics of extracting the potential clean fusion fuel  $^3\text{He}$  from the atmosphere for return to Earth, and on the utility of a nuclear steam rocket (using non-terrestrial water as the working fluid) for transportation in the inner solar system.

Introduction

In the broadest sense, an academic research center should be only loosely coupled to immediate practical concerns. Instead, it should seek vigorously to look at the broadest possible spectrum of opportunities. SERC's prime responsibility is to be the first to recognize potentially important new resources, to anticipate future human needs, to explore processing schemes and transportation techniques, and to identify the practical implications of the availability of non-terrestrial resources.

More specifically, one central effort of SERC activities is the extraction of volatiles from nonterrestrial materials for use principally as propellants. Because of the crucial role of oxygen as the dominant component of likely fuel/oxidizer combinations, extraction of oxygen from lunar and asteroidal materials has been given the highest priority. It seems clear, however, that any process that produces oxygen on the Moon will result in the coproduction of free ferrous metals in relatively large amounts. Any scheme that makes these metals into useful products with only a minor additional use of energy will greatly increase the total mass of useful product per unit of energy expended. The availability of a demonstrated, efficient scheme for coproducing oxygen and metals (and/or refractories) may be the deciding factor in the choice of the oxygen-manufacturing technology to be used on the Moon.

The two most extensively studied scheme for lunar oxygen production, the chemical reduction of ilmenite and magma electrolysis, are under intensive study at SERC. The two most pressing problems

/A-1

with ilmenite reduction are: 1) providing a reasonably clean ilmenite feedstock and 2) deciding which reducing agent to use and how to recycle it. The former is under study by Prof. Joachin Ruiz, who is working on electrostatic and magnetic beneficiation techniques for extraction of ilmenite from either the lunar regolith or crushed lunar basalts. The latter problem is under study by Prof. Farhang Shadman, who is exploring the kinetics of ilmenite reduction by gaseous hydrogen and carbon monoxide. The second scheme is being addressed Prof. Larry Haskin and Dr. Rudy Keller, who are studying electrochemical reduction of molten lunar simulants. The metallic byproducts of these two processes (metallic iron from ilmenite reduction and a complex metallic cathode deposit from magma electrolysis), as well as native ferrous metal alloys, are attractive starting materials for our extraction, separation, and fabrication schemes using gaseous carbonyl technology.

### Progress in the Past Year

We have actively pursued the issues presented by the coproduction of metals with oxygen on the Moon. The technology we have chosen to emphasize is the gaseous carbonyl process for extraction, separation, purification and deposition of the ferrous metals. The fundamental patents for nickel carbonyl extraction are owned by INCO, and Formative Products Inc. holds most of the proprietary technology for fabrication of products by vapor deposition of nickel from nickel tetracarbonyl. We have surveyed the literature on the synthesis, purification, and handling of the transition metal carbonyls, and have designed and are building simple experimental setups for investigating carbonyl process applications to extraterrestrial settings. We have enlisted the participation of William Jenkin, the founder of Formative Products and developer of the commercial nickel-deposition technology, as a consultant on this project. He is working with us in a joint effort to develop new technologies to adapt the present carbonyl technology to space materials and conditions. Historically, carbonyl chemical vapor deposition (CVD) of nickel has been carried out commercially for many years. But iron, which is much more abundant (40-93%) than nickel (6-60%) in native non-terrestrial metals, has never been commercially fabricated into any product except analytic grade iron powder. The challenge has been to find a direct use for iron carbonyl CVD in fabricating "castings" or strong films.

We in our laboratory are concentrating on the volatilization behavior of native ferrous metal alloys with compositions relevant to the lunar regolith, metallic coproducts from lunar oxygen production schemes, and meteoritic metal alloys. Jenkin has been working on techniques for carbonyl CVD of iron. He has successfully demonstrated for the first time the deposition of pure, tough films of metallic iron by varying the carrier gas composition during iron carbonyl CVD.

We have also begun a program of calculation of opportunities for scientific and resource-retrieval spacecraft missions to near-Earth asteroids and the Mars system. We have so far screened the most recently discovered asteroids (for which no trajectory calculations have been reported previously) for their accessibility from low Earth orbit (LEO) and for the ease of return to Earth-intercept.

We have also examined the energetic and technological feasibility of returning the potential clean fusion fuel  $^3\text{He}$  to Earth from the atmosphere of Uranus. The attraction of Uranus is that  $^3\text{He}$  is present in a cold, dense gas mixture (hydrogen, helium, methane) with a concentration of 45 ppm. The alternative scheme for retrieval of nonterrestrial  $^3\text{He}$  is based upon extracting solar-wind-implanted gas from the lunar regolith, where it has a concentration of only 0.01 ppm. We find that a single-stage-to-orbit nuclear rocket using liquid hydrogen as the working fluid can get the payload out of the Uranus atmosphere. The total energy cost per kilogram of  $^3\text{He}$  returned to Earth is 1000 times smaller for  $^3\text{He}$  from Uranus than from the Moon.

Finally, we have developed a scheme for fabrication of Solar Power Satellites from non-terrestrial materials in highly eccentric Earth orbit (HEEO). The advantages of HEEO are: a) HEEO is energetically more accessible than GEO (3.0 vs. 4.0 km/s above LEO) for conventional launch from Earth, and hence chemical boosters can deliver larger payloads to HEEO than to GEO, b) the total delta V for propulsive or aerobraking material return to HEEO is always much smaller than to GEO or LEO, regardless of whether the material originates from the Moon, the Mars system, or near-Earth asteroids, c) HEEO is nearly at Earth escape velocity, but allows propulsive escape burns to occur deep in Earth's gravity well, where they are most efficient, d) HEEO is much more accessible than GEO (or LEO) via electromagnetic launch from Earth's surface or the lunar surface, due to the very small post-launch delta V requirements for orbit-matching and rendezvous, e) return to Earth (or LEO) from HEEO is easier than from GEO, involving a much lower propulsive delta V and an equal or slightly higher reentry heating load. For similar reasons, HEEO is a highly desirable location for a refueling depot and propellant plant.

#### Related Publications

T.D. Jones, L.A. Lebofsky, J.S. Lewis and M.S. Marley, The Composition and Origin of the C, P and D Asteroids: Water as a Tracer of Thermal Evolution in the Outer Belt. *Icarus* **88**, 172-192 (1990).

J.S. Lewis, Asteroid Resources. In: *Proceedings of the La Jolla Workshop on Space Resources*. In press (1990).

J.S. Lewis, Lunar, Martian and Asteroidal Resources: Programmatic Considerations. In: *Proceedings of the 1989 Annual Invitational Symposium of the UA/NASA Space Engineering Research Center*, 1-10 (1990).

J.S. Lewis, Nonterrestrial Resources. In: *Space Manufacturing I*, 5-10 (1990).

J.S. Lewis, K. Ramohalli and T. Triffet, Extraterrestrial Resource Utilization for Economy in Space Missions. International Astronautical Federation, IAA 90-604 (1990).

T.D. Swindle, J.S. Lewis and L.A. McFadden, The Case for Planetary Sample Return Missions 4: Asteroids. Submitted (1991).

J. S. Lewis,  $^3\text{He}$  for Fusion Power: The Willie Sutton Principle. In preparation (1991).

J.S. Lewis and M. Elowitz, Construction Materials for an SPS Constellation in Highly Eccentric Earth Orbit. In preparation (1991).

M.L. Hutson and J.S. Lewis, Enstatite Chondrites and Achondrites as Asteroidal Resources. In preparation (1991).

52-25  
N91-24867

p.29

Production of Oxygen From Lunar Ilmenite

F. Shadman and Y. Zhao

Department of Chemical Engineering

The University of Arizona

Abstract

The kinetics and the mechanism of reduction of synthetic ilmenite by hydrogen in the temperature range of 807-1014°C were investigated. At temperatures below 876°C, the temporal profiles of conversion have a sigmoidal shape and indicate the presence of three different stages (induction, acceleration and deceleration) during the reduction reaction. The apparent activation energy for the reaction is 22.3 kcal/mole, whereas the intrinsic activation energy is 16.9 kcal/mole. Scanning electron microscopy and energy dispersive X-ray analyses show that the diffusion of Fe product away from the reaction front and through the TiO<sub>2</sub> phase, followed by the nucleation and growth of a separate Fe phase is an important step affecting the process kinetics. X-ray diffraction and wavelength dispersive X-ray results indicate that the TiO<sub>2</sub> can be reduced to lower oxides of titanium at temperatures higher than 876°C.

Introduction

Oxygen is a consumable material which needs to be produced continuously in most space missions. Its use for propulsion as well as life support makes oxygen one of the largest volume chemicals to be produced in space. Production of oxygen from lunar materials is of particular interest and is a very attractive possibility.

The solid state metallurgical processes for recovering metals from ores are important as potential replacements for conventional smelting and wet chemistry techniques. An industrially important process receiving a great deal of attention is the solid state separation of titanium dioxide and iron present in ilmenite (chemically iron titanate, FeTiO<sub>3</sub>). In industrial practice, ilmenite or titanomagnetite ores are smelted with carbon in high temperature furnaces. This process produces pig iron and a titania-enriched slag. The pig iron can be employed for castings while the slag can be further processed to extract titanium dioxide. This conventional smelting route has a number of serious disadvantages. Firstly, the electric furnace smelting is energy intensive. Secondly, in the smelting processes, it is necessary to produce a fluid titania-enriched slag. Thus, in this case, slag-forming reagents, which lower the melting point and the viscosity of the slag phase, must be added. These additives dilute the concentration of titanium dioxide in the slag and have deleterious effects on the subsequent processes for extracting titania from the slag (Merk and Pickle, 1988). Therefore, it would be beneficial to develop a direct reduction

process which produces a solid slag and coarse iron particles which can be removed by either leaching or mechanical separation methods.

In recent years there has been a rising interest in the solid state reduction of ilmenite ores. This interest is linked with the process for winning oxygen from lunar materials (Cutler and Krag, 1985; Zhao and Shadman, 1989, 1990). Ilmenite, a mineral found in substantial quantities in lunar maria (Lewis, 1987) is an attractive source of oxygen because of its relatively low reduction temperature as compared to silicon, aluminum, titanium, calcium or magnesium oxides in the lunar soil. Iron oxide reduction can also produce iron and titanium dioxide as co-products. In addition, Agosto (1986) has concluded that ilmenite can be obtained from lunar soil at high purity using electrostatic separation techniques. The ilmenite may be heated with hydrogen gas (brought up from the earth) in the temperature range of 600°C to 1000°C. The products are water vapor and an intimate, and probably sintered, mixture of solid metallic iron with titanium dioxide (the mineral rutile). The water vapor is condensed and dissociated by electrolysis. The products of electrolysis are oxygen which is liquefied for use as a propellant and for life support, as well as hydrogen, which is recycled through the ilmenite reactor.

Most previous studies have been on naturally occurring ores using carbon or CO as reducing agents (Wouterlood, 1979; Jones, 1975). From a fundamental point of view, the results of such studies are difficult to interpret because of the complex nature of the ores, the presence of many components, and the inherent variations in ore composition. Consequently, the fundamental kinetics and mechanism of ilmenite reduction by hydrogen are not well understood. Briggs and Sacco (1988) studied the reduction of ilmenite by hydrogen at 600°C and 800°C. The ilmenite used in their study contained about 8% ferric iron. They found that some preoxidation of ilmenite by oxygen prior to reduction can decrease the complete reduction time of samples. During preoxidation, the ilmenite is converted to pseudobrookite ( $\text{Fe}_2\text{TiO}_5$ ) and rutile. The single crystals of ilmenite are converted, therefore, into a polycrystalline array of pseudobrookite and a fine dispersion of rutile (Barnes and Pickles, 1988). Carbotek (1988) has developed a fluidized-bed reactor for the reduction of ilmenite by hydrogen at the temperature between 900°C and 1000°C. Terrestrial ilmenite was used in this study. They demonstrated the feasibility of producing oxygen from terrestrial ilmenite by first reducing the terrestrial ilmenite and then electrolyzing water to produce oxygen and hydrogen which is returned to the reactor. They also reported that the reaction is first order with respect to hydrogen under their experimental conditions. Bardi *et al.* (1987) investigated the kinetics of hydrogen reduction of Norwegian ilmenite ore powders. They found that the activation energy value of a surface chemical reaction was 34.8 kcal/mole in the temperature range of 654°C-1007°C. The electron microprobe analysis of the reduced Norwegian ilmenite grains showed the existence of a segregated iron phase present as spheroidal nodules and a  $\text{TiO}_2$  phase present as vein-like arrangements. Their optical

microscopic study on sections of synthetically prepared  $\text{FeTiO}_3$  showed separate reacted and unreacted zones in the sample particles.

The purpose of the present study is to obtain fundamental information on the kinetics and the mechanism of ilmenite reduction by hydrogen under conditions where the original ilmenite and the final products are well characterized. The emphasis is on ilmenite with no ferric impurities present. This is important in applying the results to the reduction of lunar ilmenite.

In this phase of the work the emphasis has been on the kinetics and mechanism of simulated lunar ilmenite reduction by hydrogen and  $\text{H}_2/\text{CO}$ , the comparison of  $\text{H}_2$  reduction with  $\text{CO}$  reduction and the development of a novel process flowsheet for the carbothermal reduction of lunar ilmenite.

### Experimental Approach

A schematic diagram of the experimental apparatus is shown in Figure 1. The main components of this system are an electronic microbalance (Cahn Instruments, Inc., Model 1000), a quartz flow through reactor, and a movable furnace with a PID temperature controller. The composition of the gaseous reactants was determined using gas chromatography. Ilmenite was used in the form of thin flakes pressed from powder. Samples were suspended from the microbalance, which allowed monitoring weight changes during the course of an experiment. A thermocouple was used to monitor the temperature of the reactor around the flake. All experiments were performed under isothermal conditions at temperatures between  $807^\circ\text{C}$  and  $1014^\circ\text{C}$ . The reducing gas entering the reactor was a mixture of  $\text{H}_2$  and  $\text{N}_2$ . The gas flow rate was 660 std.cc/min, except in the experiments conducted to determine the effect of interphase mass transfer on the reduction rate.

Samples of starting material were prepared by cold pressing 0.270 g of  $\text{FeTiO}_3$  powder (with particles size less than  $45\ \mu\text{m}$ ) in a 12.2 mm diameter die at 552 MPa for 5 minutes to form disks. The disks were then cut into flakes approximately 10 mm by 8 mm. The thickness of the disks was 0.60 mm.

Each experiment was started by first purging the reactor system at room temperature to reduce the concentration of oxygen to levels below 10 ppm. A mixture of  $\text{H}_2/\text{N}_2$  was then introduced into the reactor. To initiate the reduction, the furnace was raised rapidly. In less than three minutes, the temperature of the reaction zone was within 1% of the set point temperature. The experiments were terminated at a desired conversion by lowering the furnace.

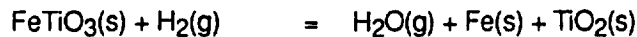
Several techniques were used for chemical analysis and characterization of the starting material and the reduced samples. Mossbauer spectroscopy was employed to determine the oxidation state of iron in our synthetic ilmenite. X-ray diffraction (XRD) with a cobalt  $\text{K}\alpha$  source was used to identify the different crystalline phases in the starting material and the products. High-

resolution scanning electron microscopy (SEM), energy-dispersive X-ray (EDX) and wavelength-dispersive X-ray (WDX) analyses were employed to examine the polished cross section of both partially and completely reduced samples and to determine the elements present in each phase. For SEM, EDX and WDX analyses, the samples were mounted in an epoxy resin and polished to expose the cross-section of the grains.

### Theoretical Approach

A mathematical model is formulated to describe the simultaneous reaction and diffusion that occur in the ilmenite flakes used in the experimental part of this study. The flakes were uniform and thin; therefore, the geometry assumed for mathematical modelling is that of an infinitely long and wide slab. This configuration was selected because it gives the desired information on the kinetics of ilmenite reduction without complications of sample shape. Thin flakes are also suitable for polishing as needed in the microprobe studies. It is assumed that the flakes consist of spherical and equal-sized grain particles of ilmenite. Based on the SEM micrographs and image analysis of grains in a flake, the overall size of a flake and the size of an individual grain do not change significantly during the reaction.

The reaction considered is as follows:



The following additional assumptions are made:

- (1) The pseudo-steady state approximation is appropriate for describing the concentration of the gaseous species within a flake.
- (2) The system is isothermal.
- (3) The effective diffusivities of gaseous reactant and product are equal and uniform throughout the flake.
- (4) The reaction is first order with respect to  $\text{H}_2$  and  $\text{H}_2\text{O}$ .
- (5) The grain particles have little porosity and react following a shrinking-core mechanism.

The conservation equations for hydrogen, A, and water, C, can be written as follows:

$$D_e \nabla^2 C_A - R_A = 0 \quad (1)$$

$$D_e \nabla^2 C_C + R_A = 0 \quad (2)$$

The local rate of reaction based on the grain particles is given by the standard shrinking core model:

$$-\rho_s \frac{dr_c}{dt} = k \frac{C_A - C_c/K}{1 + \frac{k(1+1/K)}{D_{eg}} \left(1 - \frac{r_c}{r_s}\right) r_c} \quad (3)$$

Dividing Equation (2) by K and subtracting from Equation (1) gives:

$$D_{eg} \nabla^2 (C_A - C_c/K) - R_A (1 + 1/K) = 0 \quad (4)$$

The initial and the boundary conditions for (3) and (4) are

$$\text{at } t=0 \quad r_c = r_s \quad (5)$$

$$\text{at } Z=L \quad C_A - C_c/K = C_{Ab} - C_{cb}/K \quad (6)$$

$$\text{at } Z=0 \quad \frac{d(C_A - C_c/K)}{dZ} = 0 \quad (7)$$

An expression can be obtained for the local rate of reaction  $R_A$ . For a flake in this study,  $R_A$  is given by:

$$R_A = 3 \frac{r_c^2}{r_s^3} \frac{(1-\epsilon) k (C_A - C_c/K)}{1 + \frac{k(1+1/K)}{D_{eg}} r_c \left(1 - \frac{r_c}{r_s}\right)} \quad (8)$$

The local conversion can be related to the unreacted grain radius as follows:

$$X_B = 1 - \left(\frac{r_c}{r_s}\right)^3 \quad (9)$$

The overall conversion for a flake is given by:

$$X = \left(\frac{1}{L}\right) \int_0^L X_B dZ$$

The solution to the model equations was obtained using the method given by Szekely *et al.* (1976). The method involves some approximation but is proven to represent the exact solution that must be obtained numerically.



### Results and Discussion

The impurity content of the ilmenite used in this study is given in Table 1. The XRD pattern of this ilmenite, as shown in Figure 2, suggests that the only crystalline phase in the sample is  $\text{FeTiO}_3$ . Mossbauer spectra of the sample shows that the ilmenite used in this study contains only  $\text{Fe}^{++}$ . This represents the oxidation state of iron in lunar ilmenite.

Table 1. Maximum Impurity Content in the As-Received Synthetic Ilmenite\*

Impurity	Maximum Concentration (Wt%)
Al	0.001
Ca	0.01
Cr	0.001
Cu	0.01
Mg	0.001
Si	0.1

\* CERAC, Inc.

For each experiment, the temporal profile of conversion was determined by monitoring the sample weight using a recording electrobalance. Initially, some experiments were conducted to determine the effect of transport resistance in the interphase around the flakes. The experiments were conducted at the highest temperature ( $1014^\circ\text{C}$ ) with 3.4%  $\text{H}_2$ . The results showed that the interphase resistance is not important if the flow rate is at least 660 std.cc/min. At temperatures below  $1014^\circ\text{C}$ , the interphase resistance is even less significant.

The results in Figure 3 show the effect of  $\text{H}_2$  concentration on the reaction at  $945^\circ\text{C}$ . The  $\text{H}_2$  concentration was varied between 3.4% to 14.7% in  $\text{N}_2$  atmosphere. As expected, an increase in the hydrogen concentration results in an increase in the rate and a decrease in the time required to attain certain fractional weight loss, which is defined as the ratio of weight loss of the sample to initial weight of the sample. The reaction order with respect to  $\text{H}_2$  is established using the runs which were not influenced by diffusion in the ilmenite flake. The results, shown in Figure 4, indicate that the reaction order is unity in the  $\text{H}_2$  concentration range of 3.4% to 14.7% at  $807^\circ\text{C}$  and  $876^\circ\text{C}$ . This confirms the first order kinetics assumption presented in the theoretical section.

Isothermal weight loss measurements were performed at 807, 876, 945 and  $1014^\circ\text{C}$ . The temporal profiles of conversion at these four temperatures and  $\text{H}_2$  concentration of 3.4% are shown in Figure 5. The profile at  $807^\circ\text{C}$  has a sigmoidal shape and indicates the presence of three different stages (induction, acceleration and deceleration) during the reduction reaction. The profiles at  $876^\circ\text{C}$ ,  $945^\circ\text{C}$  and  $1014^\circ\text{C}$  do not have these three stages. As shown in Figure 5, the time required to attain the weight loss corresponding to 'complete iron metallization' when all

the iron in ilmenite is reduced to metallic iron, is 210 minutes at 807°C and 52 minutes at 1014°C with 3.4% H<sub>2</sub>. The effect of temperature on the reaction rate is shown in Figure 6. The apparent activation energy calculated based on initial rates is 22.3 kcal/mole.

The model formulated in the previous section was used to extract intrinsic reaction rate constant from the experimental measurements. A list of parameters used in the model is given in Table 2. The model agrees well with the experimental measurements. Sample results for model predictions at 945°C and 1014°C are shown in Figures 7 and 8. The Arrhenius plot based on the intrinsic reaction rate constants is shown in Figure 9. The intrinsic activation energy for the reaction on ilmenite core is 16.9 kcal/mole. The fact that apparent activation energy is higher than the intrinsic activation energy is unusual and intriguing. This observation is related to the initial induction period and will be explained later.

Table 2. Values of Model Parameters

Parameter (unit)	Value
$\epsilon$	0.33
$\epsilon_m$	0.19
$r_s$ (gmol/cm <sup>3</sup> )	0.032
Average $r_s$ (cm)	$7.2 \cdot 10^{-4}$
Thickness of flake (cm)	0.06
$D_e$ (cm <sup>2</sup> /sec)	1.040 (1014°C)
	0.950 (945°C)
$D_{eg}$ (cm <sup>2</sup> /sec)	0.034 (1014°C)
	0.033 (945°C)
$K$	0.11 (1014°C)
	0.09 (945°C)

To gain insight into the mechanism of the ilmenite reduction, samples of both completely and partially reduced ilmenite were analyzed using various analytical techniques. In particular, a combination of optical microscopy, SEM, EDX, WDX and XRD analyses provided very useful information on the nature and the distribution of various solid products.

SEM backscattered electron micrographs of the polished cross-section of ilmenite flake after partial reduction at 1014°C and 807°C are shown in Figures 10a and 11a. The micrographs reveal three distinct regions which appear as bright, light gray and dark gray phases. In order to identify

these phases, quantitative EDX was performed at spots marked in Figures 10a and 11a. These results and the XRD observations (to be discussed later) show that the bright phase is primarily iron; the dark gray phase is titanium dioxide and the light gray phase is unreacted  $\text{FeTiO}_3$ . These results suggest that there is a strong tendency towards the segregation of the products iron and titanium dioxide, and that iron diffuses out of the grain particles through the  $\text{TiO}_2$  layer during the reduction. This finding has important implications for product separation and recovery of Fe and  $\text{TiO}_2$  from ilmenite, particularly for the application of magnetic separation method.

Since the reduction temperatures are much lower than the melting point of  $\text{TiO}_2$ , The  $\text{TiO}_2$  product is expected to be in polycrystalline form. Figure 10a and 11a indicate that the reaction in the grain particles proceeds according to the shrinking core model. This is because the grain particles of synthetic ilmenite are nearly nonporous, whereas the product  $\text{TiO}_2$  is porous. The corresponding X-ray map of iron and titanium, shown in Figures 10b, 10c, 11b and 11c, confirm the shrinking core configuration. Moreover, SEM micrograph in Figure 11a indicates that hydrogen penetrates more into the unreacted ilmenite at  $807^\circ\text{C}$  than at  $1014^\circ\text{C}$ . The polished cross-sections of synthetic ilmenite flakes after complete reduction at  $876^\circ\text{C}$  and  $945^\circ\text{C}$  were also examined by SEM and EDX. The results obtained at  $945^\circ\text{C}$ , as shown in Figures 12, confirm the complete segregation of products iron and titania. The EDX analyses of these samples indicate that the phase enriched in titanium is depleted in iron and vice versa.

In an earlier study in our laboratory, the kinetics and mechanism of ilmenite reduction with carbon monoxide were investigated (Zhao and Shadman 1990). The results showed that the reduction of  $\text{TiO}_2$  did not take place at any appreciable rate in the temperature range of  $800^\circ\text{C}$  to  $1100^\circ\text{C}$ . However, the experimental results for the ilmenite reduction by hydrogen in Figure 3 show that the total weight loss of the sample exceeds the weight loss corresponding to 'complete iron metallization'. This indicates that titanium dioxide can be reduced by hydrogen in the temperature range of  $876^\circ\text{C}$  to  $1014^\circ\text{C}$ . The rate of reduction of titanium dioxide depends on both the hydrogen concentration and the reaction time. The reduction of titanium dioxide has practical significance in the production of oxygen from lunar ilmenite, since 67% of oxygen in ilmenite is bound to titanium.

In order to understand the mechanism of titania reduction by hydrogen, the electron microprobe with wavelength dispersive X-ray analysis was employed to determine the atomic ratio of oxygen to titanium in the reduced titanium dioxide phase. The analyzed area of the grain in the sample reduced at  $1014^\circ\text{C}$  is shown in Figure 13. For each sample, the analyses for titanium and oxygen were performed across the two polished grains. One is located at the edge of the flake; the other is located at the center. The results obtained from these two grains are very similar. The results showing the extent of reduction of  $\text{TiO}_2$  are given by Figure 14 and indicate that the

reduction of titania took place throughout the titanium dioxide matrix in each grain. These observations suggest that the reduction of titanium dioxide in each grain and across the flake is kinetically controlled.

Another important point related to the reduction of  $\text{TiO}_2$  is its inception relative to iron reduction. To further study this, two partially reduced samples were prepared at  $1014^\circ\text{C}$  and 14.7%  $\text{H}_2$ , the first one at 35% conversion and the second one at 70% conversion. The results of WDX analysis showed that the  $\text{TiO}_2$  phases in both samples had not been reduced at either conversions. These results indicate that the reduction of  $\text{TiO}_2$  does not occur to any significant extent as long as iron metallization is not completed. It is speculated that this is related to inhibition effect of water vapor as the reaction product. During ilmenite reduction (iron metallization), the concentration of water vapor inside the  $\text{TiO}_2$  pores is high enough to inhibit the  $\text{TiO}_2$  reduction. However, as iron metallization approaches completion, the inhibition effect decreases and  $\text{TiO}_2$  reduction starts. The mechanism of  $\text{H}_2\text{O}$  inhibition is not known and is currently under study.

The XRD spectra of partially reduced samples are shown in Figure 15b. The phases present after partial reduction at  $807^\circ\text{C}$  and  $1014^\circ\text{C}$  are iron, titanium dioxide and unreacted ilmenite. Figure 15a is the XRD spectrum of sample reduced at  $807^\circ\text{C}$  with 'complete iron metallization', and indicates the presence of Fe and  $\text{TiO}_2$ . The samples reduced at  $876^\circ\text{C}$ ,  $945^\circ\text{C}$  and  $1014^\circ\text{C}$  with 13% fractional weight loss were also analyzed using XRD. The patterns, shown in Figure 15c, indicate that all the peaks of  $\text{TiO}_2$  phases disappeared, which confirms the reduction of  $\text{TiO}_2$  by  $\text{H}_2$ .

The various observations described here point to a mechanism consisting of the following main steps for the reaction in each grain:

1. Diffusion of  $\text{H}_2$  through the porous product layer of titanium oxide towards the unreacted core of the grain particles.
2. Reaction of  $\text{H}_2$  with the ilmenite core to produce  $\text{TiO}_2$  and Fe.
3. Migration of Fe through the  $\text{TiO}_2$  layer away from the unreacted core towards the grain boundary.
4. Formation of iron nuclei and their subsequent growth outside and around the reacted grain particles.
5. Further reduction of  $\text{TiO}_2$  to lower oxides of titanium by hydrogen.

Steps 3 and 4 result in almost complete segregation of the two solid products, iron and titanium dioxide, on the scale of grains.

An important point concerns the driving force behind the migration of iron followed by its nucleation and growth around the grain particles. Iron produced during the reduction reaction is distributed in the pores of the product rutile and has a higher activity than the agglomerated pure

iron mass outside the grain particles. This is related to the fact that the small iron islands on the surface are less stable and move towards a large iron mass to agglomerate. Thermodynamically, this minimizes the total surface energy.

Using the proposed mechanism, the sigmoidal profiles of conversion and the three stages observed during ilmenite reduction can be described as follows:

- i) **Induction stage :** This represents the initial stage of the reduction process when the reaction rate is relatively low. The induction period is significant and observable at low temperatures. The induction period is definitely a genuine feature of the reaction mechanism and is not due to a delay in heating or similar experimental errors. A possible mechanism for the observed induction stage is the delay in the nucleation and growth of the iron phase. Initially, the iron produced by the reaction accumulates in the porous structure of the  $\text{TiO}_2$  product layer. In this stage, the rate of iron production is faster than the rate of iron transport out of the  $\text{TiO}_2$  layer. Consequently,  $\text{TiO}_2$  pores are partially plugged and  $\text{H}_2$  access to the reaction front is restricted. The induction stage is also present in the reduction of ilmenite by CO (Zhao and Shadman, 1990). However, the induction stage in the  $\text{H}_2$  reduction ilmenite is less significant than that in CO reduction. This is because hydrogen diffusivity in the pores is significantly larger than CO diffusivity. Therefore, the effect of pore blockage on  $\text{H}_2$  reduction is less than that on the CO reduction.
- ii) **Acceleration stage :** As the reaction goes on, more iron is produced and transported to the grain boundaries, forming new nuclei and increasing the growth rate of iron phase. This facilitates the transport of the iron and opens up the  $\text{TiO}_2$  pores. Consequently,  $\text{H}_2$  transport to the reaction front is enhanced and an increase in the reaction rate is observed. It is important to note that the rise in rate during the second stage is not due to any autocatalytic effect of iron accumulation. The nucleation and accumulation of iron is outside the grain particles and not on the reaction surface. The accumulated iron and the reaction interphase are separated by a layer of non-reactive titanium dioxide.
- iii) **Deceleration stage:** Finally, depletion of  $\text{FeTiO}_3$  results in a decrease in the rate of reduction.

The results indicate that the intrinsic rate is influenced by the pore blockage effect particularly at low temperature. As temperature increases, the iron mobility, nucleation and growth are enhanced and the pore blockage effect becomes less significant. This causes an increase in the observed initial rate which is separate and in addition to the usual increase in rate caused by increasing temperature. Due to these dual effects of temperature, the apparent activation energy calculated from the initial rate data is higher than the intrinsic activation energy.

Shomate *et al.* has shown that the theoretically possible conversions for the reduction of ilmenite by CO are 5.1, 6.6 and 7.8 percent at 827°C, 1027°C and 1227°C, respectively. At the

same temperatures, the theoretically possible conversions for the reduction of ilmenite by  $H_2$  are 5.1, 10.5 and 16.7 percent. Both carbon monoxide and hydrogen would be present in the gaseous stream if the process for the production of oxygen from ilmenite is based on the use of carbonaceous waste as a carbon source. Therefore, it is very important to compare the reduction of ilmenite by CO with the reduction of ilmenite by  $H_2$ .

The mechanisms of ilmenite reduction by  $H_2$  and CO are very similar. Both reactions involve the migration and nucleation of iron, leading to the complete segregation of iron from  $TiO_2$ . The main difference between these two reactions is that  $TiO_2$  can be reduced to lower oxides of titanium by hydrogen and the reduction rate of ilmenite by  $H_2$  is faster than that of ilmenite by CO.

The effect of temperature on both reactions is shown in Figure 16. The apparent activation energy for  $H_2$  reduction of ilmenite is 22.3 kcal/mol, whereas the apparent activation energy for CO reduction of ilmenite is 29.6 kcal/mol. This suggests that the reduction of ilmenite by CO is more sensitive to temperature than that by  $H_2$ .

In order to determine the effect of reducing agents on the reaction rate and the time corresponding to the 'complete iron metallization', two sets of experiments were conducted at the same condition. The results in Figures 17 and 18 show that the initial reaction rates of ilmenite reduction by  $H_2$  are 8.6 and 11.3 times larger than those by CO reduction at 1000°C and 900°C, respectively. The times corresponding to the 'complete iron metallization' are 12.5 minutes and 34 minutes at 1000°C and 900°C for  $H_2$  reduction of ilmenite, whereas, for the CO reduction of ilmenite, times are 95 minutes and 135 minutes at 1000°C and 900°C.

The flowsheet for a novel carbothermal reduction process has been developed and is shown in Figure 19. The components and their functions in this flowsheet are described as follows:

- (1) Carbon monoxide generation section.
- (2) Reactor with lower operation temperature: This reactor is designed to deposit carbon on lunar ilmenite. The thermodynamic calculation indicates that the deposit of carbon on lunar ilmenite can increase the oxygen yield significantly.
- (3) Reactor with higher operation temperature: This reactor is to carry out the carbothermal reduction of lunar ilmenite. The major products in this reactor are Fe,  $TiO_2$ , CO and  $CO_2$ .
- (4) Oxygen production section.

The staged reactor system with carbon deposition and reduction occurring at two different temperatures is a novel scheme that overcomes the inherent yield deficiency in other ilmenite reduction process.

In view of the presence of both CO and  $H_2$  in ilmenite reduction process based on the use of carbonaceous waste and due to the technical advantages in ilmenite reduction by  $H_2/CO$ , the kinetics and the mechanism of ilmenite reduction by  $H_2/CO$  is currently under study. The preliminary result is shown in Figure 20.

Acknowledgment

This research was supported by NASA/UA Center for Utilization of Local Planetary Resources at the University of Arizona. The NASA/UA Graduate College Fellowship for Y. Zhao is gratefully acknowledged. Discussions with Dr. A. H. Cutler are very helpful in this study.

Registry No.  $\text{FeTiO}_3$ (Ilmenite), 12168-52-4; Fe(Iron), 7439-89-6;  $\text{TiO}_2$ (Rutile), 1317-80-2.

Nomenclature

$C_A$ : concentration of  $\text{H}_2$ , gmol/cc

$C_{Ab}$ : concentration of  $\text{H}_2$  in bulk gas, gmol/cc

$C_C$ : concentration of  $\text{H}_2\text{O}$ , gmol/cc

$C_{Cb}$ : concentration of  $\text{H}_2\text{O}$  in bulk gas, gmol/cc

$D_e$ : effective diffusivity in macro-pores in flake,  $\text{cm}^2/\text{sec}$

$D_{eg}$ : effective diffusivity in the micro-pores of product layer in each grain,  $\text{cm}^2/\text{sec}$

$E$ : intrinsic activation energy, kcal/mole

$E_{app}$ : apparent activation energy, kcal/mole

$k$ : surface reaction rate coefficient, cm/sec

$k_{app}$ : apparent reaction rate coefficient, mg reacted  $\cdot$  L/original mg  $\cdot$  min mol

$K$ : equilibrium constant

$L$ : half thickness of the slab, cm

$RA$ : reaction rate, gmol  $\text{H}_2/\text{cm}^3$  bulk flake  $\cdot$  sec

Rate: reaction rate, mg reacted/original mg  $\cdot$  min

$r_c$ : radius of unreacted core in each grain, cm

$r_s$ : radius of grain, cm

$t$ : time, sec

$T$  = temperature,  $^{\circ}\text{K}$

$X_B$ : conversion of each grain

$X$ : overall conversion of flake

$Z$ : distance from the center of the slab, cm

Greek Symbols

$\epsilon$ : macro porosity

$\epsilon_{\mu}$ : micro porosity

$\rho_s$ : ilmenite molar density, gmol/ $\text{cm}^3$

Literature Cited

- Agosto, W.N.; *Electrostatic Concentration of Lunar Soil Minerals*; In *Lunar Bases and Space Activities of The 21st Century*, edited by W. Mendell, Lunar and Planetary Institute, 1980, 453.
- Bardi, G.; Gozzi, D.; Stranges, S.; *High Temperature Reduction Kinetics of Ilmenite by Hydrogen*; *Mater. Chem. and Phys.*, 1987, 17, 32.
- Barnes, C.; Pickles, C.A.; *A Thermogravimetric Studies of The Catalytic Effect of Alkali Carbonates on The Reduction of Ilmenite*; *High Temp. Technol.*, 1988, vol. 6 No 4, 195.
- Briggs, R. A.; Sacco, J. A.; *Oxidation and Reduction of Ilmenite: Application to Oxygen Production on the Moon*; Symposium sponsored by NASA, Houston (1988), paper No. LBS-88-170.
- Cutler, A.H.; Krag, P.; *A Carbothermal Scheme for Lunar Oxygen Production*; in *Lunar Bases and Space Activities in the 21st Century*, edited by W. Mendell, 1985, 559.
- Lewis, J.S.; Lewis, R.A.; *Space Resources, Breaking the bonds of Earth*; Columbia University Press, New York, 1987, 200.
- Merk, R.; Pickles, C.A.; *Reduction of Ilmenite by Carbon Monoxide*; *Can. Metall. Q.*, 1988, vol. 27 No. 3, 179.
- Gibson, M.A.; Knudsen C.A.; Roeger, A.; *Development of The CarboteK Process for Lunar Oxygen Production*; *Engineering, Construction, and Operations in Space Conference*, Albuquerque; New Mexico, April 23-26, 1990.
- Shadman, F.; Zhao, Y.; *Production of Oxygen from Lunar Ilmenite*; Annual Process Report, NASA/UA Center for Utilization of Local Planetary Resources, (1988-1989, 1989-1990).
- Szekeley, J.; Evans, J.W.; Sohn, H.Y.; *Gas-Solid Reaction*, Academic Press, 1976.
- Wouterlood, H.J.; *The Reduction of Ilmenite with Carbon*; *J. Chem. Tech. Biotechnol.*, 1979, 29, 603.



- Zhao, Y.; Shadman, F.; *Kinetics and Mechanism of Ilmenite Reduction with Carbon Monoxide*; *AIChE Journal*, 1990, vol. 36, No. 9, 443.

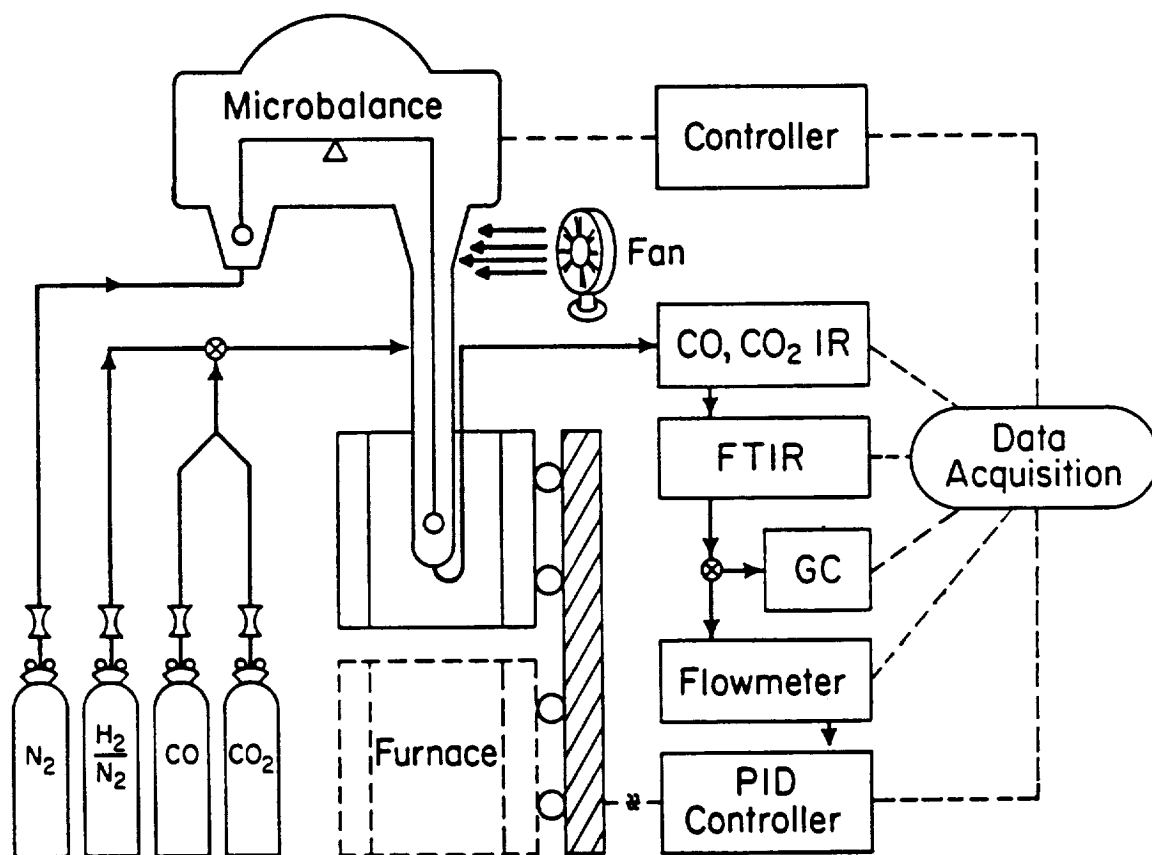


Figure 1. Schematic diagram of the reactor system. GC=gas chromatograph, IR=non-dispersive infrared analyzer, FTIR=Fourier transform infrared spectrometer

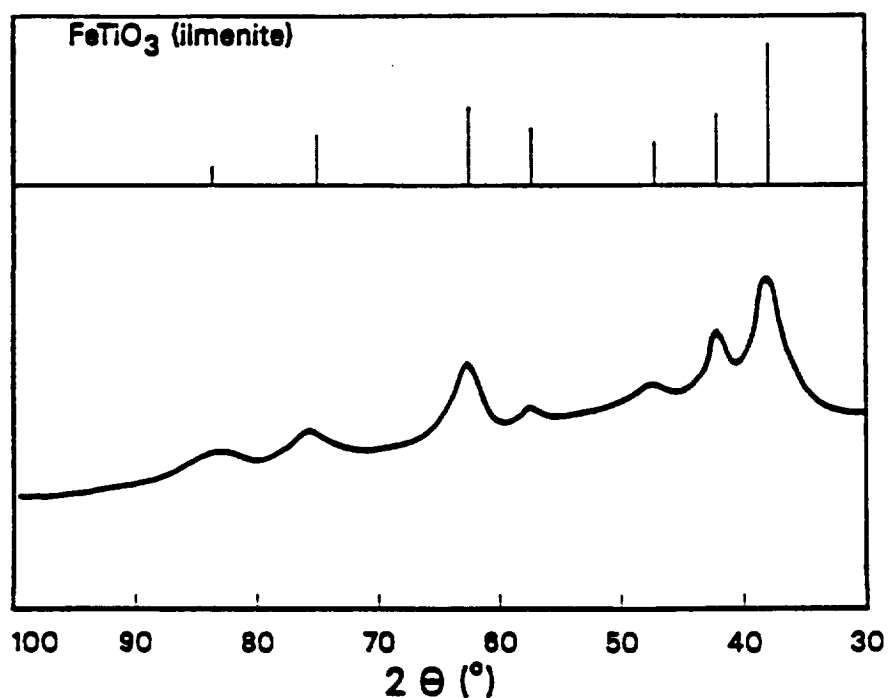


Figure 2. X-ray diffraction spectrum of synthetic ilmenite.

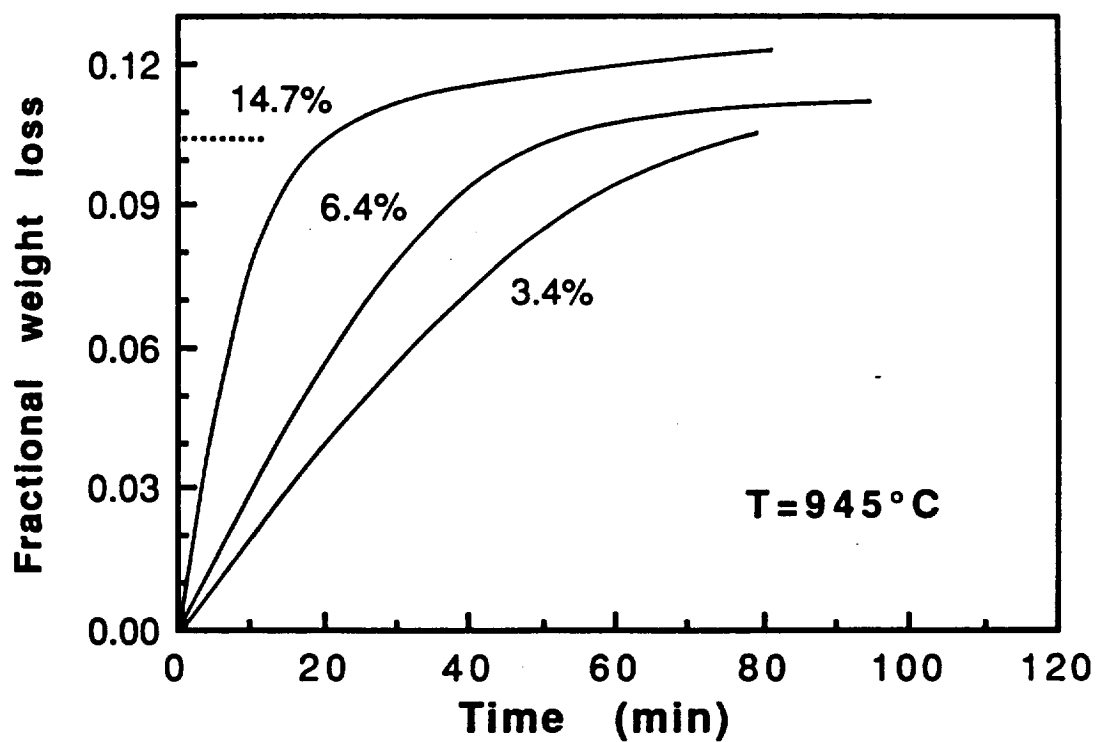


Figure 3. Effect of hydrogen concentration on the reduction of ilmenite; ..... , complete iron metallization.

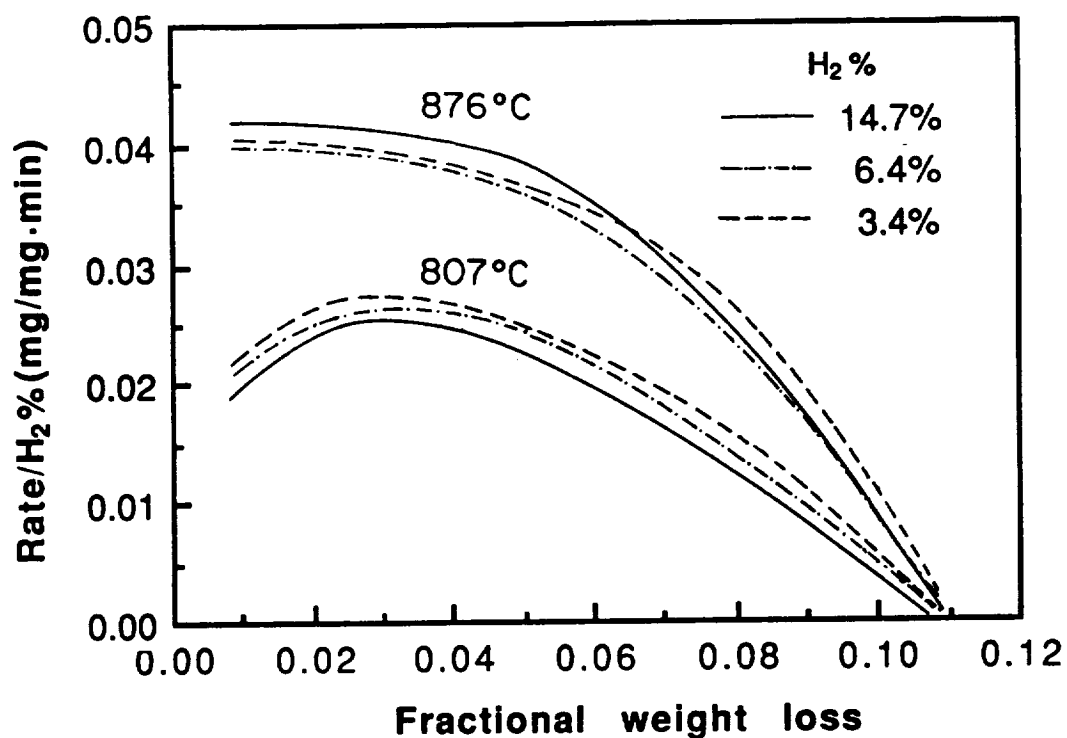


Figure 4. Effect of hydrogen concentration on the reduction rate of ilmenite

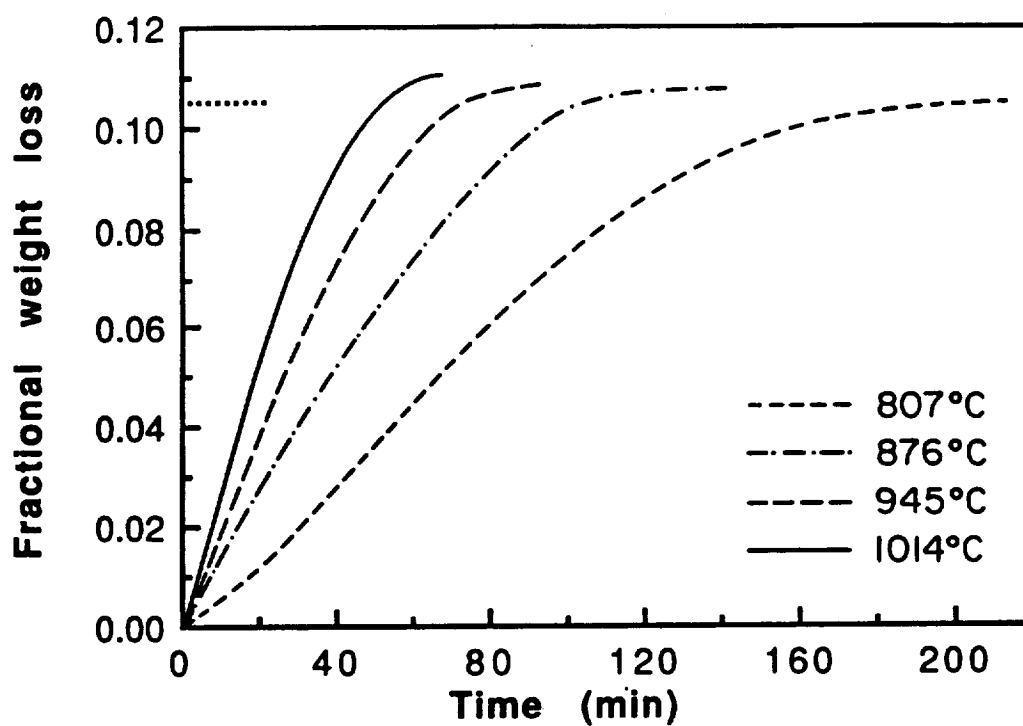


Figure 5. Effect of temperature on the reduction rate of ilmenite: H<sub>2</sub>=3.4%; ..... , complete iron metallization

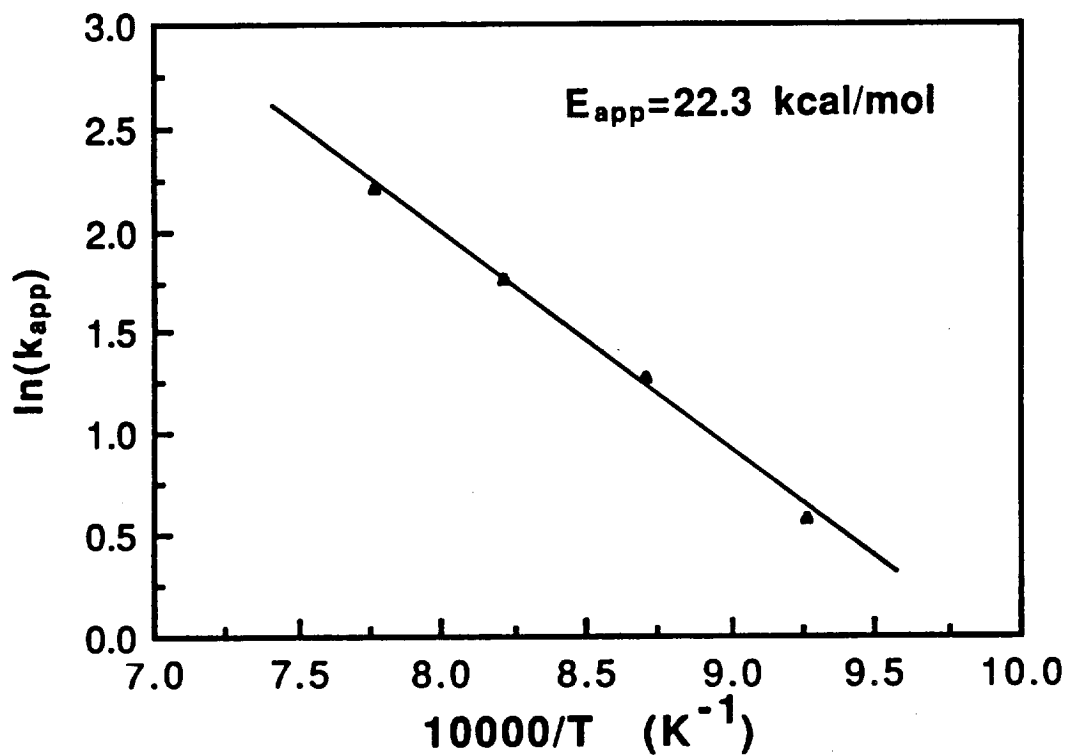


Figure 6. Temperature dependence of the apparent rate coefficient.

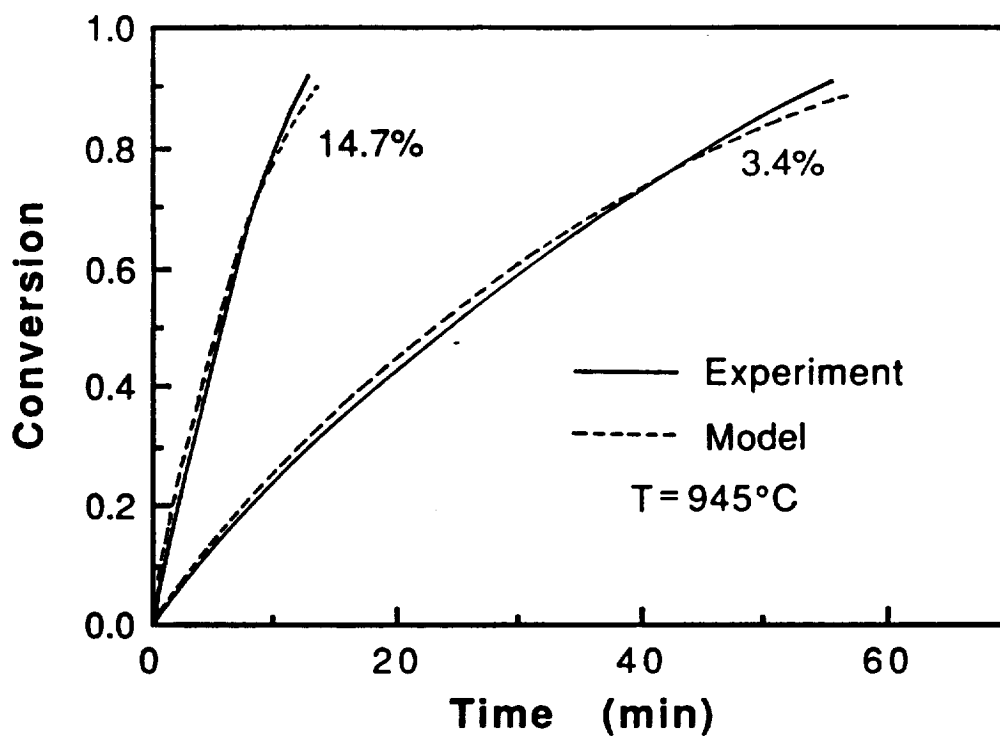


Figure 7. Comparison of experimental data with model predictions:  $H_2=3.4\%$  and  $14.7\%$ .

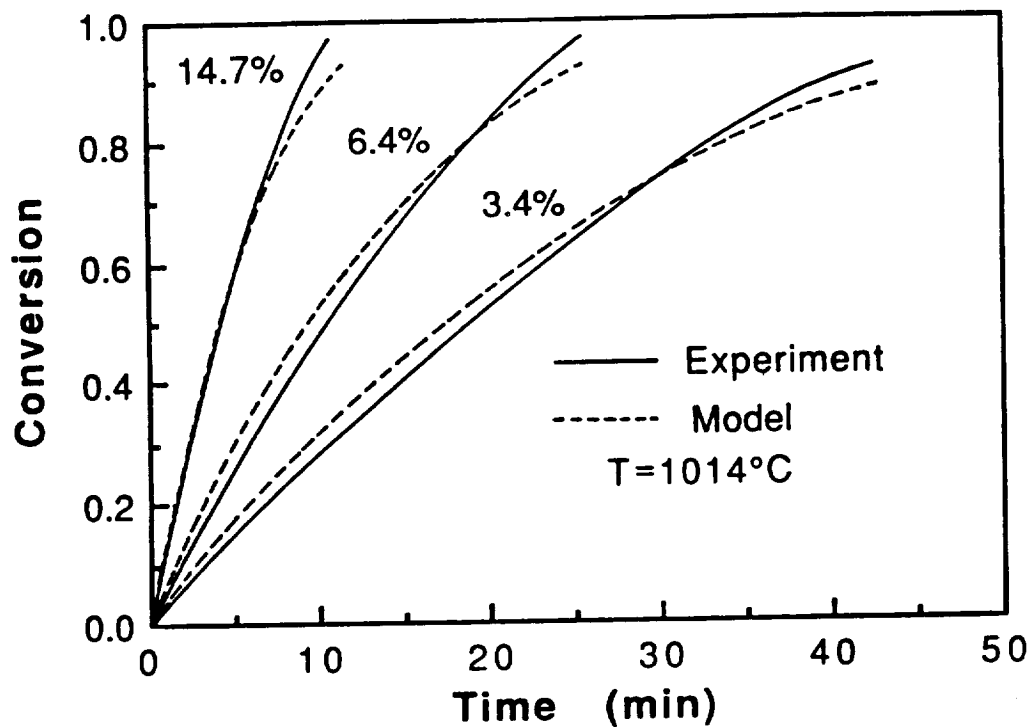


Figure 8. Comparison of experimental data with model predictions: H<sub>2</sub>=3.4%, 6.4% and 14.7%.

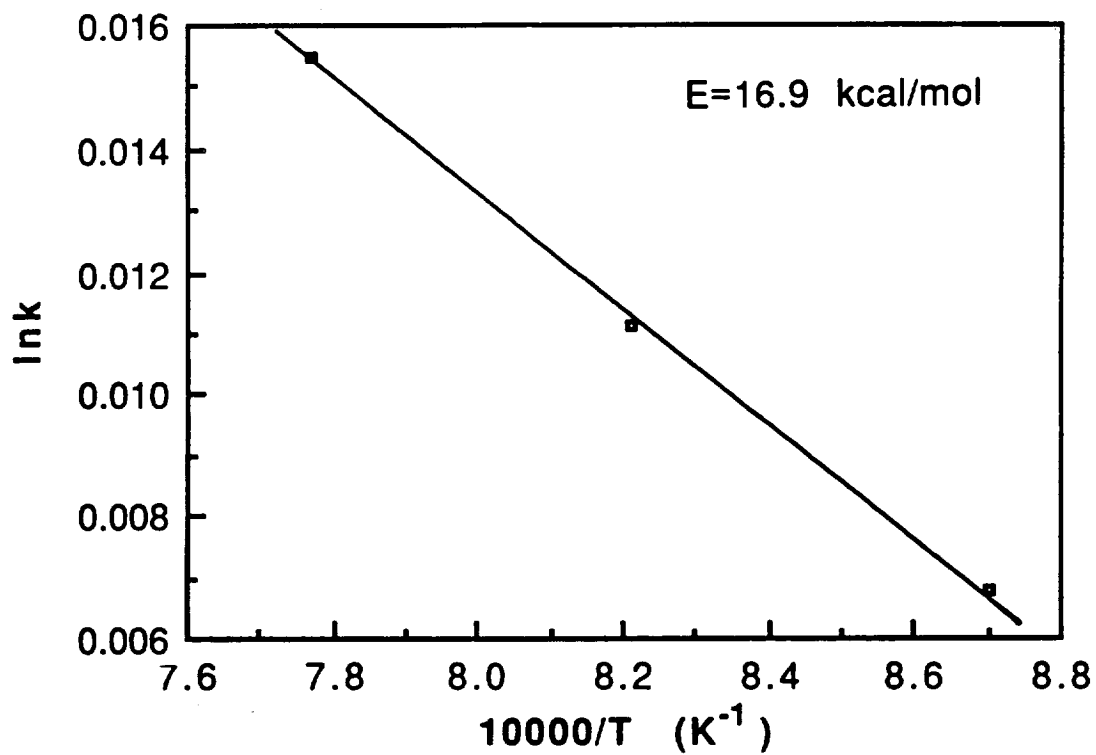


Figure 9. Temperature dependence of the intrinsic rate coefficient.

Figure 10a. Backscattered electron micrograph of the polished cross section of ilmenite flake after partial reduction,  $T=1014^{\circ}\text{C}$ , Magnification=2000X.  
Point concentrations in atom% are:

Point	Ti	Fe
1	50	50
2	51	49
3	51	49
4	2	98
5	96	4

Figure 10b. Fe  $\text{K}\alpha$  X-ray map of the cross section shown in 10a.  
Figure 10c. Ti  $\text{K}\alpha$  X-ray map of the cross section shown in 10a.

Figure 11a. Backscattered electron micrograph of the polished cross section of ilmenite flake after partial reduction,  $T=807^{\circ}\text{C}$ , Magnification=5000X.  
Point concentrations in atom% are:

Point	Ti	Fe
1	50	50
2	50	50
3	51	49
4	5	95
5	99	1

Figure 11b. Fe  $\text{K}\alpha$  X-ray map of the cross section shown in 11a.  
Figure 11c. Ti  $\text{K}\alpha$  X-ray map of the cross section shown in 11a.

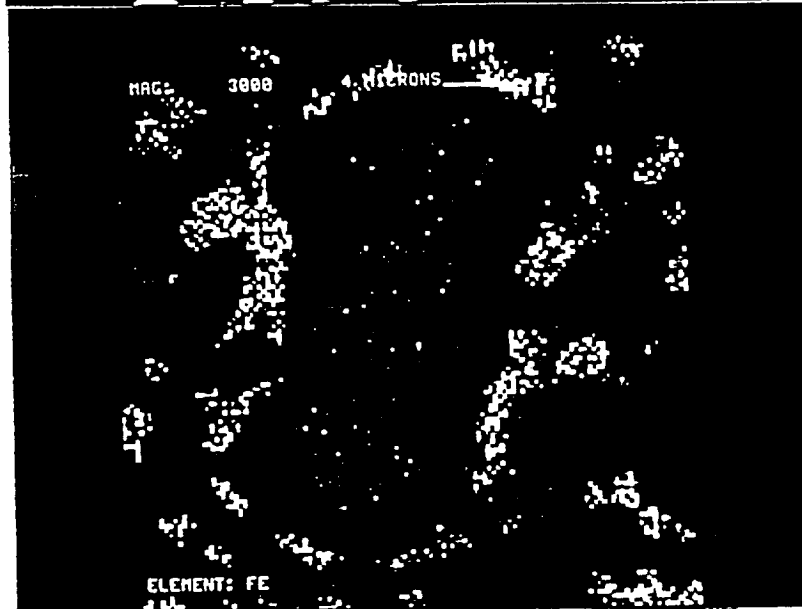
Figure 12a. Backscattered electron micrograph of the polished cross section of ilmenite flake after complete iron metallization,  $T=945^{\circ}\text{C}$ , Magnification=5000X.  
Point concentrations in atom% are:

Point	Ti	Fe
1	99	1
2	99	1
3	2	98
4	3	97

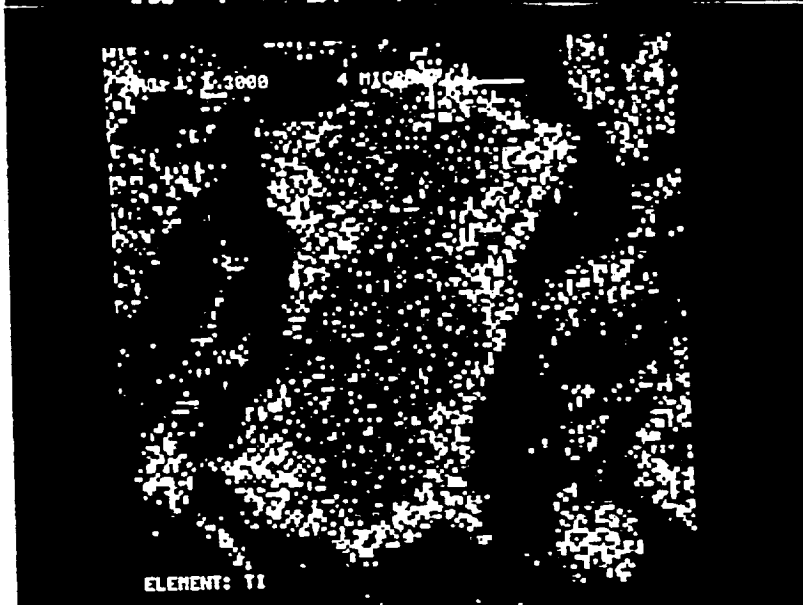
Figure 12b. Fe  $\text{K}\alpha$  X-ray map of the cross section shown in 12a.  
Figure 12c. Ti  $\text{K}\alpha$  X-ray map of the cross section shown in 12a.



Figure 10a.



10b.



10c.

ORIGINAL PAGE IS  
OF POOR QUALITY



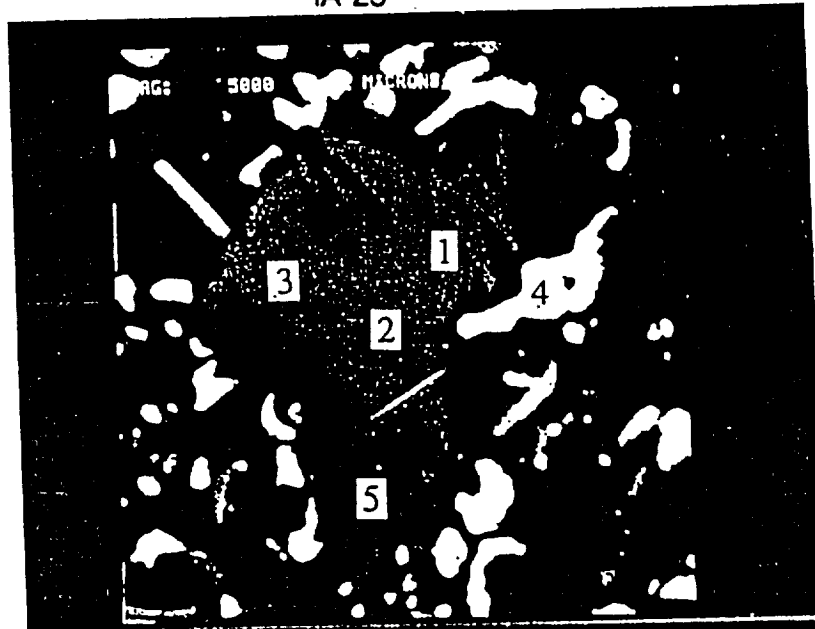
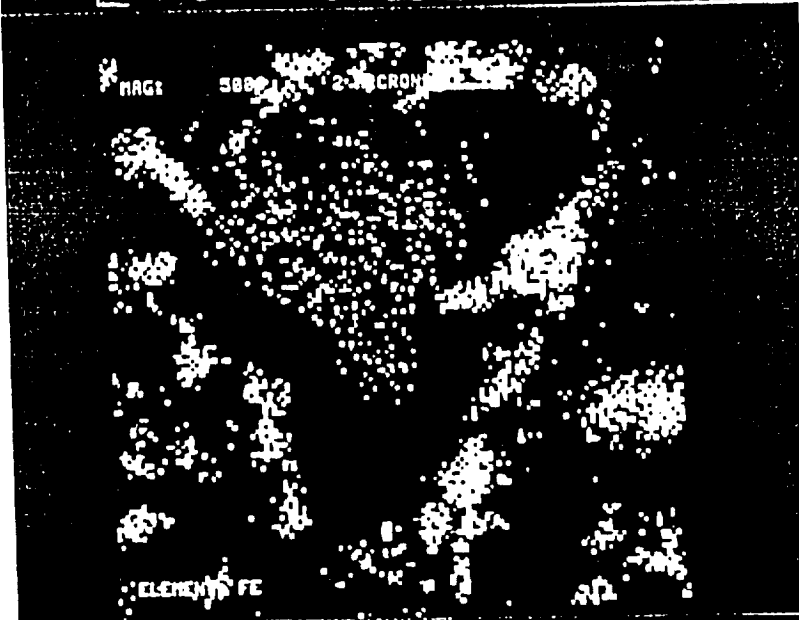
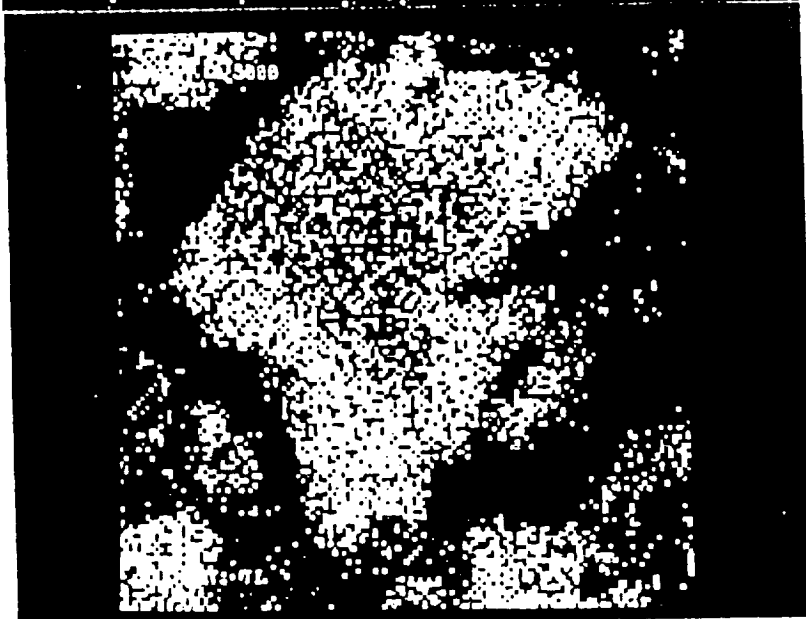


Figure 11a.



11b.



11c.

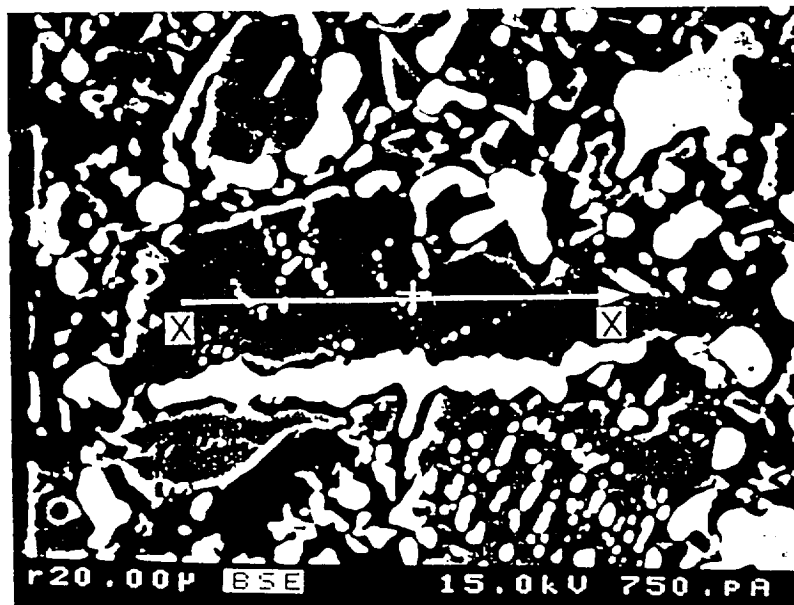
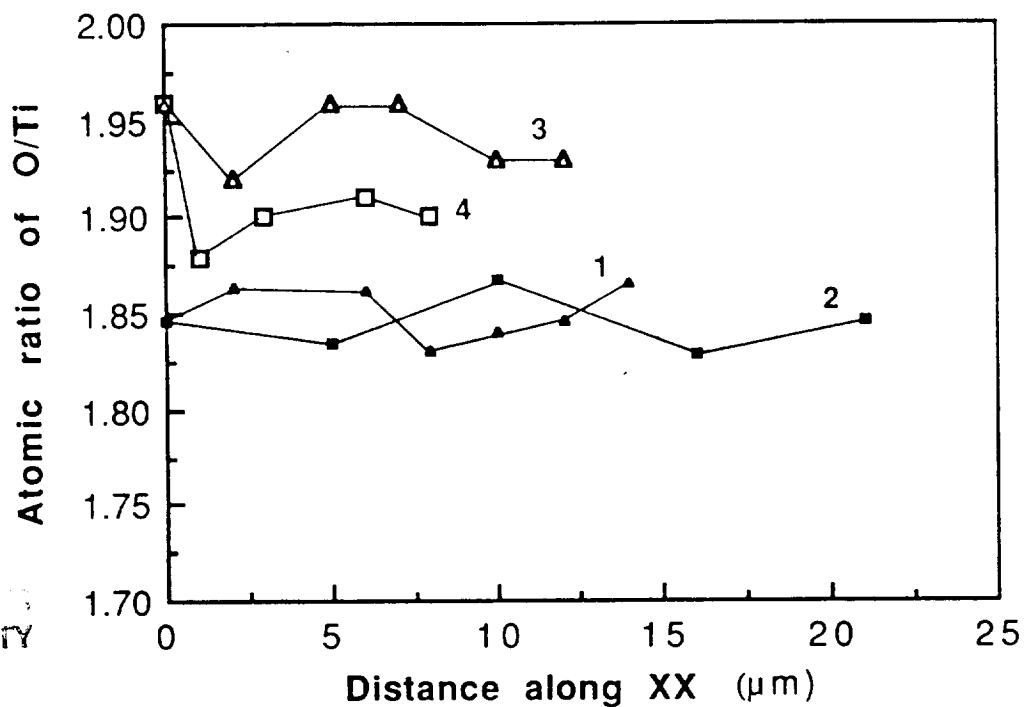


Figure 13. Backscattered electron micrograph of a reduced  $\text{TiO}_2$  phase.



ORIGINAL PAGE IS  
OF POOR QUALITY

Figure 14. Variation in the oxygen to titanium atomic ratio in flakes.

1: sample 1, edge (Figure 13),  $T=1014^\circ\text{C}$

2: sample 1, center,  $T=1014^\circ\text{C}$

3: sample 2, edge,  $T=876^\circ\text{C}$

4: sample 2, center,  $T=876^\circ\text{C}$

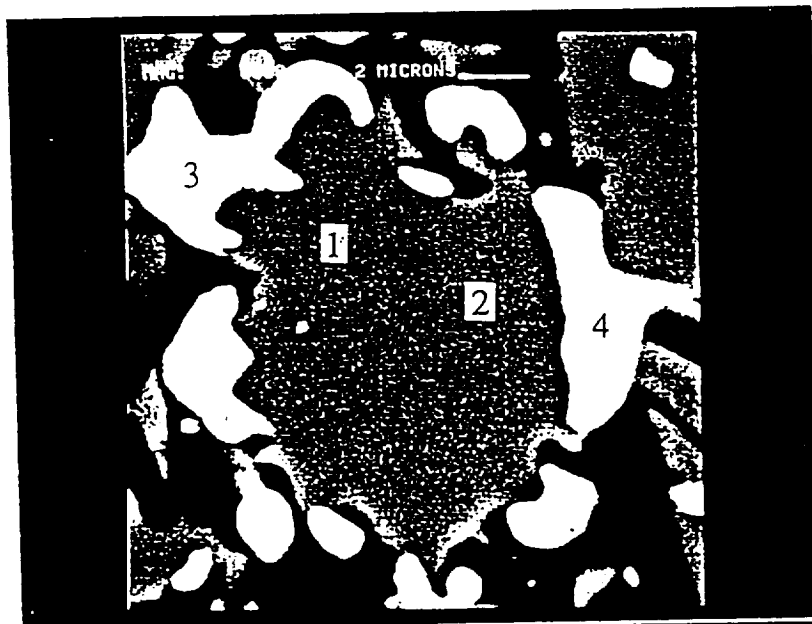
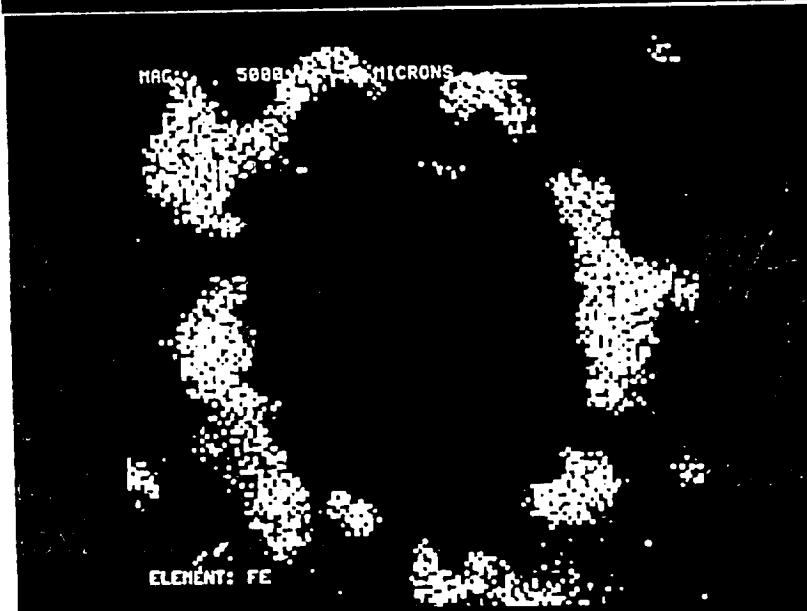
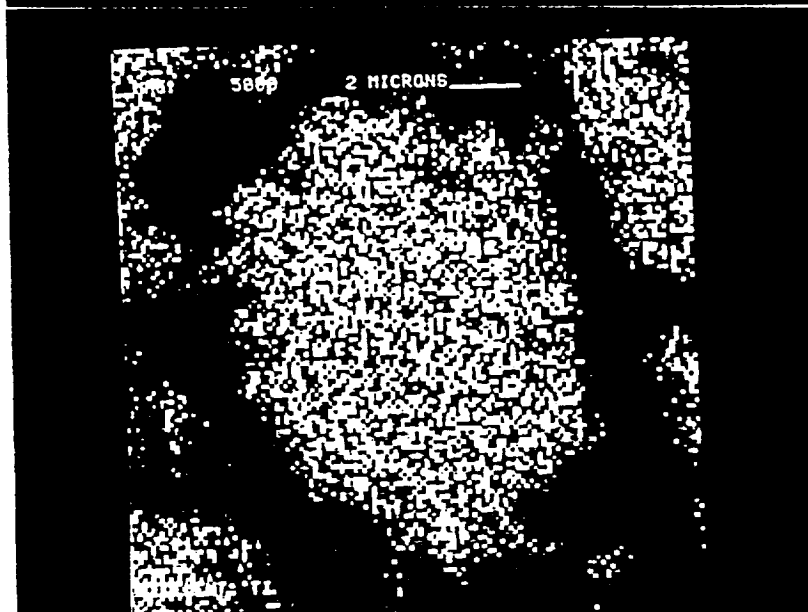


Figure 12a.



12b.



12c.

ORIGINAL PAGE IS  
OF POOR QUALITY

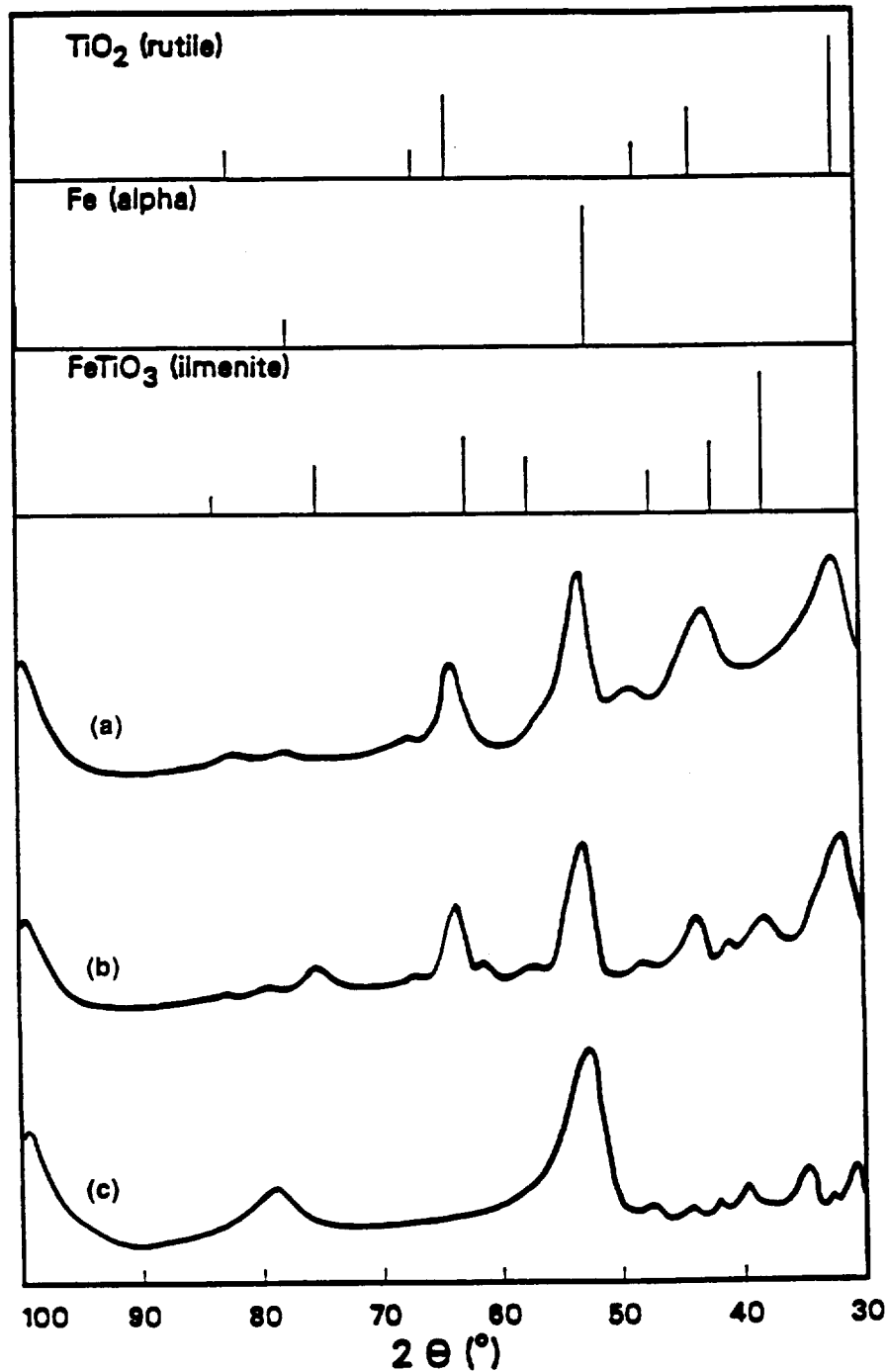


Figure 15. X-ray diffraction spectrum of:

- a) ilmenite, complete iron metallization at 807°C.
- b) ilmenite, partially reduced at 807°C or 1014°C.
- c) ilmenite, complete iron metallization and partial reduction of TiO<sub>2</sub> at 876°C, 945°C and 1014°C.

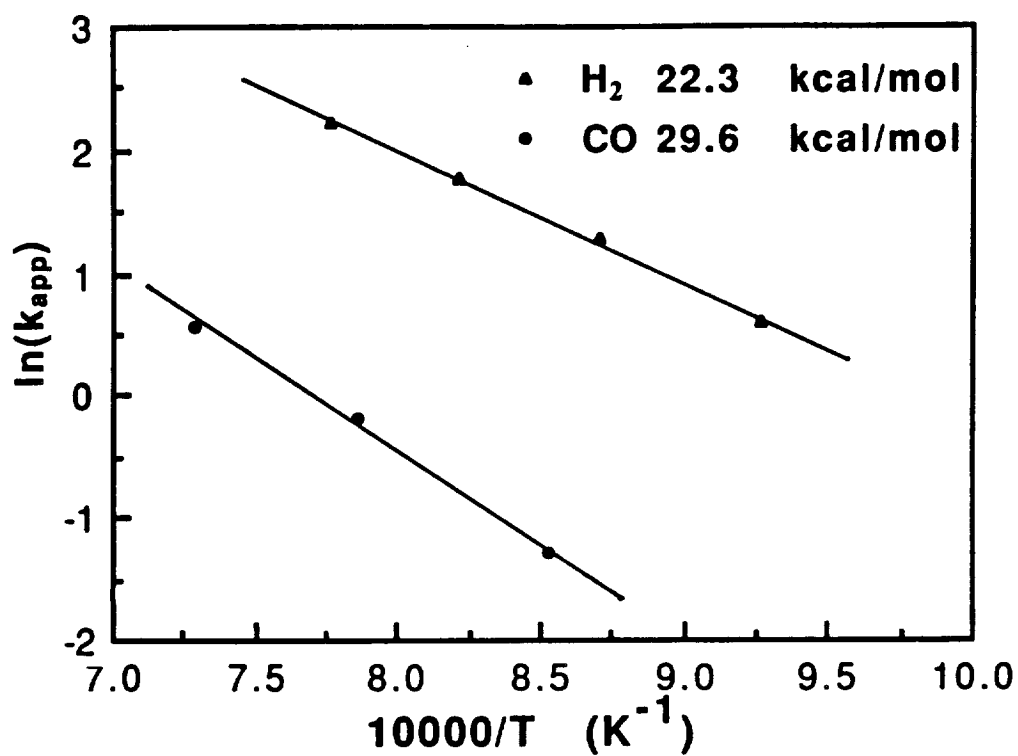


Figure 16. Temperature dependence of the apparent rate coefficient.

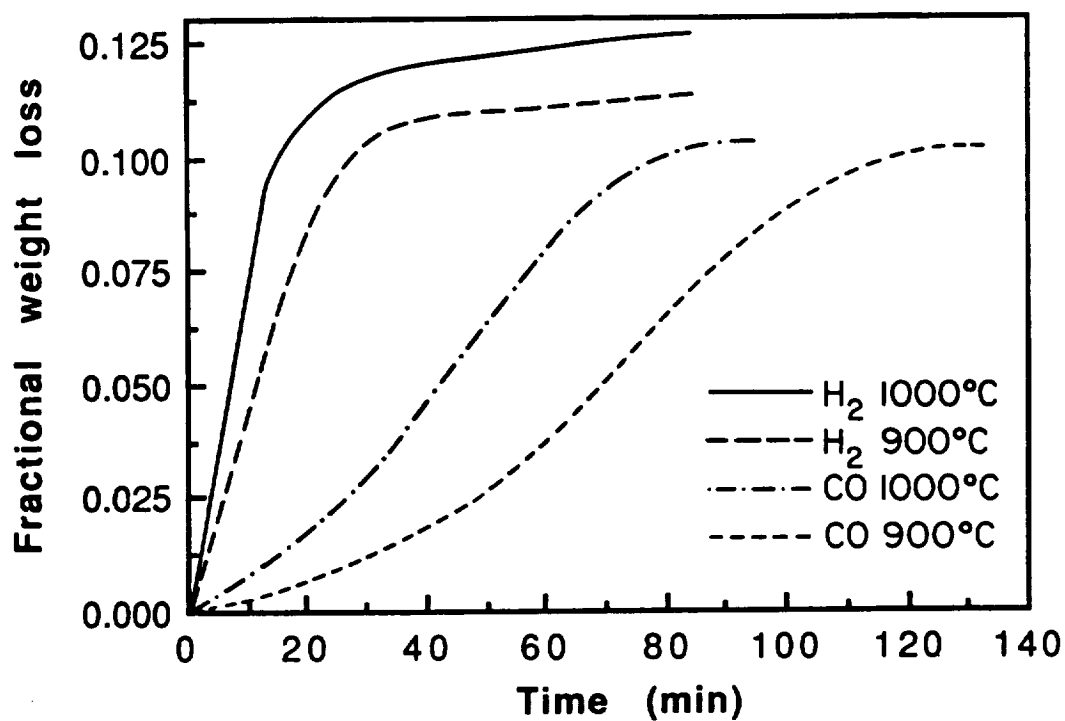


Figure 17. Effect of reducing agents on the reduction of ilmenite.

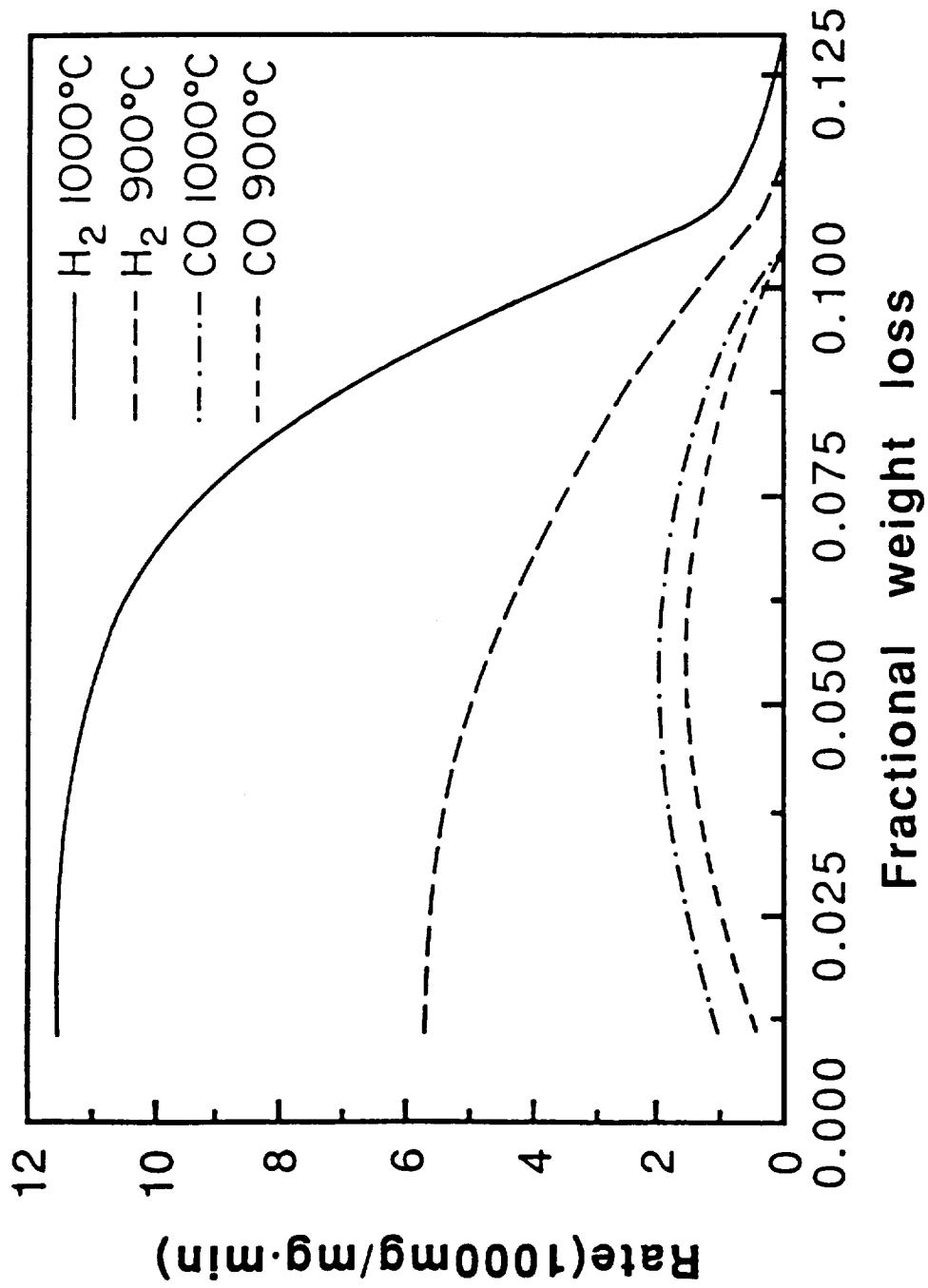


Figure 18. Effect of reducing agents on the reduction rate of ilmenite.

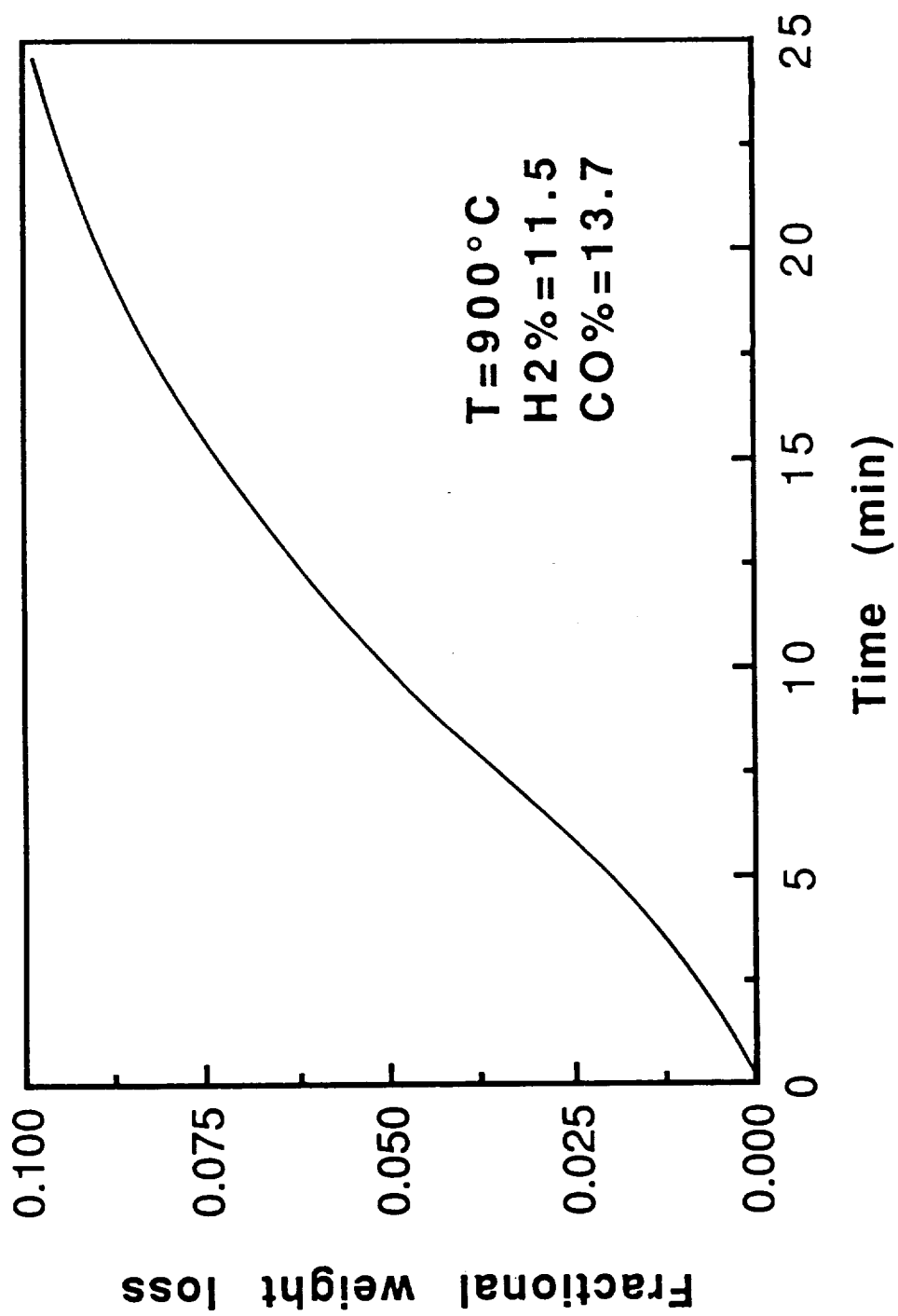


Figure 20. Reduction of ilmenite with  $\text{H}_2/\text{CO}$  mixture.

## Non-slagging Carbothermal Reduction of Ilmenite

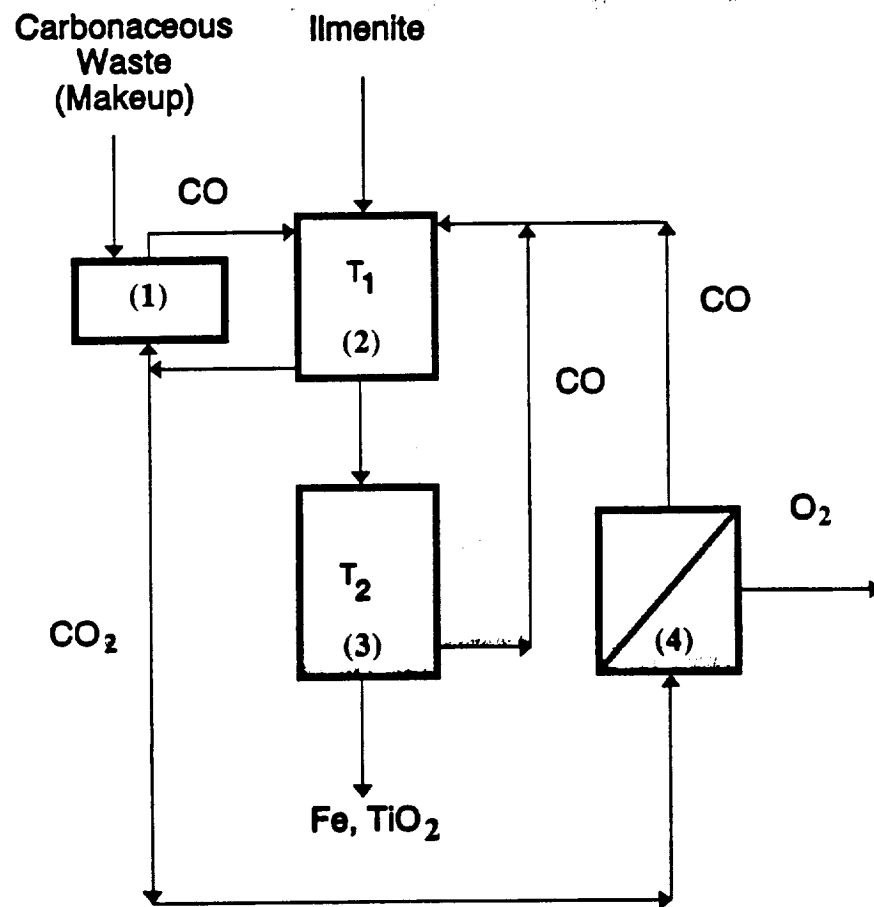


Figure 19. Flowsheet for a novel carbothermal reduction process.



N91-24368  
146-3

## Beneficiation of Lunar Ilmenite

Joaquin Ruiz  
Department of Geoscience  
The University of Arizona

P.3

### Abstract

One of the most important commodities lacking in the moon is free oxygen which is required for life and used extensively for propellant. Free oxygen, however, can be obtained by liberating it from the oxides and silicates that form the lunar rocks and regolith. Ilmenite ( $\text{FeTiO}_3$ ) is considered one of the leading candidates for production of oxygen because it can be reduced with a reasonable amount of energy and because it is an abundant mineral in the lunar regolith and many mare basalts.

In order to obtain oxygen from ilmenite, a method must be developed to beneficiate ilmenite from lunar material. Two possible techniques electrostatic or magnetic methods. Both methods have complications because lunar ilmenite completely lacks  $\text{Fe}^{3+}$ . We have tested magnetic methods on eucrite meteorites, which are a good chemical simulant for low Ti mare basalts. The ilmenite yields in the experiments were always very low and the eucrite had to be crushed to xxxx. These data suggest that magnetic separation of ilmenite from fine grain lunar basalts would not be cost effective. We are presently performing experiments with electrostatic separators and waiting for lunar regolith so that we do not have to depend on simulants.

### Introduction

A fundamental question in the utilization of lunar material for manufacturing of chemicals is the degree to which the raw material: mostly anorthosite, basalt and regolith and their mineral components can be high-graded from bulk. Specifically, ilmenite is a mineral that is abundant in regolith and in high-titanium basalts and can theoretically be used for the production of oxygen. Various processes that involve the reduction of ilmenite to liberate oxygen are being investigated in the hope that oxygen can be manufactured on the moon. This is important because oxygen is required for life support and is an important propellant. Transporting oxygen from the earth to the moon in large quantities may make lunar bases cost-prohibitive.

The most realistic separation methods for ilmenite from regolith or rock that could be used in the moon are electromagnetic since gravity aided separation techniques would not work in the low gravity environment of the moon and liquid-based separation techniques would be very difficult to control. Electromagnetic separation techniques have been used in terrestrial mines for many decades and in some cases can produce very high yields of clean separates. Producing charged particles on Earth or separating minerals with different  $\text{Fe}^{2+}/\text{Fe}^{3+}$  by magnetic methods is quite different than trying to charge particles in vacuum or magnetically separate minerals with no  $\text{Fe}^{3+}$  as is the case for lunar material.

Because we do not have lunar material yet, simulants were used in magnetic separation experiments. Lunar ilmenite is almost stoichiometric and contains no ferric iron. Consequently terrestrial ilmenite cannot be used as simulant. Meteoritic analogs were examined and the best simulant was found to be eucritic meteorites. Table 1 shows the chemical composition of lunar ilmenite from high titanium basalts and eucritic ilmenite.

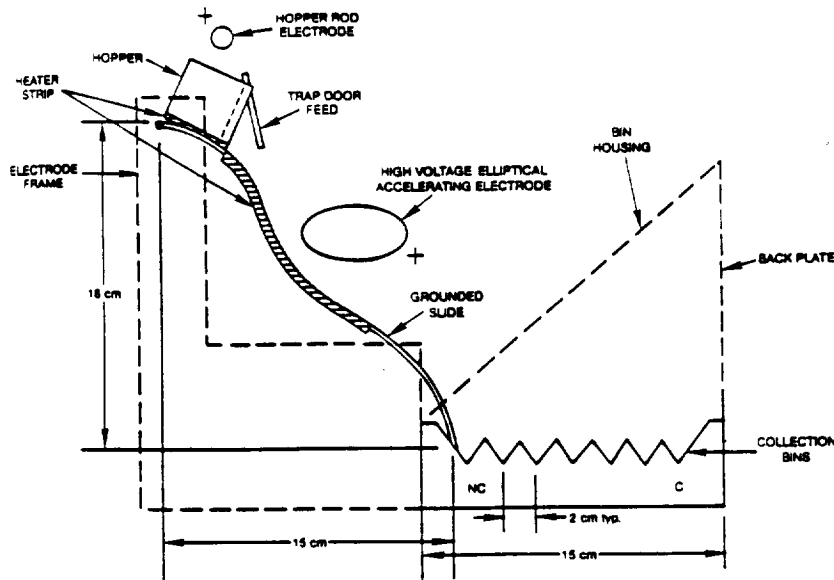
Table 1

	lunar		(wt%)	eucritic	
	mean	range		mean	range
FeO	43.3	(35.2-47.7)		44.2	(42.8-45.0)
TiO <sub>2</sub>	52.7	(49.9-55.5)		52.8	(52.5-53.0)
Al <sub>2</sub> O <sub>3</sub>	*	(0.1-0.3)		0.06	(0.03-0.11)
Cr <sub>2</sub> O <sub>3</sub>	0.64	(0.5-2.12)		0.09	(0.03-0.27)
MgO	2.23	(0.0-9.5)		1.05	(0.46-2.35)
MnO	0.42	(0.0-0.95)		0.88	(0.82-0.93)
CaO	*	(0.0-0.3)		0.10	(0.03-0.16)

Lunar data from a compilation of 133 ilmenites from hi-Ti basalts (Vaniman, et al., 1989), except for Al<sub>2</sub>O<sub>3</sub> and CaO, which are for Apollo 11 ilmenites (Mason and Melson, 1970). Eucritic data are for 8 eucrites (Bunch and Keil, 1971)

Our attempts to beneficiate eucritic ilmenite were not very successful. The best concentrate was only about 20% ilmenite. Our work generally agrees with the interpretations of Taylor and Oder (1990). It appears that electrostatic separation will be the best option for the beneficiation of lunar ilmenite. However, experiments by Agosto (1985) indicate that electrostatic separation of ilmenite from lunar soils is not very efficient because of the presence of agglutinates, which have an inherent heterogeneous behavior to electrostatic charging. It may be that rocks provide feedstock to soils. However, the use of rocks would require crushing to liberate the ilmenite. During our attempts to liberate ilmenite from the eucrite sample, the rock did not crush along grain boundaries; most of the ilmenite remained trapped in composite grains. In addition, a static cling problem was observed in which all the particles produced during crushing were covered with fine dust. The coating included FeS which would create problems during electrostatic beneficiation and reduction of the ilmenite.

Experiments with lunar regolith and rocks will be made in 1991 using an electrostatic separator based on Agosto's (1985) original design (Figure 1). The separator can be used under vacuum or under Ar or N atmospheres. Electrostatic separations will be attempted on untreated lunar regoliths and crushed regolith and rocks under vacuum and inert gas atmospheres. In addition photoelectric charging will be attempted since this technique has been very successful on terrestrial samples (Fraas, 1976).



### References

Agosto, W.N. (1985) Electrostatic concentration of lunar soils and minerals, in, Lunar Bases and Space Activities of the 21st Century. LPI p 453-464.

Fraas, F. (1976) Electrostatic separation with photoelectric charging,. U.S. Bureau of Mines Report 7610. U.S. Bureau of Mines, Minneapolis 13 p.

Taylor L.A. and Oder R.R. (1990) Magnetic beneficiation of Hi-Ti Mare soils. Concentration of ilmenite and other components. Lunar and Planetary Sciences XXI, Lunar and Planetary Institute

N 9 1 - 2 4 3 6 9

14664  
P.16

"Cold" Plasma Processing of Local Planetary Ores for Oxygen  
and Metallurgically Important Metals

D.C. Lynch, D. Bullard and R. Ortega

Department of Materials Science and Engineering  
The University of Arizona

AY 2011

Abstract

In the previous progress reports for 1988-89 and 1989-90, the utilization of a "cold" or nonequilibrium plasma in chlorination processing was discussed along with the results of some preliminary experiments. This report is a continuation of that discussion, but is focused on the progress that has been achieved in the past 12 months. During that period  $\text{TiO}_2$  has been successfully chlorinated at temperatures between 700 and 900°C without the aid of carbon. In addition to these initial experiments a technique has been developed for determining the temperature of a specimen in a plasma. Development of that technique has required evaluating the emissivity of  $\text{TiO}_2$ ,  $\text{ZrO}_2$  and  $\text{FeOTiO}_2$ , and analyzing the specimen temperature in a plasma as a function of both power absorbed by the plasma and the pressure of the plasma. We have also calibrated the mass spectrometer with  $\text{TiCl}_4$  and  $\text{CCl}_4$  vapor and are now prepared to report all future results in terms of partial pressures.

Introduction

During the first two reporting periods funding for this work was provided by the Space Engineering Research Center (SERC). During the latest period, our primary source of funding has been through the U.S. Bureau of Mines' Pyrometallurgy Generic Center at the University of Missouri at Rolla (contract # MU-USDI-G1175129 and MU-USDI-G1105129). We wish to gratefully acknowledge their support.

Support from the Bureau of Mines has not altered our basic perspective, namely, to investigate the feasibility of using a "cold" or non-equilibrium plasma in the enhancement of reaction rates and in the biasing of the thermodynamics of reactions that would not proceed if conventional means were employed. There are many reasons to explore the potential of this new technology for both terrestrial and extraterrestrial applications. However, our attention is focused on the latter in the discussion which follows.

Material requirements at a Lunar base will be varied and demanding, and can possibly be likened to that in the present day nuclear industry. The extent of requirements will depend on the critical nature of the components and/or systems involved. The demand for materials will, initially, be met by importing them from Earth. Ultimately, the great expense of transporting materials from the Earth to the Moon will dictate that general construction materials be produced from

extraterrestrial sources. Eventually as the Lunar base progresses more ambitious efforts will be undertaken to achieve greater self sufficiency with regards to materials.

Not only will there be a demand for materials at a Lunar base, there will be a demand for materials that can meet a wide range of mechanical, electrical, optical, and chemical requirements. There has been a tendency to focus on iron, produced as a by-product at lunar oxygen production facilities, as a primary construction material. Unfortunately high purity iron is susceptible to brittle failure. Iron experiences a lowering of absorbed impact energy with decreasing temperature. That phenomenon is referred to as "ductile-brittle" transition. At low temperatures a crack or surface imperfection in the iron can propagate faster than plastic deformation can occur, so that little energy is absorbed. At higher temperatures cracking is preceded by energy consuming deformation.

Just before dawn on the lunar surface, temperatures dip as low as 123 K. At that temperature high purity iron will be subject to failure by cleavage fracture through any and all impacts. This condition can be alleviated by alloying the iron.

This example demonstrates that there will be a need for recovery of multiple elements to produce materials that can be used in the Lunar environment. Except for the iron oxide in ilmenite, the Lunar soil is composed of refractive oxides. New techniques, accordingly, will be necessary to recover elements other than Fe.

We have proposed the use of a nonequilibrium plasma as one technique that may have potential for recovery of metallurgically important metals from refractory oxides. Since the reactive environment is created by an electromagnetic field one apparatus can be used in the processing of multiple feed materials. The intent of the present work is to examine the feasibility of using a non-equilibrium plasma in the chemical processing of materials.

In conventional processing reactants are heated until the chemical potential of the desired reaction is negative, and the temperature is high enough to ensure rapid reaction rates. In a cold plasma energy is used to produce radicals and heat. Radicals are produced by reducing the pressure, such that electrons, responding to electromagnetic radiation, are accelerated until they have sufficient energy to liberate bound electrons, break bonds and excite both ions and neutral species upon impact. Radicals formed in this manner from adsorbed gaseous species are available for reaction with the underlying substrate.

In the experimental program refractory metal oxides have been chlorinated without carbon as a reducing agent. A microwave induced plasma has been used to create monatomic chlorine that has been used to chlorinate both rutile and silica at temperatures below 900°C. The monatomic chlorine has a high chemical potential, and, as a result, can participate in reaction where diatomic chlorine can not.

Experiments are planned to, also, examine the feasibility of utilizing a cold plasma in hydrogen reduction of refractory metal oxides. The use of hydrogen has several distinct

advantages. Monatomic hydrogen, like monatomic chlorine, is highly reactive. However, monatomic hydrogen (unlike monatomic chlorine) when reacted with a refractory oxide produces both solid and gaseous products. By continuing to flush the reactor with fresh gaseous reactant, the back reaction can be prevented.

#### Experimental Apparatus

The construction of the experimental apparatus was, essentially, completed during the last reporting period. We have, however, added an electronic package that allows for determination of a power used to generate the plasma. We now have the capability to measure both the plasma's efficiency in absorbing the microwaves and the efficiency of which energy is converted to microwaves.

#### Plasma Characterization

A cold plasma is typically characterized by the composition of the gas, the plasma density (pressure), power absorbed by the plasma, and a geometrical factor or characteristic length. Characterization becomes complex when a solid specimen is inserted into the plasma. There are no established procedures to follow like the Gibbs phase rule. The complexity of a plasma is represented by the temperatures involved. In a cold plasma there is the electron temperature, the ion temperature, the temperature of neutrals and the temperature of the solid specimen. They are all different. In establishing the state of the plasmas employed in this investigation, the standard parameters noted above have been fixed, the size and shape of the solid specimen set, and the specimen temperature monitored during an experiment.

Measuring any temperature in a plasma is a difficult task. In a plasma, free electrons have a continuum of energy states. The electrons can absorb and emit energy at any wavelength, and, as such, it is unlikely that a solid body in a plasma could be characterized as a grey body. Because of that situation a single color optical pyrometer was employed in lieu of a two color unit. The optical pyrometer is used to monitor radiant emissions at 600 nm to determining the solid specimen temperature.

A number of preliminary experiments were required before the temperature of a solid specimen could be determined in the plasma. Proper use of the optical pyrometer required measuring the emissivity of the specimens. The task was accomplished using a resistance wound furnace, a thermocouple and the optical pyrometer. The experiments were conducted from 600°C to 1000°C and the results of that work are shown in Figure 1. Those results reveal that the emissivity of  $\text{TiO}_2$ ,  $\text{ZrO}_2$  and  $\text{FeTiO}_3$  increase only slightly over the temperature range noted.

With knowledge of the emissivity of the specimens, the effect of the plasma on temperature readings could be deduced. The temperature of a solid specimen in the plasma was monitored. Once the specimen reached a constant temperature the plasma was extinguished by turning the power off to the microwave generator. The temperature of the solid specimen was continually

monitored as it cooled. The resulting data and a least squares routine for a polynomial fit were used to predict the temperature of the specimen in the plasma as shown in Figure 2. The error in the temperature readings was found to increase as both the power absorbed and pressure decreased.

These experiments were conducted at a range of power settings and plasma densities. Some of the results of this work are presented in a three dimensional plot shown in Figure 3a and as a contour map in Figure 3b. The graphs reveal that the solid specimen temperature is a strong function of the power absorbed and a weaker function of the pressure (or density) of the plasma. These experiments were conducted with a nitrogen plasma and then later spot checked with a  $N_2$  - 10%  $Cl_2$  plasma. The chlorine was found to only slightly effect the temperature readings obtained with the nitrogen plasma. The extend of the effect is presented in Table I.

#### Plasma - Solid Reactions

A series of experiments have been conducted to test the general hypothesis that a cold plasma can be used to bias thermodynamics with the formation of radicals.

Rutile has been reacted in a nitrogen-chlorine plasma at pressures of 17 to 30 Torr and power absorption levels of 0.35 to 1.0 KW. These conditions correspond to rutile reaction temperatures of 665°C to 850°C. The mass spectrometer was used to monitor the extent of metal chloride formation. Some of the results of those experiments are presented in figure 4. Those results reveal that chlorides of Ti and Si are readily formed in the plasma, even though conventional thermodynamics indicates that the chlorides of these metals can not be formed at the conditions employed (see Figure 4). The presence of monatomic chlorine in the plasma makes the reactions possible.

The source of silicon for the silicon chlorides reported in Figure 5 is the specimen holder and the walls of the plasma confinement chamber.

#### Equipment Calibration

During the last few months we have assembled a transportation device in order to calibrate the signal from the mass spectrometer. The apparatus consists of two baths, the primary bath consisting of mineral oil and the other of ice and water. The evaporating fluid was placed in two bubblers in series as shown in Figure 6. A combination stirrer and heater was used to circulate the mineral oil around the bubbler. A nitrogen carrier gas was passed through a copper coil (not shown in the figure) immersed in the bath before entering the bubblers. The saturated gas upon leaving the bubbler was immediately passed through an expansion valve to prevent condensation. The gas then entered the mass spectrometer or exited through a secondary roughing pump.

The primary bath could be either heated or cooled. To cool the mineral oil, ice water was circulated through a second copper coil immersed in the oil. Mineral oil was used in the primary bath to guard against any accidental contact between water and  $TiCl_4$  liquid. Those two compounds react vigorously yielding HCl vapor. The temperature of the primary bath was monitored using a

partial immersion thermometer.

Both  $\text{TiCl}_4$  and  $\text{CCl}_4$  were used in the calibration of the signal from the mass spectrometer. The carrier gas was found to be easily saturated with the vapors of those compounds at gas flow rates of 30 to 100 ml/min. All of the experiments were conducted at a flow rate of 50 ml/min. The results of the calibration experiments are presented in Figures 7 and 8.

The measured vapor pressure of  $\text{TiCl}_4$  was consistently found to be greater than that predicted by data in the literature as shown in Figure 7. It is, however, encouraging to note that the slope of the lines (and therefore the calculated values of the heat of vaporization) are approximately equal. Analysis of the signal received from the mass spectrometer suggested that  $\text{TiCl}_4$ ,  $\text{TiCl}_3$  and  $\text{TiCl}_2$  were all present in the vapor as parent molecules. The concentrations of both  $\text{TiCl}_3$  and  $\text{TiCl}_2$  were well above that which is predicted by thermodynamic data. Large concentrations of hydrogen and  $\text{HCl}$  were also detected. The results from the mass spectrometer suggest that the liquid  $\text{TiCl}_4$  was contaminated.

As a result of the problems associated with the  $\text{TiCl}_4$ , carbon tetrachloride was used to calibrate the signal from the mass spectrometer. The results of that work are presented in Figure 8. At room temperature and above the results of the present work compare favorably with data published by K.K. Kelley. The discrepancy in the value obtained in the present work at  $6^\circ\text{C}$  and the calculated value is probably associated with a nonthermal equilibrium condition. A  $10^\circ\text{C}$  discrepancy between the bath temperature and the fluid temperature would account for the difference. There is a substantial difference in the measured vapor pressure of  $\text{CCl}_4$  in the present work to that calculated from the HSC data base. The values for the vapor pressure of  $\text{CCl}_4$  obtained from HSC have involved extrapolation of specific heat data.

That extrapolation leads to a normal boiling point temperature for  $\text{CCl}_4$  more than  $40^\circ\text{C}$  higher than the accepted value of  $77^\circ\text{C}$ . No such discrepancy exists with K.K. Kelley's data.

Table I. Difference in Specimen Temperature in Nitrogen and Nitrogen - Chlorine Plasmas

Press. (Torr)	Power (KW)	
	0.5	1.0
	$\Delta T$	$\Delta T$
13	$1^\circ\text{C}$	---
28	---	$3^\circ\text{C}$



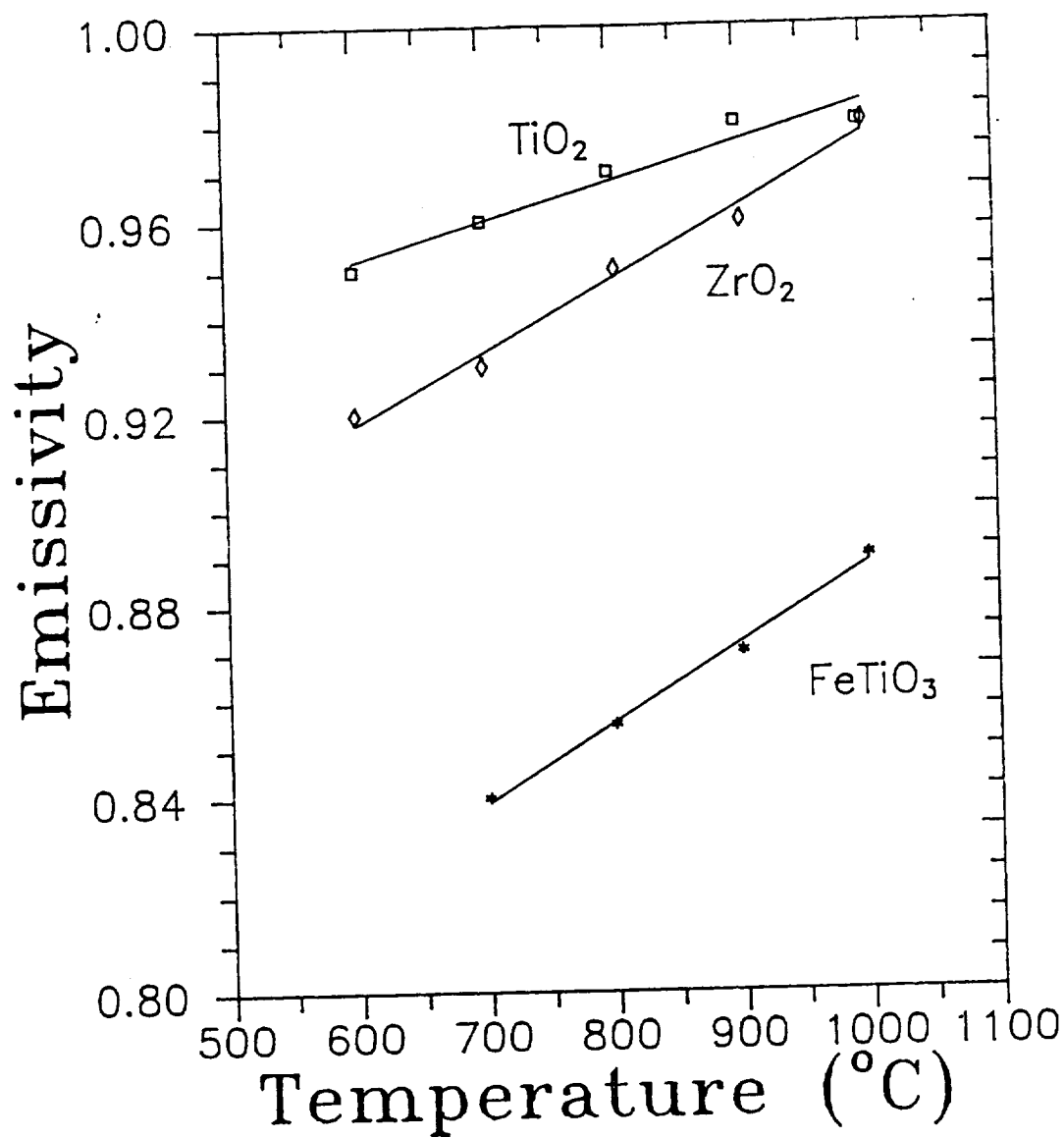


Figure 1 - Measured values of the emissivity for oxides.

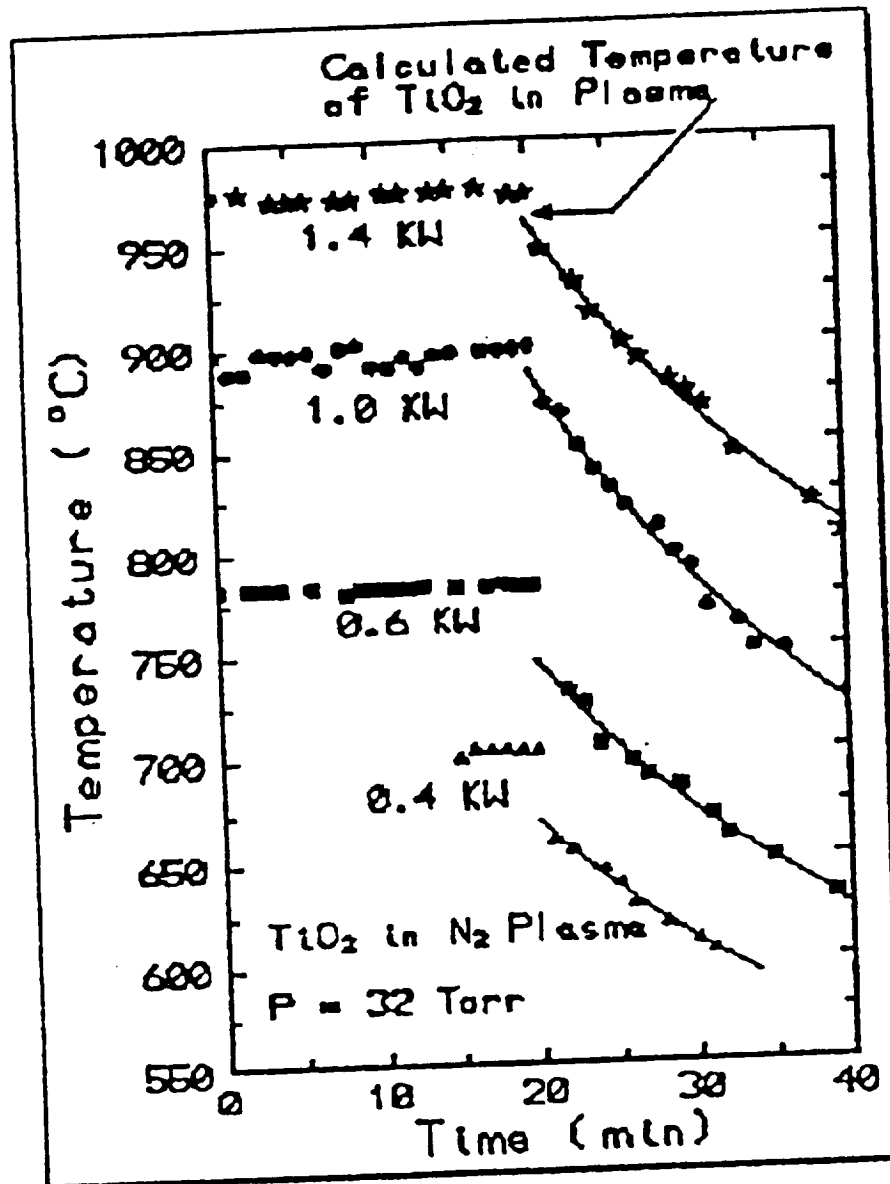
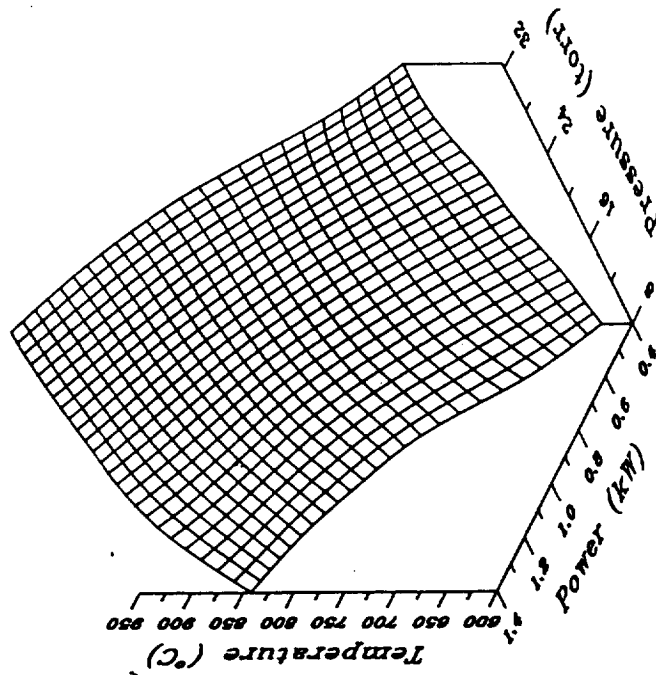


Figure 2 - Actual temperature of specimen determined by monitoring temperature before and after plasma extinguished.

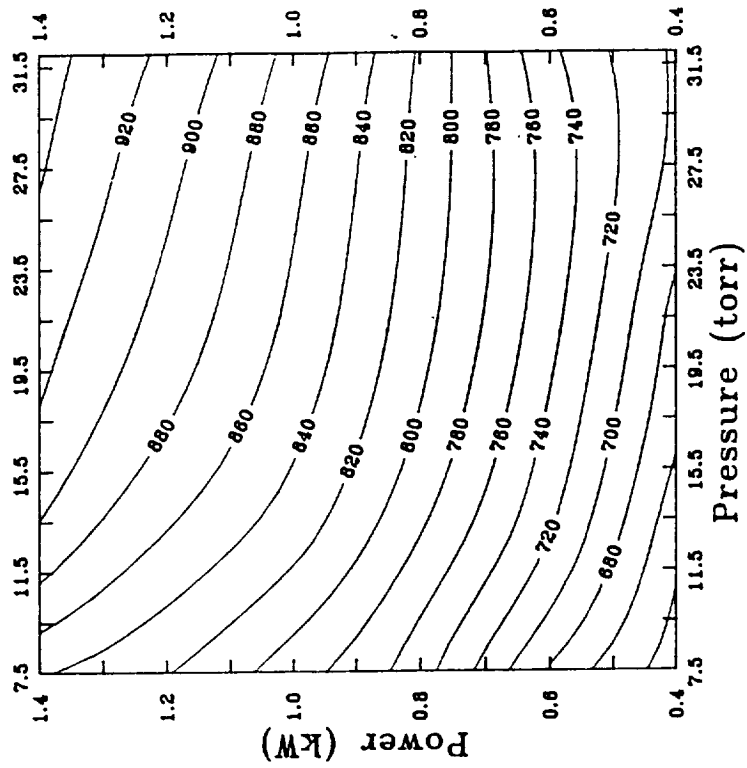
# TiO<sub>2</sub> in N<sub>2</sub> Plasma

# TiO<sub>2</sub> in N<sub>2</sub> Plasma

-Lines of Constant Temperature (°C)



(a)



(b)

Figure 3 - Temperature of rutile specimen in N<sub>2</sub> plasma as a function of power and pressure: (a) three dimensional plot, (b) isothermal contours.

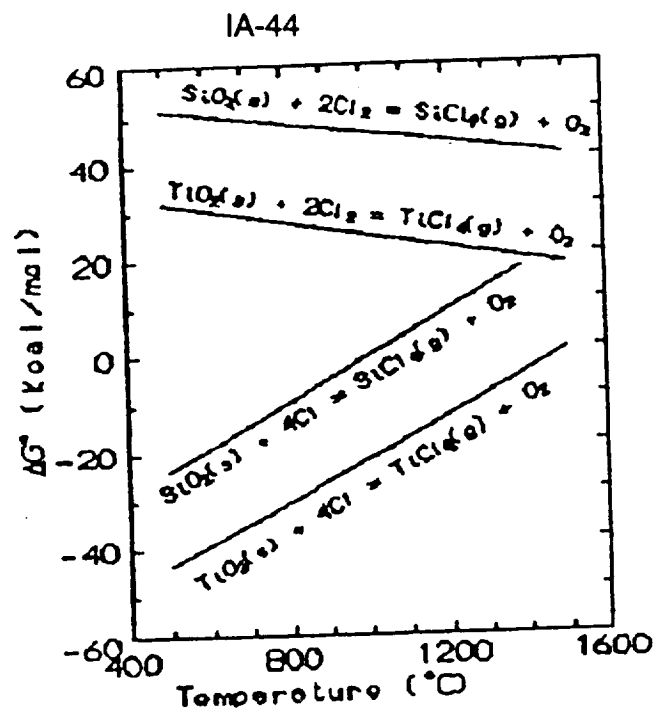


Figure 4 - Standard Gibbs energy data for formation of chlorides.

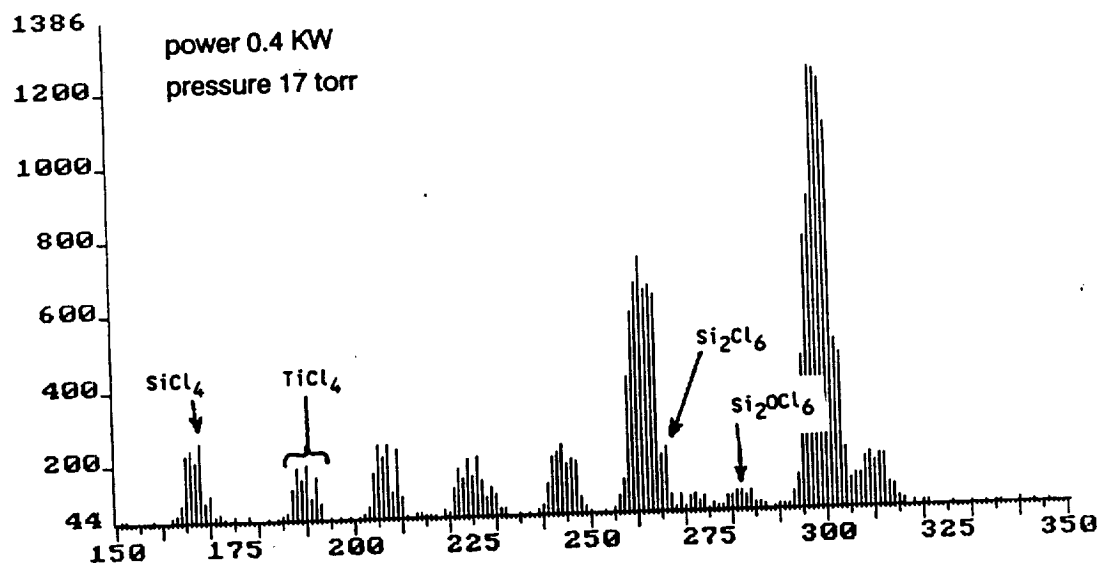


Figure 5 - Experimental results from mass spectrometer.

# APPARATUS FOR MASS-SPECTROMETER CALIBRATION USING $\text{TiCl}_4$

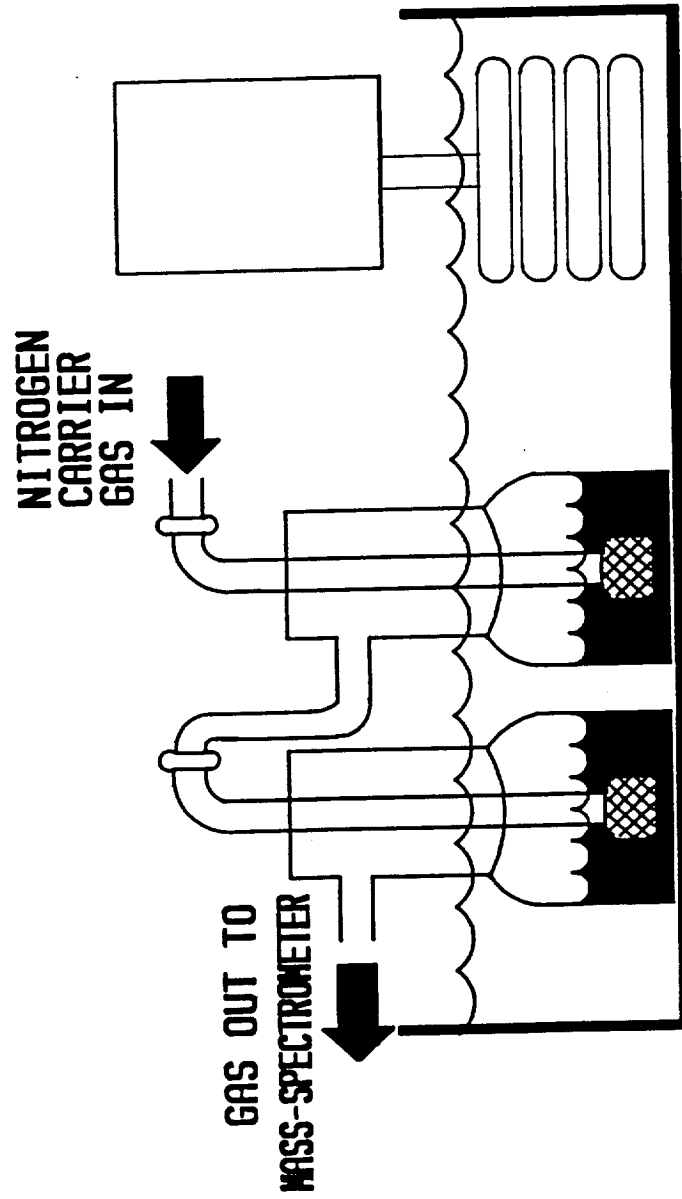


Figure 6 - Transportation apparatus, diagram does not show cooling coils, secondary bath or coil for preconditioning nitrogen before entering bubblers.

IA-46

# Vapor Pressure of $\text{TiCl}_4$

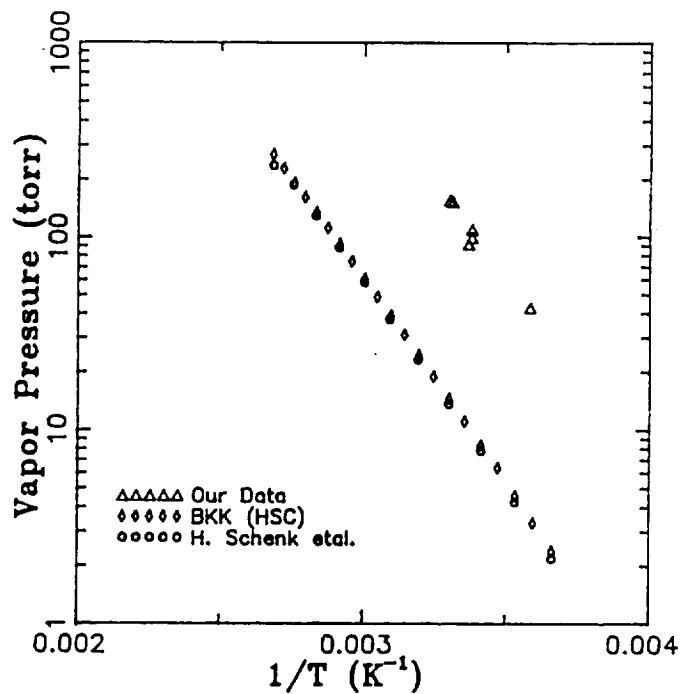


Figure 7 - Comparison of vapor pressure measurements for  $\text{TiCl}_4$ .

# Vapor Pressure of $\text{CCl}_4$

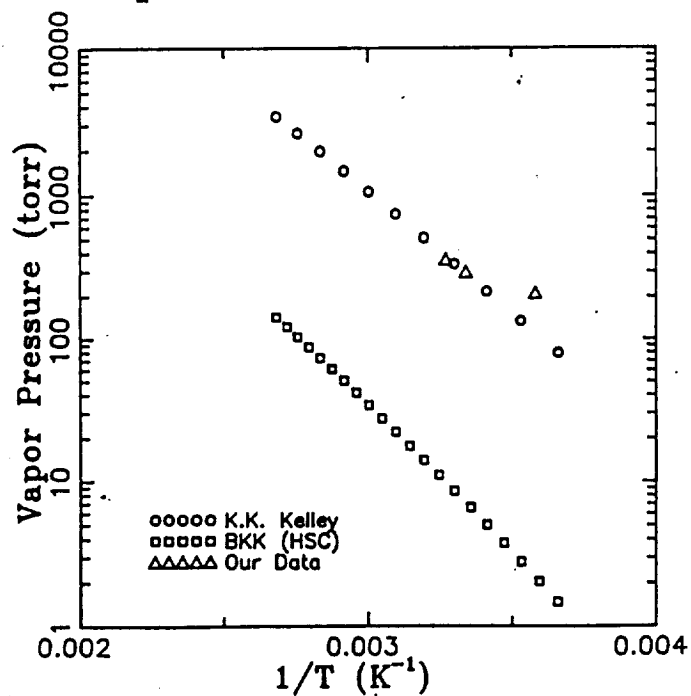


Figure 8 - Comparison of vapor pressure measurements for  $\text{CCl}_4$ .

N91-24370-25  
14665  
P.3

Innovative Techniques for the Production of Energetic Radicals  
for Lunar Materials processing Including Photogeneration

Via Concentrated Solar Energy

D. E. Osborn, D. C. Lynch, and R. Fozzolari

Department of Materials Science and Engineering

and

Solar and Energy Research Facility, Department of Nuclear and Energy Engineering

The University of Arizona

Abstract

In the previous progress report for 1989-90, a technique was discussed for photo generation of radicals that can be used in the recovery of oxygen and metals from extraterrestrial resources. This report is a continuation of that discussion, but is focused on the progress that has been achieved in the past 12 months. During that period it was necessary to move the equipment from the Arizona Materials Laboratories to the Solar Energy Research Facility at the main campus of the University of Arizona. In spite of that delay we have conducted a number of experiments and have achieved significant results.

Introduction

This program is funded by the Space Engineering Research Center, the Arizona Mining and Minerals Resources Research Institute (Grant # G1104104) and the Solar Energy Research Facility. We gratefully acknowledge their support. Because of the nature of the present funding we have submitted a pre-proposal to the Solar Energy Research Institute in Golden, Colorado and a full proposal to the U. S. Bureau of Mines for continuation of this work.

The concept behind this work has been to examine methods whereby radicals can be generated and used in the processing of refractory materials. In that regard we have focused on the use of sunlight. Sunlight provides useful energy for processing in the forms of both thermal and quantum energy. While the use of thermal energy is well accepted, the use of quantum energy of the solar photons (photonic processes) for chemical reactions presents new and exciting possibilities.

Light can affect materials thermally or through photonic processes. the absorption of light can lead to an increase in the vibrational, rotational, and translational energy of the atoms of the material. This shows up, macroscopically, as an increase in temperature and, once absorbed, the effectiveness of the energy is not dependent on the wavelength of light. Photonic processes are

wavelength dependent and are characterized by a threshold wavelength that is specific for each process and material.

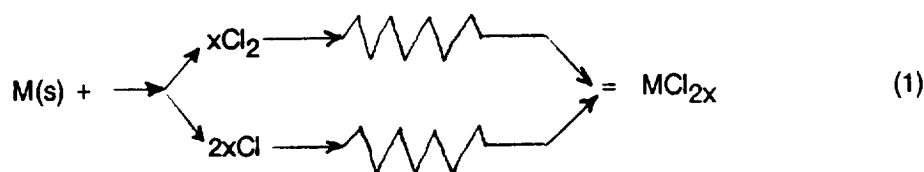
If light is absorbed by a molecule and it has sufficient energy, it can cause a transition of electrons from one orbital to another. If the electron belongs to a chemical bond, the bond may be broken by this transition. Ultra violet (UV) and near UV radiation, as the most energetic portion of the solar spectrum, can break a wide variety of bonds, including that of diatomic chlorine. It is that potential which is the focus of the present investigation.

Photo enhanced chlorination could be used to separate metals from complex alloys such as that which might be produced in situ electrolysis of Lunar regolith. Or it might also be possible to use solar energy in the chlorination and/or carbochlorination of metal oxide to produce oxygen.

A number of researchers have examined the chlorination kinetics of metals, metal oxides and metal sulfides. Certainly the most extensive and thorough work has been conducted by Dr. A. Landsberg at USBM's Albany, Oregon Research Center (1 - 6).

Dr. Landsberg found that the chlorination kinetics of both metals and metal oxides involves two separate processes that can be distinguished by the order of their dependence on the partial pressure of  $\text{Cl}_2$ . In all instances the order has been found to be either  $1/2$  or  $1$  depending on the temperature of reaction. The  $1/2$  power suggests that the splitting of diatomic chlorine is involved in the rate limiting step.

The chlorination of a metal can, in general, be represented by the following reaction:



where M represents any metal. The equation shows that two reaction paths are possible, one involving diatomic chlorine and the other monatomic chlorine. The resistors in the equation serve as reminders that while both reactions proceed in parallel it is expected that the resistance of one of the paths will be so large that it will effectively preclude that mechanism.

Carbochlorination is more complex. Barin and Schuler, however, have provided convincing evidence of the importance of monatomic chlorine in the chlorination of  $\text{TiO}_2$  (7). Those workers reacted disks of  $\text{TiO}_2$  with and without carbon in the presence of  $\text{Cl}_2$  and  $\text{Cl}_2\text{-CO-CO}_2$  gas mixtures. When the  $\text{Cl}_2\text{-CO-CO}_2$  gas mixture was used the  $\text{CO}_2/\text{CO}$  ratio was the same as in the Boudouard equilibrium for the particular temperature under investigation. The chlorination rates of  $\text{TiO}_2$  without solid carbon, but with the  $\text{CO}_2\text{-CO}$  gas mixture, was several orders of magnitude less than that achieved when solid carbon was present. Since the CO and  $\text{CO}_2$  established the same oxygen potential as that achieved with the solid carbon, Barin and Schuler deduced that the carbon activated the chlorine by splitting the diatomic molecule.



To test their theory, Barin and Schuler placed small inert spacers between the disks of carbon and  $\text{TiO}_2$ . They found that the rate of chlorination decreased as the separation between the carbon and  $\text{TiO}_2$  increased. At a separation distance of  $20\mu\text{m}$  the rate was reduced by half, and at a separation of  $100\mu\text{m}$  the rate of chlorination was equal to that experienced without solid carbon being present. Barin and Schuler postulated that the probability that monatomic chlorine (formed on the surface of the solid carbon) recombines before reaching the  $\text{TiO}_2$  increases with the separation distance.

### Experimental Results

A number of experiments have been conducted in the chlorination of metals with and without the aid of UV and near UV light. The results of some of those experiments are discussed below.

In the chlorination of Fe the resistor for the monatomic path in reaction 1 is substantially greater than the resistor involving the diatomic chlorine. The rate of chlorination of iron, unlike many other metals, has been found to be dependent only on the partial pressure of  $\text{Cl}_2$  to the first power.

To test the basic hypothesis of the present investigation, namely, that UV and near UV light can be used to generate monatomic chlorine and thereby enhance chlorination rates, identical Fe specimens were reacted in a chlorine containing gas at a fixed pressure. The results of that test are shown in Figure 1. The specimen reacted at  $292^\circ\text{C}$  was exposed to UV and near UV radiation at specified intensities while the specimen reacted at  $325^\circ\text{C}$  was not. The specimen exposed to light reacted twice as fast as the specimen not exposed to light. At  $325^\circ\text{C}$  the rate of chlorination of Fe will double approximately every  $15^\circ\text{C}$  (4). Thus, the rate observed at  $292^\circ\text{C}$  is approximately 800% greater than that which would occur at the same temperature without UV and near UV light.

The increased chlorination rate with UV and near UV radiation can most likely be attributed to augmentation of the total reaction rate by an increase in the rate of chlorination by monatomic chlorine.

These results run counter to those obtained by Landsberg and Block who attempted to use gamma rays to enhance the chlorination rate of metals (4). It is uncertain whether their intent was to activate the metal by radiation damage or to dissociate  $\text{Cl}_2$ . A gamma ray has sufficient energy to dislodge a proton or neutron from the nucleus of an atom. A gamma ray can dissociate  $\text{Cl}_2$  if there is a mechanism to assimilate the large excess energy. If no mechanism exists dissociation will not take place. In essence a gamma ray has too much energy to form monatomic chlorine by a photonic process.

### Future Work

The current experimental work involving metals will be continued. We plan, however, to also examine the potential for utilizing solar energy in enhancing both chlorination and carbochlorination of metal oxides, including ilmenite.

### References

1. Chlorination Kinetics of Aluminum Bearing Minerals, A. Landsberg, Metall. Trans. B, 6B, pp. 207-14, June 1975.
2. The Chlorination Kinetics of Zirconium Dioxide in the Presence of Carbon and Carbon Monoxide, A. Landsberg, C. L. Hoatson, and F. E. Block, Metall. Trans., 3, pp. 517-23, February 1972.
3. The Chlorination Kinetics of Tungsten, Molybdenum, and their Alloys, A. Landsberg, C. L. Hoatson, and F. E. Block, J. Electro. Chem. Soc., 118, pp. 1331-36, August 1971.
4. A Study of the Chlorination Kinetics of Germanium, Silicon, Iron, Tungsten, Molybdenum, Columbium, and Titanium, AS. Landsberg and F. E. Block, USBM RI 6649, 1965.
5. Conditions Affecting the Formation of Chlorinated Carbon Compounds During Carbochlorination, A. Landsberg, R. D. Wilson, and W. Burns, Metall. Trans. B, 19B, pp. 477-82, June 1988.
6. On the Separation of  $TiCl_4$  from  $AlCl_3$ , A. Landsberg and H. C. Ko, Metall. Trans. B, 17B, pp. 232-34, March 1986.
7. On the Kinetics of the Chlorination of Titanium Dioxide in the Presence of Solid Carbon, I. Barin and W. Schuler, Metall. Trans. B, 11B, pp. 199-207, June 1980.

# CHLORINATION OF Fe

UV enhanced vs. No UV

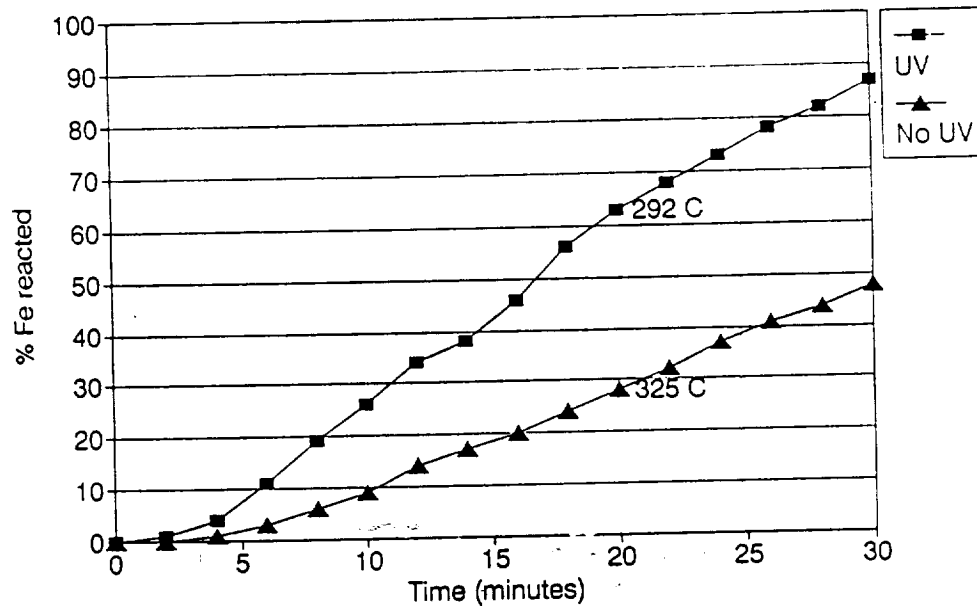


Figure 1 - Comparison of reaction results with and without UV and near UV light

N91-24371  
14666

Oxygen and Iron Production  
By Electrolytic Smelting of Lunar Soil

R.O. Colson and L.A. Haskin  
Dept. of Earth and Planetary Science  
Washington University

P. 11

W7 76031

## INTRODUCTION:

Oxygen, present in abundance in nearly all lunar materials, theoretically can be extracted by molten silicate electrolysis from any known lunar rock. Derivation of oxygen by this method has been amply demonstrated experimentally in silicate melts of a variety of compositions (e.g. Bockris et al., 1952a,b, Simnad et al., 1954, Oppenheim 1968, 1970, Kesterke, 1971, and Lindstrom and Haskin, 1979). In our previous work, we have defined further the conditions necessary to optimize oxygen production by silicate melt electrolysis. We have demonstrated that the conductivity of silicate melts and efficiencies of  $O_2$  production are sufficiently high to permit practical electrolysis of lunar materials (Haskin et al., 1991, Colson and Haskin, 1990). We have measured the dependence of conductivity on melt composition and the dependence of efficiency (fraction of current that produces oxygen) on  $FeO$  concentration in the melt. We have studied the kinetics of cathodic and anodic reactions and found them suitable for electrolysis (Haskin and Semkow, 1985).

Our work of the past year, supplementing these previous results, can be divided into three categories. These categories are the following: 1) measurement of solubilities of metals (atomic) in silicate melts; 2) electrolysis experiments under various conditions of temperature, container material, electrode configuration, current density, melt composition, and sample mass (100 to 2000 mg) measuring energy required and character of resulting products; 3) and theoretical assessment of compositional requirements for steady state operations of an electrolysis cell.

## METAL SOLUBILITIES:

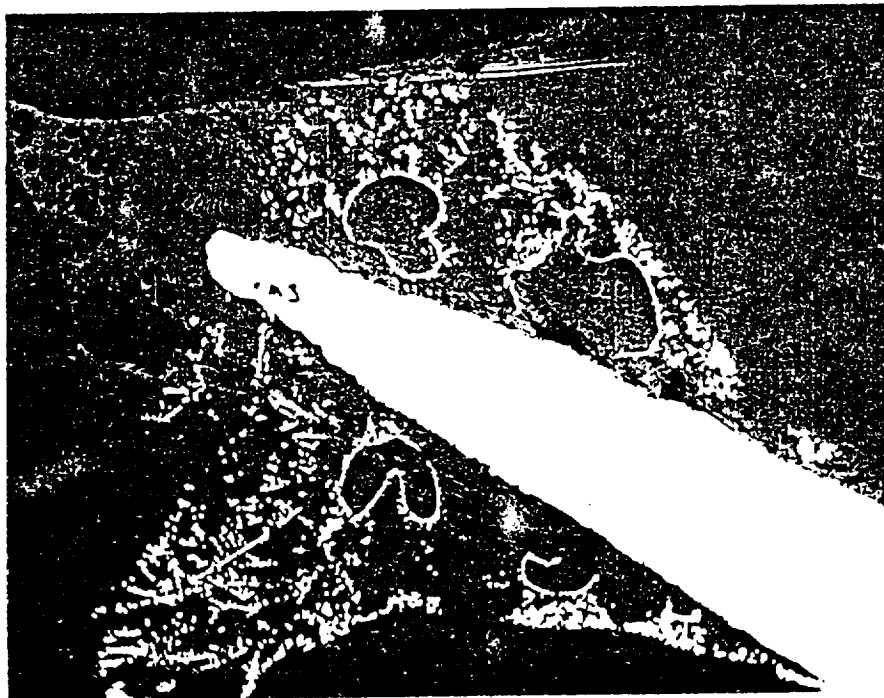
Solubility of species in the atomic state in silicate melts can potentially decrease the  $O_2$  production efficiency because  $Fe^0$  and  $Si^0$  produced at the cathode will dissolve in the melt and be reoxidized at the cathode, producing  $Fe^{2+}$  and  $Si(IV)$  rather than oxygen. We have measured the solubilities of  $Ni^0$ ,  $Co^0$  and  $Ir^0$  in silicate melts and determined an upper limit for  $Fe^0$  solubility. Results suggest that solubility of each of these species is  $<0.2$  wt%. By analogy with the concentrations of  $Fe^{2+}$  required to reduce  $O_2$  efficiency significantly (about 2-5 wt%), we conclude that metals dissolved in the silicate melt will not greatly affect production efficiency.

We measured the solubility of  $Ir$  to be approximately 200 ppm. A less rigorous measurement for  $Pt$  indicated its solubility might also be as high as 100's of ppm. This value is substantially higher than that we reported last year and, depending on how quickly the  $Pt$  equilibrates with the melt, suggests that  $Pt$  might be too soluble to be considered as an inert electrode material in electrolysis as we have suggested previously. If the silicate melt equilibrates rapidly with the  $Pt$  and is actually that high, 20% of the anode would be gone after a feedstock flowthrough of only ~1000 times its mass. Also, other observations suggest that the  $Pt$  anodes are maintained in a state of dynamic equilibrium in which the  $Pt$  is oxidized at the electrode but quickly reduced by the silicate melt as the oxidized  $Pt$  migrates away from the electrode. This results in a substantially roughened anode surface (Fig. 1). Over an extended period of time this process might destroy the  $Pt$  anode. At potentials substantially higher than the 0 to 10 volt range we are working in, the  $Pt$  anode is completely oxidized and melts. Our previous experience has indicated no tendency for  $Pt$  anodes to erode or fail, but anode stability is so important that we must learn whether there are conditions that lead to anode failure.



A12- 1Ch - near anode

Fig. 1 Platinum globs in melt near the Pt anode after electrolysis, suggesting that the Pt anode is not inert during electrolysis. Backscattered Electron Image (BEI).



A12 - 1Cg

Fig. 2 Iron dendrites that form near the cathode tend to short the cell at temperatures below the melting point of the metal. Note "bubbles" of iron. (BEI)

## ELECTROLYSIS EXPERIMENTS:

In an effort to measure energies required for electrolysis, characterize product form and composition, and identify potential problems with the electrolysis process, we have done a series of electrolysis experiments. These are of two types. The first uses 50-100mg of silicate material held by surface tension onto Pt loops about 5mm in diameter. These loops act as anodes. A second Pt electrode passes through the melt inside the Pt loop of each experiment. The composition of silicate melt used in these experiments ranged from FeO-poor (no FeO) to FeO-rich (18% FeO). Some compositions were similar to lunar soils. The second type uses 1 to 2 g of silicate material in spinel ( $\text{MgAl}_2\text{O}_4$ ) crucibles. These crucibles were 8mm inside diameter by 14mm inside length. The cathode was a Pt coil that entered the crucible through a small hole drilled in the bottom. The Pt anode entered the crucible from the top. The cathode and anode were placed about 0.5cm apart. The composition used in the experiments were chosen to represent possible steady state compositions plus a few percent lunar soil.

### Product character

We have identified the solid products of the electrolysis. They are metal (produced at the cathode) and spinel (which exsolves from the melt as  $\text{SiO}_2$  and FeO are removed from it). At potentials less than about one volt, only Fe metal is produced at the cathode. At temperatures less than the Fe melting temperature, the Fe forms dendrites that tend to short the electrolytic cell (Fig. 2). The dendrites expand into the melt as a "bubble" of metal, with melt in the interior of the bubble depleted in Fe and the exterior rich in Fe.

At higher potentials (greater than 1 volt), both Si and Fe are produced at the cathode (with minor Ti, Cr, Mn, and other trace constituents). We have observed the coexistence of as many as three metal phases (Colson, 1990). We associate these metal phases with the c, a, and melt phases in the Fe-Si system (Lyman, 1973). The highest concentration of Si in metal that we have observed is about 10wt%. In most cases, this is less than the amount of Si expected based on thermodynamic calculations. Metal more distant from the cathode has substantially less Si than metal near the cathode, suggesting that the Si in the Si-Fe alloy is reacting with the melt to form Fe in the metal and Si(IV) dissolved in the melt.

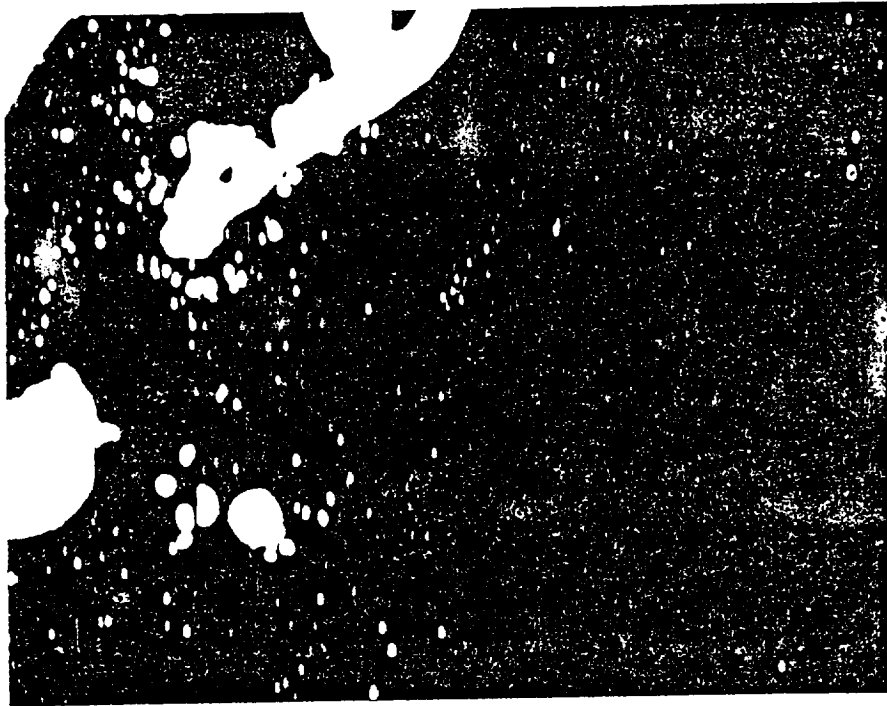
In the 50 to 100mg experiments, the metal product is often broken into small particles and mixed throughout the sample by stirring caused by the bubbles that form and escape at the anode. Substantial dissemination of metal in melt is seen in Fig. 3. This mixing probably enhances the reaction of Si with the melt. Mixing of metal back into the melt was not observed in the larger scale experiments done in spinel crucibles.

Spinel ( $\text{MgAl}_2\text{O}_4$ ) is observed to precipitate near the cathode in experiments with low FeO concentrations (<5%) run in spinel crucibles (in which the melt is saturated with spinel). This spinel sometimes forms a sheath around the cathode, increasing the cell resistance (Fig 4). In experiments containing Fe and Cr, an Fe-Cr rich spinel is observed to form near the cathode. Based on thermodynamic calculations, spinel is expected to precipitate as  $\text{SiO}_2$  is removed from the melt by electrolysis.

Spinel crucibles appear to be stable, as expected, in a spinel-saturated silicate melt. After several hours of contact with the melt, the spinel does not deteriorate (Fig. 4). The stringers of melt invading the spinel in Fig. 4 probably have followed fractures induced by the thermal shock caused by repeatedly putting the sample in the furnace and taking it out.

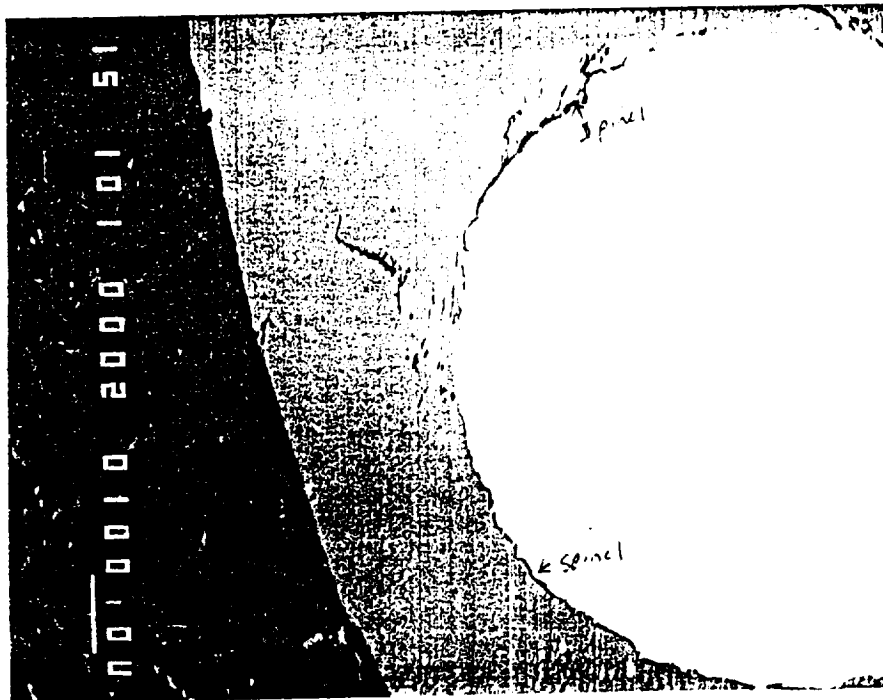
One spinel crucible nearly failed during actual electrolysis. Figure 5 shows the spinel crucible wall after only forty minutes of electrolysis. The spinel is substantially corroded and invaded by the melt. This destruction of the spinel occurred in the immediate vicinity of the cathode suggesting a reaction with a cathodic product. The vesicles in the vicinity of the cathode, also seen in Fig. 5, suggest the formation of a gas phase at the cathode. This gas appears to be a cathodic product, and may actually have attacked the spinel wall. The presence of vapor-deposited Pt in the vesicles seen in the figure suggests that this gas mobilized Pt. We have

IA-55



A12 - 1ci

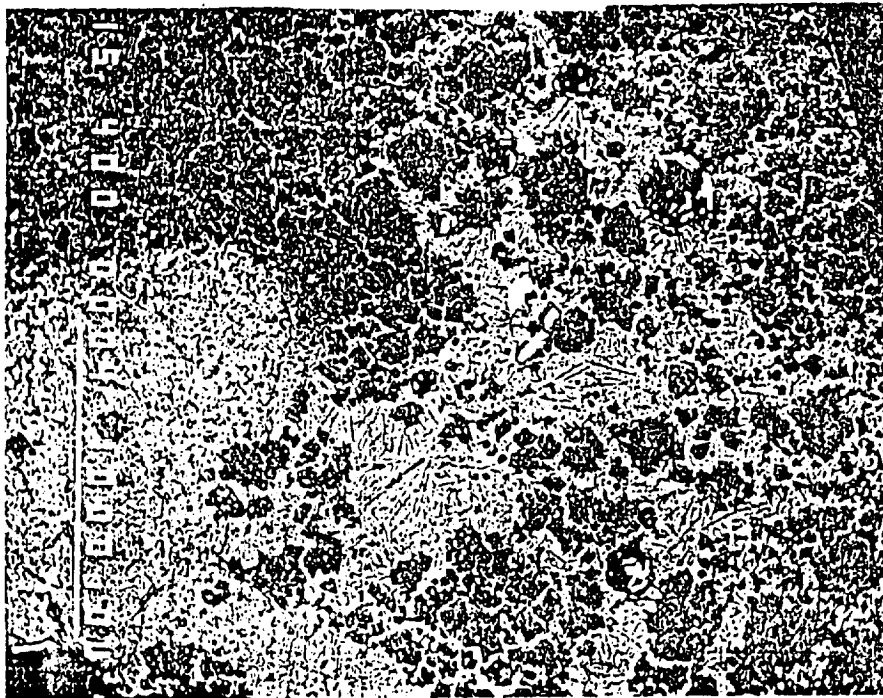
Fig. 3 Metal disseminated in glass as small metal beads. This is probably caused by violent mixing of the small sample by oxygen bubbles formed at the anode. (BEI)



Elec55 6

Fig. 4 Spinel is the darker phase forming a narrow sheath around the bright Ir cathode. Spinel also forms the crucible wall seen on the left. The spinel crucible does not appear to be corroded by the melt. (BEI)

ORIGINAL PAGE IS  
OF POOR QUALITY



Elec5520

Fig. 5 Darker areas are pieces of the spinel crucible corroded and invaded by the lighter colored melt. Black circles are vesicles partially filled with bright Pt crystals. This picture is taken near the base of the crucible and near the cathode. This picture is evidence that the spinel crucible is corroded by a gaseous product of electrolysis. (BEI)

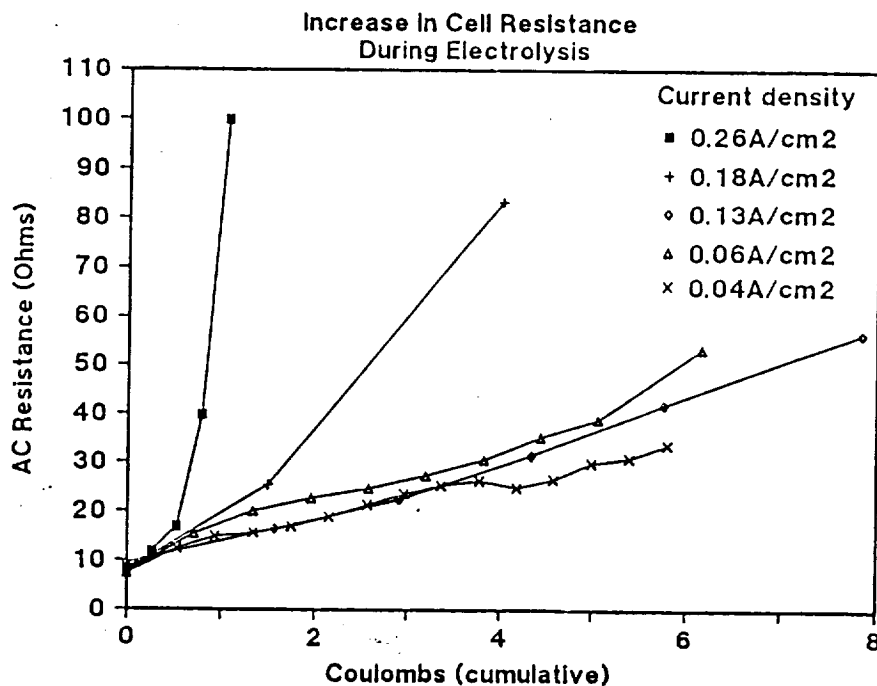


Fig. 6 Dependence of AC resistance on total current for experiments in composition SS1. We believe that the sharp increase in resistance during electrolysis is due to frothing of the melt, resulting from failure of the oxygen generate at the anode to escape sufficiently quickly from the melt.



determined that the gas forms at the cathode in air,  $\text{CO}_2$ , and argon atmospheres when the only constituents of the melt are  $\text{SiO}_2$ ,  $\text{CaO}$ ,  $\text{MgO}$ , and  $\text{Al}_2\text{O}_3$ , or when  $\text{FeO}$  is present as well. We have found the gas to form at the cathode using either a Pt or Ni cathode. We speculate that the gas may contain a silicon monoxide species analogous to carbonyls. However, this problem requires further study to determine what the gas is and what effect, if any, it has on the spinel container and how any effect can be minimized.

### Energy measurements

In the 1 to 2 g experiments, cell resistance during electrolysis (from which energy use can be calculated by  $\text{energy} = I^2 R \text{time} + \text{theoretical energy to reduce melt}$ ) was measured as a function of current density, depth of anode in the melt, and melt composition. Results are shown in Figs. 6-8.

The sharp and progressive increase in resistance during electrolysis is due primarily to frothing of the melt caused when bubbles generated cannot escape sufficiently quickly. Using lower current densities or placing the anode at different depths in the melt yields little improvement (Figs. 6 and 7). We also tried different types of anodes (i.e. straight wire rather than a coil, Pt screen, and more or less tightly coiled Pt anodes) without much improvement. We tried "stirring" the melt by moving the anode up and down about 1-2mm at about one cycle every 2 seconds but this caused the frothing melt to be quickly lost out the top of the crucible.

Lower concentrations of  $\text{SiO}_2$  and  $\text{Al}_2\text{O}_3$  result in lower viscosities (Bottinga and Weill, 1972) and surface tension (Walker and Mullins, 1981). At lower concentrations of these species, the frothing does not occur (Fig. 8). Frothing will probably constrain us to use lower  $\text{SiO}_2$ ,  $\text{Al}_2\text{O}_3$  melts (<about 55%  $\text{SiO}_2 + \text{Al}_2\text{O}_3$ ) as the steady state composition of the cell. However, it is possible that in larger pots, in which the surface energy between the crucible and the melt is not as important, the frothing problem may not be significant.

The use of the lower  $\text{SiO}_2 + \text{Al}_2\text{O}_3$  melt as the steady state "flux" in the 1 to 2 g experiments results in an energy requirement for the electrolysis less than 30% greater than the theoretical minimum (presuming that 85% or more of the current goes to producing oxygen, after Haskin et al., 1991). This very low energy requirement is substantially less than has been suggested for most other processes, which require 2 to 4 times the theoretical energy (Colson and Haskin, 1990) and is less than the energy requirement we calculated on theoretical grounds for batch electrolysis (Haskin et al., 1991).

However, Haskin et al. (1991) presumed a current density of about  $1 \text{ A/cm}^2$  whereas the experiments in composition SS2 (the lower  $\text{SiO}_2 + \text{Al}_2\text{O}_3$  experiments) in which no frothing occurred had a current density of about  $0.1 \text{ A/cm}^2$ . At higher current densities in the vicinity of  $0.8$  to  $1 \text{ A/cm}^2$ , resistance varied erratically, as though frothing periodically increased and dissipated, and energy requirements were correspondingly higher.

### **COMPOSITIONAL REQUIREMENTS OF STEADY STATE:**

Several considerations must be made in assessing the ideal composition of the steady state melt maintained as a "flux" in the electrolysis cell. These include the need to minimize the energy requirements of electrolysis (generally, decreasing  $\text{SiO}_2$ ,  $\text{Al}_2\text{O}_3$ , and  $\text{FeO}$  improves efficiency of the process; Haskin et al., 1991, and Taylor et al., 1991), the need to provide a composition in which the chosen container and electrode materials are not consumed (for example, spinel as a container or electrode requires a melt in equilibrium with it; Colson and Haskin, 1990, and McCullough and Mariz, 1990), and the composition of the feedstock. The variables we can use to control the steady state composition include the feedstock composition (which can presumably be varied within certain limits), the composition of the metal product (which can be varied by adjusting cell potential and feedstock flow-through rate), and the temperature (which places constraints on the composition of a melt in equilibrium with a container or electrode material).

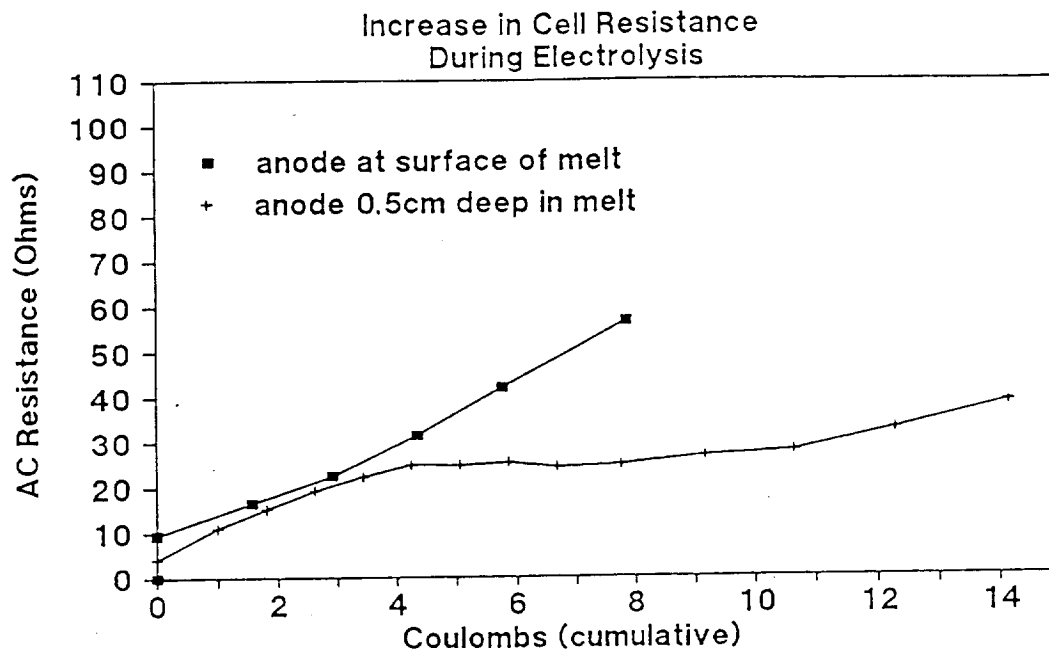


Fig. 7 Dependence of frothing (indicated by increase in resistance with current) on the depth of the anode in the melt for composition SS1.

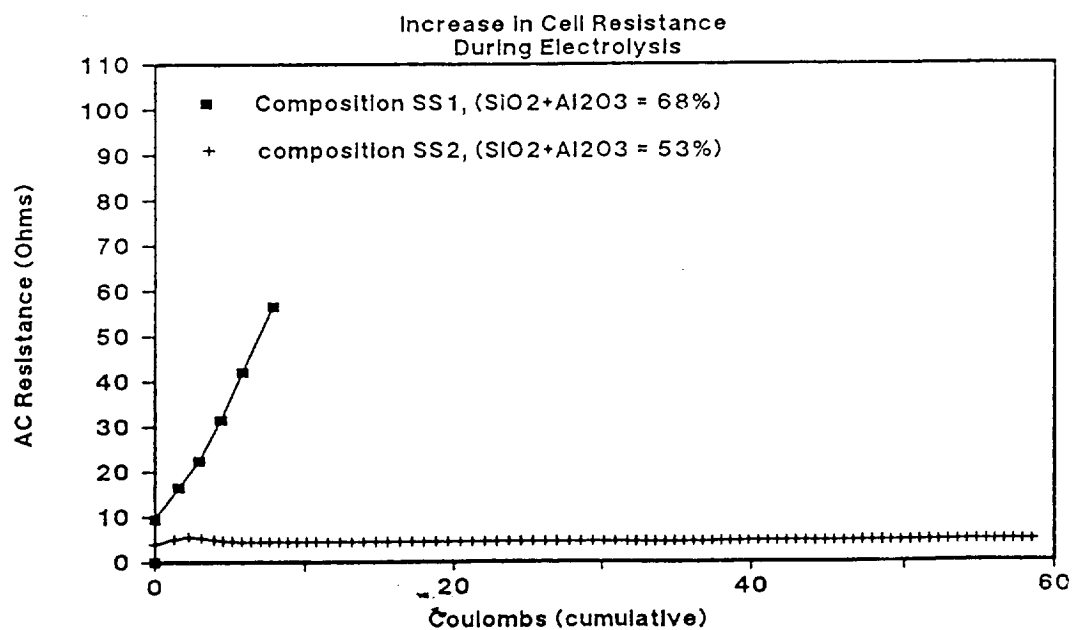


Fig. 8 Dependence of frothing (indicated by increase in resistance with current) on melt composition.

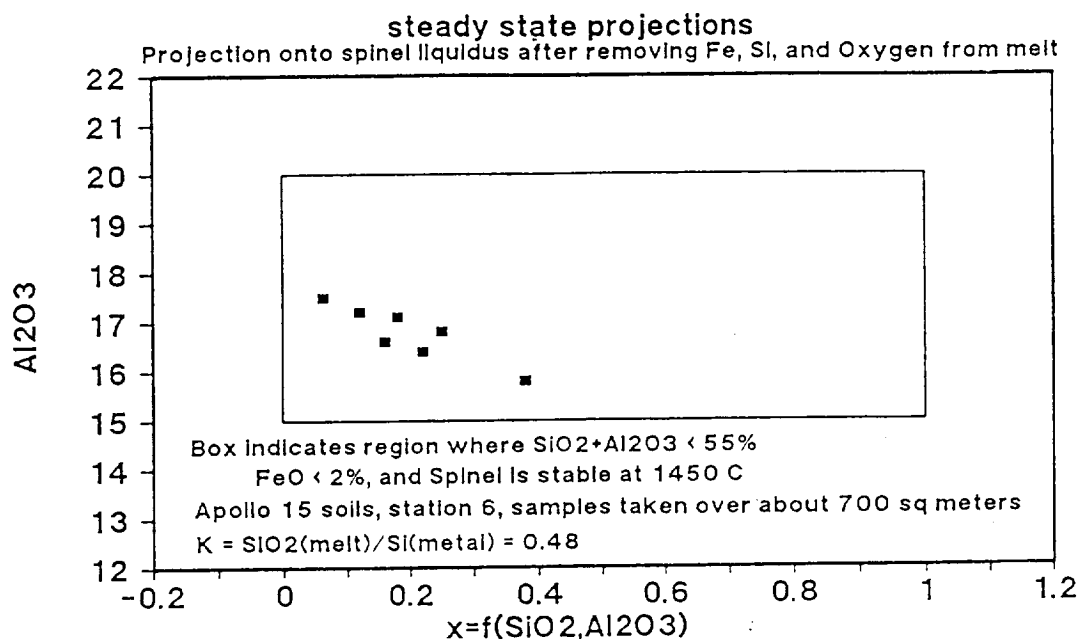


Fig. 9 Theoretical calculation of the steady state melt composition for several Apollo 15, station 6 soil compositions projected onto the spinel liquidus surface, illustrating that for given values of temperature and cell potential, all station 6, Apollo 15 soils in this data set meet the criteria defined in the text for efficient electrolysis and spinel stability. These projections are made by first removing  $\text{FeO}$ ,  $\text{TiO}_2$ , and  $\text{SiO}_2$  from the melt according to the selected value for  $K$ , then projecting from spinel onto the surface defined by the spinel liquidus at  $1450^\circ\text{C}$ . Data are from Korotev (1987) and Morris et al (1983).

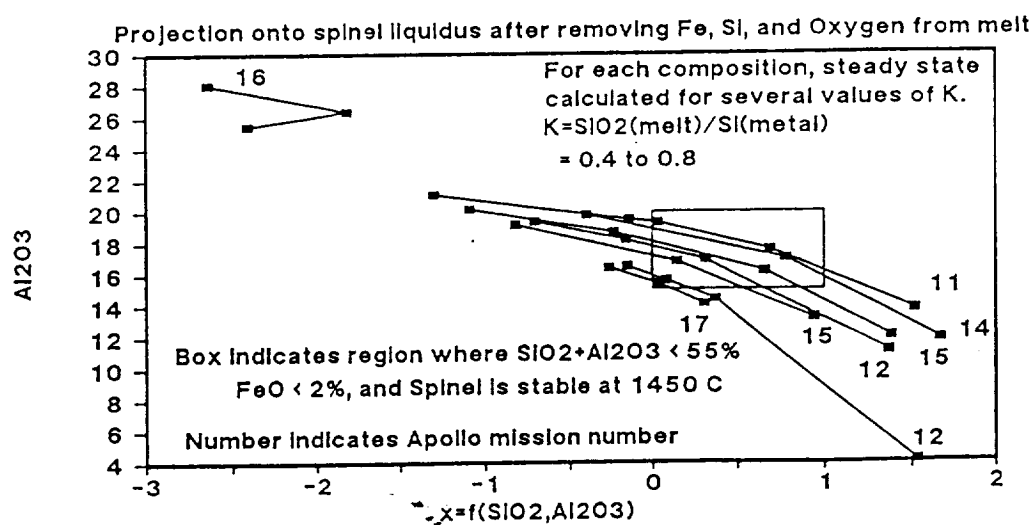


Fig. 10 Illustration that steady state for soils from most Apollo missions can be maintained on the spinel liquidus, and at compositions compatible with efficient electrolysis by adjusting cell potential. Points on the curves represent steady state calculations done for different cell potentials (different values for  $K$ ). Data are from Taylor (1982).

In the following example, we constrain the steady state concentration of FeO to be less than 2% (to maximize oxygen production/current, Haskin et al, 1991),  $\text{SiO}_2 + \text{Al}_2\text{O}_3$  to be less than 55% (to minimize frothing and maximize melt conductivity, Haskin et al, 1991, and this report), and the steady state melt to be in equilibrium with spinel ( $\text{MgAl}_2\text{O}_4$ ). Depending on the potential imposed between the electrodes, and on the residence time of the melt, Si/Fe in the metal product can vary between 0 and  $\text{Si}(\text{melt})/\text{Fe}(\text{melt})$ . In this exercise we assume the feedstock achieves equilibrium at the imposed potential. Therefore, the amounts of Fe, Ti, and Si metal produced are defined by  $K_{\text{Fe}} = f(E) = \text{FeO}(\text{melt})/\text{Fe}(\text{metal})$ ,  $K_{\text{Si}} = f(E) = \text{SiO}_2(\text{melt})/\text{Si}(\text{metal})$ , and  $K_{\text{Ti}} \sim K_{\text{Si}}$ . Here, E is cell potential, and, for this exercise, the activities are approximated by wt%  $\text{SiO}_2$  in melt and mole fraction Si or Fe in metal. (This does not constrain the produced molten alloy to be in equilibrium with any solid Fe-Si alloy, as might be desired if a solid Fe-Si metal is used as a cathode.) The amount of spinel removed from the melt is determined from phase equilibria (e.g. pg. 185 in Levin et al, 1969). After a sufficient length of time, the steady state composition is defined by the relationship:

$$\text{Wt fraction A in Cell} = (a-bc)/(1-c)$$

where a = weight fraction of A in feedstock, b = weight fraction of A in product, and c = weight fraction of feed that yields product.

Two questions are of interest. How much variation can there be in feedstock composition for a given set of electrolysis conditions (temperature, cell potential) without causing the steady state compositions to deviate from the ranges defined above (that is, how sensitive is the process to feedstock variations)? Secondly: How wide a variation in feedstock composition can be accommodated by adjusting temperature and cell potential to maintain the steady state composition within the compositional range defined above (that is, how robust is the process with respect to feedstock composition)?

Figure 9 illustrates that the process is not sensitive to anticipated local variations in feedstock composition. Over a region of about 700 square meters at station 6, Apollo 15, variations in the soil composition are small enough such that the steady states for all compositions are within the range defined above. The axes of Fig. 10 are chosen such that the stability field of spinel at 1450°C can be approximately plotted on the figure. That region of the spinel stability field which also meets the other criteria outlined above is shown by a box on the figure.

When data for more soils from Apollo 15 sampled over several square kilometers are included, they do not all fall within the box. However, by adjusting the value of K (which is a function of cell potential and therefore can be controlled), the steady state arising from these other soil compositions could be brought into the box on the figure. In fact, steady states deriving from many of the soils sampled by the Apollo missions can meet the criteria defined above (Fig. 10), demonstrating the versatility of the electrolysis process with respect to feedstock composition. By adjusting the cell potential, the steady state composition for all the example soils except that from Apollo 16 can meet the combined criteria for high conductivity, low viscosity, high production efficiency, and spinel on the liquidus. We point out that whether or not spinel is ultimately chosen as a container material determines whether the rather stringent criteria of maintaining the steady state composition in equilibrium with spinel is actually required. If some other container is ultimately chosen, some of the above criteria may be relaxed, or may be replaced by others, e.g., if it is desirable to keep some other liquidus phase present. This discussion is given as an example illustrating that the process is versatile with respect to feedstock composition but is not particularly sensitive to variations in feedstock composition over a small region.

Bockris, J. O'M., Kitchener, J. A. and Davies, A. E. (1952a) Electric transport in liquid silicates, Trans. Faraday Soc., 48, pp. 536-548.

Bockris, J. O'M., Kitchener, J. A. Ignatowicz, W. and Tomlinson, J. W. (1952b) Electric conductance in liquid silicates, Trans. Faraday Soc., 48, pp. 75-91.

- Bottinga Y. and Weill D. F. (1972) The viscosity of magmatic silicate liquids: a model for calculation, *Am. J. Sci.*, 272, pp. 438-375.
- Colson, R. O. (1990) Characterization of metal products of silicate melt electrolysis, *Lunar Planet. Sci. XXI*, pp. 214-215. The Lunar and Planetary Inst., Houston.
- Colson R. O. and Haskin L. A. (1990) Lunar oxygen and metal for use in near-earth space: Magma electrolysis, in *Engineering, Construction, and Operations in Space: Vol 1* (ed Johnson, S. W. and Wetzel, J. P.), ASCE New York.
- Haskin, L. A., Colson R. O., Lindstrom, D. J., Lewis, R. H. and Semkow, K. W. (1991) Electrolytic smelting of lunar rock for oxygen, iron and silicon, in *Lunar Bases and space Activities of the 21st Century (II)*, Mendell, W. W. (ed.), LPI, in press.
- Kesterke D. G. (1971) Electrowinning of oxygen from silicate rocks. U. S. Bureau of Mines Report of Investigations 7587. 10pp.
- Korotev R. L., (1987) Mixing levels, the Apennine front soil component, and compositional trends in the Apollo 15 soils, *Proc. 17th Lunar Sci. Conf.*, *J. Geophys. Res.* 92, E411-E431.
- Levin E. M., Robbins C. R., and McMurdie H. F. (eds) (1969) *Phase Diagrams for Ceramists*, Vol 2, The American Ceramic Society.
- Lindstrom D. J. and Haskin L. A. (1979) Electrochemical preparation of useful material from ordinary silicate rocks. in *Space Manufacturing Facilities*, Gray, J. and Krop C. (eds.) AIAA, pp. 129-134.
- Lyman T. (Ed.) (1973) *Metals Handbook*, Vol. 8, 8th Ed. Metallography, structures and phase diagrams, Am. Soc. for Metals, Metals Park, OH.
- McCullough, E. and Mariz, C. (1990) Lunar oxygen production via magma electrolysis, in *Engineering, Construction and Operations in Space*, Johnson, S. W. and Wetzel, J. P. (eds.) New York: American Soc. Civil Eng. pp. 347-356.
- Morris R. V., Score, R., Dardano C., and Heiken G. (1983) *Handbook of lunar soils*, NASA/JSC publication 67, Houston.
- Oppenheim, M. J. (1968) On the electrolysis of molten basalt, *Mineral. Mag.*, 36, pp. 1104-22.
- Oppenheim, M. J. (1970) On the electrolysis of basalt, II: experiments in an inert atmosphere, *Mineral. Mag.*, 37, pp. 568-577.
- Semkow, K. W. and Haskin L. A. (1985) Concentrations and behavior of oxygen and oxide ion in melts of composition  $\text{CaO MgO } x\text{SiO}_2$ , *Geochim. Cosmochim. Acta* 49, pp. 1897-1907.
- Simnad, M. T., Derge, G. and George, I. (1954) Ionic nature of liquid iron-silicate slags, *J. Metals*, 6, pp. 1386-1390.
- Taylor S. R. (1982) *Planetary Science: A lunar perspective*, Lunar and Planetary Inst., Houston.
- Taylor L. A., Cooper B, McKay D. S., and Colson R. O. (1991) Oxygen production on the moon: Processes for different feedstocks, *Metallurgy processing fundamentals: Lunar mining and Processing*, Soc. of Mining, Metallurgy, and Exploration (SME) (in press).

Walker, D. and Mullins, Jr., O. (1981) Surface Tension of natural silicate melts from 1,200 -1500 C and implications for melt structure, Contrib. Mineral. Petrol., 76, pp. 455-462.

N 9 1 - 2 4 3 7 2 5

Experimental Study of the Electrolysis of Silicate Melts

R. Keller and K. T. Larimer

EMEC Consultants

R.D. 3, Roundtop Road

Export, PA 15632

14667

p. 8

E 1 560 304

Abstract

To produce oxygen from lunar resources, it may be feasible to melt and electrolyze local silicate ores.

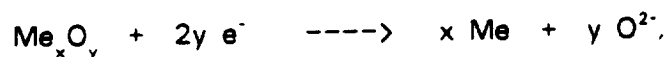
This possibility was explored experimentally with synthesized melts of appropriate compositions. Platinum electrodes were employed, at a melt temperature of 1425 °C. When silicon components of the melt were reduced, the platinum cathode degraded rapidly, which prompted the substitution of a graphite cathode substrate. Discrete particles containing iron or titanium were found in the solidified electrolyte after electrolysis of 3 hours duration.

Electrolyte conductivities did not decrease substantially, but the escape of gas bubbles, in some cases, appeared to be hindered by high viscosity of the melt. Several key issues of the approach remain to be examined in further experimentation: electrolyte conductivity; current efficiency; separation of products; and stability of electrode and container materials.

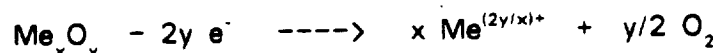
Principles of "Magma Electrolysis"

Raw materials readily available on the lunar surface are generally oxides. They contain copious amounts of oxygen for potential use as propellant or for life support. A suitable chemical oxidation process is required to produce valuable molecular oxygen. Electrolysis of the oxides is a possibility. Melting available silicates and electrolyzing this melt appears particularly attractive because of the conceptual simplicity of this approach, which has been called "magma electrolysis". Its fundamentals have been studied in recent years at Washington University in St. Louis [1] [2].

Lunar raw materials for in-situ utilization are silicates that contain various amounts of other oxides such as aluminum oxide, calcium oxide, magnesium oxide, iron (Fe<sup>II</sup>) oxide, titanium oxide, etc. These oxides can be molten, typically at temperatures of 1400 °C and higher, and electrolyzed, reducing metal components at the cathode,



and oxidizing oxides to oxygen gas at the anode,



When the electrolysis is conducted to produce oxygen as the useful product of

primary interest, the melt can be partially electrolyzed and residual oxides discarded. Reduction potentials and mass transport conditions determine which metals will be preferentially reduced.

For the feasibility of "magma electrolysis" to produce lunar oxygen, we consider at this stage the following to be key issues:

(1) Electrolyte Conductivity. To maintain acceptable production rates at reasonable space-time yields and energy efficiency, the specific conductance of the molten material must be high and remain high during the electrolysis.

(2) Current Efficiency. The process must have an acceptable faradaic yield. Low current efficiencies may result from reoxidation of cathode products; metals often are soluble in molten electrolytes. Current efficiencies can also be affected by the oxidation of lower valent species to higher valent ones, as in the case of  $\text{Fe}^{II}$  to  $\text{Fe}^{III}$ .

(3) Separation of Products. Products need to be removed from the system. This applies to the oxygen gas as well as to metals that form at the cathode.

(4) Stability of Electrode and Containment Materials. As high temperatures and aggressive melts are involved, materials requirements are anything else but trivial.

Work on the electrolysis of molten silicates representative of lunar resources has been performed in very-small-scale experiments at Washington University [1] [2]. Molten material suspended on a small platinum wire loop was electrolyzed, thereby avoiding problems with containment materials. Recently small crucibles of magnesium-aluminum spinel have been employed.

Some disturbing phenomena were observed in these small scale experiments. The melt resistance appeared to increase after a short time of electrolysis; retainment of gas bubbles was suspected as the main reason. In some electrolytes, gas was found trapped in the melt after its solidification, indicating relatively high viscosities and potential problems in electrolysis. It was the main goal of the present effort to see if such phenomena also exist in a somewhat larger scale and if new problems become evident.

### Electrolyte Composition and Conductivity

Lunar raw material may be molten and electrolyzed in a batch mode. In such a case, the electrolyte composition changes during the course of electrolysis, which is carried to a certain point at which the residual melt is discarded. Such an approach was discussed in an earlier publication by Washington University authors [1].

Alternatively, the electrolysis may be conducted in a quasi-continuous mode. Fresh ore is added to an electrolyte which represents partially electrolyzed raw material. While components that reduce most easily are continuously electrolyzed, electrolyte is gradually removed from the system. This approach is represented in Figure 1.



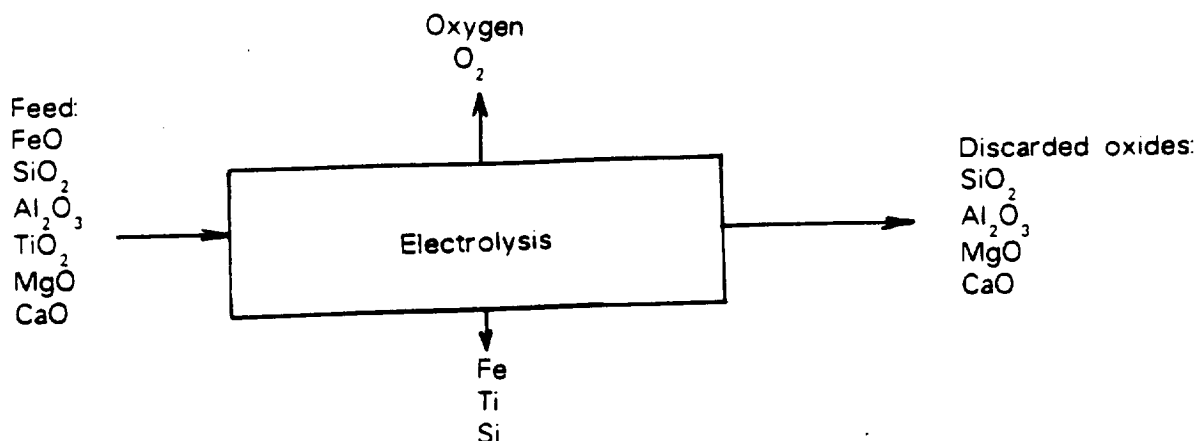


Figure 1: Continuous Electrolysis of Molten Lunar Oxides

Table 1 presents compositions that represent potential lunar raw materials: (1) a basaltic material given as typical by [1]; (2) a simulant of mare soil, as provided as MLS-1 by the University of Minnesota [3]; and (3) anorthosite considered by EMEC Consultants as raw material for the electrolysis in molten salt [4]. Table 2 gives compositions that may be expected after partial electrolysis of basaltic material, or compositions of electrolytes as they may be present in continuous electrolysis.

Electrolyte conductivities vary remarkably with composition. Haskin et al [1] give the following regression equation (for 1425 °C):

$$\ln \lambda = 5.738 - 12.6[\text{SiO}_2] - 10.0[\text{AlO}_{1.5}] - 3.7[\text{TiO}_2] + 1.89[\text{FeO}] + 0.07[\text{MgO}] - 1.25[\text{CaO}]$$

(symbols for oxides stand for mole fractions;  $\lambda$  in  $\text{ohm}^{-1}\text{cm}^{-1}$ )

Conductivity values included in Tables 1 & 2 have been calculated based on this equation.

High iron oxide contents obviously lead to relatively high conductivities. Excessive silicon contents result in low conductivities. In practice, one may expect to be operating with electrolytes of specific conductances of about  $0.3 \text{ ohm}^{-1}\text{cm}^{-1}$ .

### Electrolysis Experiments

In our electrolysis experiments, mixtures of oxides were placed in alumina crucibles and melted in a DELTECH furnace equipped with silicon carbide heating elements. Typically, 70 g of a mixed oxide composition was used. The electrolysis was conducted between two electrodes. Platinum was used as the anode material, platinum and carbon as cathode substrate. Currents were applied at current densities approximating  $0.5 \text{ A/cm}^2$ . Electrolysis durations of 2-4 hours were targeted. A temperature of 1425 °C was normally maintained.

**Table 1:** Composition of Lunar Raw Materials

<u>Component</u>	<u>Lunar Soil [1]</u>	<u>MLS - 1</u>	<u>Anorthite</u>
FeO	17.4 wt%	13.40 wt%	
Fe <sub>2</sub> O <sub>3</sub>		2.60 wt%	
SiO <sub>2</sub>	46.2 wt%	43.86 wt%	43.2 wt%
Al <sub>2</sub> O <sub>3</sub>	12.6 wt%	13.68 wt%	36.6 wt%
TiO <sub>2</sub>	2.8 wt%	6.32 wt%	
MgO	10.4 wt%	6.58 wt%	
CaO	10.6 wt%	10.13 wt%	20.2 wt%
Na <sub>2</sub> O		2.12 wt%	
K <sub>2</sub> O		0.28 wt%	
P <sub>2</sub> O <sub>5</sub>		0.20 wt%	
$\lambda$	0.320 ohm <sup>-1</sup> cm <sup>-1</sup>	0.304 ohm <sup>-1</sup> cm <sup>-1</sup>	0.029 ohm <sup>-1</sup> cm <sup>-1</sup>

In initial experiments, a pair of platinum electrodes was lowered into the molten silicates. Problems were encountered as the platinum bent rather readily and the original electrode geometry was not maintained; electrodes even contacted each other in some cases. This problem was alleviated when the molten electrolyte charge was raised mechanically to the mounted electrodes rather than the electrodes lowered into the melt by hand; this was possible because the furnace bottom can be raised and lowered.

In a successful experiment, a basaltic composition was electrolyzed for 3 hours at 1 A. The cell voltage decreased from an initial 8 V to 3-4 V; no increase was observed in the initial period. The anode appeared essentially unchanged after the experiment, while the cathode was brittle. The electrolysis ran smoothly, but no obviously metallic cathodic products could be found after solidification of the electrolyte.

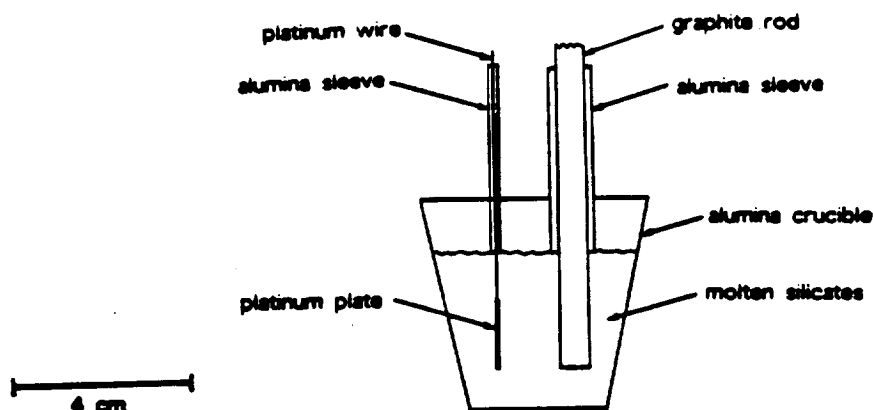
When "partially electrolyzed" compositions were used, the electrolysis could be conducted only for a short period of less than 10 minutes. The platinum cathode was attacked, presumably due to reduced silicon; electrical contact was lost.

The electrolysis could be executed successfully when a graphite cathode substrate

**Table 2:** Composition of Electrolytes in Continuous Electrolysis

<u>Component</u>	all FeO reduced	all FeO, TiO <sub>2</sub> & 50 % SiO <sub>2</sub> reduced	all FeO, TiO <sub>2</sub> & 50 % SiO <sub>2</sub> reduced; 10 % feed added
FeO	0	0	1.58 wt%
SiO <sub>2</sub>	55.9 wt%	40.74 wt%	41.24 wt%
Al <sub>2</sub> O <sub>3</sub>	15.25 wt%	22.22 wt%	21.35 wt%
TiO <sub>2</sub>	3.4 wt%	0	0.25 wt%
MgO	12.6 wt%	18.34 wt%	17.62 wt%
CaO	12.85 wt%	18.69 wt%	17.95 wt%
$\lambda$	0.073 ohm <sup>-1</sup> cm <sup>-1</sup>	0.286 ohm <sup>-1</sup> cm <sup>-1</sup>	0.313 ohm <sup>-1</sup> cm <sup>-1</sup>

was substituted for platinum. A graphite rod of 6 mm diameter was shielded by an alumina tube above the melt and exposed to the electrolyte as the cathode. The simple arrangement is shown in Figure 2. The cell resistance decreased by about a third during the course of a two-hour electrolysis. Some melt, however, flowed over the top of the crucible, most likely indicating hindrance in the discharge of the anode gas from the melt into the gas phase above the melt.

**Figure 2:** Electrolysis Arrangement with Graphite Cathode

The cell of one experiment was cut into two halves after solidification following termination of the experiment. The cross section is shown in Figure 3. It shows the alumina crucible (1), the carbon cathode (2), the thin platinum sheet anode (3) and the electrolyte (4). Voids probably formed on solidification. Marks from the cutting with a diamond-studded saw blade are visible.

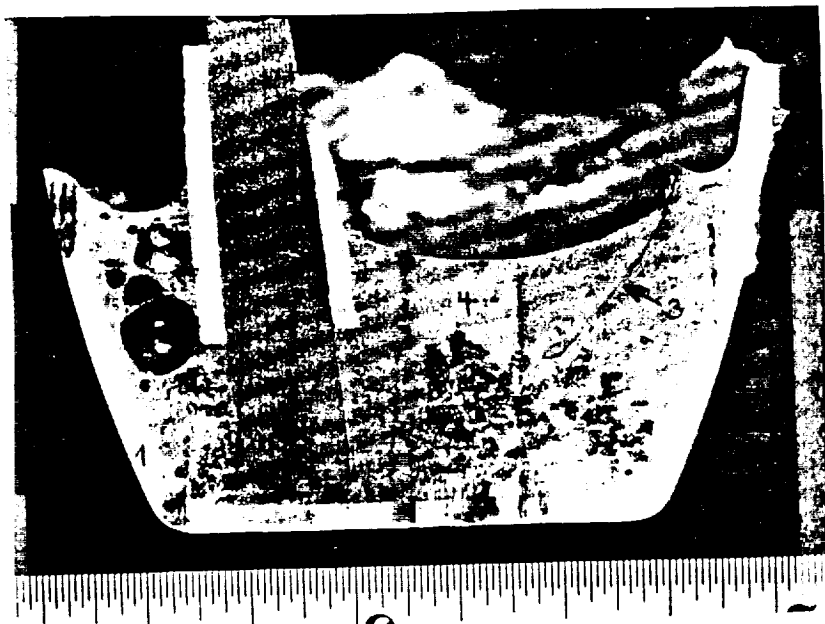
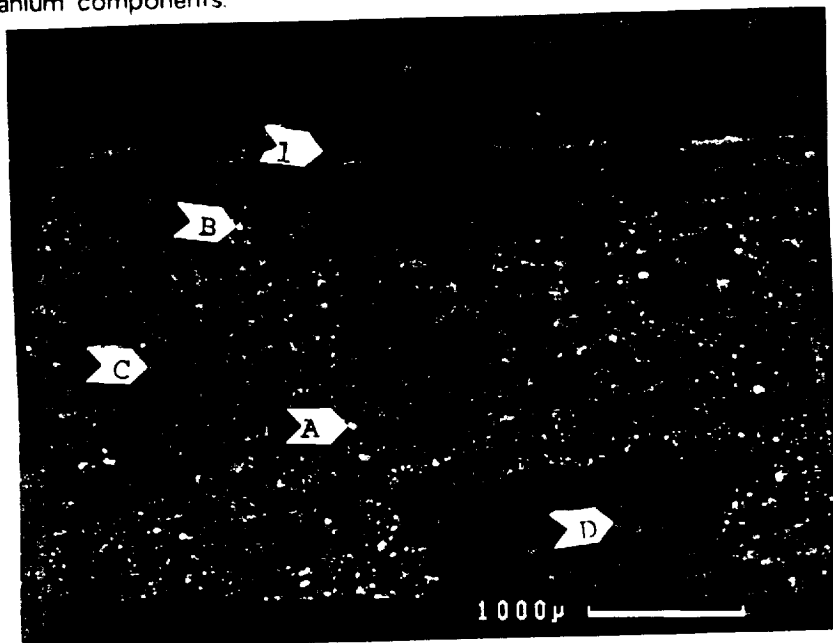


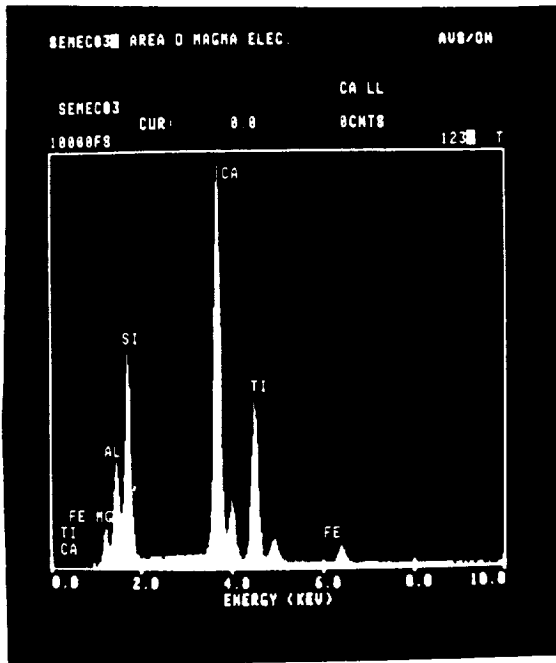
Figure 3: Cross Section of Crucible after Experiment

A cross section of the electrolysis cell prepared after the experiment was examined by scanning electron microscopy. Figure 4 shows the interface between the graphite cathode and the solidified electrolyte. No distinct metal coating on the graphite surface is indicated, although the analytical results represented in Figure 5 revealed at position 1 a somewhat higher titanium content than in the electrolyte. Particles that appear to be metal, however, were found dispersed in the electrolyte phase. Essentially pure iron was indicated at location A, essentially pure titanium at location C, while titanium with minor amounts of silicon and iron was indicated at location B. Calcium, aluminum, silicon, iron and titanium all were present in the electrolyte (position D), presumably as oxides. Evidently the electrolysis was not conducted much beyond the reduction of iron and titanium components.

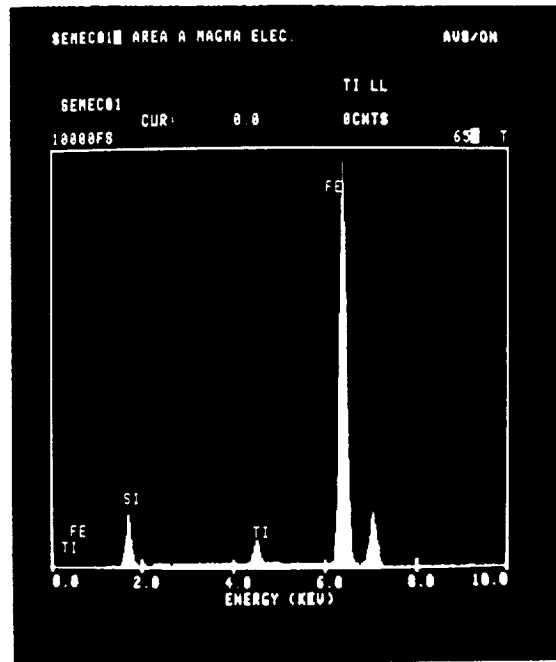


ORIGINAL PAGE IS  
OF POOR QUALITY

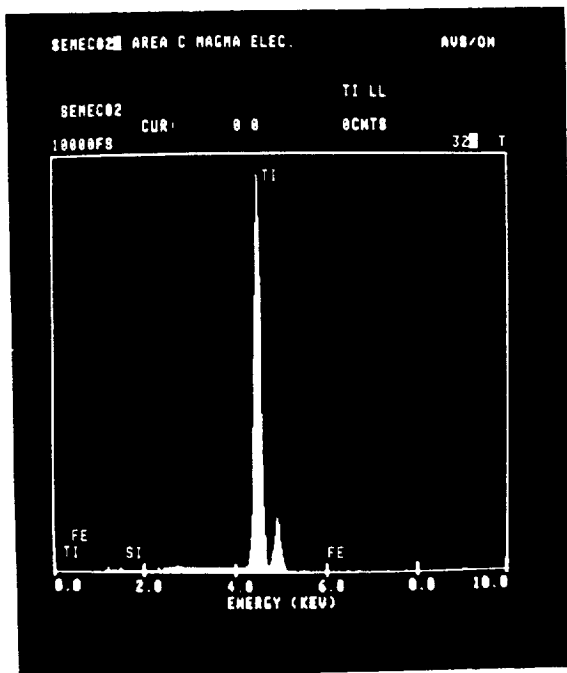
Figure 4: Scanning Electron Microscopic Image of Solidified Electrolyte After Electrolysis



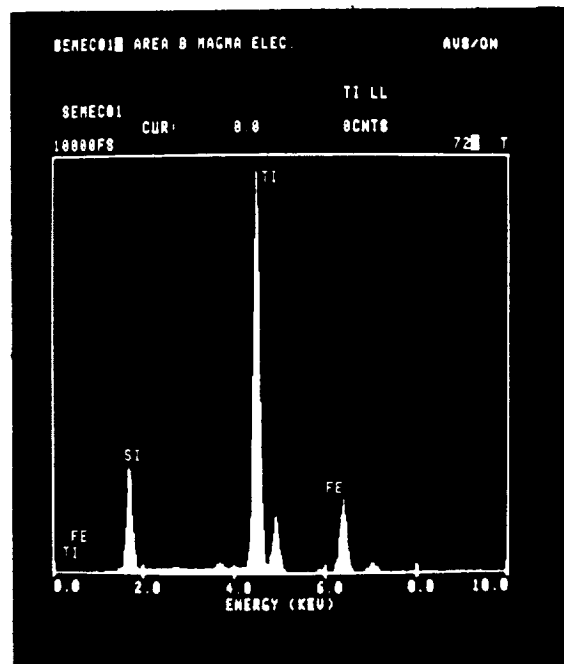
electrolyte, area D



particle, area A



particle, area C



particle, area B

ORIGINAL PAGE IS  
OF POOR QUALITY

Figure 5: EDX Spectra for Sample of Figure 4

### Summary of Observations and Conclusions

The electrolysis of molten silicates could be performed smoothly between platinum electrodes if the iron oxide content was relatively high. When silicon was reduced, substitution of a graphite cathode was necessary because the platinum cathode disintegrated.

No substantial conductivity increase in the initial phase of electrolysis was observed. The cell voltage, on the contrary, showed a tendency to decline with time, possibly due to the growth of reduced species from the cathode.

Rising of the electrolyte level, presumably due to hindered discharge of anodically formed gas bubbles from the melt, was observed in electrolytes with low iron oxide content. Trapped gas bubbles could be observed in the solidified electrolyte after conclusion of the experiment.

Products with high iron and titanium content were identified, although the analytical technique did not permit the distinction between the presence of metal or oxide. Not much silicon was found in apparent metallic particles; the reduction of titanium seems to occur preferentially. The reduction of iron, the oxidation of  $\text{Fe}^{II}$  at the anode and the reoxidation of reduced metals by anodic products require further investigations.

### References

- [1] L. A. Haskin, R. O. Colson, D. J. Lindstrom, R. H. Lewis, and K. W. Semkow .  
Electrolytic Smelting of Lunar Rock for Oxygen, Iron, and Silicon .  
*Revised Manuscript* , 1989 .
- [2] L. A. Haskin and R. O. Colson .  
Oxygen and Iron Production by Electrolytic Smelting of Lunar Soil .  
*Progress Report to University of Arizona NASA Space Engineering Research  
Center* September , 1990 .
- [3] P. W. Weiblen .  
Minnesota Lunar Simulant - 1 .  
*Pamphlet, Space Science Center, University of Minnesota, Minneapolis*  
1989 .
- [4] R. Keller .  
*Dry Extraction of Silicon and Aluminum from Lunar Ores* .  
Final Report Contract NAS 9-17811 , EMEC Consultants , 30 September 1989

N 9 1 - 2 4 3 7 3

An Investigation of the Thermal Shock Resistance of Lunar  
Regolith and the Recovery of Hydrogen From Lunar  
Soil Heated Using Microwave Radiation

T. T. Meek

Department of Materials Science and Engineering  
The University of Tennessee, Knoxville

14668

P. 10

TN 500003

Abstract

The objective of this project is to develop a better understanding of the thermal shock properties of lunar regolith sintered using 2.45 GHz electromagnetic radiation and to do a preliminary study into the recovery of bound hydrogen in lunar soil heated using 2.45 GHz radiation. During the first phase of this work lunar simulant material was used to test whether or not microhardness data could be used to infer thermal shock resistance and later actual lunar regolith was used. Results are included on the lunar regolith since this is of primary concern and not the simulant results. They were similar, however. The second phase of this work investigated the recovery of hydrogen from lunar regolith and results indicate that microwave heating of lunar regolith may be a good method for recovery of bound gases in the regolith.

Introduction

In the first phase of work, we wished to show that a simple hardness test could be used to describe the thermal shock properties of lunar regolith thus avoiding costly time consuming mechanical property measurements. First through it was necessary to validate the premise that material hardness is related to the fracture toughness of the material. Palmquist<sup>1</sup> originally put forth the idea that there is a relationship between the extent of cracking that emanates from a microhardness indentation in a brittle material and that materials fracture toughness. It is known that the fracture toughness of a brittle material will remain the same or slightly increase up to the thermal shock temperature and then abruptly fall off. Further work showed that material hardness is related to the fracture toughness of that material and the relationship is shown in Equation (1).

$$H = \frac{\beta^2 E P}{K_c^2 C_o^3} \quad (1)$$

where

- $\beta$  = a material independent constant for Vickers induced radial cracks
- $\beta$  =  $0.16 \pm .04$  for brittle materials
- E = Young's modulus
- H = material hardness

$P$  = indentation load

$C_0$  = radial crack length

From Eq. (1) it is expected that material hardness will increase or stay constant up to the thermal shock temperature at which time it will abruptly decrease due to the decrease in Young's modulus. As the number of microcracks increase  $E$  is expected to decrease thus causing a decrease in hardness. This approach has been used to examine the fracture toughness of SiC whisker reinforced  $Al_2O_3$  and we have used it to determine the thermal shock properties of Ytria-2 w% Zirconia composite material.

Microhardness data has been obtained on lunar regolith material which was first sintered at 2.45 GHz. Hardness measurements were performed using a LECO M-400 digital microhardness tester. Figures 1-3 show how material hardness behaved as a function of thermal shock temperature. Apollo 15 and 16 samples (which were crystalline) showed an increase in hardness up to the thermal shock temperature and then showed an abrupt fall off while the glassy Apollo 11 sample showed a steady decrease in hardness with increasing thermal shock temperature. Figure 4 shows typical microhardness indentations on an Apollo 15 sample. The curves of Figures 1-3 were obtained by averaging many data points for each thermal shock temperature.

More work needs to be done to relate observed thermal shock to the microwave sintered microstructure. There does appear to be an increase in thermal shock resistance due to the sintering in a 2.45 GHz electromagnetic field. At present individual grains of simulant Apollo 11 material are being examined using TEM to determine the structure of the grain surface. Initial results indicate that the outer 500 Å of a typical 1 micron size grain is amorphous while for the same material conventionally sintered the entire grain is crystalline. If this holds true for the surface of closed pores then the enhanced thermal shock resistance may be due to the hindrance of each pore to the formation of microcracks during the thermal shock test. Usually microcracks originate at pore surfaces during thermal shock. Also mechanical properties should be different if grain boundaries and a large region between grains are amorphous because viscous flow will dominate in the region between the grains while conventional brittle fracture mechanics will dominate within each crystalline grain.

One final topic should be addressed before proceeding on to a discussion of Task 2. This is a relative comparison of energy requirements to process lunar soil when it is heated using 2.45 GHz radiation versus conventional  $10^{13}$  Hz radiation (IR heating). An approximation of the energy density required to heat lunar soil may be made using data previously obtained.<sup>2</sup> An error in reference 2 is the ordinate of the power density curves should be cal/sec-cc not as shown cal/cc. Using the information in Figure 3 of reference 2 showing power density in a lunar soil for an electric field intensity of 300 V/cm in the soil one arrives at a power density of 400 cal/sec-cc to maintain a sample temperature of 1200°C. Heating the sample for thirty minutes (1800 seconds) to fully densify the lunar soil then requires (400 cal/sec-cc) (1800 sec) or  $7.2 \times 10^2$  k cal/cc. Converting this to kw hr we



obtain a value of 0.837 kw hr/cc of lunar soil. When compared to conventional heating significant energy savings will be achieved since heating rates of many thousands of degrees per hour can be achieved when microwave heating; however, depending on the thermal processing step conventional heating rates for oxide materials are limited to only 100-200°C/hr. Also microwave energy is deposited directly to the object being heating while in conventional heating, much of the energy is lost in heating the surrounding material. If we assume just the heating of lunar soil, then perhaps a solar furnace may be more efficient than microwave heating; however, the material will require a much longer time to achieve a uniform temperature throughout the material.

In Task 2 a preliminary investigation into the recovery of bound hydrogen in lunar regolith was carried out using 2.45 GHz radiation to heat the regolith. In this work a 1.5 gram sample of Apollo 15 and Apollo 16 regolith material was heated in an enclosed pyrex sample holder through which first a helium carrier gas was passed and later in the Apollo 16 work an Argon carrier gas was used. According to the work of Epstein and Taylor<sup>3</sup> hydrogen starts to be released from lunar regolith at around 500°C and continues until around 700°C. The amount of hydrogen released is of the order of 1 µg/gram of sample. In this work very sophisticated equipment is usually used such that extremely small quantities (of the order of 1 µg) of sample may be used. For our work the gas chromatograph used required a much larger sample (of the order of 1 gram or more). The model used in this work is a Varian Gas Chromatograph Model 90P-3 manufactured in 1966.

Since the lunar samples used for this work had been used for a prior experiment in which water and carbon material was used, each sample was analyzed at Los Alamos National Laboratory as to the amount of carbon present. Sample number 6999.75A (Apollo 16) had 6.8 ppm carbon; sample number 15999.126A (Apollo 15) had 69.5 ppm carbon; and sample number 10089.4A (Apollo 11) had 186.4 ppm carbon. For this work we used only a sample of Apollo 15 and one of Apollo 16 since they had much less carbon than did Apollo 11.

In gas chromatography a carrier gas is passed over one side of a wheatstone bridge while the carrier plus sample is passed over the other side of the bridge. Since the wheatstone bridge is heated to approximately 250°C any change in gas thermal conductivity will cause a change in bridge temperature. This change will be reflected in a change in electrical resistance. It is then possible to determine the amount and composition of an unknown gas in a sample by this technique. It was decided to first use as a carrier gas helium since the only known gas with a higher thermal conductivity is hydrogen. Everything else that might be released will then yield a positive peak while only hydrogen will yield a negative peak. This experiment was performed using a 1.5 gram sample of Apollo 15 material and the results are shown in Figure 5. Hydrogen release appears to occur at a lower temperature; however, in all probability the actual grain or intergranular temperature is much higher than the observed temperature. This is explained in a previous paper by Meek.<sup>4</sup>

In the next experiment Argon was used as a carrier gas. The resultant curve (Figure 6) yielded what appears to be a hydrogen peak in about the same temperature range as the previous experiment. Also as is shown in Table 1 only methane and ethane would show a negative peak and those peaks would be very small. The presence of water would not be detected using Argon while with He it would yield a positive peak. The other most likely gas to be released in these samples would be CO<sub>2</sub> and in Argon it again would be almost nondetectable. It thus appears that probably the strongly negative peaks observed in both of the experiments appear to be hydrogen. The Argon data were analyzed and indicate that much more hydrogen is released than was reported by other researchers, on the order of 70 µg of hydrogen per gram of Apollo 16 regolith. This may be due to the manner in which the 2.45 GHz radiation couples to the regolith or it may be due to error in our interpretation of the data. Clearly more work needs to be done to substantiate the preliminary data obtained above. If further work in this area is done, it may be worth while using a different carrier gas namely neon. The cost of neon may be prohibitive; however, as seen in Table 1 it is intermediate between He which gives a small hydrogen peak and Argon which yield a very large negative peak.

Table 1. Response Factor for Some Carrier Gases and Some Sample Gases.

Gas	Thermal Conductivity (Cal/sec cm <sup>2</sup> °C/cm) x 10 <sup>-6</sup>	Response Factor $1 - \frac{\lambda_s}{\lambda_c}$		
		He	Ar	Ne
He	360.36			
Ar	42.6			
Ne	115.71			
H <sub>2</sub>	446.32	-0.24	-9.5	-2.85
CO <sub>2</sub>	39.67	+0.89	+0.07	+0.66
H <sub>2</sub> O	42.57	+0.88	~0.0	+0.62
CH <sub>4</sub>	81.83	+0.77	-00.91	+0.30
C <sub>2</sub> H <sub>6</sub>	51	+0.84	-0.19	+0.56

References

1. S. Palmquist, in Arch. Eisenhüttenwes. 33, 1962, 629.
2. T. T. Meek, D. T. Vaniman, R. D. Blake, and F. H. Cocks, "Electromagnetic Energy Applied to and Gained From Lunar Materials," Proceedings of Symposium 86, The First Lunar Development Symposium, 1986, 40a.
3. S. Epstein and H. P. Taylor, Proceedings of Apollo 11 Lunar Science Conference, 1970, 1085.
4. T. T. Meek, "Proposed Model for the Sintering of a Dielectric in a Microwave Field," Journal of Materials Science Letters, 6, 1987, 638.

Apollo-16 Thermal Shock Test  
(Loading: 300/15sec.)

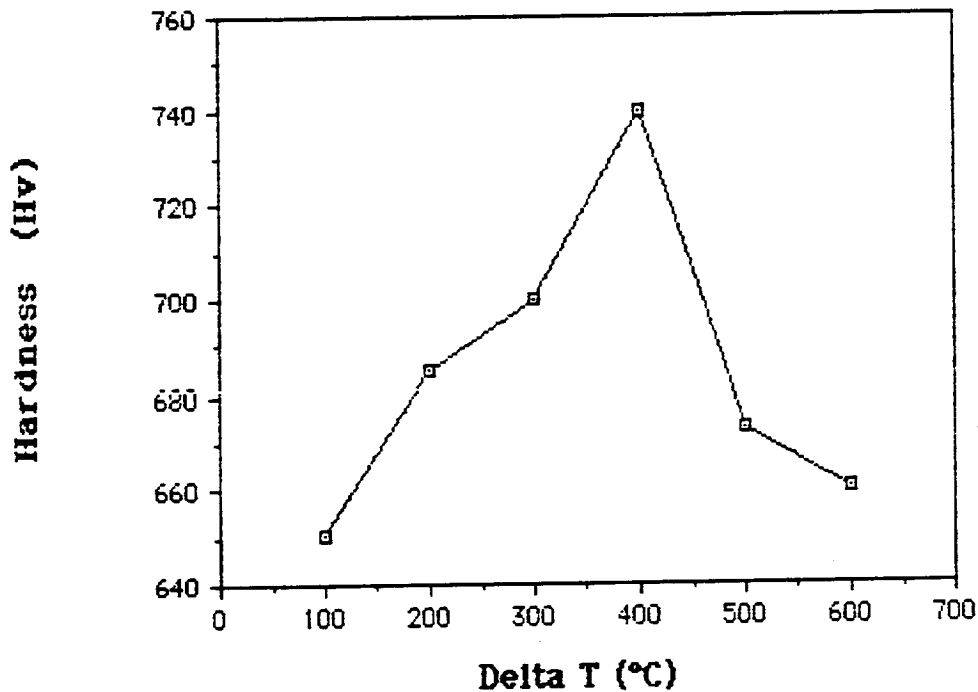


Figure 1. Microhardness vs. Delta T (°C) data for Apollo 16 soil.  
 $\Delta T_C = 400^\circ$ . Hardness is in  $\text{kg}/\text{nm}^2$ .

Apollo-15 Thermal Shock Test  
(Loading: 100g/15sec.)

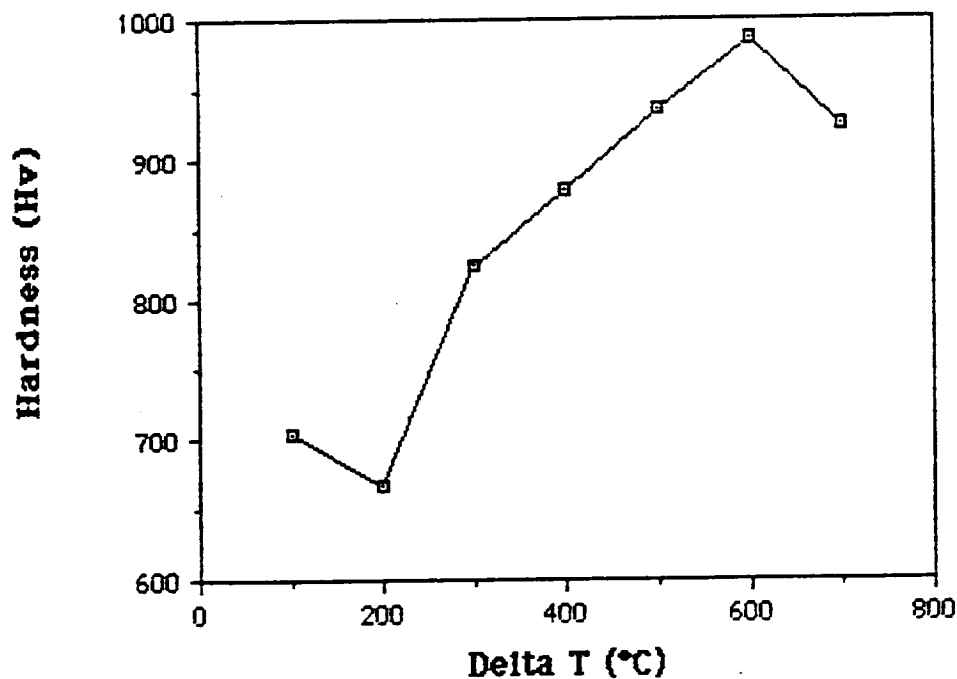


Figure 2. Microhardness vs. Delta T (°C) data for Apollo 15 soil.  
 $\Delta T_C = 600^\circ\text{C}$ . Hardness is in  $\text{kg}/\text{nm}^2$ .

Apollo-11 Thermal Shock Test  
(Loading: 200g/15sec.)

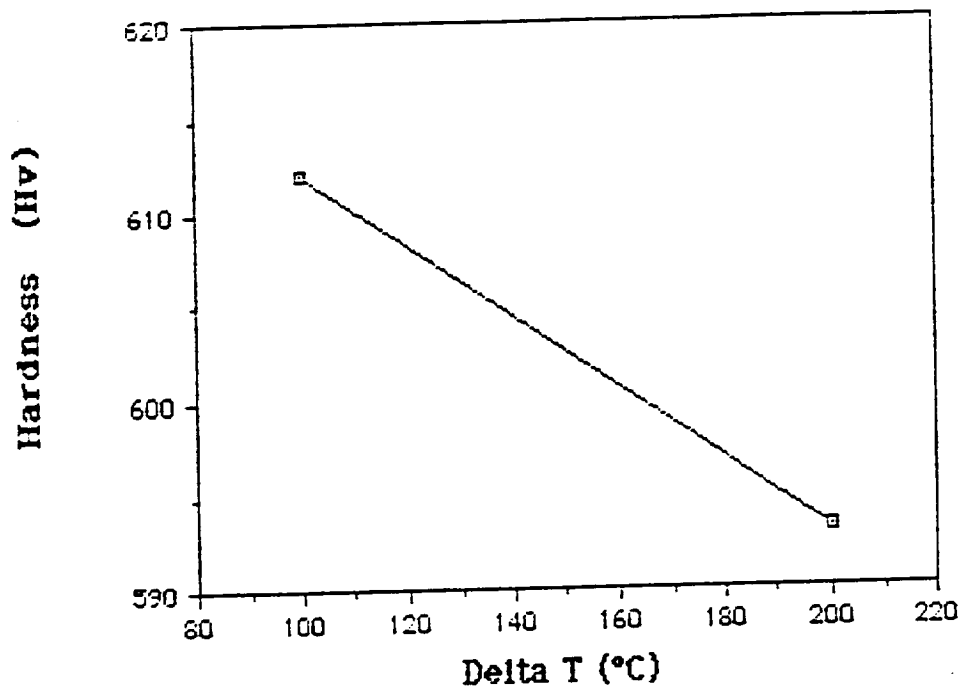
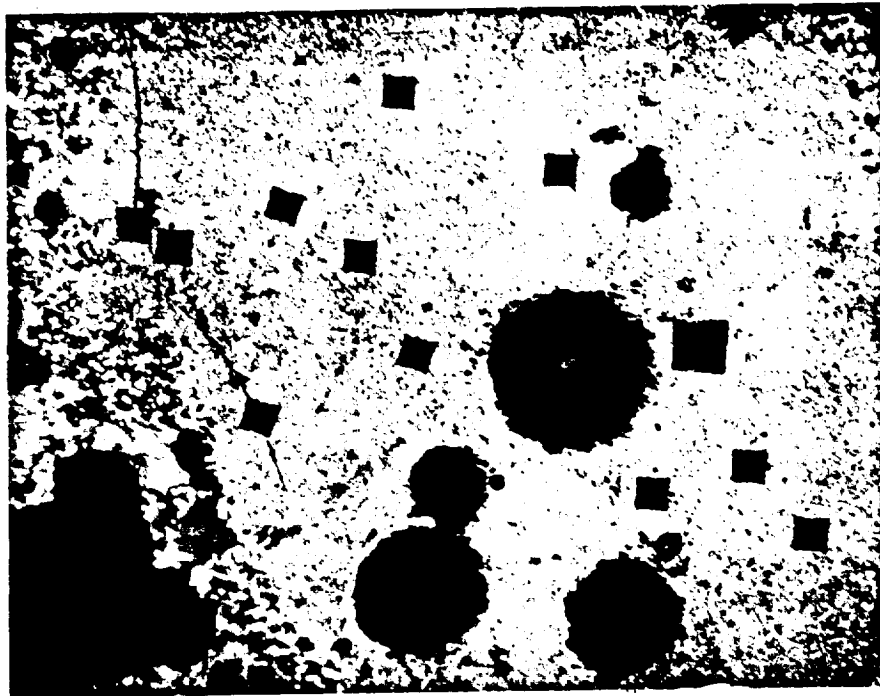


Figure 3. Microhardness vs. Delta T (°C) data for Apollo 11 soil.  
 $\Delta T_c = 100^\circ$ . Hardness is in  $\text{kg}/\text{nm}^2$ .



ORIGINAL PAGE IS  
OF POOR QUALITY

Figure 4. Typical microhardness indentations on an Apollo 15 sample sintered using 2.45 GHz radiation..

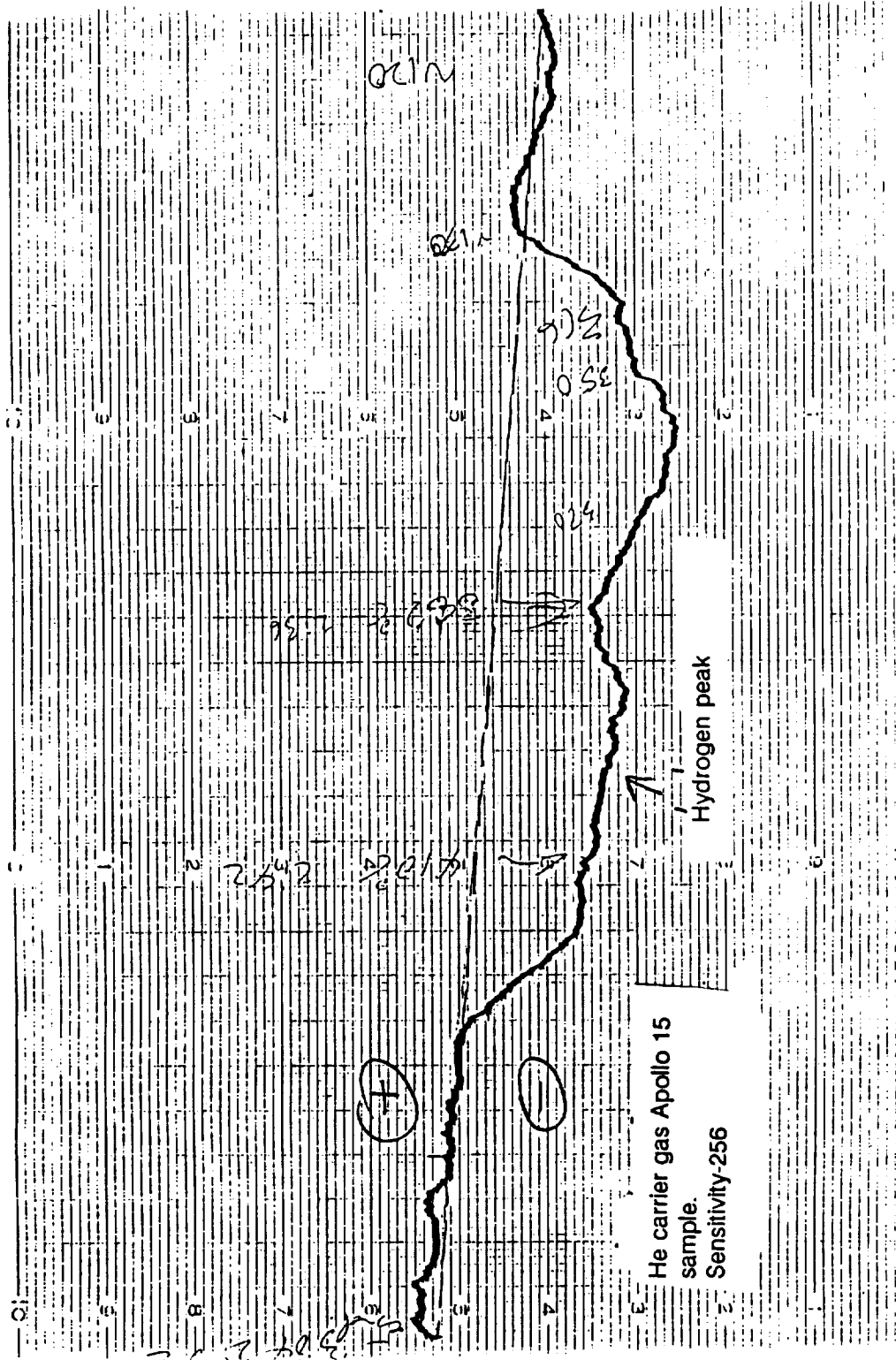


Figure 5. Gas chromatograph of hydrogen release in Apollo 15 soil heated using 2.45 GHz radiation. Carrier gas is He.

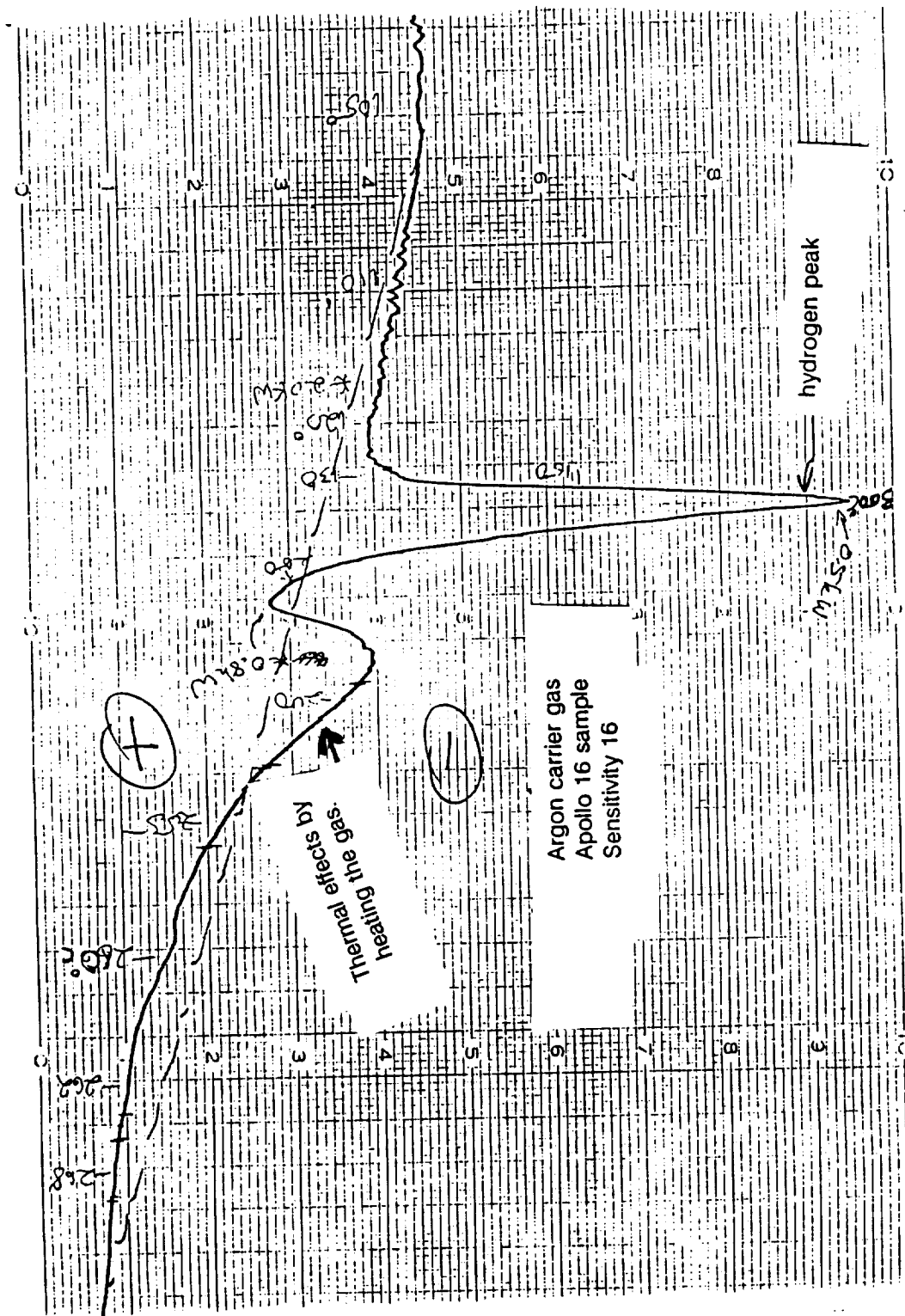


Figure 6. Gas chromatograph of hydrogen release in Apollo 16 soil heated using 2.45 GHz radiation. Carrier gas is Argon.

ORIGINAL PAGE IS  
OF POOR QUALITY

## **B. REDUCTION OF CARBON DIOXIDE**



N 9 1 - 243-24

Oxygen Plant Breadboard Design, and  
Techniques For Improving Mission Figure-of-Merit

14669

P.8

Kumar Ramohalli  
UA NASA SERC and Aerospace and Mechanical Engineering  
University of Arizona

**ORIGINAL CONTAINS  
COLOR ILLUSTRATIONS**

**Abstract**

A breadboard oxygen plant to process anaerobic carbon dioxide is designed and constructed; the objective is not only to produce a key propellant component extraterrestrially, but also to develop the important technologies that are necessary for a successful operation of In-Situ Materials Utilization hardware. The solid electrolytic cells are supplied to our specifications by an established vendor. The cell thermal control, electrical control and flow control are installed after detailed designs. Extensive data are obtained that characterize the operation of the plant as the input parameters are varied. The initial mass, energy and volume needs provide the input to a figure-of-merit software program to calculate the impact of various candidate technologies upon the overall mission. The desirability of studies on storage and high-density propellants is brought out. This task dovetails into other tasks that are evaluating alternative cell materials, catalysis for compactness, and smart sensors for effective control. The breadboard design and operation of the complete system are believed to represent engineering "firsts".

**Introduction**

Various studies have indicated the desirability of in-situ resource utilization, or in-space materials utilization (ISRU/ISMU) for significantly reducing the costs of space missions. Since a large fraction of any mission cost is associated with space transportation (access to space), it has been recognized that reducing our dependence upon earth-transported propellants would be a valuable first step. Since a large fraction of the chemical propellants consists of oxidizers, oxidizer production at extraterrestrial sites should receive primary attention. The actual plant design and testing will depend upon various factors such as consistency with our Center mission, available resources, synergism with current tasks, scientific merit and appropriateness for university research; another important factor is the likelihood of impact and transferability of results to industry.

After a very careful consideration of all of these factors, it was the unanimous decision of the center Advisory Committee that a plant designed to extract oxygen from gaseous carbon dioxide meets most, if not all, of the above criteria. Aside from its obvious application to Mars missions (MSR, MO, MR and MMM), the plant can also be used in lunar missions that utilize the popular carbothermal reduction of lunar materials (ilmnite), where carbon dioxide is one of the

byproducts. More important is the opportunity that such a plant provides to study and execute innovative designs in electrochemistry, thermal controls, flow controls, autonomous operations, packaging and a test-bed for obtaining long-term engineering data. Simplicity and the absence of major unknowns were also factors.

The next section describes the basic oxygen plant, the components and the overall design. The operation and preliminary results follow. The summary section outlines the future work on the plant. At the time of this reporting, the plant has been successfully designed and operated. The oxygen production rate has been shown to be consistent with electrochemical considerations. The cell thermal control has been proven through modern IR diagnostics. The product gases have been unambiguously identified through gas chromatography on site (and mass spectroscopy at a local laboratory). The important plant characteristics of long-term operation, possible cell contamination, scaleability and a host of related issues, including exhaust products utilization, will be the subject of future research.

### The Plant Design

The heart of the plant consists of a solid electrolytic cell maintained at a temperature sufficient to dissociate the incoming carbon dioxide, while the potential difference across the cell separates the oxygen from the other gases. The cell geometry was chosen to be cylindrical, 14" long and approximately 1" O.D. The cell wall is coated with platinum for conductivity. The cell is wrapped by resistance heater coils of nichrome. The entire assembly is contained inside a stainless steel tube. The tube is then packaged into a thermal box that is insulated with a non-asbestos type fiber cloth.

The flow into the cell is from a specially ordered anaerobic carbon dioxide bottle, regulated down to one bar pressure. The question of the optimum operating pressure is being studied at the present time; factors include the plant mass, terrestrial testing operations, plant volume and the ease of compressing the extraterrestrial gases (Martian carbon dioxide is at 6-8 mbar) to the operating design pressure. The output flow from the oxygen side is led into a collection jar, which is through the downward displacement of water, at the present time for clear visual demonstration of gas evolution. The exhaust gases (carbon dioxide and carbon monoxide) are carefully vented out, although plans are underway for using this stream both thermally and chemically. The electric potential is maintained across the cell through a simple power supply unit. The overall plant is schematically shown in figure 1 and an external view of the assembled hardware is shown in figure 2.

## Plant Operation and Preliminary Results

The plant has been operated at different cell temperatures, different flow rates and different voltages. The principal results are shown in figures 3 and 4. Figure 3 shows that the oxygen production rate varies nearly linearly with the applied cell voltage. The manufacturer suggested a production rate of 4 ml per minute at 2 volts, whereas we have consistently obtained 5-6 ml per minute at this voltage. The basic Nerst potential equation suggests production rates closer to values reported here. The flow rate of the carbon dioxide is a parameter, but not a strong one, suggesting electrochemical control of production rather than fluid dynamic control. However, there is a flow rate at which fluid dynamic control does become perceptible, as seen in figure 4. Beyond a flow rate of 300 ml per minute of carbon dioxide, the oxygen production rate reaches "saturation" at 5.6 ml per minute. Beyond 700 ml per minute of carbon dioxide flow rate, the oxygen production rate actually decreases, suggesting that the residence time is not sufficient for the production/separation of oxygen. The cell voltage and temperature were held constant during these tests.

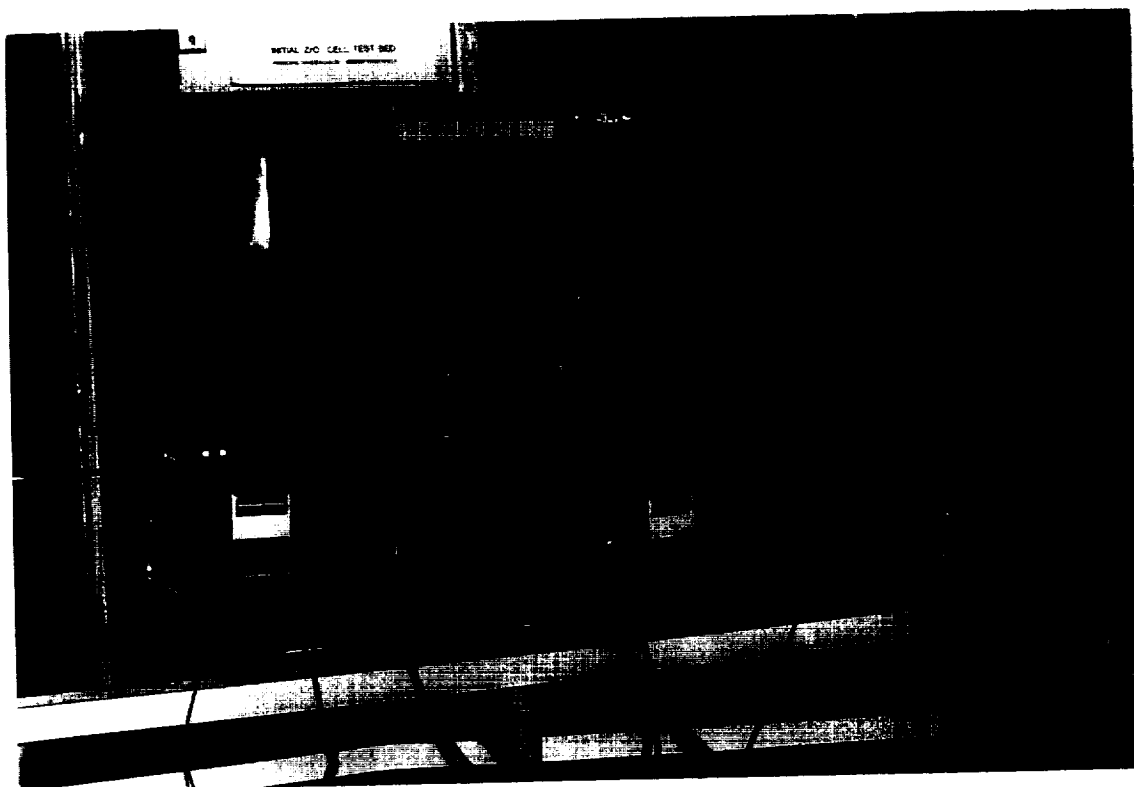
Detailed theoretical (equilibrium) calculations were made to determine the minimum operating temperature both from the point of view of production rates and from the point of view of minimizing solid carbon formation on the cell walls and within the cell. These calculations were performed using the NASA CET86 program, and are reported elsewhere in this report. It was shown that at temperatures above 650 C, the carbon formation was minimal. This brings us to the important aspect of the cell thermal environment. The mean cell temperature is hardly as important as the local cold/hot spots that can promote carbon depositions, or, destroy the cell. Hence, a good overall thermal scanner was needed. This is provided through a color coded infrared video monitor. Preliminary results are shown in figure 5, that shows that the temperature of the cell is maintained reasonably uniform in the present design. More work is underway.

## Summary

The oxygen plant design has been completed with a single cell. The eventual design calls for a bank of 175 cells in order to produce 2 kg of oxygen per (24 hr) day; this assumes cell operation slightly below the full capacity of 6 ml/min. The overall geometry of the cell banks may have to be considerably different from the simple cylindrical geometry used here. Alternative disk geometries and alternative materials (other than Zirconia), and catalysis for compactness are all being studied. The thermal control, the electrical control and the eventual automation all need more study. The high-temperature seals at the ends are particularly vulnerable to attack by oxygen,

and are being separately studied.

This project is providing input to various other tasks and is receiving inputs from several other tasks, indicating a true engineering design principle in action. The eventual breadboard is expected to consist of the compact packaging of components shown in several figures in the report by professor Nikraves (elsewhere in this report).



# O<sub>2</sub> PRODUCTION VS CELL VOLTAGE

TEMPERATURE = 1000 C  
12/21/90

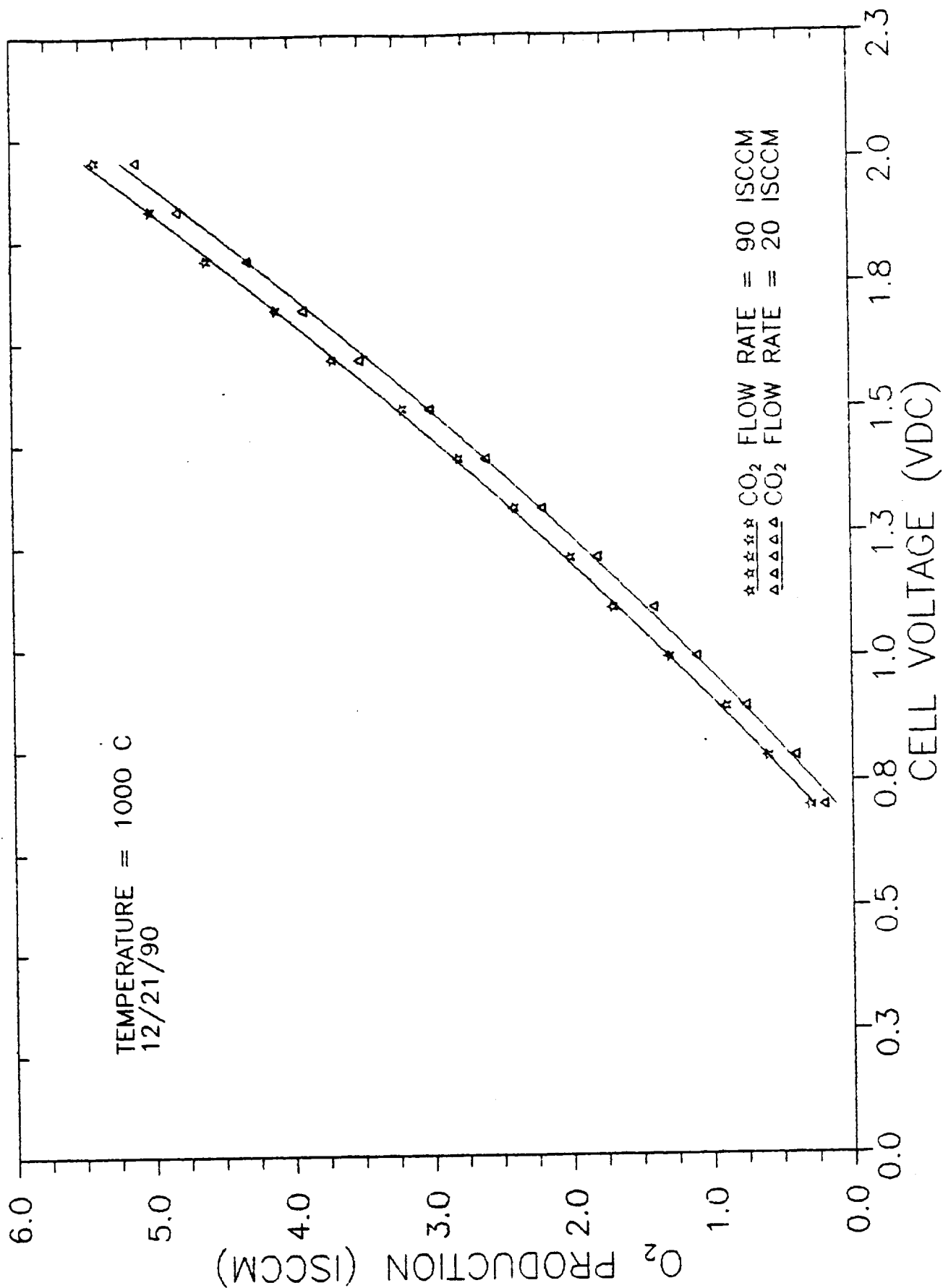


Figure 3

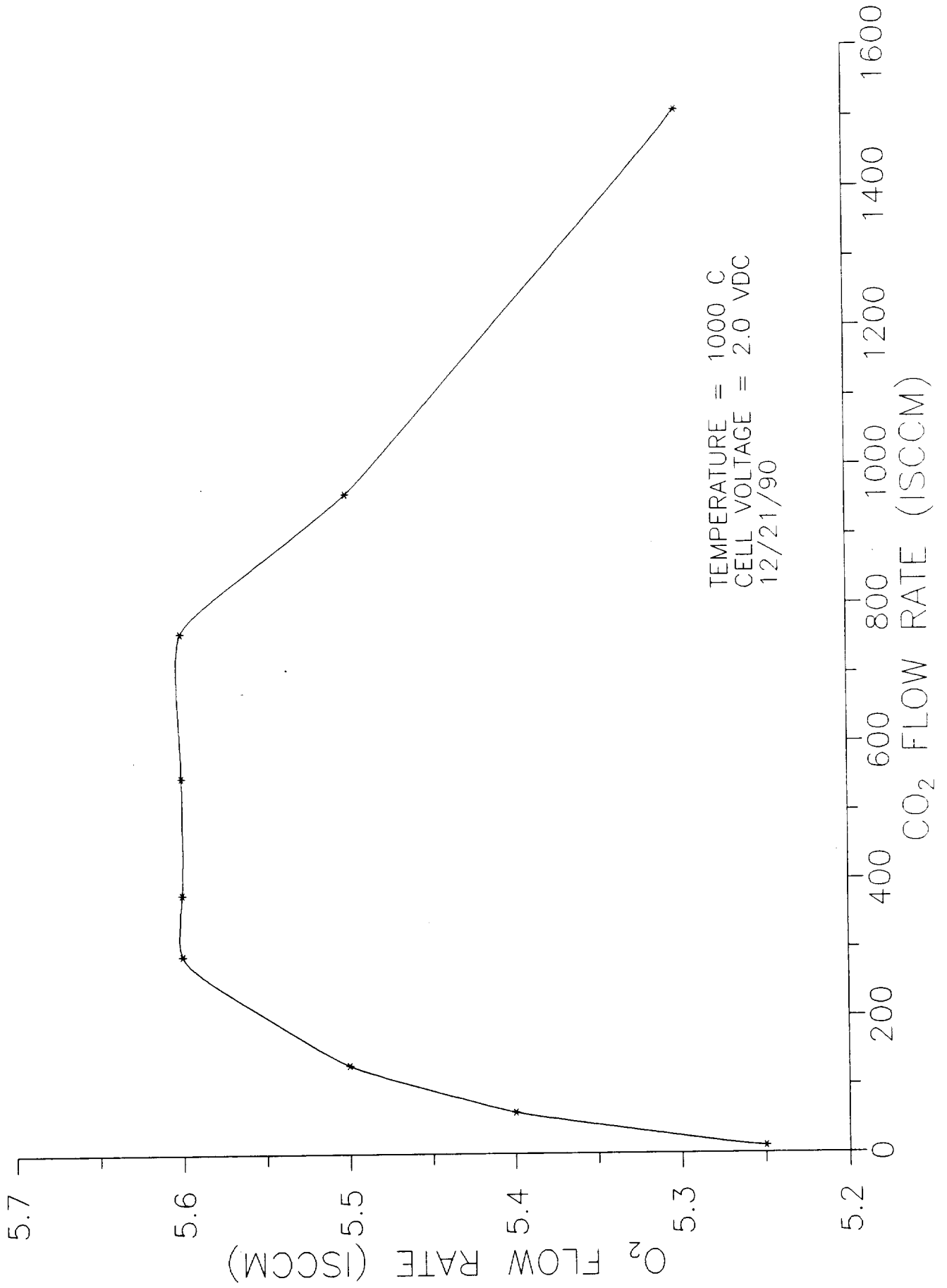
O<sub>2</sub> PRODUCTION vs CO<sub>2</sub> FLOW RATE

FIGURE 4

ORIGINAL PAGE  
COLOR PHOTOGRAPH

ORIGINAL PAGE IS  
OF POOR QUALITY

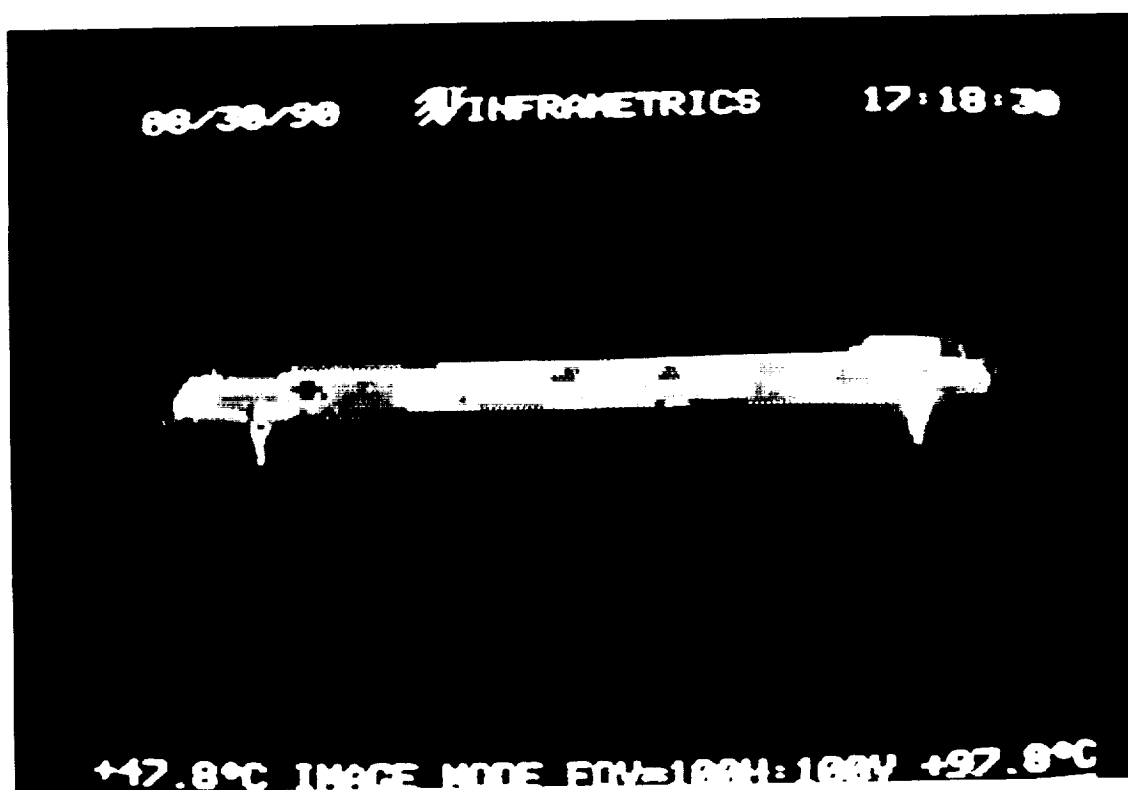


FIGURE 5. INFRARED IMAGE OF THE OXYGEN CELL



N 9 1 - 2 4 3 7 5

Thermal Analysis, Optimisation and Design of a Martian  
Oxygen Production Plant

Venkatesh A. Iyer and K.R. Sridhar  
Department of Aerospace and Mechanical Engineering  
The University of Arizona

14670

1.12

AX 8529

Abstract

The objective of this work is to optimally design the thermal components of a system that uses carbon dioxide ( $\text{CO}_2$ ) from the Martian atmosphere to produce oxygen ( $\text{O}_2$ ) for spacecraft propulsion and/or life-support.  $\text{CO}_2$  is thermally decomposed into carbon monoxide ( $\text{CO}$ ) and  $\text{O}_2$  followed by the electrochemical separation of  $\text{O}_2$ . The design of the overall system and its various individual components depends on, among other things, the fraction of the stoichiometric yield of  $\text{O}_2$  that can be realised in the system and the temperature of operation of the electrochemical separation membrane. The analysis performed indicates that a substantial reduction could be obtained in the mass and power requirements of the system if the unreacted  $\text{CO}_2$  were to be recycled. The report also discusses the concepts of an optimum temperature of the Zirconia cell and impracticality of plant operation at low cell efficiencies. The design of the thermal equipment would be such that the mass and power requirements of the individual components and of the overall system would be optimised.

Introduction

There has been tremendous interest in recent years on the need for in-situ-propellant-processing (ISPP) [1,2]. More than 80% of a spacecraft's mass is due to the propellant. Hence production of propellants at locations remote from the Earth is essential for frequent and extended space explorations. Here, the production of Oxygen from the predominantly  $\text{CO}_2$  atmosphere of Mars is explored. The system that would be used on Mars would have a filter at the  $\text{CO}_2$  intake end to remove the dust and particulates from the supply gas. It would also have a liquefaction and storage unit at the  $\text{O}_2$  production end. These components are not being designed by UA/NASA

SERC presently. However, they will be part of our future investigations. The system currently being designed incorporates the sub-systems necessary for supplying the  $\text{CO}_2$  at Martian pressures and temperatures. This system will be designed, fabricated and tested extensively on our ground-based facilities. To distinguish it from the future flight-tested system for Mars, the ground-based testing system will be referred to as the "Test Bed".

#### Description of the Test Bed

The Test Bed, shown in figure 1, can roughly be divided into 4 sub-systems:

1. The simulation sub-system consists of  $\text{CO}_2$  supply and a Cryo-Vacuum Chamber cooled by a Cryo-cooler. This simulates the Martian ambient conditions of 6.4mbar pressure and a temperature of 200K. Though the Martian atmosphere contains only 95.3%  $\text{CO}_2$ , presently the supply gas is composed entirely of  $\text{CO}_2$ .
2. The compressor, heat exchanger and heater form the  $\text{CO}_2$  preparatory sub-system. In order to avoid a very bulky system at high  $\text{CO}_2$  mass flow rates, the supply gas is pressurized from 6.4 mbar to higher pressures. At the present time  $\text{CO}_2$  is assumed to be pressurized to 1bar. The reasons for this are two-fold. The Test Bed is operated on the Earth and operating the system at 1 bar minimises the probability of gas leaks. Secondly, electrochemical separation membranes have been tested extensively with other gases at 1 bar and higher pressures and its performance at lower pressures is not known currently. The effect of lower pressures on the electrochemical separation is the subject of a related investigation at UA/NASA SERC. After the compressor, the pressurized  $\text{CO}_2$  enters a waste heat recovery heat exchanger to gain energy from the gases exhausting from a Zirconia ( $\text{ZrO}_2$ ) Cell, which will be discussed later. The  $\text{CO}_2$  supply gas then enters a heater where it reaches the same temperature as the  $\text{ZrO}_2$  electrochemical separation membrane unit. Thermal decomposition of  $\text{CO}_2$  occurs in the heater. Since the temperature of the gases entering the separation unit is the same as that of the unit itself, the separation unit is not subjected to any thermal shocks.
3. The mixture of  $\text{CO}$ ,  $\text{O}_2$  and  $\text{CO}_2$  passes through the  $\text{ZrO}_2$  cell, which electrochemically

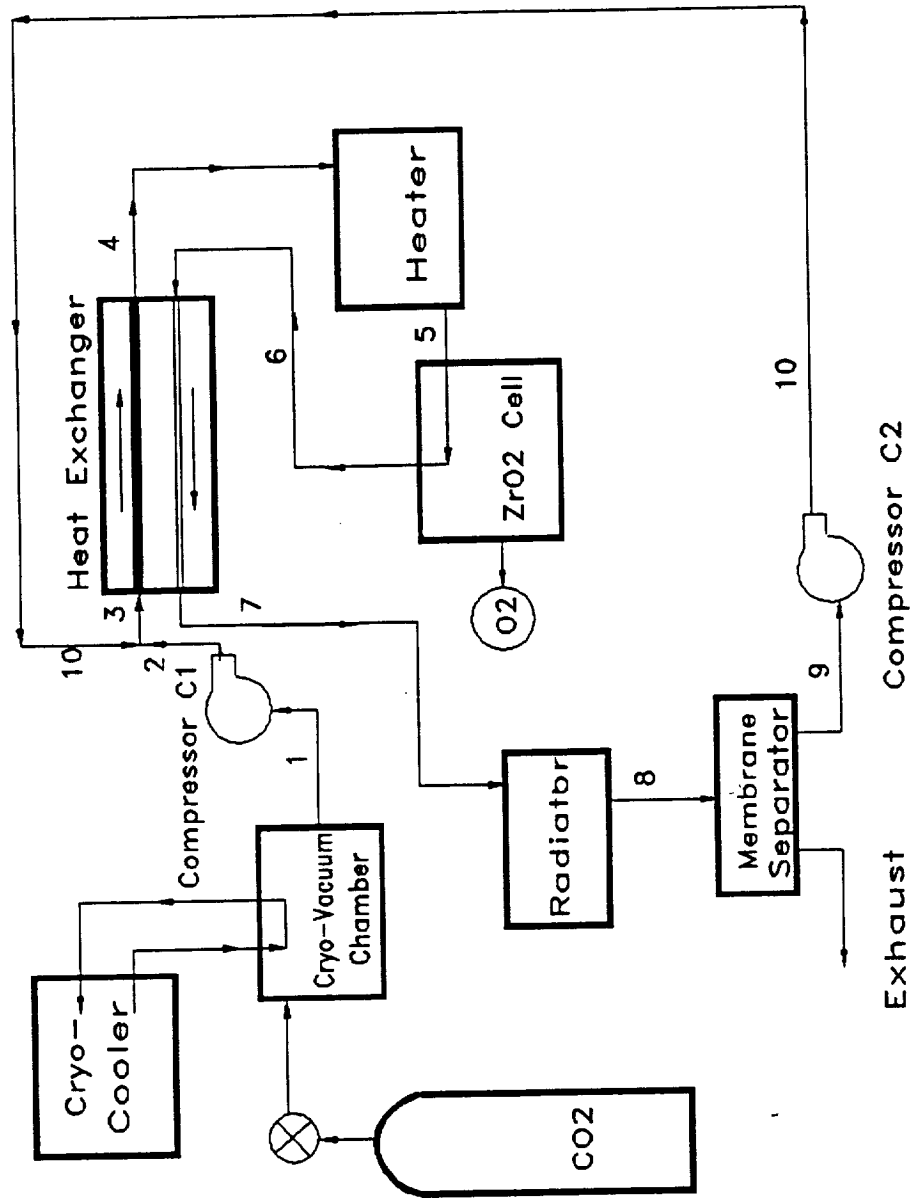


Fig 1: Test Bed With Recycling of Carbon Dioxide

separates the  $O_2$  from the mixture. This  $O_2$  is then fed to a storage device for later use. The cell forms the oxygen separation sub-system.

4. The exhaust from the Cell, after passing through the heat exchanger, loses energy in a radiator before passing through a polymeric membrane separator which separates the unreacted  $CO_2$ . The radiator is essential because polymeric membrane separators cannot withstand the high exhaust temperatures. There is a substantial pressure drop across the membrane separator, which requires a second compressor to re-pressurize the  $CO_2$  to 1 bar. The  $CO_2$  then re-enters the loop just before the heat exchanger. The system is depicted in figure 1.

Figure 2 illustrates the system without recirculation. The exhaust gas, after passing through the heat exchanger, is expelled from the system. Henceforth, the system with recycling is referred to as case 1, and the one without, as case 2. The number of moles of CO,  $CO_2$  and  $O_2$  flowing at various points in the system for both cases 1 and 2 is shown in table 1.

### Nomenclature

$\epsilon$  = Fraction of  $O_2$  produced that is electrochemically separated by the cell.

$\mu_{sep}$  = Membrane Separation Factor =  $\frac{\text{Amount of } CO_2 \text{ at Point 9}}{\text{Amount of } CO_2 \text{ at Point 8}}$

This is only for case 1.

$\alpha$  = Cell Factor = moles of unreacted  $CO_2$  for each mole of  $O_2$  produced

This determines the cell efficiency  $\tau_{cell}$  as:

$$\tau_{cell} = \frac{\text{moles of } O_2 \text{ actually produced}}{\text{theoretical max. no. of moles of } O_2 \text{ possible}} = \frac{2}{2+\alpha}$$

The Cell reaction is:



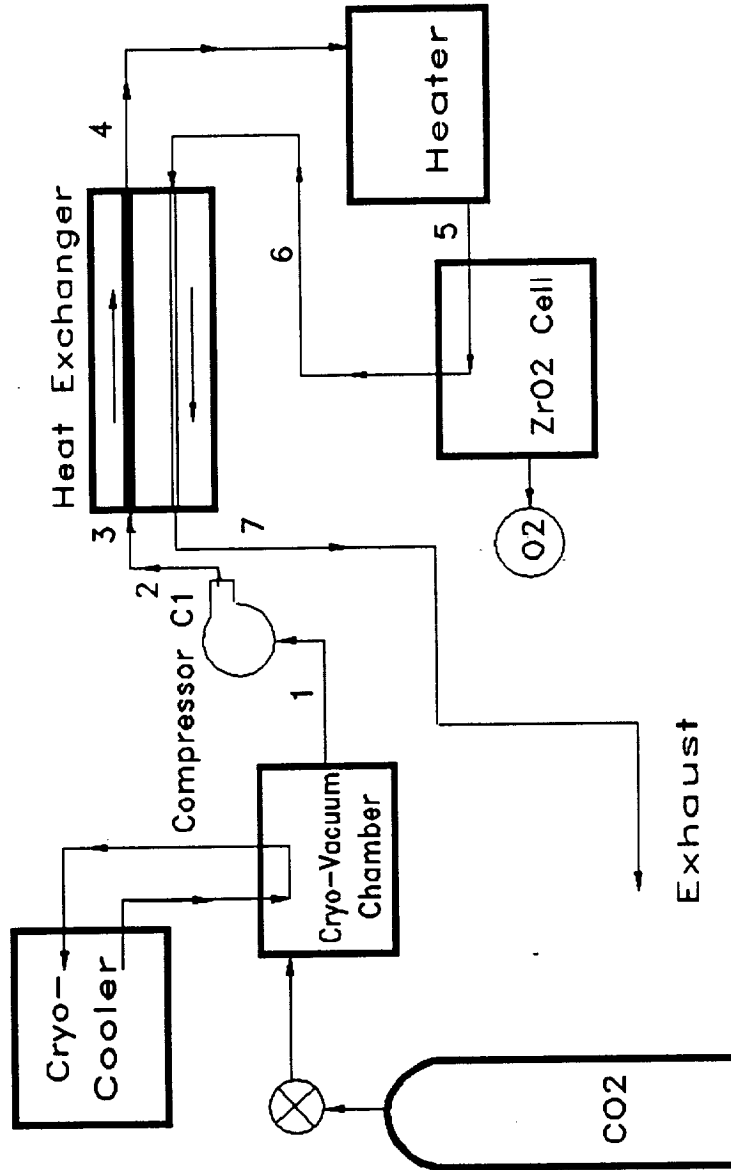


Fig 2: Test Bed Without Recycling of Carbon Dioxide

Table 1: For Oxygen Production of 1 mole

Point	Case 1	Case 2
1	$\frac{(2+\alpha-\mu_{sep}\alpha)}{e}CO_2$	$\frac{(2+\alpha)}{e}CO_2$
2	$\frac{(2+\alpha)}{e}CO_2$	$\frac{(2+\alpha)}{e}CO_2$
3	$\frac{(2+\alpha)}{e}CO_2$	$\frac{(2+\alpha)}{e}CO_2$
4	$\frac{(2+\alpha)}{e}CO_2$	$\frac{(2+\alpha)}{e}CO_2$
5	$\frac{(2+\alpha)}{e}CO_2$	$\frac{(2+\alpha)}{e}CO_2$
6	$[2/e]CO + [(1-e)/e]O_2 + [\alpha/e]CO_2$	$[2/e]CO + [(1-e)/e]O_2 + [\alpha/e]CO_2$
7	$[2/e]CO + [(1-e)/e]O_2 + [\alpha/e]CO_2$	$[2/e]CO + [(1-e)/e]O_2 + [\alpha/e]CO_2$
8	$[2/e]CO + [(1-e)/e]O_2 + [\alpha/e]CO_2$	
9	$[\mu_{sep}\alpha/e]CO_2$	
10	$[\mu_{sep}\alpha/e]CO_2$	

Assumptions

The thermodynamic analysis has been performed based on the following assumptions:

1. The Membrane Separator filters out all the CO and O<sub>2</sub> from the exhaust gases. It is known that the purity of the separated gases is very high. Hence this is a valid first-order approximation.
2. Only a steady state analysis has been performed.
3. Pressure drop and heat losses in the pipes, valves and bends are negligible.
4. The Compressors have been assumed to be isentropic, with specified mechanical and isentropic efficiencies. Radiation losses from their surfaces have been neglected since they are small in comparison.

The analysis gives the total heat transferred from the exhaust to the fresh CO<sub>2</sub>. Using an iterative procedure, the cold side outlet temperature and the Logarithmic Mean Temperature Difference (LMTD) are determined. Knowing the mass flow rates, the heat exchanger can be designed. The power requirement of the ZrO<sub>2</sub> cell - the Nernst potential and the ionic component of the current

corresponding to the oxygen ion flow can be calculated precisely. For a fixed  $O_2$  production rate, it is a constant.

### Discussion of Results

The analysis was performed with the help of an interactive program written in Pascal. The program has pull-down menus using which the user can change any of the input variables. This was necessary because the optimal cell temperature, cell efficiency and membrane separation factor is presently not known. Concurrent research is being done at UA/NASA SERC to investigate the optimum system performance conditions. Some graphs have been obtained from the data generated by using the program for an oxygen production rate of 10 kg/day, which corresponds to the production rate needed for an unmanned sample return mission [2]. Figure 3 shows the variation of the specific heats of  $CO_2$ ,  $CO$  and  $O_2$  with temperature. Empirical relationships [3] have been used to determine these curves.

This variation in the specific heat ( $C_p$ ) precludes treating  $C_p$  as a constant, say, across the heat exchanger. Over the entire range of temperatures considered, it is seen that  $C_p$  increases with temperature for all three gases, with the curve for  $CO_2$  increasing most sharply. Figure 4 shows the graph of heater power with cell temperature ( $T_5$ ). The power consumed by the heater increases with  $T_5$  as expected, for

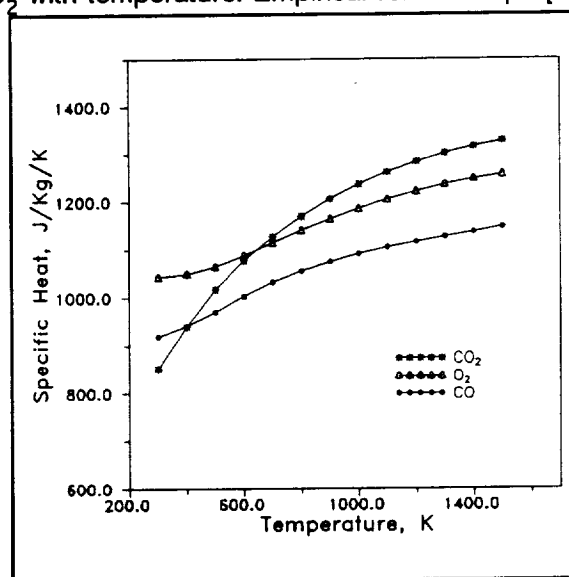


Fig 3: Variation in  $C_p$

low values of  $T_5$ . It reaches a maximum, and then, contrary to expectations, starts dropping. Figures 6 and 7 show plots of temperature of the cell ( $T_5$ ) with the outlet temperature  $T_4$  of the cold  $CO_2$  from the heat exchanger. Though not apparent from the figures,  $(T_5 - T_4)$  actually increases with  $T_5$ . The anomalous behaviour of figure 4 can be explained by the fact that though  $C_p$  itself increases, and  $(T_5 - T_4)$  also increases, the integral of  $C_p dT$  over the temperature range

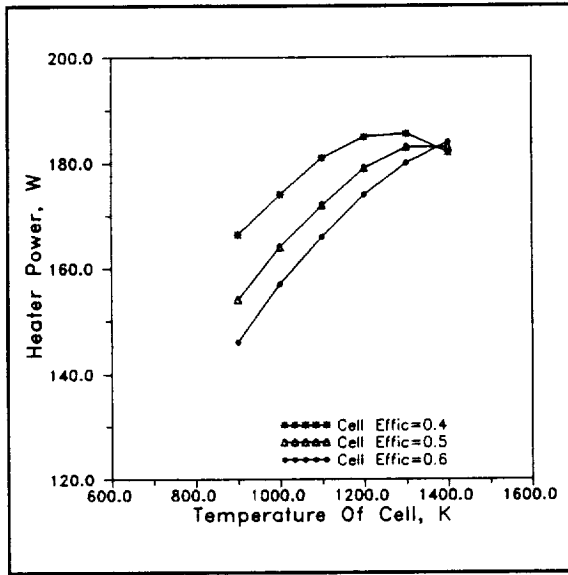


Fig 4: Heater Power - Case 1

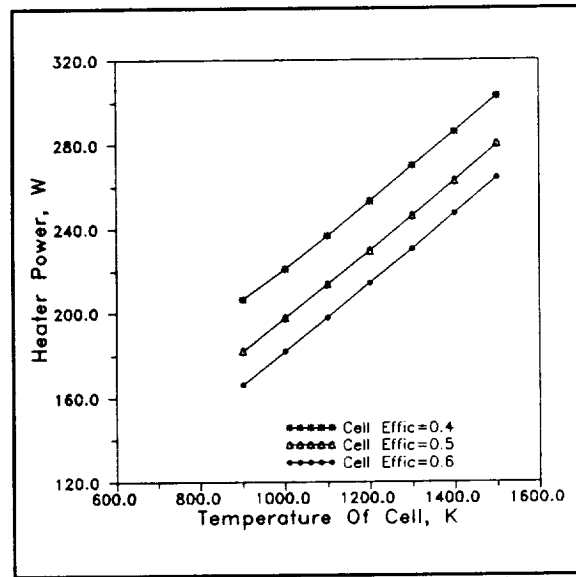
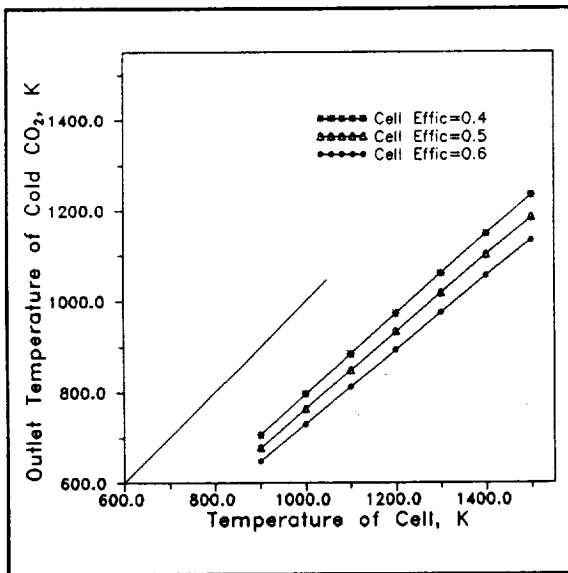
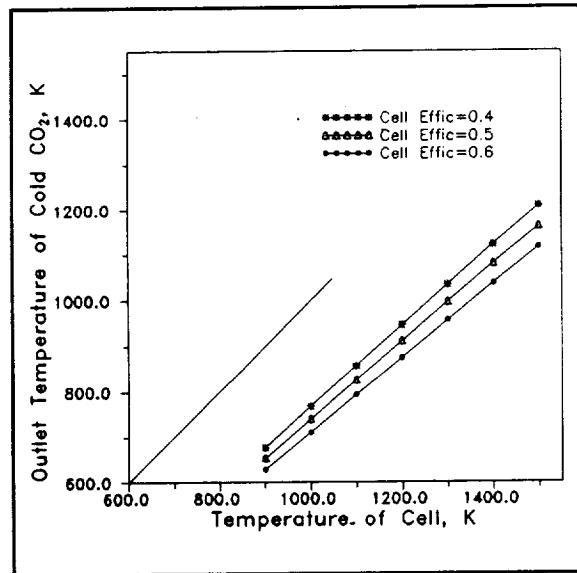


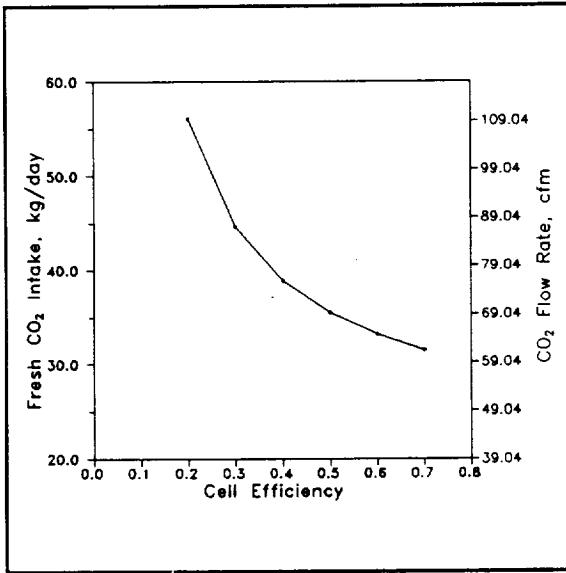
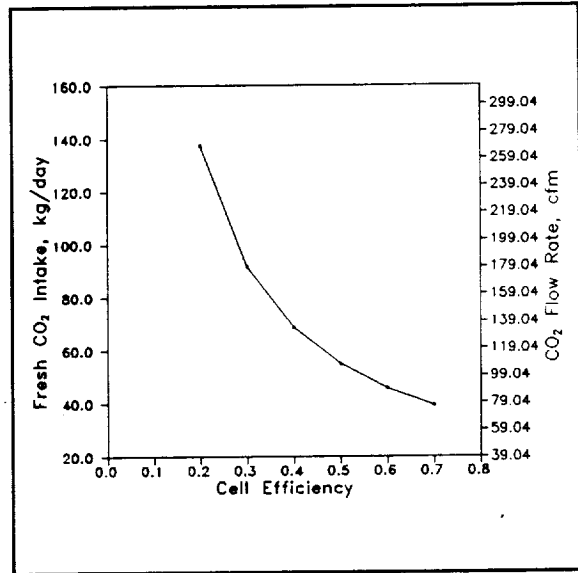
Fig 5: Heater Power - Case 2

Fig 6:  $T_4$  v/s  $T_5$  - Case 1Fig 7:  $T_4$  v/s  $T_5$  - Case 2

$T_4$  to  $T_5$  actually decreases after a point. This is opposed to the almost linear increase of heater power with temperature in case 2 as shown in figure 5. In this case, though the mass flow rates of  $\text{CO}_2$  at points 4 and 5 are the same as in case 1,  $T_3$ , and hence  $T_4$ , are lower for the same value of  $T_5$ . This is because the recirculating  $\text{CO}_2$  is at a higher temperature than that of the  $\text{CO}_2$  at point 2. Hence, the increased  $(T_5 - T_4)$  term counters the decrease in the slope of the  $C_p$  curve

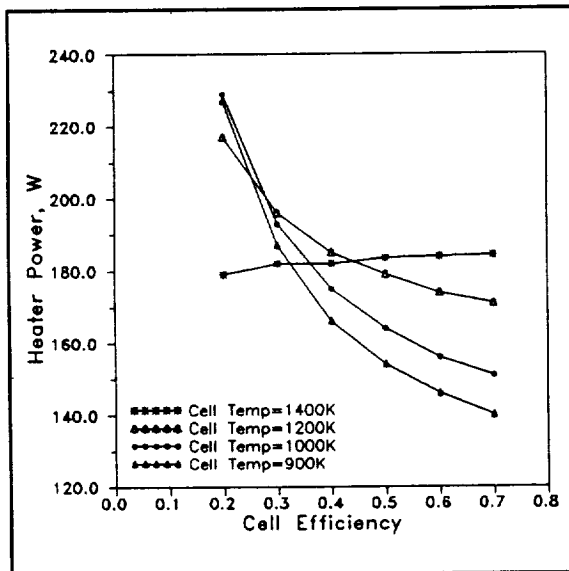
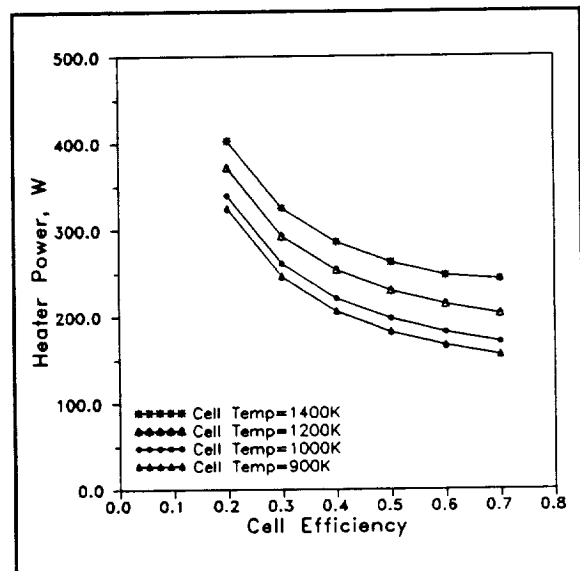


enough to cause the heater work to increase. Here, and in discussions later in this report, we freely use the " $(T_5 - T_4)$ " argument. Although the empirical relations used for  $C_p$  were fourth-order polynomials in temperature, terms such as  $(T_5^4 - T_4^4)$  etc. depend essentially on  $(T_5 - T_4)$ . Note that the magnitude of heater work is greater for case 2 than for case 1, for a fixed  $T_5$ . It may be expected that at cell temperatures higher than those considered, figure 5 behave similar to figure 4. However, in practice, cell temperatures higher than 1500K are not of interest.

Fig 8: CO<sub>2</sub> Intake - Case 1Fig 9: CO<sub>2</sub> Intake - Case 2

Figures 8 and 9 show the CO<sub>2</sub> intake required for cases 1 and 2 respectively. Clearly, the intake required increases sharply as the cell efficiency approaches zero. The intake in cubic-feet per minute (cfm) at the inlet pressure of 6.4 mbar gives us an idea of the size of pumps that we will require. Note that for a given cell efficiency, the intake required in case 2 is greater than that in case 1, especially at lower efficiencies. Since the slope of the curve decreases rapidly with increasing efficiency, and keeping in mind that the intake determines the capacity of the Compressor  $C_1$ , the conclusion is that the compressor capacity becomes impractical at very low efficiencies. For a start, we take an efficiency of 0.2 which is reasonable at this point of time. The pumping speed required is about 280 cfm for case 2 and about 115 cfm for case 1. If we take an

off-the-shelf vacuum pump which can fulfil these requirements, then for case 2, an S Series Rotary Vane Pump Model S630F manufactured by Leybold Vacuum Products Inc. will suffice. It weighs 1450 lb and has a power requirement of 25 hp. For case 1, where the  $\text{CO}_2$  is recycled, a much smaller pump such as the Leybold Model S160C, which weighs 310 lb and consumes 7.5 hp can do the job. Also required in case 1 is a much smaller pump (compressor  $\text{C}_2$ ) to compensate for the pressure drop across the membrane separator. For this a small pump like the Leybold TRIVAC Rotary Vane Pump Model D2A will do. This pump weighs 41 lb and consumes 0.33 hp. This clearly indicates that at this point, though case 2 appears compelling from the points-of-view of system simplicity and reliability, we must recycle the  $\text{CO}_2$  in order to design a reasonably compact system. Note that we must also consider the mass added to the system by the radiator and the membrane separator. However, the reduction in compressor mass and power obtained by recycling offsets the increase in mass due to the radiator and membrane separator. Having decided on recycling, we take an optimistic look at what our requirements would be if we were successful in obtaining a cell efficiency of, say, 0.5, which gives us a  $\text{CO}_2$  intake of about 70 cfm. To take care of this requirement, a first approximation would be a pump like the Leybold S100C, with a mass of 220 lb and a power requirement of 5.0 hp. This makes the system design very feasible as far as its mass requirements go. Obviously, for an actual mission, a much more

Fig 10: Heater Power v/s  $\tau_{\text{cell}}$  - Case 1Fig 11: Heater Power v/s  $\tau_{\text{cell}}$  - Case 2

sophisticated pump with better materials and design would be used. But it would depend on whether an efficient Zirconia cell can be designed. Figure 10 is a graph of heater power versus cell efficiency for case 1. In the light of information obtained from figures 4 and 10, we realise that at low efficiencies the heater power increases because of increased  $\text{CO}_2$  mass flow rate. But the interesting point made by this graph is that at higher cell temperatures and lower efficiencies, the effect of the cell temperature prevails, and causes the slope of the curve to decrease. In fact, the curve for a cell temperature of 1400K is almost flat, suggesting that there could be a temperature  $T_5$  between 1400K and 1200K at which the load on the heater is almost constant. Also important is the fact that it is a lower temperature difference ( $T_5 - T_4$ ) that "overcomes" the increase in the slope. Figure 11, for case 2, is clearly a follow-up of figure 5. Here, the temperature difference ( $T_5 - T_4$ ) does not fall sufficiently to cause the slope to decrease.

#### Plans For The Future

1. The system design depends, to a large extent, upon the system operating pressure. The optimum system pressure needs to be examined. If the system pressure were low, then the option of using a blower (lower mass) instead of a compressor will be examined.
2. The heat exchanger design presently limits the exhaust gas temperature to 700K, due to fears of carbon deposition. Suitable changes will be made in the design when a related investigation by Prof. D.C. Lynch, Department of Materials Science, University of Arizona, provides results on the seriousness of carbon deposition.
3. The pressure and heat losses in the system components and piping will be incorporated in the analysis and
4. The individual components will be designed and tested.

#### Acknowledgements

The graphics routines of the Pascal program used in the analysis were written by Mario Rascon and Kirby Hnat. Their help is gratefully acknowledged.

References

1. K. Ramohalli, E. Lawton & R. Ash, "Recent Concepts in Missions to Mars: Extraterrestrial Processes", Journal of Propulsion and Power, Vol 5, pp 181-187, 1989
2. R.L. Ash, W.L. Dowler & G. Varsi, "Feasibility of Rocket Propellant Production on Mars", Acta Astronautica, Vol 5, pp 705-724, 1978
3. Thermophysical Properties of Matter, The TPRC Data Series, Vol 6, p 50, 145 & 154, IFI/Plenum, 1970

511-25  
N91-24376  
p.15

Issues On The Production And Electrochemical Separation Of Oxygen  
From Carbon Dioxide

P. Kaloupis and K.R. Sridhar

Department of Aerospace and Mechanical Engineering

University of Arizona

ABSTRACT

There is considerable interest at the present time in in-situ propellant manufacturing on the Moon and Mars. One of the concepts of oxygen production that is being actively pursued is the processing of atmospheric carbon dioxide on Mars to produce oxygen by means of thermal decomposition and electrochemical separation. The key component of such a production facility is the electrochemical separation cell that filters out the oxygen from the gas mixture of carbon dioxide, carbon monoxide and oxygen. Efficient design of the separation cell and the selection of electrolyte and electrode materials of superior performance for the cell would translate to significant reduction in the power requirement and the mass of the production facility. The objective of this investigation is to develop the technology required to produce the cells in-house and test various electrolyte and electrode materials systematically until the optimal combination is found. The effect of fabrication methods on the performance of the cell will be studied. Tests will be conducted to investigate the performance of the cell at sub atmospheric ( < 1 bar ) CO<sub>2</sub> supply pressures. An effective technique has been developed for the fabrication of disk shaped cells. Zirconia and Ceria cells have been made in-house. Complete modules of the electrochemical cell and housings have been designed, fabricated and tested. Extensive experiments aimed at characterizing the materials will be underway shortly.

INTRODUCTION

With the renewed interest in space exploration, and in light of the The Report of the National Commission on Space [1], it is expected that some sort of mission, either manned or unmanned, will be forthcoming for surface exploration or sample return from Mars. It has been recognized that one way to reduce the overall weight requirements of such a mission, and hence its costs, is the use of in-situ propellant manufacturing [2]. To this end, several concepts have been proposed for the manufacturing of oxygen from local Martian resources [3-5]. The production of oxygen alone

would provide a tremendous advantage for sample return missions, in which oxygen is the primary propellant mass. The Martian atmosphere, with its known composition of 95.3% carbon dioxide, can provide an excellent source of oxygen. Since such a production plant would be independent of landing site, it is ideally suited for such a concept.

Although the design of a complete oxygen production plant involves many different components, such as collection, separation, storage, and associated power systems, the main consideration here is the oxygen separation system. Carbon dioxide is thermally decomposed into carbon monoxide and oxygen by heating it to high temperatures. Oxygen is separated from the gas mixture using an electrochemical separation cell. With the design of the most efficient system possible, savings can be realized on the power requirements and weight characteristics of the overall plant.

The basic separation cell is shown schematically in Fig. 1. The oxygen separation capability of the system is due to the oxygen ion conduction of the electrolyte material selected. Oxygen vacancies exist in the crystal lattice of the electrolyte. These vacancies provide conduction sites for the transport of oxygen ions through the electrolyte. The driving force for the ions is a potential applied across the electrolyte material.  $\text{CO}_2$  is heated so that it thermally dissociates into CO and  $\text{O}_2$ . The gas mixture is then passed over the cell which consists of an electrolyte sandwiched between electronically conductive porous electrodes. The diatomic oxygen diffuses through the porous electrode to the electrolyte/electrode interface, and the  $\text{O}_2$  molecule decomposes into oxygen ions with a negative charge of two. The applied potential supplies the electrons at the cathode, and provides the potential gradient to drive the oxygen ions through the crystal lattice structure. The oxygen ions move from vacancy to vacancy until they arrive at the electrolyte/electrode anode interface. Here they give up the excess electrons and reform  $\text{O}_2$ , which then diffuses through the porous electrode. The pure diatomic oxygen can then be collected for use.

The properties of the electrolyte and the electrode are of paramount importance in determining the overall characteristics of the cell. For example, operation at a high temperature is desirable since this improves the oxygen ion conductivity through the lattice. Also, a porous electrode is preferred since the oxygen must be able to pass freely through it, however good electronic conductivity (which requires less porosity) is also necessary. These, and other requirements, along with the restrictions they impose on material selection, are considered in more detail in the following sections.

In order to be able to examine many different types of electrolyte/electrode combinations, an

experimental system was devised which allows for easy investigation of manufactured cells. The disk design was selected because of its simplicity. Once the electrolyte has been manufactured, the electrode is applied and the system is sealed inside a manifold. The process is described in more detail in a later section. With this design, the fabrication of cells is quick and relatively easy, allowing for experimentation with many different combinations of materials.

The main emphasis at this time has been in developing an understanding of the electrochemical processes, and in the fabrication techniques associated with building an operational cell. Once this groundwork has been laid, it will then be possible to select electrolyte/electrode combinations that meet the requirements for an actual system.

### THE ELECTROLYTE

The single most important element in the electrolytic separation of oxygen from carbon dioxide is the selection of the electrolyte. A substantial amount of work has been performed in this area by Suitor, et. al. [6], who have identified a search process based on certain criteria. The present work parallels their approach, which identifies classes of likely compounds and then attempts to use a systematic approach in selecting potential oxygen ion conductors. It is desirable to select an electrolyte that has the highest possible conductivity at the lowest possible operating temperature, so as to reduce the overall mass and power requirements of an oxygen plant.

#### Theory

The most important consideration in selecting an electrolyte is the overall conductivity. It must have the maximum possible oxygen ion conduction with very little electron or secondary ion conduction. It must also be non-porous and have good micro-structural stability. The electrolyte must also be stable in chemistry and in phase during prolonged exposure to high temperatures and repeated cycling. In addition, it must resist cracking due to mechanical stresses that arise due to differing thermal expansion coefficients of the electrode and casing, and it must be economical and relatively easy to fabricate.

To achieve the highest possible oxygen ion conductivity it is required to have a high concentration of oxygen vacancies, low activation energy, and weak bonding at the oxygen sites. Suitor, et. al. [6] identify compounds by fitting them to these three categories. High vacancy concentrations can be found in defect structure oxides, materials doped with lower valence cations, and open structures where oxygen ions occupy interstitial sites. Low activation energies are found in oxides with low packing densities (more open paths are available), and in oxygen salts of large polyvalent single valence cations. Weakly bonded oxygen sites are found in metastable structures and

structures stabilized with large dopant ions, glasses made from oxides of large polyvalent single valence cations, and low packing density oxides with non-equivalent oxygen sites.

An extensive search of currently unknown materials that may meet the above requirements is not feasible, since many of the possible compounds are not researched in the literature [6]. However, known oxygen electrolytes such as Zirconia, Thoria, delta Bismuth Oxide, and Ceria have been extensively investigated by many authors [7-11]. These materials are good oxygen ion conductors and mostly exhibit low electron conductivity. In order to begin the present investigation Zirconia and Ceria were selected because of their availability and ease of fabrication. There is some evidence to indicate that Zirconia may prove to be the most probable choice for an oxygen separation cell [6], even though it does not exhibit the highest conductivity.

Both Zirconia ( $\text{ZrO}_2$ ) and Ceria ( $\text{CeO}_2$ ) are oxides of quadrivalent cations which crystallize with a fluorite, or distorted fluorite, structure (Fig. 2). These oxides become oxygen conductors when they are doped with lower valence cations such as Calcium, Yttrium, or Scandium. These dopants stabilize the cubic fluorite structure and create anion vacancies. The magnitude of the conductivity depends on dopant concentration, type of dopant, and temperature. The effect of dopant concentration for Yttria stabilized Zirconia is shown in Fig. 3 [6]. As the mole percentage of dopant increases, so does the conductivity until it reaches a maximum. This maximum occurs because the migration energy of the oxygen ion increases with the increased presence of dopant cations, even though more oxygen anion vacancies exist. The importance of high conductivity at low temperature is obvious. The savings in power requirements for a cell operating at even 100 °C lower operating temperature is quite significant.

For the present study we investigated only  $\text{ZrO}_2\text{-Y}_2\text{O}_3$  8% mole and  $\text{CeO}_2\text{-CaO}$  15% mole to establish the fabrication techniques required for the electrolyte. These molar percentages represent maximum conductivities based on past investigations [6,12].

#### Fabrication of the Electrolyte

There are several potential techniques for fabricating the electrolyte that may be used. These include slip casting, tape casting, and cold pressing. Other techniques such as sputtering or flame spraying are not considered because of the difficulty of making uniform, non-porous samples.

Tape casting involves the use of a slurry that is prepared by adding the ceramic powder, solvent, dispersant, and binder and making a smooth paste. The slurry is then poured onto a flat surface, and a blade is drawn over it to cast the slurry into a uniformly thick layer. The net result is a flat, flexible layer of material from which any shape can be cut. This green material can then be



fired to form the electrolyte disk. Cold pressing involves a dry powder consisting of the ceramic powder and binder which is uniaxially pressed to form the disk. The method selected here is the cold pressing because of its simplicity and cost. At this preliminary stage of investigation it is important to be able to produce many disks without much cost and/or involved fabrication techniques. As the investigation progresses it is anticipated that other techniques, such as tape casting, will be considered for the manufacture of the electrolyte disks.

The two electrolytes fabricated at the present time are  $\text{ZrO}_2\text{-Y}_2\text{O}_3$  8% mole and  $\text{CeO}_2\text{-CaO}$  15% mole. The Ceria has been prepared via oxide and nitrate routes. The fabrication techniques for the two electrolytes follow.

In order to prepare the Zirconia disks two commercially available powders were used. These are the TOSOH TZ-8Y and the Magnesium Elektron Inc. SCY8. The method of preparation for the two powders is the same. A 15% volume slurry was made from the dry powder by adding  $\text{H}_2\text{O}$ , and then 1.5% weight binder was added. The mixture was stirred for 20 minutes, and was then pan-dried at  $60^\circ\text{C}$ . The dried powder was then sieved through a #45 sieve to ensure uniform particle size. The fine powder was then ready to be cold pressed into the green disks.

The preparation of the Ceria disks was more involved, since no commercially available Calcia stabilized Ceria was readily available. Two preparation techniques were used to make the powder.

The first technique is preparation via the oxide route. Appropriate quantities of dry Alfa Products  $\text{CeO}_2$  (IV) and  $\text{CaO}$  corresponding to 15% mole are dry mixed and then ball milled in Ethanol (ETOH) for 24 hours. The ETOH is then boiled off by drying at  $60^\circ\text{C}$ , and the powder is calcined at  $1000^\circ\text{C}$  for 12 hours. The calcined powder is then ball milled in ETOH for an additional 12 hours, at which point 0.5% weight organic binder is added. This is then milled for an additional 4 hours. The wet powder is pan-dried at  $60^\circ\text{C}$  and sieved through a #45 sieve for uniformity.

The second technique for preparing the Ceria is via the nitrate route. A 60% volume slurry in water is made from  $\text{Ca}(\text{NO}_3)_2 \cdot 4\text{H}_2\text{O}$ . This slurry is mixed until a smooth consistency is obtained. While this mixture is being agitated, nitric acid ( $\text{HNO}_3$ ) is added until the solution becomes clear. The  $\text{CeO}_2$  powder is then blended into the solution. The  $\text{H}_2\text{O}$  is evaporated by heating over a hot-plate. The recovered powder is then calcined at  $1000^\circ\text{C}$  for 12 hours. The powder is then removed and ball milled in ETOH for 24 hours. A 0.5% weight organic binder is then added to the solution, and the mixture is milled for an additional 2 hours. The final slurry is removed and pan-dried at  $60^\circ\text{C}$ . The powder is then sieved through a #45 sieve for uniformity.

In all cases the binder was added to allow cold pressing of the green disks. A commercially

available Zirconia powder TSAM-105 from Huls America with binder already added was also tried, but was not very successful. It is believed that the particular binder used in this commercial product was not very effective for our application.

Once the finished powders were ready, they were cold pressed in a die. Uniaxial compression of 8000-19000 lbs/in<sup>2</sup> was used to make the green disks. Several thicknesses ranging from 1-3 mm were produced, with a diameter of 1.5 inches. Once the green disks were formed they were sintered for final use.

The disks were sintered at varying temperatures for different time spans. Because of limited access to a furnace, the disks were sintered at a rapid rate. Typically, the furnace was ramped to 1400 °C in 2 hours, and allowed to remain there for 1/2 hour. The temperature was then ramped to 1600 °C in 1 hour, and remained there for 1 hour. The disks were then removed.

During the cooling of the disks following the firing in the furnace, some of the disks warped. Many disks proved to be unusable because they were not flat. It is believed that the rapid temperature rise caused internal stresses within the disks which caused them to warp. Now, access to a furnace has been obtained with longer usage times, and this problem will be avoided. The placement of flat weights (1 gm/cm<sup>2</sup>) over the disks during the sintering process has also proven to be helpful in reducing this problem.

At the present time the disks have not been tested for porosity, however they are believed to be quite dense. Analysis of the disks with the aid of an electron microscope for this purpose has been planned for the future.

### THE ELECTRODE

The selection of the electrode and the technique used to apply it to the electrolyte surface is very important. The properties of the electrode and the electrolyte/electrode interface are critical to the overall performance of the cell. Typical electrode materials are precious metals and conducting oxides, doped with some impurity, as well as perovskites.

#### Theory

The most important considerations for the selection of an electrode material are its electronic conductivity, the thermal expansion coefficient, its porosity, oxidation resistance, and chemical and electrical stability. The thermal expansion coefficient must match that of the electrolyte as closely as possible, so that mechanical stresses do not arise at the interface. This could lead to cracking of the electrolyte during prolonged exposure to high temperature and thermal cycling. Also, it is necessary that the electrode be porous so that the oxygen ions can move freely through it. However,

a balance exists between good conductivity and free movement of oxygen ions. Another important consideration in selecting the electrode is the potential catalytic effect that it may have on the oxygen kinetic reactions, both on the cathode and the anode side of the cell [13]. The electrolyte/electrode interface is also of significance. If the electrolyte is very thin, then the major ohmic loss will occur at the interface with the electrode [13]. Minimizing the losses at the point of contact could significantly change the performance of the cell.

Much work has been done with precious metals [14,15] such as Silver, Palladium, and Platinum. They are very expensive and do not match the thermal properties of the electrolyte surface. Other types of electrodes that have been investigated are chemically stable oxides doped with impurities, such as Tin oxide doped Indium oxide [16], and perovskites [6]. These have excellent thermal properties with relation to the electrolytes, and they reduce thermal stresses that may arise during thermal cycling. However, these materials typically have complicated manufacturing and application procedures and hence have not been investigated at the present. At this time we have considered only precious metals. Plans for the future include testing the oxides and perovskites as potential electrodes.

#### Application of the Electrode

The application of the electrode material to the electrolyte surface can be done in many ways. Direct application techniques include sputtering, vapor deposition, flame spraying, and direct paste application. There is some evidence to suggest that sputtering is not an effective application technique [17], since it can destroy the electrolyte surface. Also, because techniques such as vapor deposition and flame spraying are expensive and difficult, only paste application has been investigated at this time.

The electrode material most often applied to the electrolyte to date is Platinum, although Silver has also been used. Commercially available unfritted Pt paste supplied by Heraeus Cermalloy has been used, and a thin layer of the electrode paste is painted onto the electrolyte surface. The lead wire is a spiraled wire of the same material as the electrode, which is pressed into the paste before it dries. The paste is then set by heating in a furnace to 950 °C. The finished cell, shown in Fig. 4 is then ready to be manifolded.

#### THE CELL MANIFOLD

Once the electroded disk is made, it is sealed in a manifold for experimentation. The configuration, before being sealed is shown in Fig. 5a, and the schematic of the sealed cell is shown in Fig. 5b. There is a CO<sub>2</sub> supply tube and a CO + CO<sub>2</sub> exhaust tube on the cathode side, and an

O<sub>2</sub> outlet tube on the anode side. The whole system can be heated to the operating temperature of 800-1000 °C. Experiments can be performed to investigate the overall oxygen production capabilities of a particular electrolyte/electrode combination. Based on these test results conclusions can be drawn as to the effectiveness of particular cells.

#### CONCLUDING REMARKS AND SUMMARY

To date we have developed an understanding of the processes involved in electrolytic separation of oxygen from carbon dioxide, and are currently in a position to begin investigating materials that may afford increases in ion conductivity that will result in increased cell performance.

An effective technique has been established for the fabrication of cells, and we have demonstrated the ability to manufacture working cells. A test-bed has been built to conduct experiments, which are currently under way.

Future work will include investigation of electrolytes other than the fluorite structures, and oxide or perovskite electrodes. Also, some of the other fabrication techniques such as tape casting will be investigated. In addition, electrode application techniques will be considered in great detail. The overall oxygen plant design will be significantly simplified if the electrochemical cell operated efficiently at close to Martian atmospheric pressures. Hence, extensive tests will be performed to study the effect of sub atmospheric ( < 1 bar ) CO<sub>2</sub> supply pressures.

#### REFERENCES

1. The Report of the National Commission on Space, "Pioneering the Space Frontier," Bantam Publishing, New York, 1986.
2. Ash, R. L., Dowler, W. L., and Varsi, G., "Feasibility of Rocket Propellant Production on Mars," Acta Astronautica, Vol. 5, Sept. 1978, pp. 705-724.
3. Ash, R. L., Huang, J. K., and Johnson, P. B., "Elements of Oxygen Production Systems Using Martian Atmosphere," Paper No. AIAA-86-1586, AIAA/ASME/SAE/ASEE 22nd Joint Propulsion Conference, June 16-18, Huntsville AL, 1986.
4. Ash, R. L., Richter, R., Dowler, W. L., Hanson, J. A., and Uphoff, C. W., "Autonomous Oxygen Production for a Mars Return Vehicle," Paper No. IAF-82-210, 33rd Congress of the International Astronautical Federation, Paris, France, Oct. 1982.

5. Ramohalli, K., Lawton, E., and Ash, R. L., "Recent Concepts in Missions to Mars: Extraterrestrial Processes," J. of Propulsion and Power, Vol. 5, No. 2, March-April, 1989, pp. 181-187.
6. Suitor, J. W., Berdhal, C. M., Ferrall, J. F., Marner, W. J., Schroeder, J. E., and Shlichta, P. J., "Development of an Alternate Oxygen Production Source Using Zirconia Solid Electrolyte Membrane," Technical Progress Report for Fiscal Years 1986 and 1987, Report No. JPL-D-4320, May 1987.
7. Richter, R., "Basic Investigation into the Production of Oxygen in a Solid Electrolyte Process," Paper No. AIAA-81-1175, AIAA 16th Thermophysics Conference, June 23-25, Palo Alto CA, 1981.
8. Erstfeld, T. E., and Mullins Jr., O., "Carbon Dioxide Electrolysis Using a Ceramic Electrolyte," Paper No. AIAA-79-1375, Fourth Princeton/AIAA Conference on Space Manufacturing Facilities, May 14-17, Princeton NJ, 1979.
9. Dell, R. M., and Hooper, A., "Oxygen Ion Conductors," Solid Electrolytes, General Principles, Characterization, Materials, Applications, ed. Hagenmuller, P., and Van Gool, W., Academic Press, New York, 1978, pp. 291-312.
10. Miyayama, M., Nishi, T., and Yanagida, H., "Oxygen Ionic Conduction in  $Y_2O_3$  Stabilized  $Bi_2O_3$  and  $ZrO_2$  Composites," J. of Materials Science, Vol. 22, 1987, pp. 2624-2628.
11. Graia, T., Conflant, P., Boivin, J. C., and Thomas, D., "High Ion Conduction in a Bismuth Oxide-Conductivity and Transport Number Measurements; Structural Investigations," Solid State Ionics, ed. Boyce, J. B., DeJonghe, L. C., and Huggins, R. A., North Holland, Amsterdam, 1985, pp. 751-755.
12. Subbarao, E. C., ed., Solid Electrolytes and their Applications, Plenum Press, New York, 1980.
13. Isaacs, H. S., Olmer, L. J., Schouler, E. J. L., and Yang, C. Y., "Electrode Reactions at Solid Oxide Electrolytes," Solid State Ionics, 1981, pp. 503-507.

14. Isaacs, H. S., and Olmer, L. J., "Comparison of Materials as Oxygen Catalytic Electrodes on a Zirconia Electrolyte," J. of the Electrochemical Society: Solid State Science and Technology, Feb. 1982, pp. 436-443.
15. Rohr, F. J., Eysel, H. H., and Kleinschmager, H., "Electronically Conducting Oxides as Cathodes of Interconnection Materials in High Temperature Fuel Cell Batteries," Fourth International Symposium on Fuel Cells, Antwerp, Belgium, Vol. 1, 1972.
16. Rohr, F. J., "High Temperature Fuel Cells," Solid Electrolytes, General Principles, Characterization, Materials, Applications, ed. Hagenmuller, P., and Van Gool, W., Academic Press, New York, 1978, pp. 431-450.
17. Suitor, J. W., Jet Propulsion Lab, Private Communication, Dec. 1990.

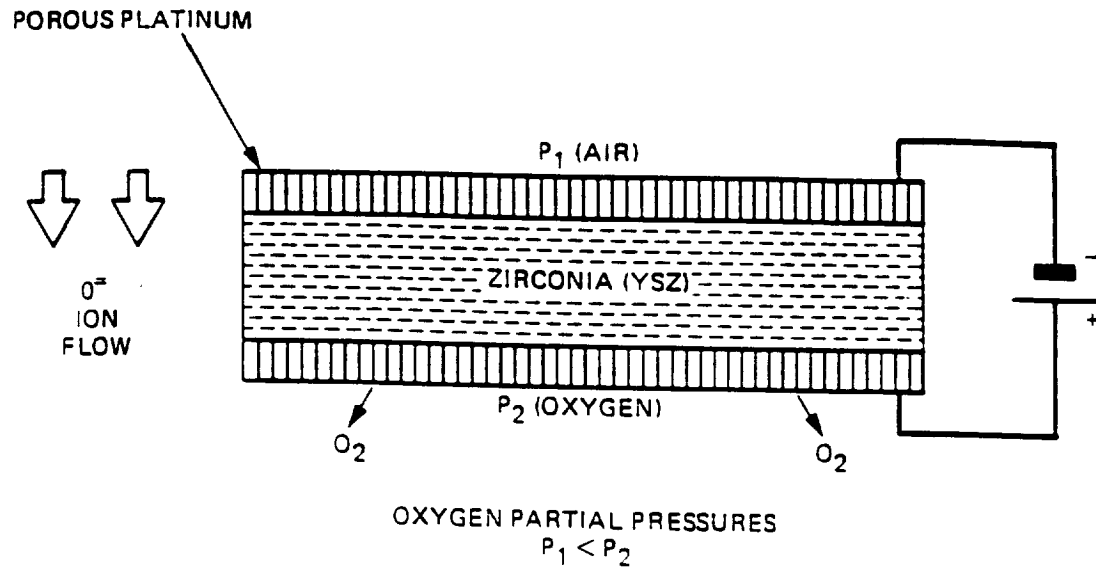


Fig 1: Schematic of an Electrochemical Separation Cell [6]

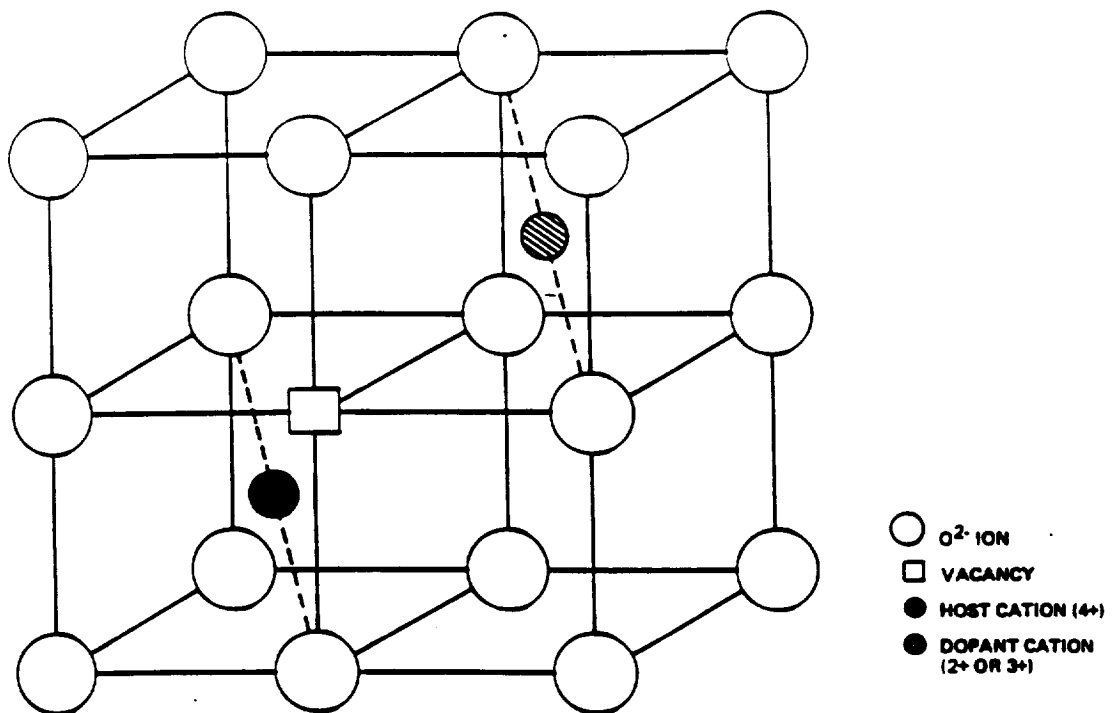


Fig 2: Distorted Fluorite Structure [6]

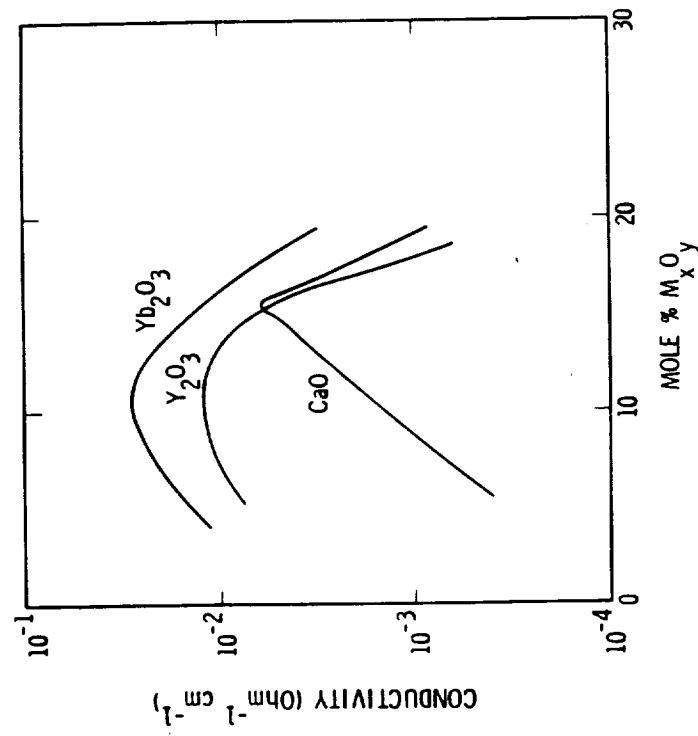


Fig 3: Dopant Concentration For Yttria Stabilized Zirconia [6]



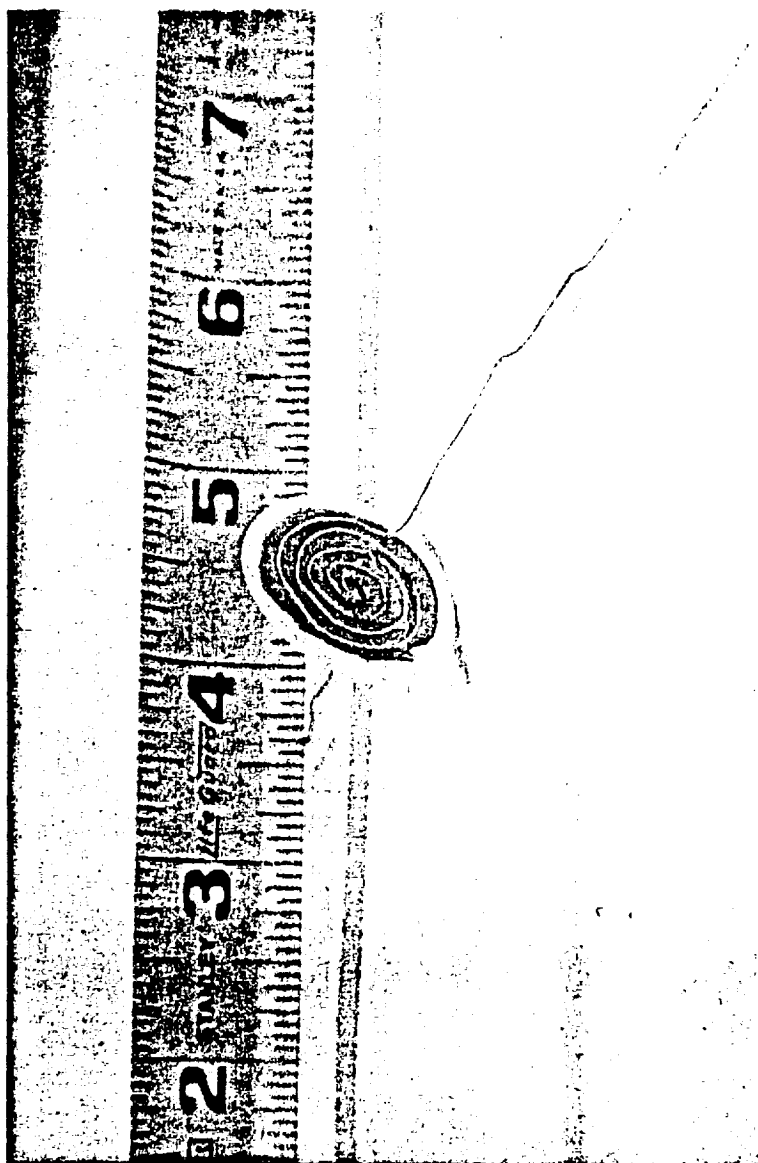


Fig 4: Electroded Electrochemical Disk With Lead Wires

ORIGINAL PAGE IS  
OF POOR QUALITY

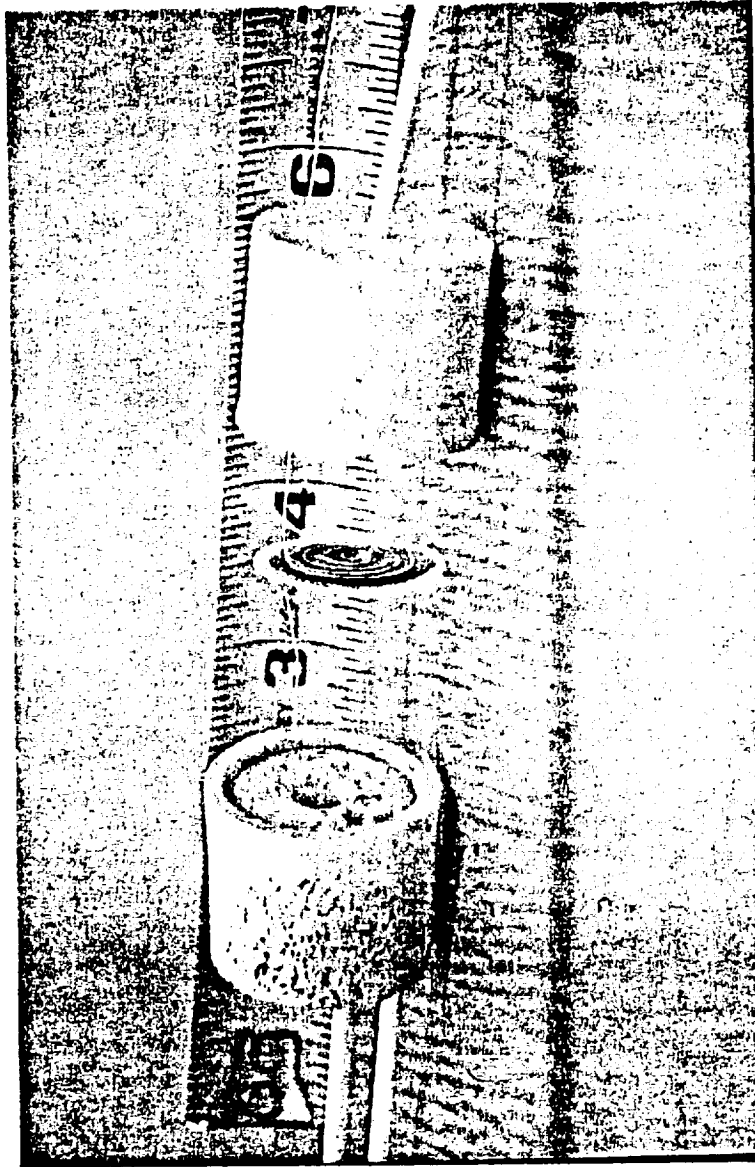


Fig 5a: Disk With Manifolds and Supply Wires Ready to be Assembled

ORIGINAL PAGE IS  
OF POOR QUALITY

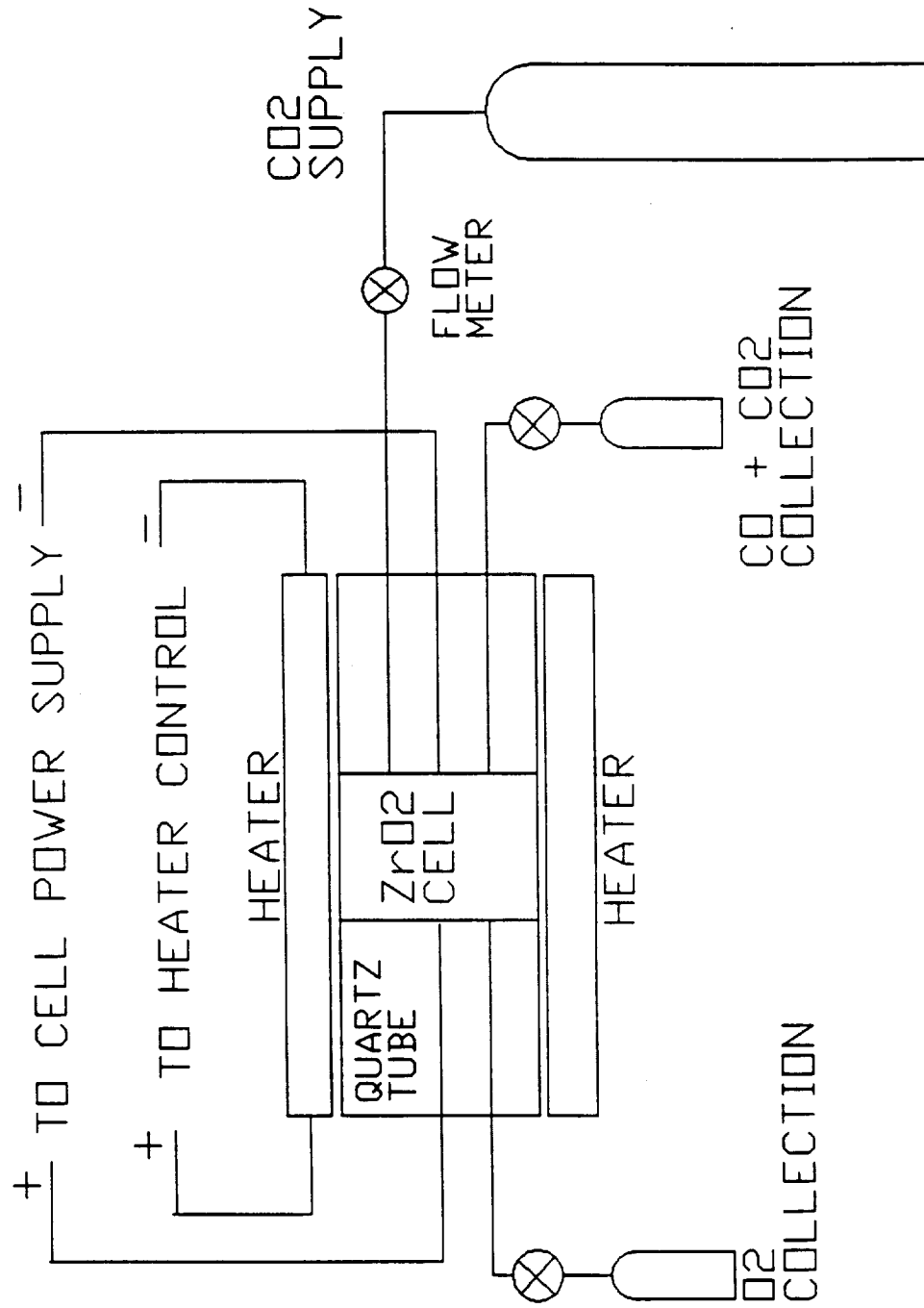


Fig 5b: Schematic of an Assembled Disk Module For Oxygen Production

512-25  
N91-243772  
P.5

Compression Of Martian Atmosphere For Production Of Oxygen

D. C. Lynch, A. H. Cutler, and P. E. Nolan

Department of Materials Science and Engineering  
and  
Space Engineering Research Center  
The University of Arizona

AY 352 375

Abstract

This research program deals with the compression of  $\text{CO}_2$  from the Martian atmosphere for production of  $\text{O}_2$  via an electrochemical cell. Design specifications call for an oxygen production rate of 10 kg. per day and for compression of 50 times that mass of  $\text{CO}_2$ . Those specifications require a compression rate of over 770 cfm at standard Martian temperature and pressure (SMTP). Much of the  $\text{CO}_2$  being compressed represents waste, unless it can be recycled. Recycle can reduce the volume of gas that must be compressed to 40 cfm at SMTP. That volume reduction represents significant mass savings in the compressor, heating equipment, filters and energy source. Successful recycle of the gas requires separation of CO (produced in the electrochemical cell) from  $\text{CO}_2$ ,  $\text{N}_2$ , and Ar found in the Martian Atmosphere. That aspect has been the focus of our work during the first year.

Background

The Space Engineering Research Center (SERC) at the University of Arizona is in the progress of designing and building a prototype system for production of  $\text{O}_2$  from  $\text{CO}_2$ . While SERC is currently addressing conditions typical of the Martian atmosphere, the technology being developed is applicable wherever  $\text{CO}_2$  is produced and can be used as a raw material.

Recycle of the gas leaving the electrochemical cell has a distinct advantage of reducing the volume of the Martian atmosphere that must be compressed. Successful recycle, however, requires separation of the CO produced in the cell from the remainder of the compressed atmosphere. Carbon dioxide and carbon monoxide are not easily separated as both have the same approximate kinetic diameters since both molecules are linear. That fact precludes the use of zeolites for the separation of CO from  $\text{CO}_2$ . Polymeric membranes are used to separate  $\text{CO}_2$  from CO. Since the gas stream under consideration consists primarily of  $\text{CO}_2$  an extensive membrane surface area would be required. In addition the membranes are susceptible to failure at elevated temperatures.

Cooling the gas leaving the electrochemical cell to a temperature where polymeric membranes could be used to separate CO<sub>2</sub> from CO could result in carbon deposition. That deposition, if not controlled, could lead to failure of the entire system.

Thermodynamic analysis of the exit gas, as proposed, has revealed that carbon deposition is possible at temperatures below 500 °C. The reaction involved,



is referred to as the disproportionation reaction. At temperatures below 600 °C the reaction is sluggish, but is known to be catalyzed by ferrous metals[1-4]. That knowledge can be used in conjunction with reaction 1 to remove CO and thereby provide for recycle of CO<sub>2</sub>.

### Approach

The basic approach to the experimental program involves testing the effectiveness of various catalyst for disproportionation of CO from a gas stream consisting primarily of CO<sub>2</sub>. To accomplish that task an apparatus consisting of a tube furnace, controller, gas chromatography and gas delivery system has been assembled as shown in Figure 1.

An experiment is initiated by placing the catalyst in the tube furnace and purging the entire system with an inert gas. After the desired temperature has been obtained in the furnace, a CO<sub>2</sub>-CO-N<sub>2</sub> gas mixture is allowed to contact the catalyst. Both the inlet gas stream to the furnace and exit gas stream from the furnace are sampled and the resulting specimens analyzed using a gas chromatography. The resulting data is used to determine the effectiveness of the catalyst in the disproportionation of CO. This technique is being used to test a number of catalysts.

Those catalysts that prove effective in the disproportionation of CO will under go repeated tests in order to evaluate long term effects. That testing will include burnout of the carbon using CO<sub>2</sub> at temperatures above 700 °C. Following burnout the catalyst will, again, be exposed to the CO<sub>2</sub>-CO-N<sub>2</sub> atmosphere for carbon deposition. The effectiveness of the catalysts will be plotted as a function of the number of cycles. It is anticipated that the effectiveness of the catalyst will depend in large part on its surface morphology and how it changes with repeated use. Scanning electron microscopy will be used to evaluate any changes.

### Experimental Results

A number of catalytic carriers have been selected based on their surface area and pore size distribution. All of the carriers are ceramic, and as such are not expected to be effective in enhancing the disproportionation reaction. A typical result for Celite which has a surface area of

67 m<sup>2</sup>/g and a mean pore diameter of 0.19  $\mu$ m is shown in Figure 2. It is necessary to conduct these experiment to achieve a minimum base line for comparison purposes. In order to improve the performance of the carriers we are investigating methods whereby the surface of the carrier can be partially coated with an active metal. The catalytic carrier serves to provide a stable structure with a high surface area over which micro droplets of metal are distributed. Those droplets will coalesce. The rate at which coalescence occurs will depend on both the temperature and duration at which the catalyst is exposed to that temperature. Without the carrier both surface diffusion and vapor phase transport could significantly reduce the surface area of metal particles.

#### Student Participation

Mr. Peter E. Nolan, a U. S. citizen, is working on this project. Peter has an Applied Physics Degree from the University of California at San Diego. After completing his undergraduate degree he served several years as an officer in the U. S. Navy. Peter joined our group in July, and since then has been responsible for construction and testing of the experimental apparatus. He is currently in our M. S. degree program and has applied to NASA for admission for astronaut training.

#### References

1. Kinetics and Microscopic Aspects of Catalytic Carbon Growth, M. Audier and M. Coulon, Carbon, 23, pp. 317-23, 1985.
2. Disproportionation of CO on Iron-Cobalt Alloys - I, Thermodynamic Study, M. Audier, M. Coulon, and L. Bonnetian, Carbon, 21, pp. 93-98, 1983.
3. Disproportionation of CO on Iron-Cobalt Alloys - II, Kinetic Study on Iron- Cobalt Alloys of Different Composition, M. Audier, M. Coulon, and L. Bonnetian, Carbon, 21, pp. 99-104, 1983.
4. Disproportionation of CO on Iron-Cobalt Alloys - III, Kinetic Laws of the Carbon Growth and Catalyst Fragmentation, M. Audier, M. Coulon, and L. Bonnetian, Carbon, 21, pp. 105-110, 1983.

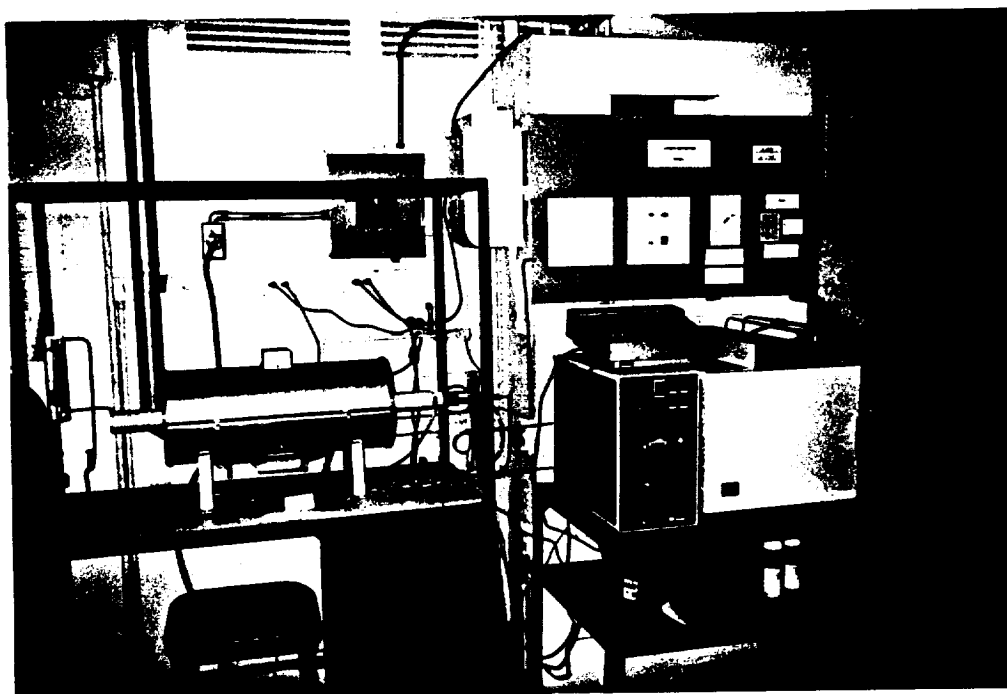


Figure 1 - Experimental Apparatus

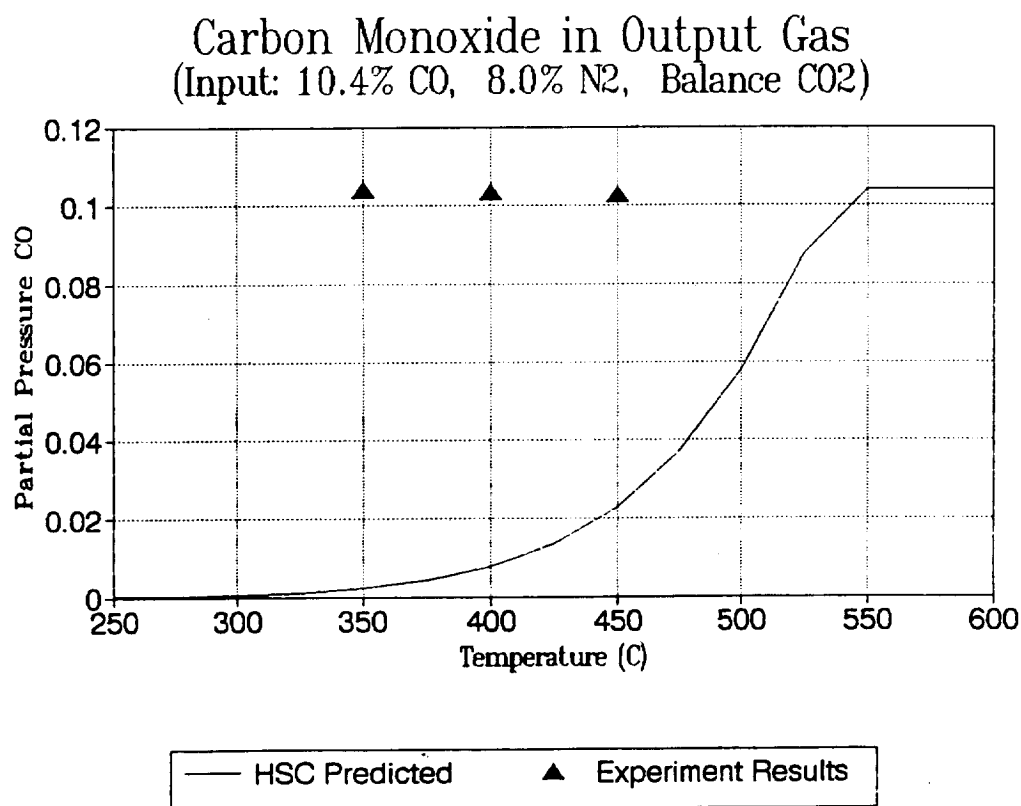


Figure 2 - Experimental Results With Catalytic Carrier, Celite

## **C. REDUCTION OF CARBONACEOUS MATERIALS**



513-25

N 9 1 - 2 4 3 7 8 7 3  
P. 14

# DEHYDRATION KINETICS OF TALC AT 1 BAR

J. Ganguly and K. Bose  
Department of Geosciences  
The University of Arizona

## Abstract

We present experimental results on the dehydration kinetics of talc, which is likely to be a major potential resource for water and hydrogen in carbonaceous chondrites. The rate of dehydration of an essentially pure Mg-end member natural talc,  $(\text{Mg}_{.99}\text{Fe}_{.01})_3\text{Si}_4\text{O}_{10}(\text{OH})_2$ , was studied by measuring in situ weight change under isothermal condition at 1 bar as a function of time in the temperature range 775-985°C. The grain size of the starting material was 0.7-1 micron. It was found that the data up to 50-60% dehydration can be fitted by an equation of the form  $\alpha = \exp(-Kt^n)$ , where  $\alpha$  is the weight fraction of talc remaining, K is a rate constant and n is a numerical constant for a given temperature. For any set of isothermal data, there is a major change in the value of n for larger dehydration. For up to ~ 50% dehydration, all rate constants can be described by an Arrhenius relation with an activation energy of 432 ( $\pm 30$ ) kJ/mol; n has a nearly constant value of 0.54 between 775 and 875°C, but increases almost linearly according to  $n = -10.77 + 0.012T(^{\circ}\text{C})$  at  $T \geq 875^{\circ}\text{C}$ .

## Introduction

Carbonaceous chondrites are usually believed to be the primary constituents of near-Earth asteroids and Phobos and Deimos, and are potential resources of fuels that may be exploited for future planetary missions. The most volatile-rich members of this class of meteorite are known as C1 (or CI) and C2 (or CM) classes. Our group has been involved in an integrated study on the thermodynamics and kinetics of reactions of the volatile-bearing phases that are likely to be present in carbonaceous chondrites. The results will provide important constraints on fundamental aspects concerning nature, abundance, and time scale of formation of volatile-bearing phases in the solar nebula, and the practical problem of the feasibility of extraction of volatiles for fuels from carbonaceous chondrites.

In collaboration with Dr. Surendra Saxena (Professor of Geochemistry at the Brooklyn College, City University of New York, and Uppsala University, Sweden), we have been engaged in deriving and systematizing a set of internally consistent thermochemical data for the minerals that could form within the range of bulk compositions displayed by carbonaceous chondrites, and computer calculations of equilibrium phase relations, along with modal abundance and composition of the phases through the minimization of Gibbs free energy. Although this is an on-going project, subject to revisions and refinements with the improvement and expansion of thermochemical data

base, the results of the calculations carried out so far suggest that talc,  $(\text{Mg,Fe})_3\text{Si}_4\text{O}_{10}(\text{OH})_2$ , and antigorite,  $(\text{Mg,Fe})_{48}\text{Si}_{34}\text{O}_{85}(\text{H})_{62}$ , with or without magnesite,  $(\text{Mg,Fe})\text{CO}_3$ , are likely to be the major volatile-bearing inorganic phases in the C1 and C2 carbonaceous chondrites (Ganguly and Saxena, 1989).

Having identified the most likely mineralogical source of volatiles in the carbonaceous chondrites, we have begun a program of systematic kinetic study of devolatilization reactions, along with our on-going research on thermochemical properties and phase equilibrium calculations. The results will provide the framework for the most energy efficient Engineering designs for the extraction volatiles.

From considerations of the structural properties of phyllosilicates (e.g Bailey, 1988, Evans and Guggenheim, 1988), it is clear that on the average, the hydroxyl groups are more strongly bonded in talc than in antigorite. This is reflected in their relative thermal stabilities. Consequently, the dehydration kinetics of talc is expected to be significantly slower than that of antigorite. During the course of the current funding cycle (March, 1990- February, 1991), we have begun and made significant progress in understanding the dehydration kinetics of talc, as reported below. Work is currently in progress to evaluate the effect of surface area and Fe/Mg ratio on the reaction kinetics, and the mechanism of dehydration reaction.

#### Experimental Methods

The dehydration kinetics of talc has been determined by monitoring the in situ weight change of a natural talc as a function of temperature and time at 1 bar pressure. A schematic of a **Thermogravimetry Apparatus** constructed for this purpose is shown in Fig. 1.

The sample is suspended in an alumina crucible inside a vertical furnace, which has about 2" hot spot of constant temperature near the center. The temperature distribution has been determined by shifting the position of thermocouple along the length of the furnace. The temperature of the sample is monitored by a thermocouple placed very close to the alumina crucible. The bottom of the furnace is closed by a plexiglass so that the position of the sample and the thermocouple can be observed during a run by a mirror, placed underneath the furnace. In order to determine in situ weight change, it is extremely important to ensure that the sample is suspended freely without touching the furnace wall or the thermocouple.

During a run, the suspension of the sample inside the furnace is supported by a needle passing through a small loop in a platinum wire connected to the sample crucible, and resting on a glass tube. The sample weight is determined at desired intervals by connecting the platinum wire to an extension support connected to the pan of an analytical balance through the bottom end. The connection between the analytical balance and the loop in the platinum wire is made by a rigid wire

# Thermogravimetry Apparatus

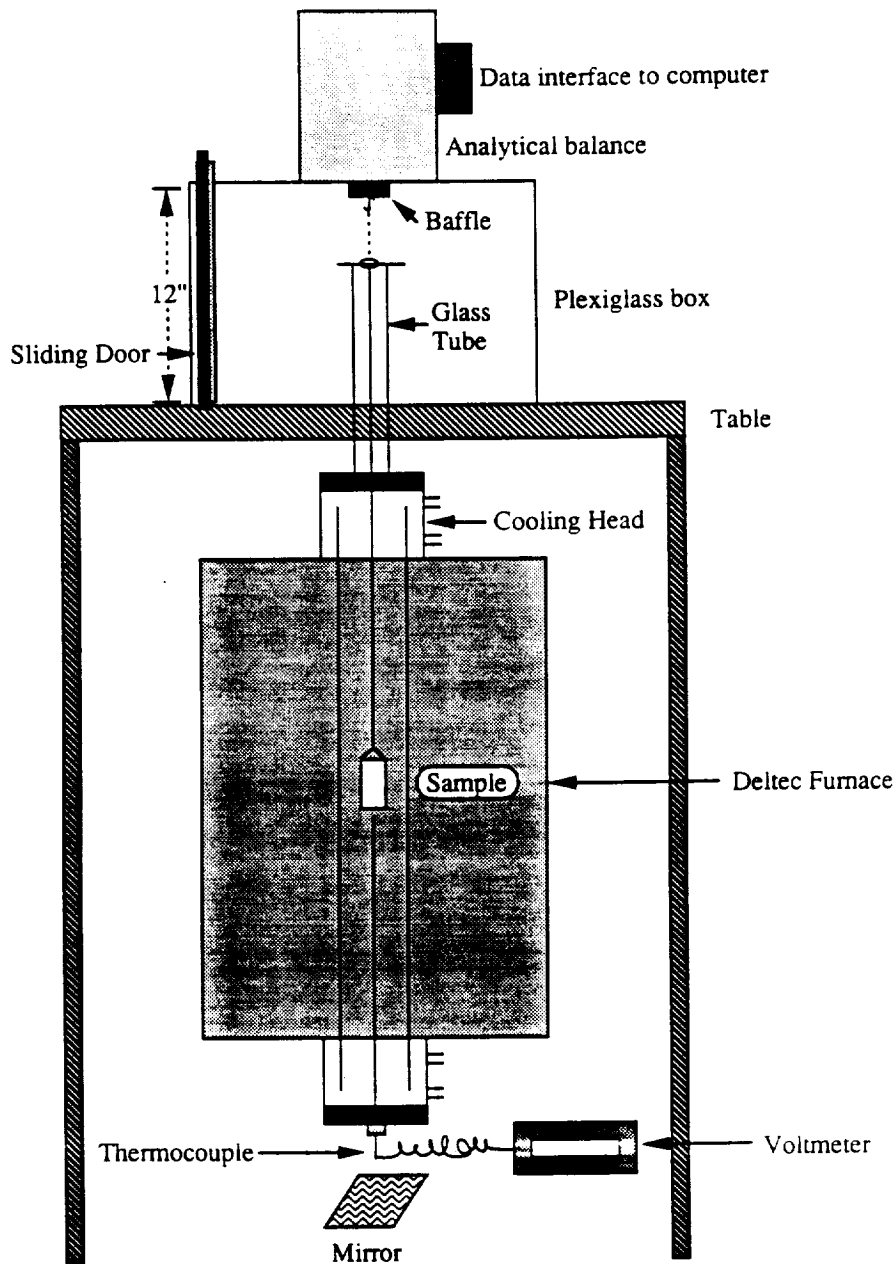


**Fig. 1:** Schematic of the apparatus designed for the measurement of in situ weight change as a function of temperature and time. The plexiglass box (supporting the balance) has a sliding door to permit access to the suspension assembly. The base of the analytical balance is fitted with a baffle to prevent disturbance of the weighing pan (supporting the suspension hook) by thermal current rising from the furnace.

of controlled length and removing the supporting needle such that the position of the sample inside the furnace is not disturbed. The output from the weight transducer in the balance is taken directly to a computer through an interface attached to the balance. The weight of the sample is then recorded in the computer by averaging over a short time interval, 90-120 seconds, after the initial fluctuations resulting from the attachment of the sample to the balance have stabilized. Typically it needs about 2-3 minutes to stabilize these fluctuations, after which there is a small fluctuation ( $\pm 0.0001$  gm), which is an intrinsic property of the balance.

We initially kept the sample suspended directly from the analytical balance so that the weight change can be monitored continuously as a function of time. However, this method has to be finally abandoned owing to the creep of the weight transducer, usually in runs greater than half-hour. The creep effect was discovered by monitoring the weight of a sample directly on the pan of the balance in the usual manner as a function of time, and ensuring that there is no disturbance through air circulation. The creep effect is illustrated in Fig. 2 by comparing the weight monitored continuously as a function of time with that determined by the method described above at essentially the same temperature.

The thermal current rising from inside the hot furnace causes another perturbation (Fig. 3) to the determination of weight change of a sample suspended inside the furnace. Fig. 3a shows the fluctuations of the weight of a crucible measured as a function of time. The fluctuations are usually in the range of  $\pm 0.0005$  gm. In this example, the creep effect was fortuitously quite small. Fig. 3b shows how the measured weight of a sample oscillates as the furnace is repeatedly heated and cooled. The effect of the thermal current was greatly minimized by putting a baffle at the bottom of the balance, with a small hole to allow free passage of the suspension attachment. The effect of putting the baffle is shown in Fig. 4. In this case, the weight of the sample was monitored at 1 minute interval using the arrangement illustrated in Fig. 1. The initial induction period is about 2 minutes, after which the system achieves a stable state with intermittent fluctuations of  $\pm 0.0001$  gm.

In each run, the furnace was first preheated to the desired temperature, and the sample was then suspended near the top of the furnace at about 250°C (which is about 140°C below the equilibrium dehydration temperature at 1 bar) for at least 24 hours to drive off absorbed water. The weight change of the sample was monitored as function of time to ensure complete removal of absorbed water. The sample was then lowered to the hot spot of the furnace, and its weight monitored at desired intervals, as discussed above. Before each weighing, the balance was calibrated using a computer controlled internal calibration, and the calibration was cross checked by weighing a certified weight on the pan of the balance. Because the maximum possible weight change (due to complete dehydration) was 4.5% of the initial weight, and there was about  $\pm 0.0001$

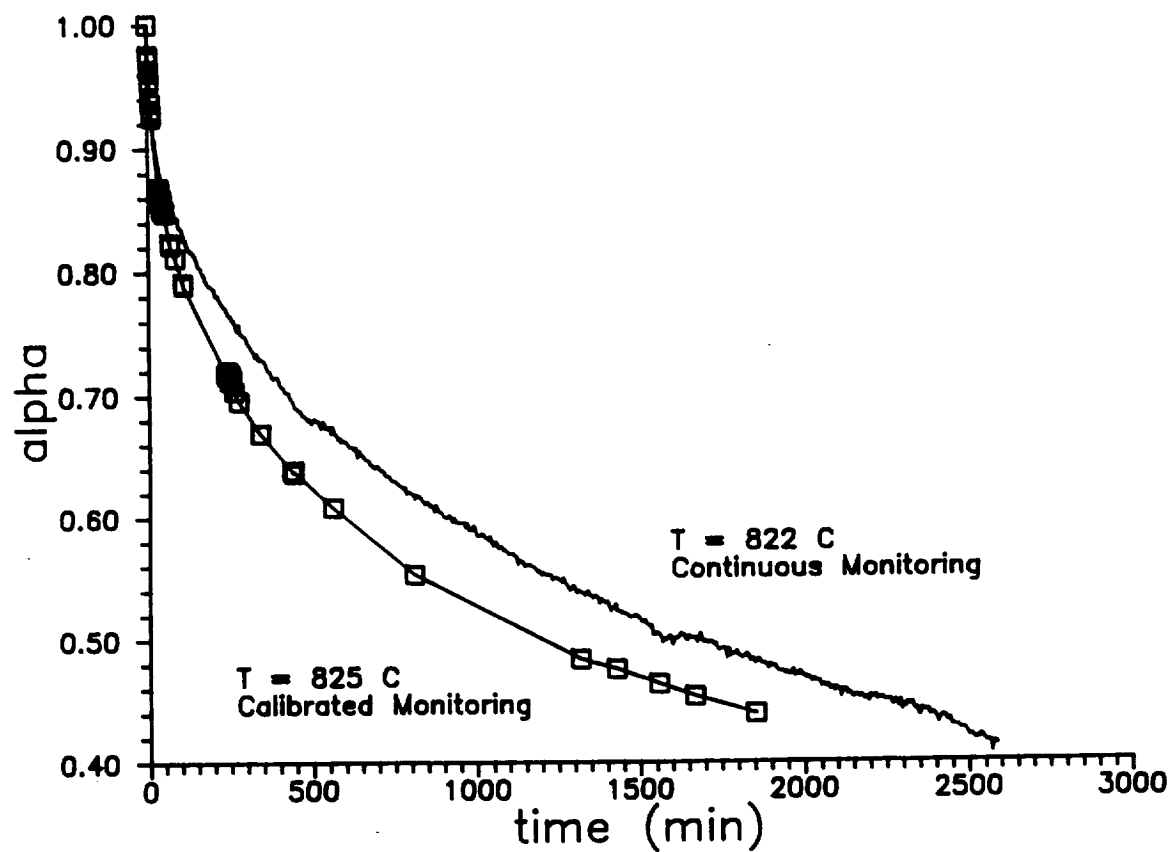
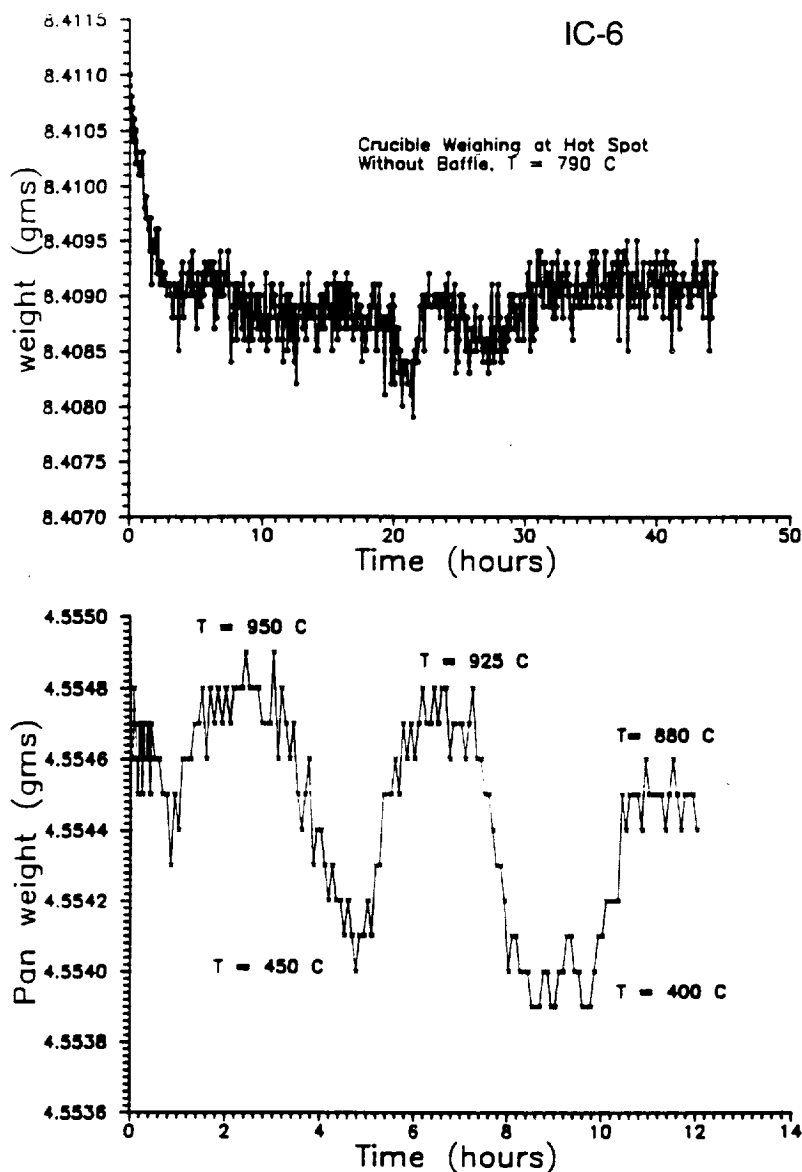
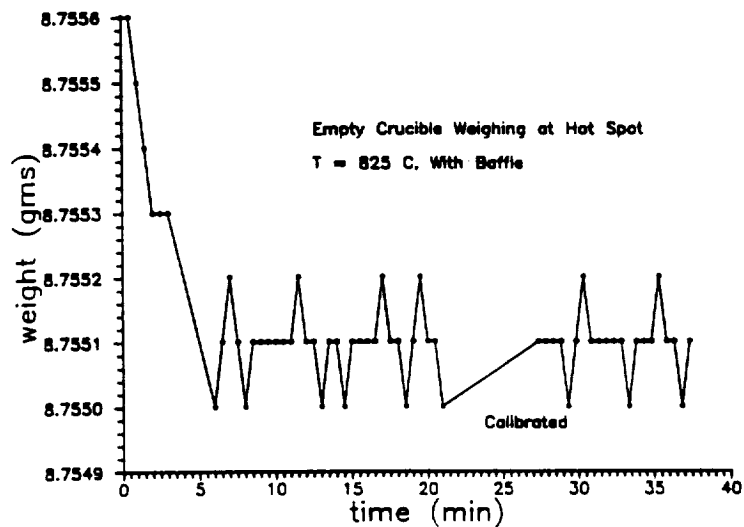


Fig. 2: Comparison of weight change of talc monitored continuously (through a data interface linking the output from a weight transducer to a computer) with that determined after calibrating the balance at discrete intervals.  $\alpha$  is the weight fraction talc remaining as defined by eqn. (1).



**Fig. 3:** Effect of thermal current on the measurement of the weight of a sample crucible suspended inside a furnace, as illustrated in Fig. 1. No baffle was used at the base of the balance. (a) Fluctuations in the measured weight of the crucible held at a constant temperature of  $790^{\circ}\text{C}$  inside the furnace. (b) Change in the measured weight of the crucible as the temperature inside the furnace is raised and lowered, as shown in the figure.



**Fig. 4:** The effect of introducing a baffle at the base of the balance (Fig. 1) on the measurement of the weight of a sample crucible.

gm statistical fluctuation of the weight recorded by the balance, it was necessary to use a sufficiently large amount of sample so that the statistical fluctuations were small compared to the recorded weight changes. Typically about a gram quantity of sample was used in each run.

#### Starting Material

The starting material was made of 0.7-1.0 micron grain size separates obtained by coring a block of talc with a diamond coring tool. It was thought that crushing may introduce too many defects that might enhance the dehydration kinetics. The X-ray diffractogram of the material did not show any other phase. However, a few grains of tremolite was detected in the electron microprobe analysis. The average of several spot analysis in the microprobe yields the following composition of the natural talc used in this study:  $\text{Mg}_{(0.99)}\text{Fe}_{(0.01)}\text{Si}_4\text{O}_{10}(\text{OH})$ .

#### Experimental Results and Theoretical Analysis

The weight change of talc as a function of time was measured at 775, 825, 875, 925, 975, 985°C. Selected run data are illustrated in Fig. 5 a-b. Here  $\alpha$  is the weight fraction of talc remaining at time  $t$ , i.e.

$$\alpha = \frac{W_t - W_{\infty}}{W_0 - W_{\infty}} \quad (1)$$

where  $W(t)$  is the weight of the sample at time  $t$ , and  $W_0$  and  $W_{\infty}$  are the sample weights at  $t=0$  and  $t = \infty$ .  $W_{\infty}$ , thus, corresponds to the weight of the sample after complete dehydration. The theoretical weight loss of the sample after complete dehydration is 4.5%.  $W_{\infty}$  was also checked experimentally by making a very long run at 985°C, which is shown in Fig. 6. The weight after 49 hours is within 1.2% of the theoretical weight after complete dehydration. Thus, the theoretical value of  $W_{\infty}$  was accepted in calculating  $\alpha$  from eqn. (1). In each run,  $W_0$  was taken to be the measured weight of the sample after it was introduced into the hot spot of the furnace, allowing about 3 minutes time for the stabilization of the system. This induction time was subtracted from the total time of the run.

To analyze the experimental data, we begin by assuming that the dehydration of talc is controlled by a nucleation and growth law of the form

$$\alpha = \exp(-Kt^n) \quad (2)$$

where  $K$  is a rate constant. In an earlier study, Ward (1975) was able to fit the dehydration of talc with  $n = 1$ . The eqn. (2) can be linearized to the following form.

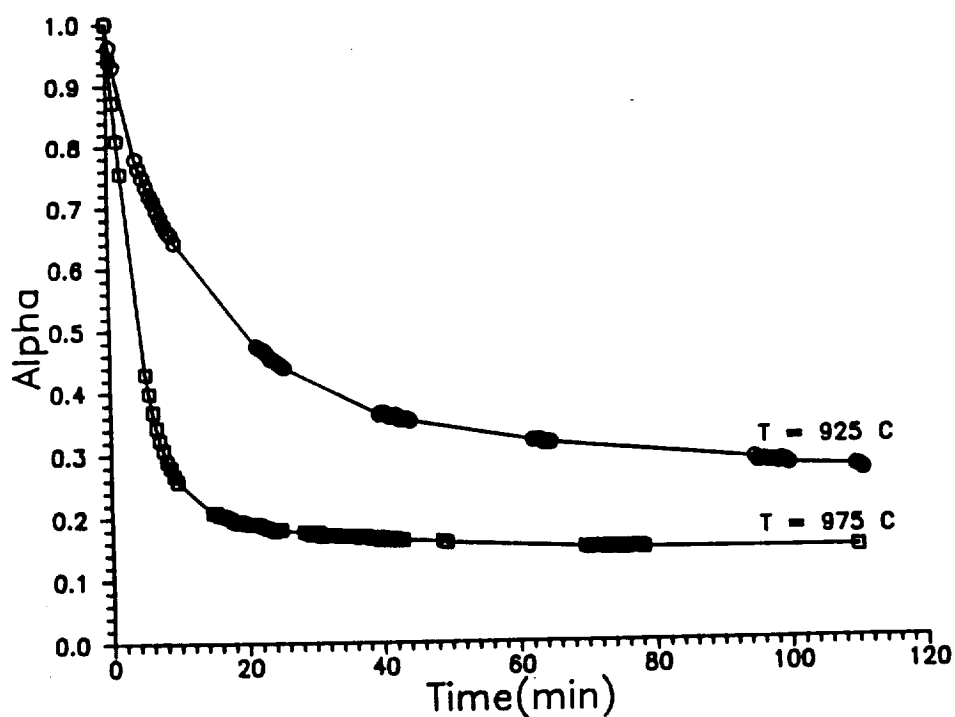
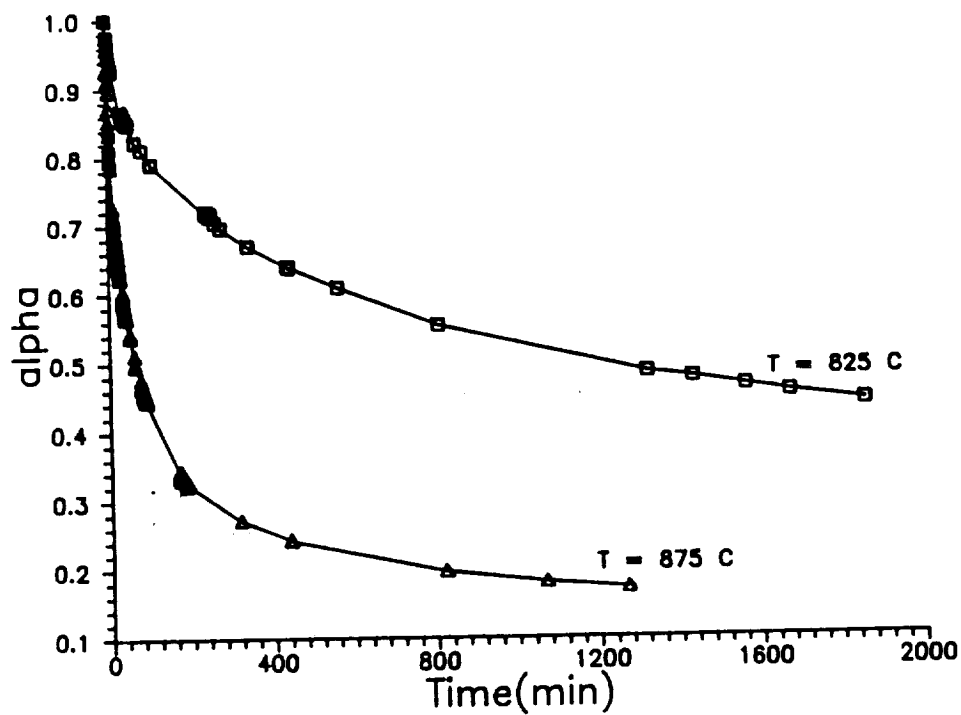


Fig. 5: Selected examples of the change in the weight of talc as function of time, as measured at discrete intervals. The balance was calibrated before each measurement, and the effect of thermal current was essentially eliminated by putting a baffle at the base of the balance (Fig. 1).



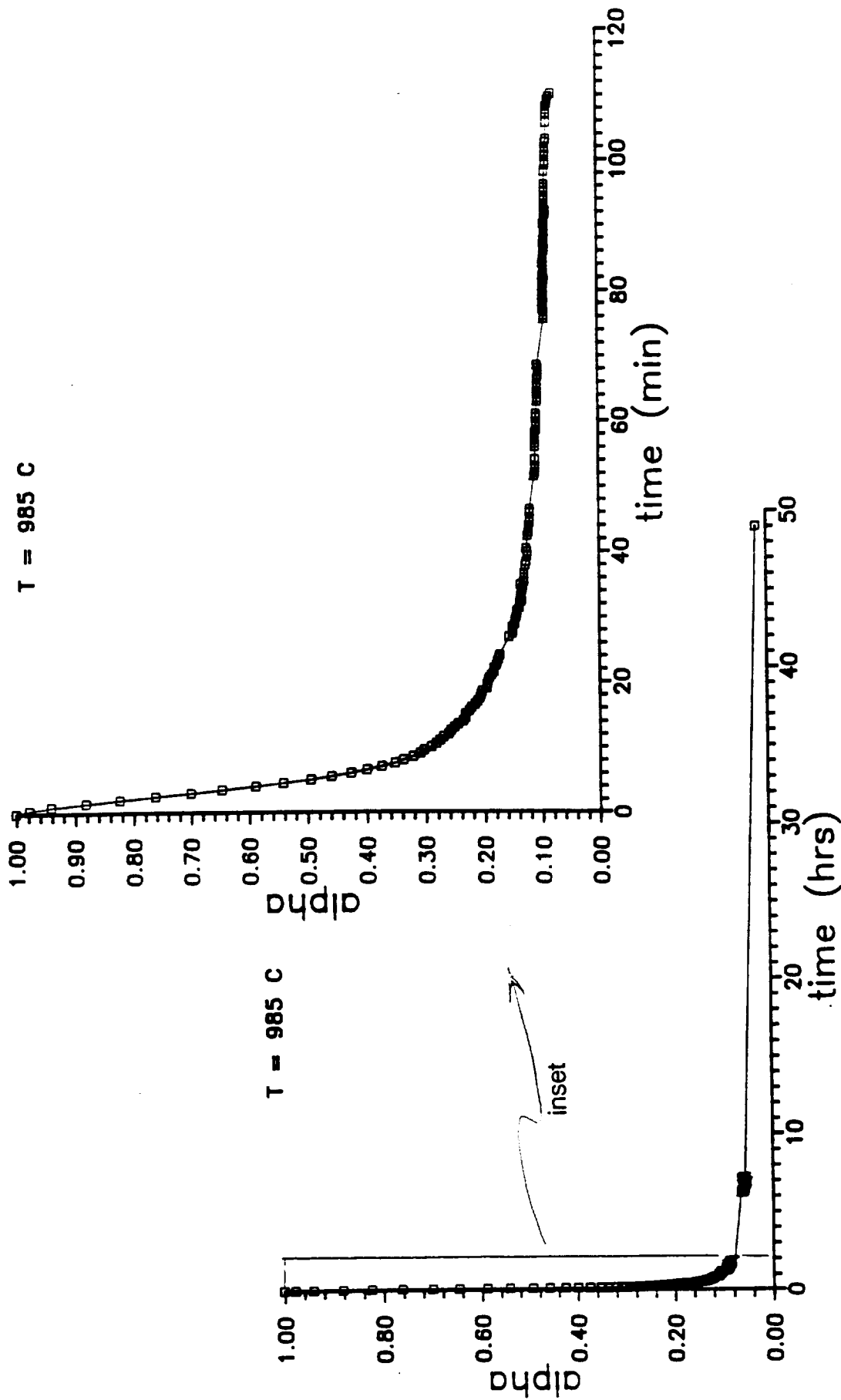


Fig. 6: A long run (49 hrs) at  $985^\circ\text{C}$  to determine the weight loss after complete dehydration (i.e.  $W_u$ ) of the natural talc used in the experimental studies. The weight of talc remaining at the end of the run is only 1.2% less than the theoretical limit, calculated from the chemical formula.

$$\ln(-\ln\alpha) = n\ln K + n(\ln t) \quad (3)$$

Fig. 7 shows a typical isothermal plot of  $\ln(-\ln\alpha)$  vs.  $\ln t$ . It is clear that eqn. (3) can describe the experimental data only up to 60 % dehydration. The change of slope typically takes place in the range of 50-60% dehydration.

If we restrict ourselves to dehydration up to the above linear range, then the dehydration rate can be described as function of temperature and time according to eqn. (2) with

$$K = 3.906(10^{21})\exp(-Q/(R^*T)) \text{ min}^{-1} \quad (4.1)$$

where the activation energy  $Q = 432 (\pm 20)$  kJ/ mol. The value of  $n$  remains essentially constant at  $\sim 0.54$  between 775 and 875°C, but increases almost linearly according to

$$n = -10.77 + 0.0122T(^{\circ}\text{C}) \quad (4.2)$$

The Arrhenian relation of the rate constant is illustrated in Fig. 8. The results are also compared with those of Ward (1975). The rate constants for the two sets of data agree within an order of magnitude at  $T \leq 875^{\circ}\text{C}$ , but there is strong disagreement at higher temperature. The results of Ward (1975) are suggestive of a change of dehydration mechanism around 875°C, which is in contrast to our results.

#### Effect of the Dilution of H<sub>2</sub>O in the Vapor Phase

Ganguly and Saxena (1990) have presented detailed simulations of equilibrium heating at fixed bulk composition of C1 and C2 chondrites, which show that in the environment of dehydrating talc in carbonaceous chondrites, the concentration of H<sub>2</sub>O in the vapor phase will be considerably diluted owing to the presence of other volatile species, primarily H<sub>2</sub>, CH<sub>4</sub>, CO<sub>2</sub> and CO. Consequently, there may be an enhancement of dehydration kinetics of talc due to the displacement of equilibrium dehydration to lower temperature as a result of dilution of H<sub>2</sub>O in the vapor phase. This type of effect is often called the 'thermodynamic effect' on reaction kinetics, which may be calculated as follows.

The net rate of dehydration reaction ( $R_{\text{net}}$ ) represents the difference between the rates of forward ( $R^*$ ) and backward ( $R^-$ ) reactions. It follows from transition state theory (e.g. Lasaga, 1981) that

$$R_{\text{net}} = R^*(1 - \exp(m\Delta G/RT)) \quad (5)$$

where  $m$  is constant and  $\Delta G$  is the Gibbs free energy change of the dehydration reaction at temperature  $T$ . Since  $R^* = K^*C_{\text{Talc}}$ , where  $K^*$  is the intrinsic forward rate constant and  $C_{\text{Talc}}$  is the concentration of talc, it is not affected by the change in the composition of the vapor phase. Consequently, one obtains

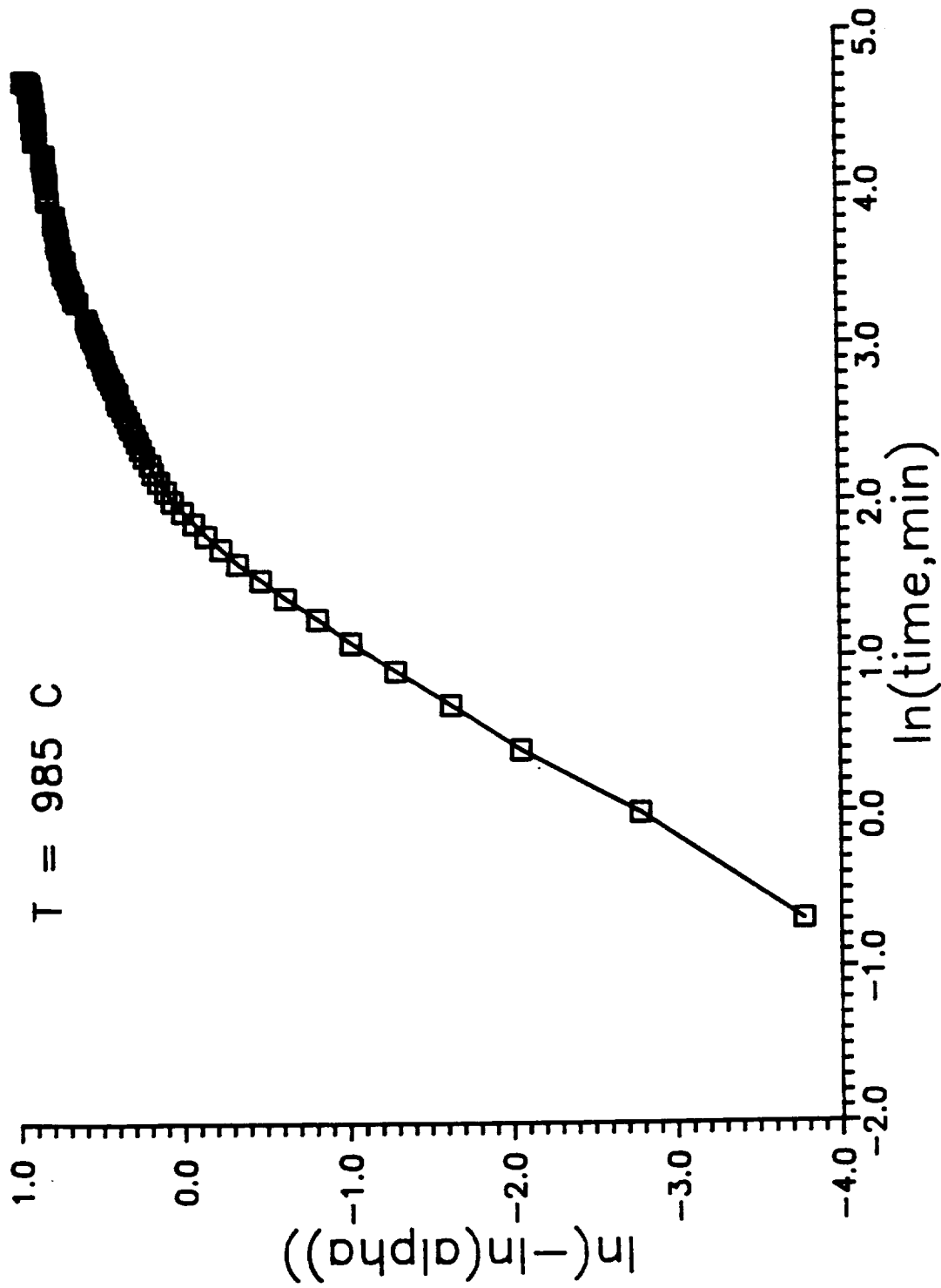
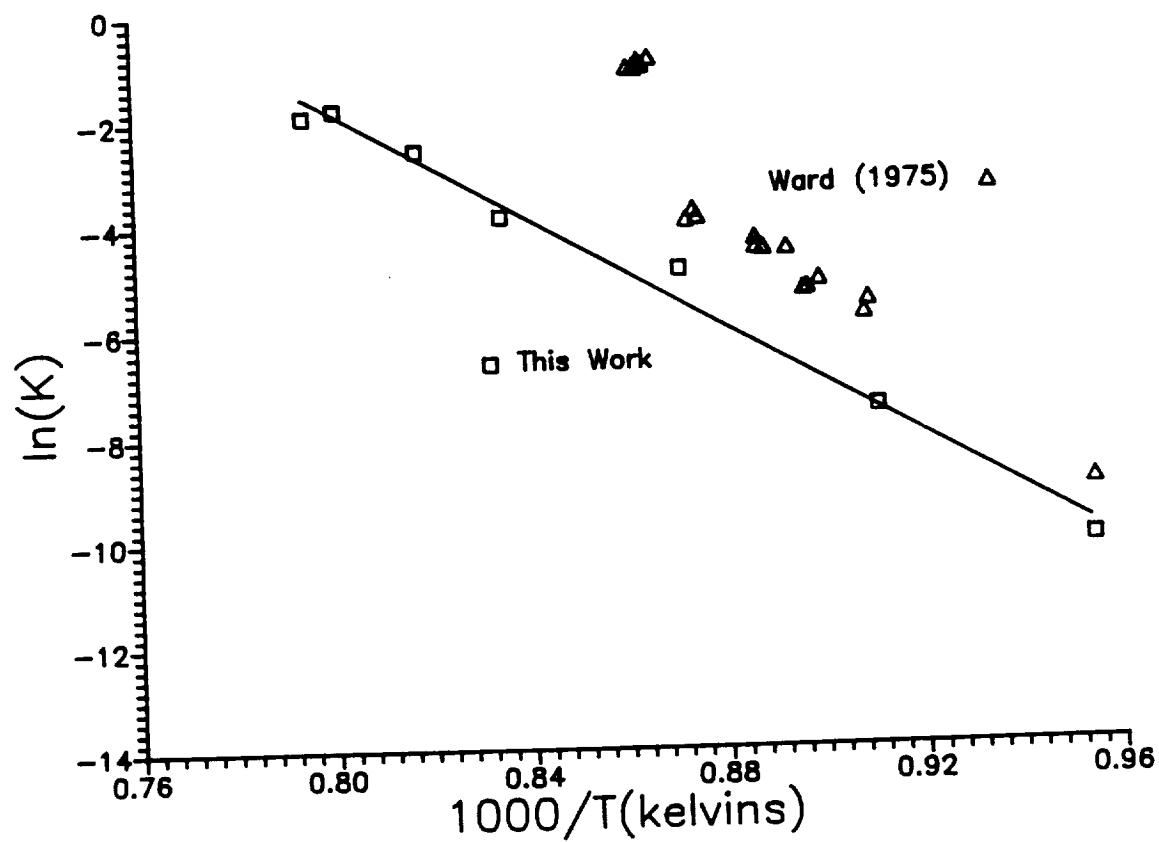


Fig. 7: Plot of isothermal dehydration data in terms of  $\ln(-\ln\alpha)$  vs  $\ln t$ . The relationship should be linear if the dehydration is controlled by nucleation and growth law of the form  $\alpha = \exp(-kt^n)$ , where  $n$  is a constant.



**Fig. 8:** Arrhenian relation of dehydration rate constant between 775 and 985°C at 1 bar. Squares represent the results of present study, whereas the triangles represent those of Ward (1975). In this work, the rate constant is obtained by fitting experimental data up to 50-60% dehydration (see text for discussion)

$$R_{net}(X) = \frac{1 - e^{m\Delta G(X)/RT}}{1 - e^{m\Delta G^*/RT}} \cdot R_{net}^* \quad (6.1)$$

$$-(A) \times R_{net}^* \quad (6.2)$$

where X stands for the mole fraction of H<sub>2</sub>O in the vapor phase, and the superscript \* denotes XH<sub>2</sub>O = 1.

Work is currently under progress to identify the reaction controlling the dehydration of talc in our experiments. It does not seem to be the simple breakdown of talc to enstatite (MgSiO<sub>3</sub>) plus quartz (SiO<sub>2</sub>), as suggested in the work of Ward (1975). However, if we assume that the free energy change of the dehydration reaction of talc is comparable to that of the reaction



then we can approximately evaluate the quantity A in eqn. (6), which determines the 'thermodynamic effect' on the dehydration kinetics. The results of our calculation show that at any temperature of practical interest at which  $\Delta G^* \ll 0$ , the value of A deviates very little from unity as a result of dilution of H<sub>2</sub>O in the vapor phase. Thus the thermodynamic effect on dehydration rate of talc is expected to be negligible for the practical purpose of volatile extraction. However, the additional volatile species may have a significant effect on the dehydration kinetics through a change of dehydration mechanism (e.g. Schramke et al., 1987). This problem can only be answered by careful experimental studies.

#### References

- Bailey, S. W. (1988) Introduction; Polytypism of 1:1 layer silicates. In S.W. Bailey (ed.) *Hydrous Phyllosilicates, Reviews in Mineralogy*, **19**, 1-27. Min. Soc. Amer..
- Evans, B. W. and Guggenheim, S. (1988) Talc Pyrophyllite and related minerals. In S.W. Bailey (ed.) *Hydrous Phyllosilicates, Reviews in Mineralogy*, **19**, 225-294. Min. Soc. Amer.
- Ganguly, J. and Saxena, S. K. (1989) Theoretical predictions of the volatile abundances and volatile bearing phases in carbonaceous chondrites. In *Space Manufacturing 7: Space Resources to Improve Life on Earth. Proceedings of the ninth Princeton/AIAA/SSI Conference, 1989*. American Institute of Aeronautics and Astronautics, Washington D. C..

- Lasaga A. C. (1981) Transition State Theory. In Kinetics of Geochemical Processes, Reviews in Mineralogy, **8**, 135-169. Min. Soc. Amer..
- Schramke, J. A., Kerrick, D. L. and Lasaga, A. (1987) The reaction muscovite + quartz = andalusite + K-feldspar + water. Part 1. Growth kinetics and mechanism. Amer. J. Sci., **287**, 517-559.
- Ward, J. R. (1975) Kinetics of talc dehydration. Thermochim. Acta, **13**, 7-14.

---

## **II. PRODUCTION OF STRUCTURAL AND REFRACTORY METALS**

5/4-26  
N91-24379<sup>74</sup>  
8.14

Recovery of Precious Metals From Space

Henry Freiser, Director

Strategic Metals Recovery Research Facility

Department of Chemistry

University of Arizona

AKG-1975

ABSTRACT

The overall objective of this project is to develop efficient and economical separation and recovery methods for the platinum group and other precious metals. The separation of Pd(II) from Pt(II), Ir(III) and Rh(III) with trioctylphosphine oxide (TOPO) in heptane using centrifugal partition chromatography (CPC) has been investigated for the first time. Activities to achieve this objective to date have focussed on selection and evaluation of extraction systems for the PGM and modification of selected systems for multistage operation with a view to scaling up to desired macro levels. On the basis of preliminary evaluation of a series of simple metal complexing agents and chelating agents, the trioctylphosphine oxide (TOPO) in heptane was selected as a likely system for isolating of Pd(II) and Pt(II) from the other PGM. A novel multistage apparatus capable of configuration as a simple rugged device, called centrifugal partition chromatograph (CPC) was shown to be effective. The extraction of Pd(II) has been studied by CPC and batch solvent extraction. The distribution ratios for Pd(II) determined by both methods agree well. In low HCl concentrations ( $<0.1$  M), the extracted species was



$\text{PdCl}_2 \cdot (\text{TOPO})_2$ , irrespective of the chloride concentration, while at acid concentrations above 0.1 M, the Pd was extracted as the ion pair,  $2(\text{TOPO} \cdot \text{H}^+) \cdot \text{PdCl}_4^{2-}$ . Base line separation of Pd(II) and Pt(II) in CPC was obtained under a variety of chloride and HCl concentration with the average number of theoretical plates being  $390 \pm 40$  at a flow rate of  $0.47 \pm 0.05$  mL/min. It was demonstrated that the efficiency of CPC for metal separation was limited by chemical kinetic factors rather than instrumental factors, strongly suggesting that dramatic improvements (up to 1300 theoretical plates, achieved with simple organic distribuends) can be achieved by studying reaction kinetics of formation and dissociation of the extractable metal complex.

### INTRODUCTION

The separation of platinum group metals, while widely investigated, continues to pose challenges (1,2). Ion pair extractions of the chloro anions are reasonably rapid but not so selective. Extraction as chelates are more selective but these have very slow formation/dissociation kinetics. The selectivity problem can be addressed by the use of multistage methods.

The separation of platinum group metals by multistage methods, namely, extraction chromatography has been previously attempted (3). This process in which, an organophosphorus reagent was loaded on a silica solid support, was tedious and difficult, and the efficiency of separation and resolution of the individual elements was not good. Further, the coated extractant leached from the solid support. In this laboratory, the approach has involved the use of multistage solvent extraction using the principle of countercurrent distribution as well as the use of derivatized supports which would avoid the problem of reagent leaching (4). Another possible approach is centrifugal partition chromatography (CPC). CPC is based on the principle of counter current distribution (5). Two immiscible phases, namely, an organic phase like heptane containing an extractant and an aqueous phase at the appropriate pH are used. One phase is held stationary in cartridges by the action of centrifugal force and the other phase is pumped through the stationary phase, achieving multistage solvent extraction. An analyte

mixture is injected into the CPC and the "chromatogram" of the separated components is obtained using a UV-VIS detector. The chromatogram can be analyzed by the usual equations (6). This technique has been widely applied for the separation of natural products (7). There have been a few attempts to separate metal ions, like lanthanides (8,9). These attempts generally had poor column efficiencies and incomplete resolutions of the analyte components. We have recently demonstrated a much improved analytical scale separation of adjacent lanthanides (10). Complete base line separation of adjacent lanthanides were achieved with a column efficiency of  $320 \pm 40$  plates while the best previous efficiency was about 50 plates (10). Described here are our results for the separation of Pd(II) from Pt(II), Ir(III) and Rh(III) by CPC using TOPO as the extractant, selected from examination of organophosphorus reagents which show promise for the extraction separation of platinum group metals (1,3).

### EXPERIMENTAL

#### Reagent

TOPO (>99% purity, Aldrich), was used as received. All other reagents were of analytical grade. Metal free heptane and water solutions were equilibrated overnight before being used in CPC experiments. Palladium, platinum, iridium and rhodium stock solutions of  $10^{-2}$  M were prepared by dissolving a weighed quantity of palladium(II) chloride (59.9% Pd, Alfa Products), sodium tetrachloro platinum(II) (44.3% Pt, Johnson Mathey, Inc.), sodium hexachloroiridium(III) (36.0% Ir, Alfa Product) and Rhodium(III) chloride trihydrate (39.0% Rh, Aldrich Chemical Company, Inc.) in  $10^{-2}$  M HCl solution. Deionized-distilled water was used throughout this study.

#### Apparatus & Procedure

CPC experiments were performed with a Sanki, Co., Japan assembly consisting of a model SPL centrifuge containing 6 analytical/semi-preparative cartridges each having 400 channels (2400 total channels), a model CPC FCU-V loop injector and a model LBP-V pump. CPC experiments were conducted with 0.1 M TOPO in heptane as the stationary phase and water at the appropriate pH and chloride (using NaCl) concentration as the mobile phase, pumped in the descending mode. Equilibration of the two phases at 800 rpm and 25 °C provided 22 mL of heptane and 110 mL of water. A UV-VIS spectrophotometric detector (model 770, Schoeffel Instrument Co.) with a 0.1 mL cell volume of 8 mm path length was used, which was set at 238 nm. Data was acquired every 20 seconds using a IBM/PC interfaced to the detector. One mL

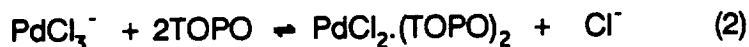
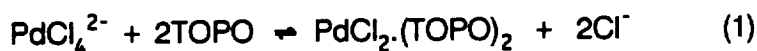
of a mixture of the metals was injected into the CPC for a single run. Flow rates between 0.5 and 2 mL/min. were used in these experiments.

Single stage solvent extractions were carried out by shaking equal volumes (10 mL) of heptane containing TOPO with an aqueous phase containing  $4 \times 10^{-4}$  M Pd in a glass vial with a box type Eberbach shaker. Determination of the distribution ratios (D) of Pd(II) as a function of time indicated that equilibrium was achieved within 5 minutes or less, depending on the chloride and TOPO concentrations. The heptane-aqueous mixtures were equilibrated for one hour to ensure complete equilibrium. The aqueous Pd concentration was determined using an ICP-AES (model 6500, Perkin-Elmer Co., USA) at its most sensitive wavelength, 340.458 nm (detection limit = 1.2 ppm). Standard solutions of Pd (10, 20, 30, and 40 ppm) were prepared daily for calibration in the same matrix as sample to eliminate all matrix effects. All pH measurements were made with an Accumet pH meter (model 925) which was calibrated daily with standard buffer solutions.

## RESULTS AND DISCUSSION

### Extraction Equilibria of Pd(II) Species by Solvent Extraction and CPC

The chloro-palladium species extracted is a function of chloride concentration (Figure 1) (11). The extraction equilibria of Pd(II) species were characterized by both solvent extraction and CPC as a function of chloride and TOPO concentrations. The extraction equilibria were inferred from the dependence of  $\log D_{Pd}$  on  $\log [Cl^-]$  and  $\log [TOPO]$ , namely from the slopes of these plots (12). These equilibria are:



The extraction equilibrium constants for each Pd species can be calculated by using the equilibrium expressions:

$$\log K_{ex,4} = \log D_{Pd} + 2\log [Cl^-] - 2\log [TOPO] - \log \alpha_4 \quad (4)$$

$$\log K_{ex,3} = \log D_{Pd} + \log [Cl^-] - 2\log [TOPO] - \log \alpha_3 \quad (5)$$

$$\log K_{ex,2} = \log D_{Pd} - 2\log [TOPO] - \log \alpha_2 \quad (6)$$

where  $\alpha_4$ ,  $\alpha_3$ , and  $\alpha_2$  are the fraction of each Pd species,  $PdCl_4^{2-}$ ,  $PdCl_3^-$ , and  $PdCl_2$ , respectively

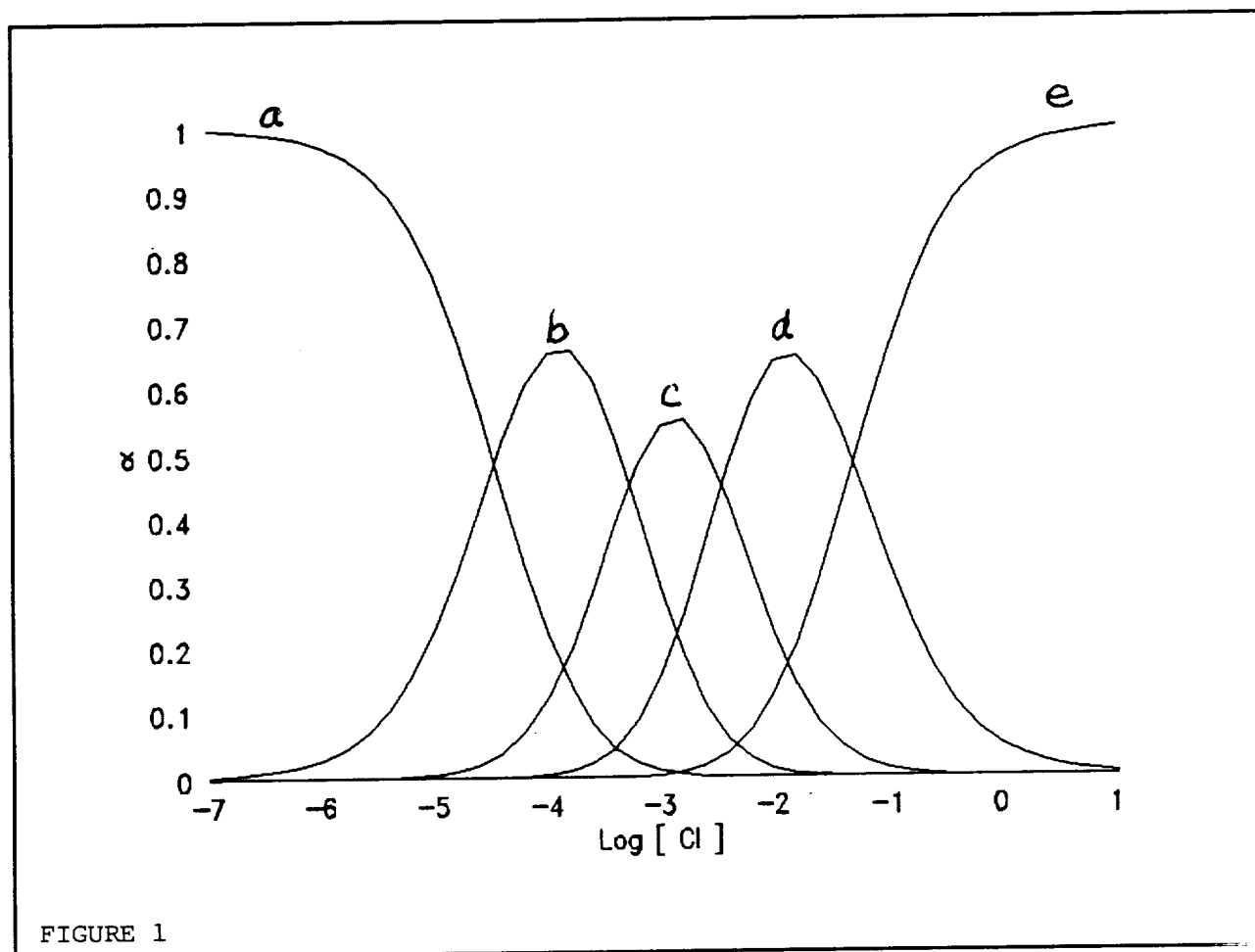
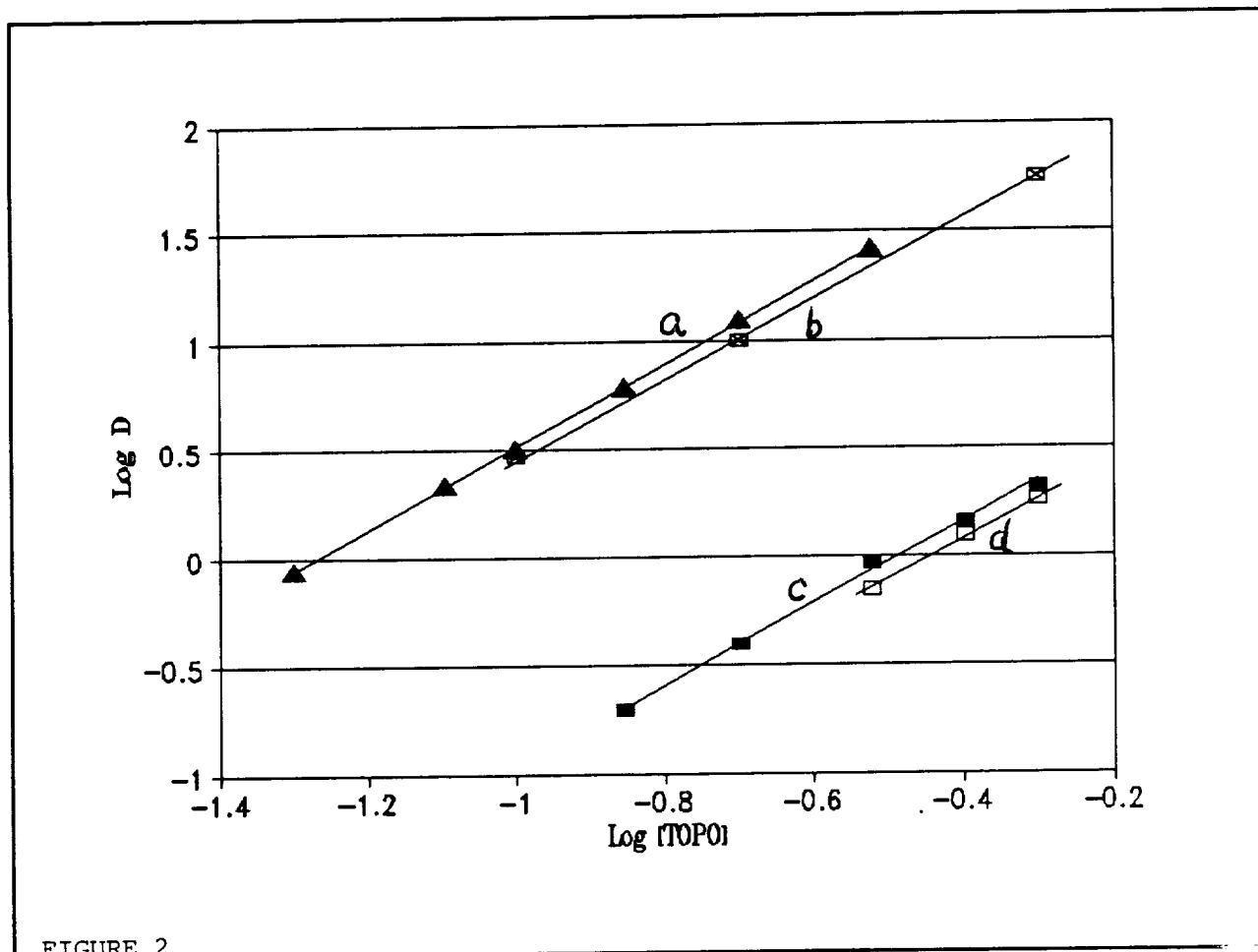


FIGURE 1

in aqueous phase as shown in Figure 1.

Plots of  $\log D_{Pd}$  VS  $\log [TOPO]$  at  $10^{-3}$  M and 0.1 M  $[Cl^-]$  yielded a slopes of 1.89 and 1.88, respectively (Figure 2). This indicates that each Pd species is bound to 2 TOPO. A similar plot of  $\log D_{Pd} - \log \alpha_n$  of each Pd species as a function of  $\log [Cl^-]$  yielded slopes of -1.97, -0.97, and 0.003 were obtained for  $PdCl_4^{2-}$ ,  $PdCl_3^-$ , and  $PdCl_2$  species respectively. These indicate the number of chloride ions released from  $PdCl_4^{2-}$ ,  $PdCl_3^-$ , and  $PdCl_2$  species to be 2, 1, and 0 respectively (equations 1-3).

The extraction constants,  $K_{ex.4}$ ,  $K_{ex.3}$  and  $K_{ex.2}$ , can be calculated from equation 4, 5 and 6 to be 0.14,  $2.75 \text{ M}^{-1}$ , and  $794.3 \text{ M}^{-2}$  respectively (Table 1). This  $K_{ex.2}$  value is smaller by about



5 orders of magnitude compared to the  $K_{\text{ex.2}}$  value for the extraction of  $\text{PdCl}_2$  by  $\text{R}_2\text{S}$  (2), as expected for a harder ligand.

TABLE 1. Equilibrium Data for Extraction of Palladium by TOPO.

A. Dependence on [TOPO].

$\text{Pd(II)} = 4 \times 10^{-4}$ ,  $[\text{Cl}^-] = 0.1$ ,  $\text{pH} = 3$

[TOPO], M	Log D	Log $K_{\text{ex.2}}$ ( $\alpha_2 = 0.011$ )	Log $K_{\text{ex.3}}$ ( $\alpha_3 = 0.330$ )	Log $K_{\text{ex.4}}$ ( $\alpha_4 = 0.658$ )
0.50	0.32	2.86	0.40	-0.8
0.40	0.16	2.89	0.43	-0.86
0.30	-0.03	2.95	0.49	-0.80
0.20	-0.39	2.94	0.47	-0.82

0.14      -0.71      2.93      0.48      -0.81

TABLE 1. Equilibrium Data for Extraction of Palladium by TOPO. B.

Dependence on [Cl<sup>-</sup>]

Pd(II) =  $4 \times 10^{-4}$  M, [TOPO] = 0.5 M, pH = 3

[Cl <sup>-</sup> ], M	Log D	Log K <sub>ex.2</sub>	Log K <sub>ex.3</sub>	Log K <sub>ex.4</sub>
0.10	0.32	2.86	0.40	-0.89
0.14	0.08	2.87	0.41	-0.88
0.20	-0.19	2.87	0.41	-0.88
0.30	-0.52	2.86	0.40	-0.89
0.40	-0.72	2.89	0.43	-0.86
0.50	-0.92	2.88	0.42	-0.87

The comparison of distribution ratios (D) determined by single stage batch solvent extraction and by CPC are also shown in Figure 2. The data from two methods are well in agreement within experimental error. The D values from CPC experiments were obtained by the following equation:

$$V_r = V_m + DV_s \quad (7)$$

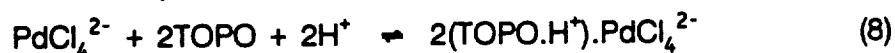
where  $V_r$  = retention volume of sample

$V_m$  = mobile phase volume or dead volume

$V_s$  = stationary phase volume

#### Extraction at High Acid Concentration

We have found that TOPO can be protonated at higher HCl concentration, and the protonated TOPO can extract  $\text{PdCl}_4^{2-}$ . These experiment were carried out at 1 M HCl where the  $\text{PdCl}_4^{2-}$  is the predominant species (99.50%). The dependence of log  $D_{\text{Pd}}$  on log [TOPO] and log  $[\text{H}^+]$  yielded the slopes of 2.01 and 1.95 respectively  $D_{\text{Pd}}$  was also independent of chloride concentration, leading to the overall equilibrium in equation 8.



The equilibrium constant,  $K'_{\text{ex.4}}$ , can be calculated from the following equation:

$$\text{Log } K'_{\text{ex.4}} = \text{Log } D_{\text{Pd}} - 2\text{Log}[\text{TOPO}] - 2\text{Log}[\text{H}^+] - \text{Log } \alpha_4 \quad (9)$$

where  $\alpha_4$  is very close to unity as evident from Figure 1.

The determination of the equilibrium constant,  $K'_{\text{ex.4}}$ , by varying the concentration of either TOPO or acid is  $93.3 \text{ M}^{-4}$ . This  $K'_{\text{ex.4}}$  value is smaller than  $K_{\text{ex.2}}$  ( $794.3 \text{ M}^{-2}$ ) but larger than  $K_{\text{ex.4}}$  (0.14), the equilibrium constants for the extraction of  $\text{PdCl}_2$  and  $\text{PdCl}_4^{2-}$  by protonated TOPO. This indicates that  $\text{PdCl}_4^{2-}$  is more efficiently extracted by protonated TOPO than by neutral TOPO.

#### Separation of Pd from Pt, Ir and Rh using CPC

CPC experiments were conducted at  $\text{pH} = 3$  and  $10^{-3} \text{ M } [\text{Cl}^-]$ . Experiments were not carried out at lower pH to avoid corrosion or damage to the instrument. The distribution ratio of Pt is very small under these conditions. The Pt peak in the chromatogram always appeared at a position close to the chloride peak (dead volume peak). The degree of separation of two peaks is defined as resolution,  $R_s$ , determined by the following expression:

$$R_s = 2d / (W_A + W_B) \quad (10)$$

where  $d$  is the distance between the peak maxima and  $W$  is width of each peak. The larger the resolution, the better the separation. The separation of Pd from Pt in Figure 4 shows base line separation of Pt and Pd with a resolution of 1.54 or  $< 0.3\%$  peak overlap. The retention volumes ( $R$ ) of Pt and Pd are 110 mL and 135 mL respectively. The equation for countercurrent distribution together with the  $D$  values of Pt and Pd from the experiment in Figure 4 ( $D_{\text{Pt}}=0.11$ ,  $D_{\text{Pd}}=1.4$  and  $N=360$ ) can be used to simulate the chromatogram.

The fraction,  $F_o$ , of a given analyte with a distribution ratio,  $D$ , in the organic phase where the ratio of the volume of the organic phase to the volume of the aqueous phase is  $R_v$  is given by the following equation:

$$F_o = DR_v / (DR_v + 1) \quad (11)$$

In a countercurrent distribution involving  $N$  stages,

$$(F_o + F_w)^N = 1 \quad (12)$$

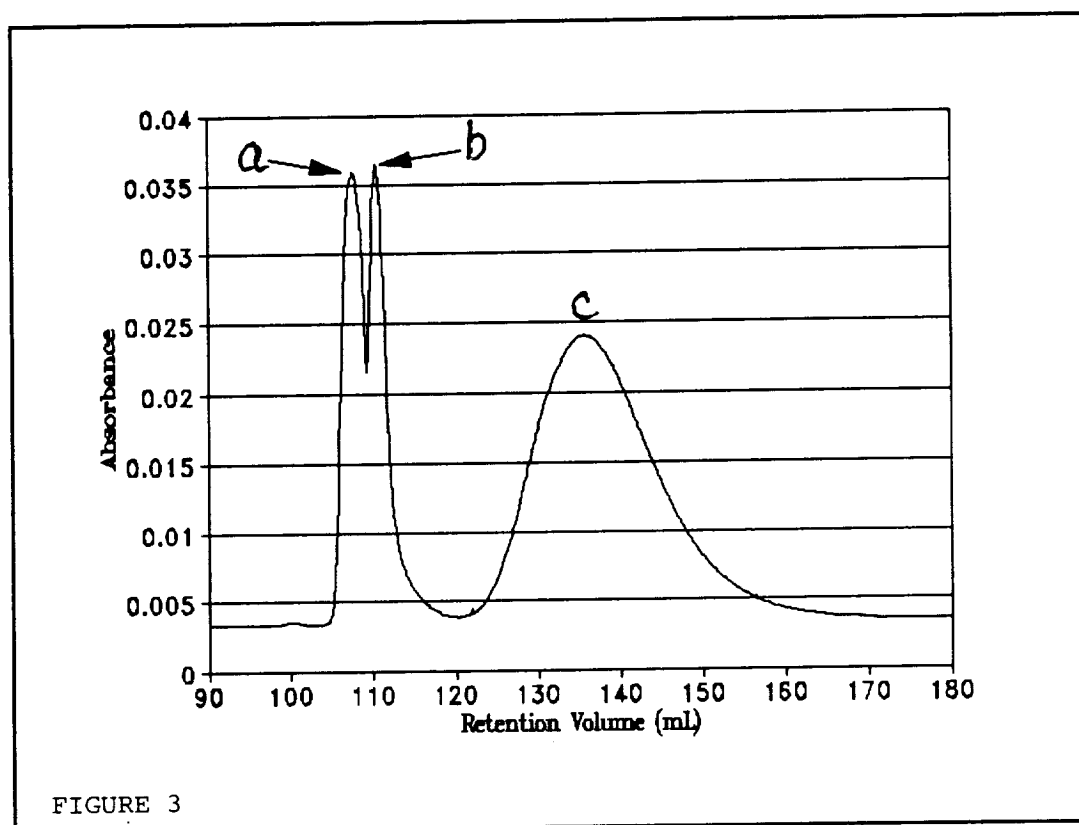


FIGURE 3

where  $F_w$  is the fraction of the analyte, and  $C_m$ , its concentration in the aqueous phase. The concentration of the analyte in the  $m^{\text{th}}$  stage of the separation is given by

$$C_m = [N!/m!(N-m)!] F_o^{N-m} F_w^m. \quad (13)$$

The computer-simulated chromatogram shows the R values of both Pt and Pd corresponding to the experiment, 111 mL and 134 mL respectively (Figure 5). Figure 6 shows the base line separation of Pd from the other platinum group metals (Pt, Ir, and Rh). It may be seen that partial resolution of Pt(II) from Ir(III) and Rh(III) was obtained under these conditions. However, complete separation of the four platinum group metals was not possible using TOPO.

The efficiency of CPC is determined by the number of theoretical plates (N) and can also be expressed as a number of channels per plate by dividing the total number of channels (2400) by N. The N of the column is calculated by the ratio of the elution volume,  $V_r$ , and the band width, W, as in equation 14.



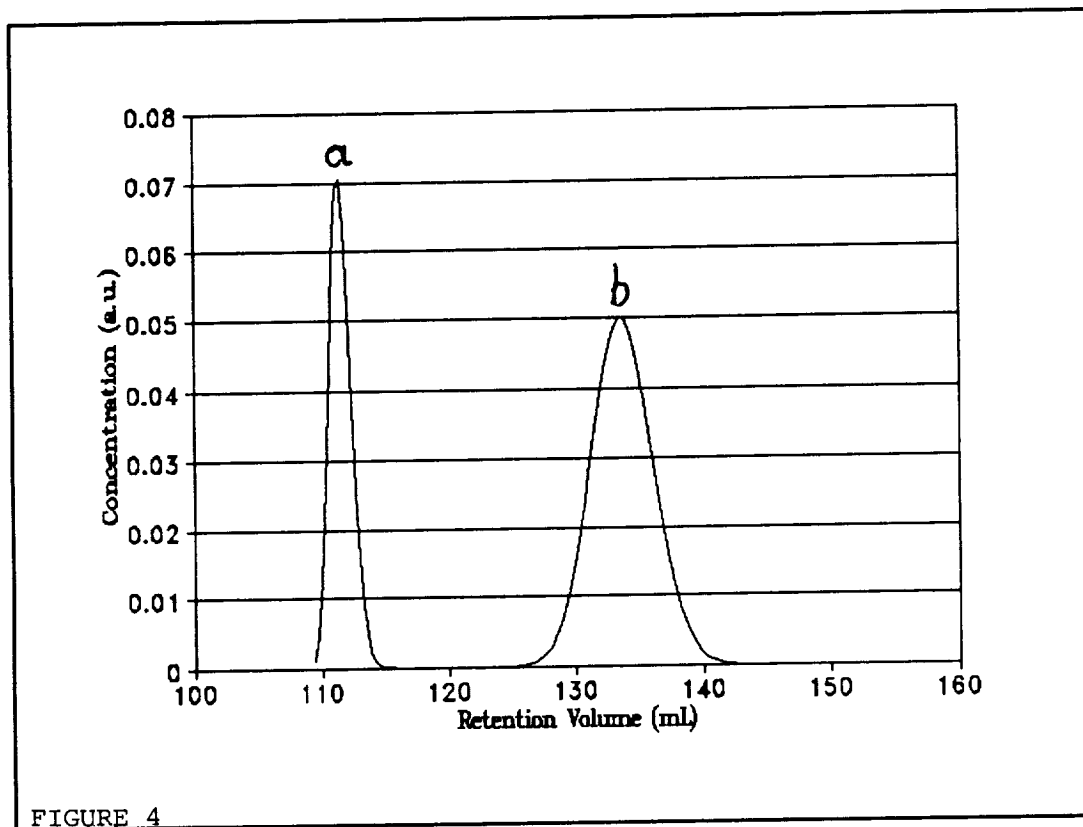


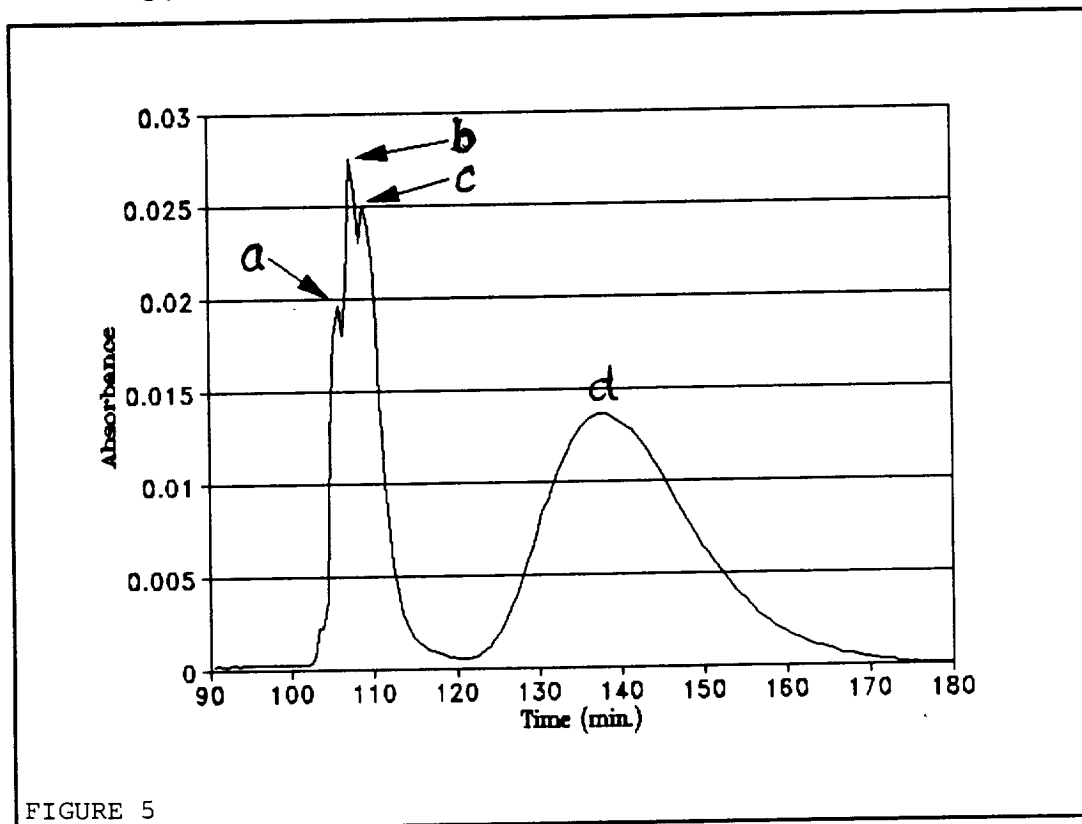
FIGURE 4

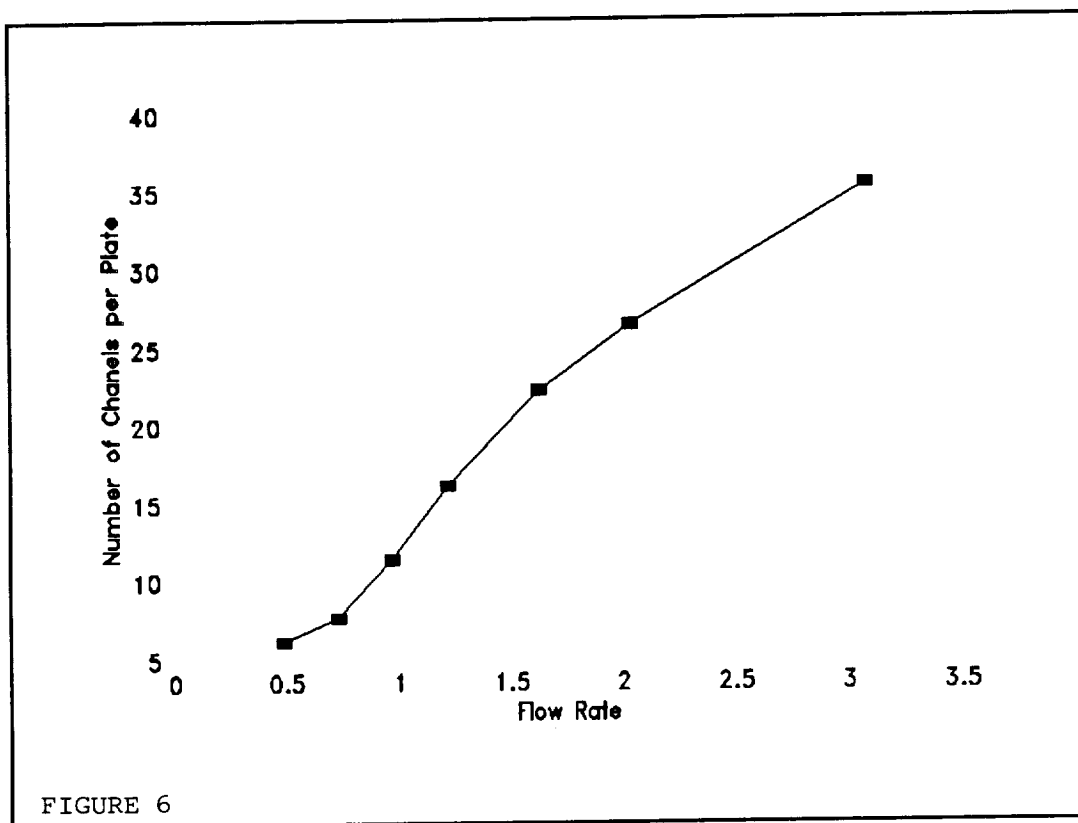
$$N = 16(V_r/W)^2 \quad (14)$$

#### Effect of Flow Rate on Column Efficiency

The column efficiency decreased as the flow rate was increased from 0.5 mL/min. to 3 mL/min. The number of channels/theoretical plate increased with flow rate as shown in Figure 7. This Van Deemter type plot is similar to those observed in HPLC experiments and opposite to that observed for the separation of organic compounds by CPC using two immiscible organic solvents (6). The same behavior was observed for the CPC separation of lanthanides by cyanex 272 (10). The maximum column efficiency in the separation of Pd(II) from Pt(II) was  $390 \pm 40$  at 0.47 mL/min, which is about the same as that observed in lanthanide separation (10). The factors affecting CPC column efficiency in separation of simple organic distribuends are much more similar to those encountered in traditional liquid chromatography. For example,  $\gamma$ -picoline with retention characteristics similar to Pd(II) indicated CPC efficiency of 1220 theoretical plates. Obviously, chemical kinetic factors in extractable complex

formation and/or dissociation limit the observed number of theoretical plates. This strongly suggests the value of a study of kinetics which is now in progress.





### CONCLUSIONS

We have shown that Pd(II) can be completely separated from Pt(II), Ir(III) and Rh(III) using CPC under a variety of conditions using TOPO. We have been able to partially separate Pt(II) from Ir(III) and Rh(III). This illustrates the usefulness of the multistage solvent extraction technique, CPC. The nature of the species extracted and the extraction equilibrium constants for Pd(II) extraction by TOPO have been determined under a variety of condition using batch solvent extraction experiment and CPC. The results from batch solvent extraction an CPC agree well and indicate that  $\text{PdCl}_2$  has the best extractibility among the various Pd(II)-chloro complexes.

### REFERENCES

1. K. Saito and H. Freiser, *Anal. Sci.* **5**, 538 (1989).
2. S.J. Al-bazi and H. Freiser, *Solv. Extr. Ion Exch.* **5**, 265 (1987).
3. I. Akaza, and T. Kiba, *Bull. Chem. Soc. Japan* **43**, 2063 (1970).
4. H. Freiser, unpublished observations.
5. D.W. Armstrong, *J. Liquid Chromatogr.* **11**, 2433 (1988).
6. A. Berthod and D.W. Armstrong, *J. Liquid Chromatogr.* **11**, 567 (1988).
7. K. Hostettmann, M. Hostettmann and A. Marston, Preparative Chromatographic Techniques: Applications in Natural Product Isolation, Springer Verlag, Berlin, 1986.
8. T. Araki, T. Okazawa, Y. Kubo, H. Ando and Asai, *J. Liquid Chromatogr.* **11**, 267 (1988).
9. K. Akiba, S. Swai, S. Nakamura and W. Murayama, *J. Liquid Chromatogr.* **11**, 2517 (1988).
10. S. Muralidharan, R. Cai and H. Freiser, *J. Liquid chromatogr.* (in press).
11. R.M. Smith and A.E. Martell, Critical Stability Constants, Vol., 4, Inorganic Complexes, Plenum Press, New York (1976).
12. G. Morrison and H. Freiser, Solvent Extraction in Analytical Chemistry, John Wiley, New York (1957).

FIGURE CAPTIONS

- FIGURE 1. The Pd(II)-chloro species as a function of chloride concentration, a) Pd, b)  $\text{PdCl}^+$ , c)  $\text{PdCl}_2$ , d)  $\text{PdCl}_3^-$  and e)  $\text{PdCl}_4^{2-}$ .
- FIGURE 2. Dependence of log D as a function of log [TOPO] at a)  $10^{-3}$  M  $[\text{Cl}^-]$  from solvent extraction, b)  $10^{-3}$  M  $[\text{Cl}^-]$  from CPC, c) 0.1 M  $[\text{Cl}^-]$  from solvent extraction and d) 0.1 M  $[\text{Cl}^-]$  from CPC.
- FIGURE 3. Chromatogram of the separation of Pd(II) from Pt(II) at 0.1 M  $[\text{Cl}^-]$ , 0.5 M [TOPO], pH = 3 and flow rate = 0.54 mL/min., a) chloride peak corresponding to dead volume, b)  $10^{-3}$  M Pt and c)  $4 \times 10^{-3}$  M Pd.
- FIGURE 4. The computer simulated chromatogram of the separation of Pd(II) and Pt(II) at  $N = 360$ ,  $D_{\text{Pt}} = 0.11$  and  $D_{\text{Pd}} = 1.4$ .
- FIGURE 5. The chromatogram of the separation of Pd(II) from Pt(II), Ir(III) and Rh(III) at 0.1 M  $[\text{Cl}^-]$ , 0.5 M [TOPO], pH = 3, and flow rate = 0.63 mL/min., a) chloride peak corresponding to the dead volume, b)  $5 \times 10^{-4}$  M Ir(III) and Rh(III), c)  $10^{-3}$  M Pt(II) and d)  $4 \times 10^{-3}$  M Pd.
- FIGURE 6. The efficiency of CPC as a function of flow rate for Pd(II)-TOPO system at 0.1 M [TOPO],  $10^{-2}$  M  $[\text{Cl}^-]$  and pH = 2.

N 9 1 - 2 4 3 8 0

14675

p. 8

A 7 2

Processing of Glass-Ceramics from Lunar Resources

B. D. Fabes and W. H. Poisl

Department of Materials Science and Engineering

The University of Arizona

ABSTRACT

The goal of this project is to fabricate useful ceramic materials from the by-products of lunar oxygen production processes. Specifically, we are studying the crystal nucleation and growth kinetics of ilmenite-extracted lunar regolith, in order to produce glass-ceramics with optimal mechanical, thermal, and abrasion resistant properties. In the initial year of the program, we finished constructing and calibrating a high temperature viscometer, used for determining the viscosity of simulated lunar glasses. A series of lunar simulants were also prepared, and the viscosity of each was determined over a range of temperatures. We found that an increase in the concentration of  $\text{Fe}_2\text{O}_3$  decreases the viscosity of the glass. While this may be helpful in processing the glass,  $\text{Fe}_2\text{O}_3$  concentrations greater than approximately 10 wt % resulted in uncontrolled crystallization during viscosity measurements. Impurities (such as  $\text{Na}_2\text{O}$ ,  $\text{MnO}$ , and  $\text{K}_2\text{O}$ ) in the regolith appeared to decrease the viscosity of the parent glass. These effects, as well as those of  $\text{TiO}_2$  and  $\text{SiO}_2$  on the processability of the glass, however, remain to be quantified.

I. INTRODUCTION

Many processes proposed for obtaining oxygen from the lunar regolith are based on reducing ilmenite. Ilmenite, however, is present in the regolith at a concentration of only about 10 wt %. In order for any oxygen production scheme to be efficient, the ilmenite must be concentrated before it is reduced. This will produce a large amount of ilmenite-extracted regolith, which has many potential uses. We are examining the production of ceramic materials from these by-products.

In general, two approaches can be taken to examining the usefulness of ilmenite-extracted regolith. One might process the regolith using a multitude of heating and cooling schedules, and then test the properties of the resulting material. Or, one might study the effect of composition and heating on the development of microstructure in the ceramic material and, based on this knowledge, engineer materials with specific microstructures and, hence, properties, to meet specific needs. We are taking the latter approach, as a generic route to producing glass-ceramics from the by-products.

Glass-ceramics are polycrystalline materials produced by the carefully controlled crystallization of a glass. In the production of a glass-ceramic, a melt is cooled rapidly to avoid

crystallization, resulting in a homogeneous glass. The glass is heated to nucleate small crystallites, which are then grown at a slightly higher temperature. After crystallization, a typical glass-ceramic contains from 1 to 10 vol % residual glass.

The properties of a glass-ceramic depend strongly on controlling the size, shape, composition, and distribution of the crystal and glass phases. When properly controlled, extremely strong, abrasion resistant, highly refractory materials can be produced. In addition to these desirable properties, glass-ceramics are based on standard glass forming processes, which lend themselves to easy formation of complex shapes and components.

The nucleation and growth rates of the crystallites in glass-ceramics are extremely sensitive to the viscosity of the glass, which depends on both temperature and composition. Therefore, in order to control the crystallization process of the glass, the effect of composition on viscosity must be understood. In the first phase of our research, we are investigating the effects of composition on the viscosity of lunar glasses. This will allow us to determine ranges of compositions which are robust with respect to variations of feedstock on the final microstructure and, hence, properties of the glass-ceramic. In the second phase of this research we will examine the microstructure and properties of glass-ceramics produced using simulated lunar glasses. Finally, we will combine our understanding of the effects of composition on the development of microstructure with our understanding of the effects of microstructure on properties to prepare glass-ceramics with tailored mechanical, thermal, and abrasion resistant properties.

During the past year we began the first phase of this research. We finished constructing and calibrating an apparatus for determining high temperature viscosity of small glass samples. A series of lunar regolith simulants was prepared, and the viscosities of the different simulants were measured using this instrument. The effects of  $\text{Fe}_2\text{O}_3$ ,  $\text{TiO}_2$ , and minor impurities on the viscosity were investigated.

## II. VISCOMETER

A schematic drawing of the viscometer is shown in Figure 1. Viscosity is measured using a three point bending scheme. First, samples measuring approximately  $2.6 \times 0.5 \times 0.4$  cm are cut from prepared glass blocks. The samples are then placed in a fused silica holder and introduced into a furnace assembly which is preheated to the temperature of interest. An LVDT measures the deflection rate at the midpoint of the sample. A typical deflection versus time curve is shown in Figure 2. Assuming that the glass behaves as a newtonian fluid, the deflection should be a linear function of time, as demonstrated in Figure 2. The viscosity is then calculated from the slope of this line. This process is then repeated at each temperature of interest for each sample, so that the change in viscosity with temperature can be determined.

### III. VISCOSITY OF LUNAR GLASSES

Glass blocks were prepared by melting both reagent grade oxides and terrestrial simulants in air at temperatures between 1500 and 1600 °C. The melts were cast into a 6 cm diameter water-cooled copper mold to form glass blocks. The thickness of the glass blocks ranged from 2 to 4 cm, depending primarily on the quantity of glass melted. (Crystallization was never observed during this process.) The compositions investigated are shown in Table 1. Samples A12 and A17, prepared from reagent grade oxides, approximate the average compositions of the lunar regolith at the Apollo 12 and 17 sites, respectively, with all the ilmenite extracted, and without any minor impurities. Samples B12 and B17 were similar to the A12 and A17 compositions, except that the concentration of  $\text{Fe}_2\text{O}_3$  was reduced even further. For all of these reagent grade samples, approximately 5 wt %  $\text{TiO}_2$  was added, since rutile is used as a nucleating agent during the glass-ceramic process. The MLS-2 and MLS-3 samples were prepared from Minnesota Lunar Simulant.\* MLS-3 contained ilmenite, while MLS-2 had the ilmenite electrostatically separated.

The variation of viscosity with temperature for each composition is shown in Figure 3. From Figure 3 it can be seen that the viscosity decreases as the iron content increases (samples B17, B12 and A17). This result is not surprising, since iron is an effective fluxing agent for silicate glasses. For processing of glass-ceramics, a reduction in viscosity will decrease the maximum temperature required for effective working of the glass, as well as increase the working range of the glass.

Comparing the viscosities and compositions of MLS-2 and A17 (ilmenite-extracted terrestrial and ilmenite-extracted oxide simulants) we see that MLS-2 has a lower viscosity at all temperatures than A17. They both have similar iron contents, but the  $\text{SiO}_2$  content is somewhat higher in MLS-2. The addition of  $\text{SiO}_2$  (a glass former) should increase the viscosity of the glass, but this is not seen. Hence, the differences between these compositions must be due either to the smaller concentration of  $\text{TiO}_2$  content or to the impurities in the MLS-2 sample. Most of the impurities are glass modifiers, and should decrease the viscosity of the glass. The role of  $\text{TiO}_2$  has not yet been determined, but may also account for the difference in the viscosity between the samples. It is known that  $\text{TiO}_2$  can enter a glass as either a network former or modifier. Hence, this is an area which must be explored further.

From the above results we would expect that the MLS-3 and A12 samples (those with high concentrations of  $\text{Fe}_2\text{O}_3$ ) would have a low viscosity due to the  $\text{Fe}_2\text{O}_3$ . However, they appear to have higher viscosities than any other samples. This is probably due to crystallization of

---

\* P.W. Weiblen and K.L. Gordon, "Characteristics of a Simulant For Lunar Surface Materials," in Lunar Bases and Space Activities in the 21st Century, LPI, Houston TX, 1988.



the samples during the measurements. This was suggested by a nonlinear deflection rate during viscosity measurements (the viscosity which is reported here was obtained from the initial deflection rate at each temperature) and by observation of crystalline-like striae in the samples after removal from the furnace. In fact,  $\text{Fe}_2\text{O}_3$  has been reported to be an effective nucleating agent for silicate glasses at high concentrations\*.

It is interesting that the apparent activation energies for deformation, as given by the slope of the  $\log(\eta)$  vs.  $1/T$  curves in Figure 3, are different for the two samples which appeared to crystallize. We do not understand the implications of this difference, although it is a clear indication of the pivotal role that iron oxides will play in forming glass-ceramics. Finally, we must keep in mind that the effect of ferrous vs. ferric iron has not yet been examined. The oxidation state of the iron has been shown to effect the viscosity of anorthitic glass-ceramics<sup>§</sup> and therefore is likely to have an effect on the processing of lunar glass-ceramics.

#### IV. CONCLUSIONS

For  $\text{Fe}_2\text{O}_3$  concentrations less than 10 wt %, increasing concentrations of iron result in a decrease in the viscosity of lunar glasses. Microstructural effects aside, this decrease in viscosity should improve the processability of glass-ceramics. However, in order to control the crystallization process, the concentration of iron must be kept below approximately 10 wt %, since crystallization occurs readily above this concentration. Increasing concentration of  $\text{TiO}_2$  appears to increase the viscosity at any given temperature, although this effect may also be due to the minor impurities in the regolith.

#### V. FUTURE WORK

To complete this first phase of the research, the effect of  $\text{TiO}_2$ ,  $\text{SiO}_2$ , and minor impurities on viscosity must be quantified, and the upper limit of iron content needs to be more firmly established. In addition, the ratio of ferric to ferrous iron, which has been shown to effect viscosity, must be considered and controlled. Based on these results the second phase of this research – studying the kinetics of crystallization and microstructural development and the effects of microstructure on mechanical properties – can begin.

---

\* M. Cukiermann et al, "Viscous Flow and Crystallization Behavior of Selected Lunar Compositions," in Proceedings of the Fourth Lunar Science Conference, (1973) pp. 2685-2696.

§J. Williamson, A.J. Tipple, and P.S. Rogers, "Influence of Iron Oxides on Kinetics of Crystal Growth in  $\text{CaO-MgO-Al}_2\text{O}_3\text{-SiO}_2$  Glasses," *Journal of the Iron and Steel Institute*, (1968) 898-903.

Table 1: Chemical Compositions of Melts (wt %)

	A12	A17	B12	B17	MLS2 <sup>§</sup>	MLS3 <sup>§</sup>
SiO <sub>2</sub>	46.7	46.8	50.2	49.4	54.0	43.9
Al <sub>2</sub> O <sub>3</sub>	13.6	14.65	14.6	15.45	14.6	13.7
Fe <sub>2</sub> O <sub>3</sub> <sup>*</sup>	14.4	9.9	8.0	5.0	9.3	16.1
CaO	10.5	12.6	11.35	12.3	13.4	10.1
MgO	9.8	11.0	10.5	11.6	7.6	6.8
TiO <sub>2</sub>	5.0	5.0	5.37	5.3	0.9	6.32

<sup>§</sup> Only major constituents reported

<sup>\*</sup> All Fe assumed to be in the form of Fe<sub>2</sub>O<sub>3</sub>

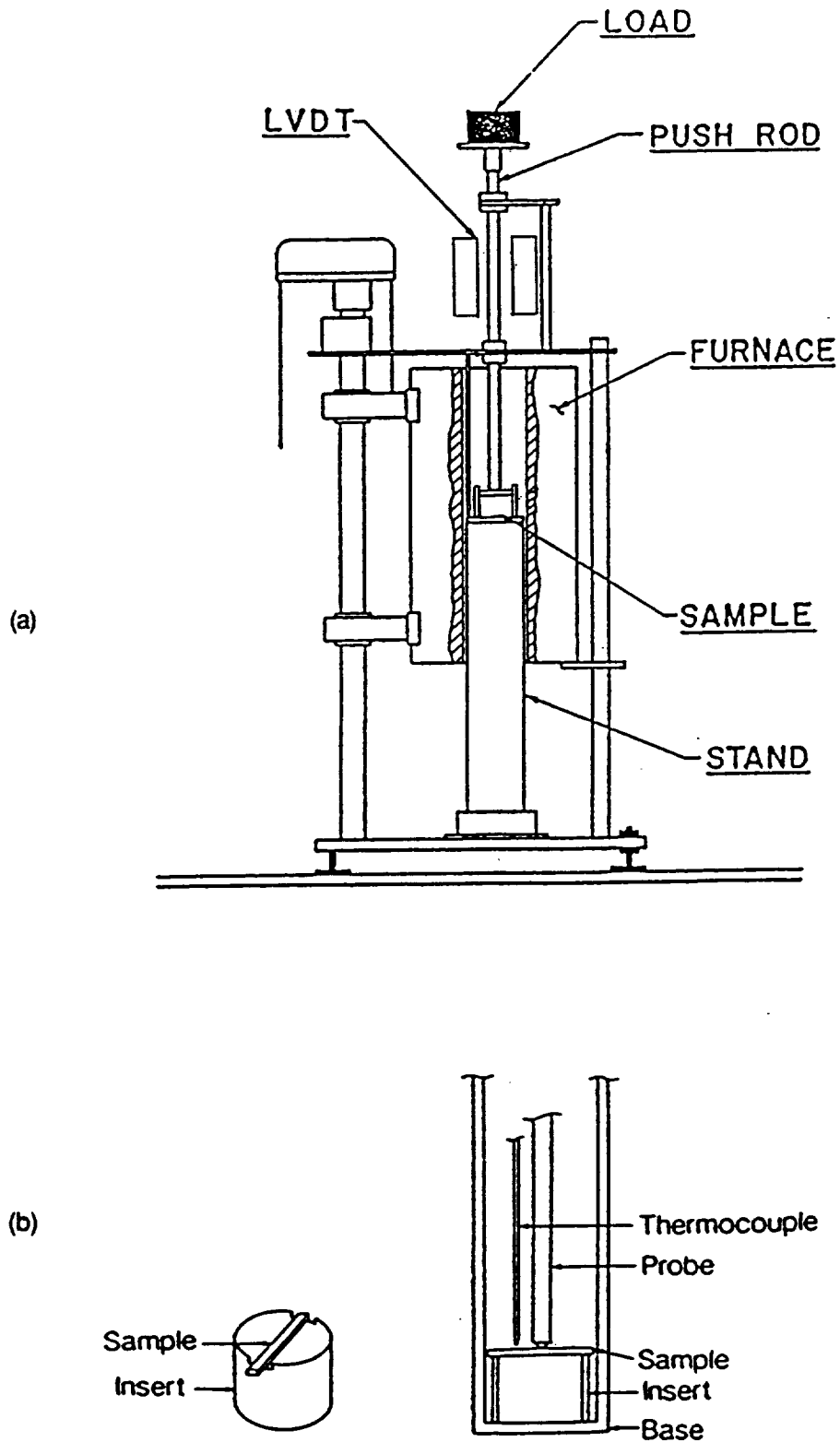


Figure 1: (a) Schematic diagram of viscometer, showing the positioning of the LVDT, pushrod, and sample assembly. (b) Fused silica insert with sample and probe assembly.

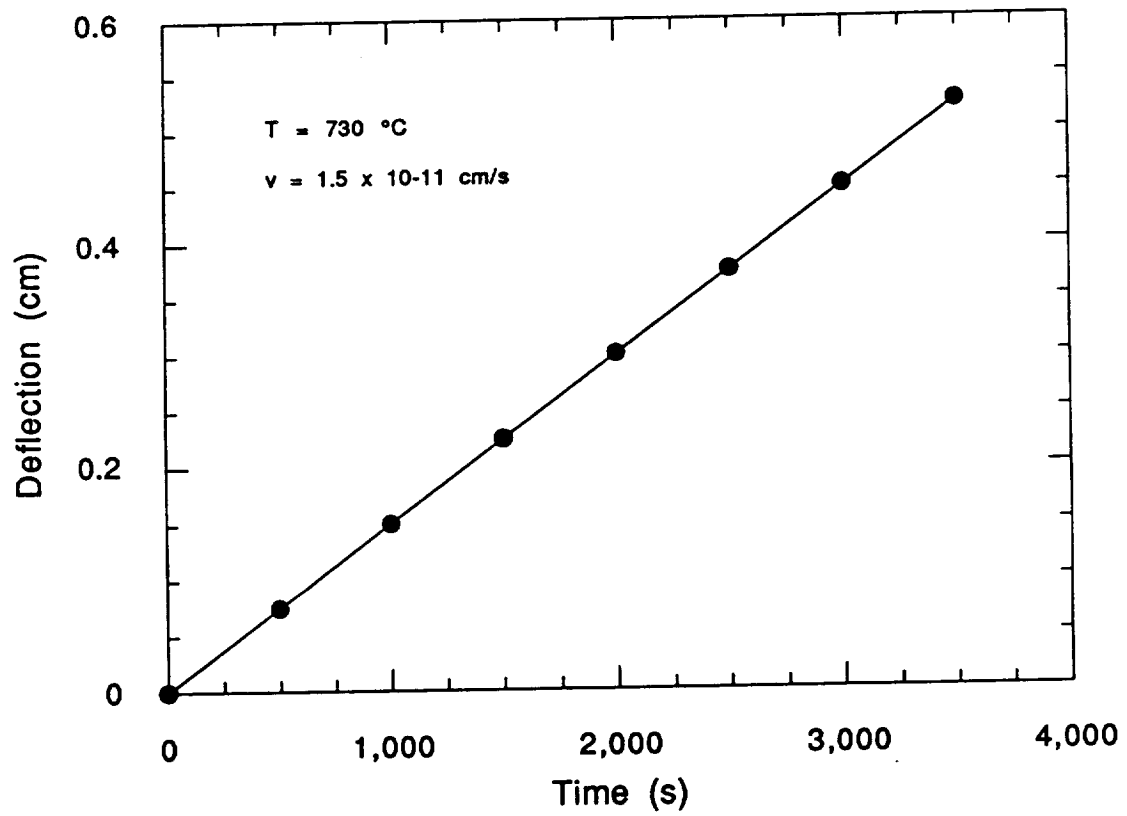


Figure 2: Typical deflection vs. time curve for a simulated lunar glass at 730 °C. Solid line represents a least squares linear fit of the data.

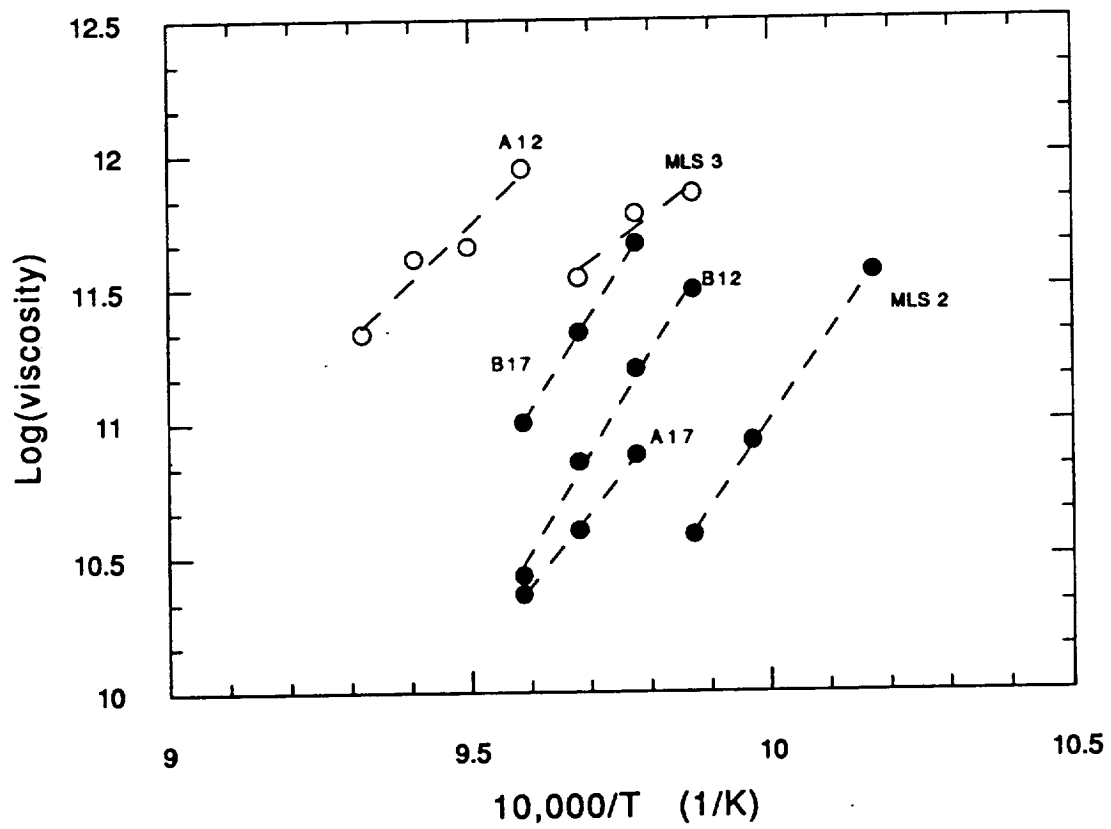


Figure 3: Variation of viscosity with temperature for simulated lunar glasses. Dashed lines are least squares, linear fits.

N 9 1 - 2 4 3 8 1

DEVELOPMENT AND MECHANICAL PROPERTIES OF  
STRUCTURAL MATERIALS FROM LUNAR SIMULANT

Chandra S. Desai

Department of Civil Engineering and Engineering Mechanics

The University of Arizona

14676  
p.8

AY 100-100

Abstract

Development of versatile engineering materials from locally available materials in space is an important step toward testablishment of outposts such as on the Moon and Mars. H e r e development of the technologies for manufacture of structural and construction materials on the Moon, utilizing local lunar soil (regolith), without the use of water, is an important element for habitats and explorations in space. It is also vital that the mechanical behavior such as strength and flexural properties, fracture toughness, ductility and deformation characteristics are defined toward establishment of the ranges of engineering applications of the materials developed.

The objectives here include two areas: (1) thermal "liquefaction" of lunar simulant (at about 1100°C) with different additives (fibers, powders, etc.),<sup>1,2</sup> and (2) development and use of a new triaxial test device in which lunar simulants are first compacted under cycles of loading, and then tested with different vacuums and initial confining or insitu stress. The second area has been described in previous progress reports and publications<sup>3,4</sup>; since the presently available device allows vacuum levels up to only  $10^{-4}$  torr, it is recommended that a vacuum pump that can allow higher levels of vacuum is acquired.

Introduction and Results to Date

The development of new construction materials through liquefaction of lunar simulants with various admixtures (powders and fibers), and determination of mechanical properties using various laboratory testing devices to perform bending and flexure, cylindrical triaxial, and three-dimensional multiaxial tests are the main objectives in this progress report.

The lunar simulant used, called Arizona Lunar Simulant, has been developed locally from a basaltic rock found near Hanford, WA. This material has a mineralogical composition similar to that of the lunar mare soil. The rock is ground so that its grain size distribution falls well within that of the distribution envelopes for the samples of the lunar regolith brought to earth by Apollo missions, Fig. 1.

In order to achieve various engineering properties such as flexure, compressive, tensile and fracture strengths, deformation characteristics, and ductility, the lunar simulant is combined with various powders and fibers. These include steel, stainless steel, aluminum, and fiberglass. The simulant itself, and with various percentages of powders or fibers, is liquefied in a furnace with a temperature capacity of 1700°C. The material is placed and compacted in molds made of

graphite and titanium so that appropriately sized specimens for various tests can be obtained (see Table 1). Diagrams of these samples with loading conditions are shown in Figure 2.

In the thermal liquefaction, the simulant melts at about 1100°C and forms a matrix that can be made into various specimen sizes and shapes. The resulting intermediate ceramic, formed solely by the simulant, is relatively brittle. With addition of a powder or fiber, the liquefaction may involve melting of the admixture at a lower or higher temperature than that for the soil simulant. Thus the powder/fiber melts before the heated soil particles or vice versa, resulting in a "ceramic composite." Such composites can possess a wide range of the aforementioned mechanical properties.

An objective of the research is to perform a parametric study in which the ratio of simulant to powder/fiber is varied, together with different levels of temperature and cycles of temperature, the latter is expected to add "prestressing" due to residual expansion of the powder/fiber. It has been noted that such powders and fibers can be manufactured from the lunar regolith. Table 2 shows details of the initial batch of samples made for beam bending tests.

Specimens of the material combinations thus developed will be tested for bending, fracture, ductility, and stress-strain-strength properties using laboratory testing methods as described previously. This is a vital step toward potential engineering applications of the materials developed, because based on the parameters and constants determined, the ranges and type of application of the materials developed in space construction can be established.

The current research so far has included: 1. Acquisition of the furnace, 2. development of a beam bending device as per the ASTM standard, 3. production of a number of beam specimens with varying admixture content (Table 2), and 4. testing of a number of beam specimens for their load-displacement behavior. Typical test results are shown in Figure 3. It can be seen that the addition of fibers contributes greatly to the load-carrying capacity and ductility of the material.

Development of cylindrical and multiaxial specimens will be the subjects of future research. The latter will be tested in unique three-dimensional devices (Figure 4) that allow application of three independent principal stresses, different paths of loading, and static and cyclic loading. Future work will also involve use of the Arizona simulant and the simulant developed at the University of Minnesota to include determination of the effect of agglutinates in this type of research. Agglutinate is a small glass-welded aggregate of rock, mineral, and glass fragments formed during micrometeorite impacts into the regolith. Also considered will be acquisition and use of a pump with higher vacuum levels and testing of specimens under higher levels of vacuum, about  $10^{-12}$  torr. This will also be used to continue the study using the new vacuum triaxial device.

The final objective of the research is to develop a methodology by which structural materials can be produced on the Moon using locally available and derived (fibers, powders, etc.)

materials, formed into useful shapes by thermal solar energy and compaction. In addition to the development of materials, attention must be given to the determination of the mechanical properties necessary to structural design so that the material can be used in a wide range of engineering applications such as roads, foundations, blocks, walls, floors, buildings, support systems, and shields. The research results are expected to represent a significant contribution towards construction of facilities on the Moon.

#### References

1. C.S. Desai, K. Girdner, H. Saadatmanesh, and T. Allen, "Mechanical Properties of Structural Materials from Lunar Simulants," Proc. Conf. on Resources of Near-Earth Space, Univ. of Arizona, 7-11 January, 1991.
2. K. Girdner, "Development and Mechanical Properties of Construction Materials from Lunar Simulants," The SERC Newsletter, Vol. 2, No. 1, Dec. 1990.
3. C.S. Desai, K. Girdner, and G. Frantziskonis, "Development of Construction Materials Like Concrete from Lunar Soil Without Water," Page II-14, Annual Progress Report, NASA Space Eng. Res. Ctr., Univ. of Arizona, 1988-89.
4. C.S. Desai, H. Saadatmanesh, and T. Allen, "Effect of Vacuum on Density and Stress-Strain-Strength Behavior of Compacted Lunar Soil Simulant," Report to NASA Space Eng. Res. Ctr., CEEM Department, 1990.
5. C.S. Desai, H. Saadatmanesh, and T. Allen, "Behavior of Compacted Lunar Simulants Using New Vacuum Triaxial Device," J. Aerospace Eng. Div., American Society of Civil Engineers, submitted, 1991.



Table 1. Various specimens

SHAPE	SIZE	TEST	STATUS
Rectangular	1.0 x 2.5 x 25 cm.	Bending	Current
Cylindrical	5.5 cm.diam. x 15 cm.ht.	Triaxial	Future
Cubical	10 cm. x 10 cm. x 10 cm.	Multiaxial	Future

Table 2. Beam samples prepared to date

## 1. Lunar Simulant Only

<u>Sample</u>	<u>p. gm/cc</u>
1 -	2.43
2 -	2.44

2. Fibers

	<u>% By Weight</u>	<u>% Volume</u>	<u>Matrix p. gm/cc</u>
Steel	15.0	4.65	2.17
Steel	30.0	10.95	2.26
Stainless	7.5	2.32	2.39
Stainless	15.0	4.54	2.20
AL	7.5	7.27	2.61
AL	15.0	--	--
AL shavs	10.0	--	--

- 20 samples have been made so far.
- Each of these is cut into 1-3 beams for testing.
- All batches were heated at the same cycle. Heat of 1100C was held for 1 hour, then cooled over an eight hour period.
- AL = Aluminum

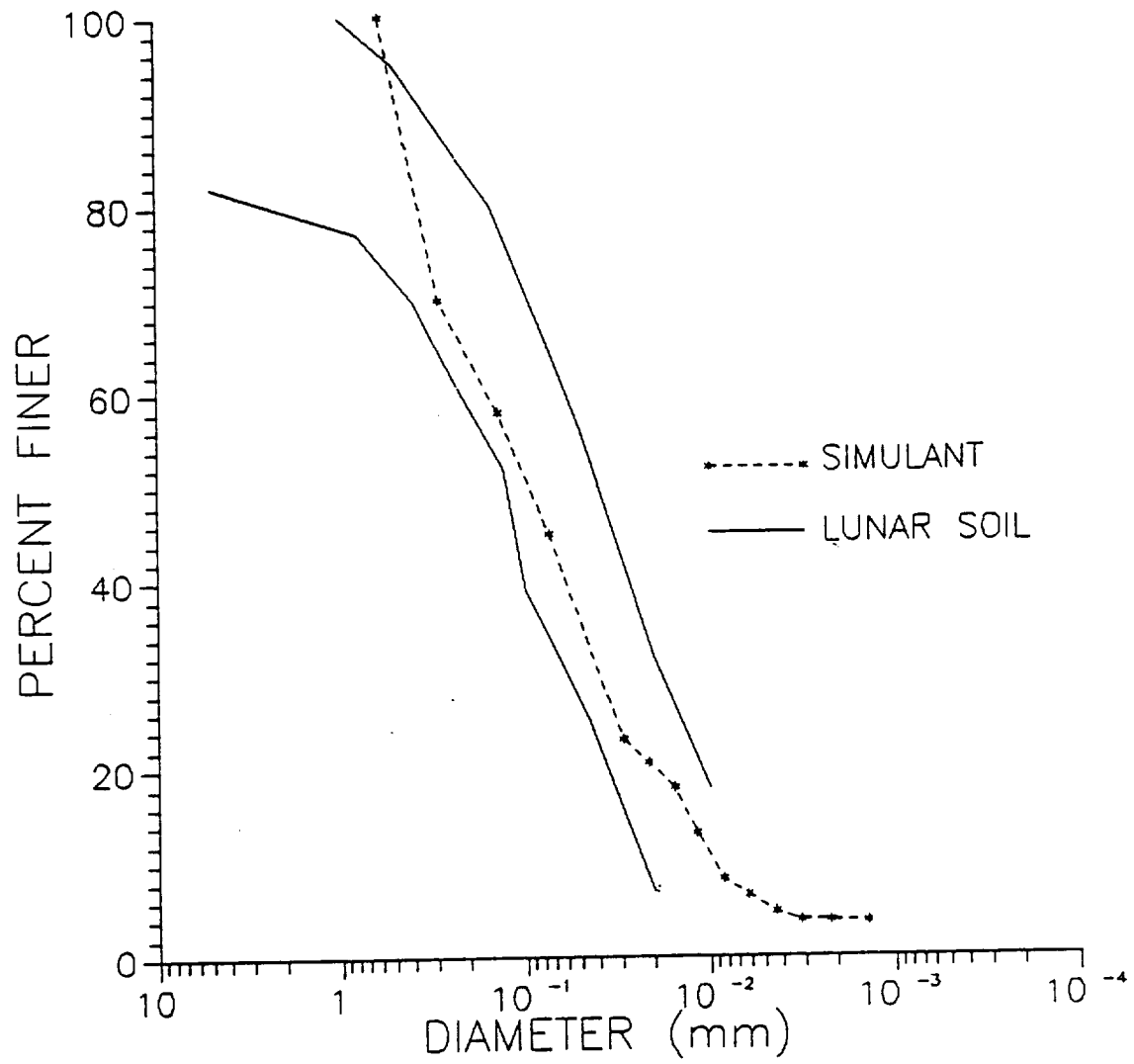
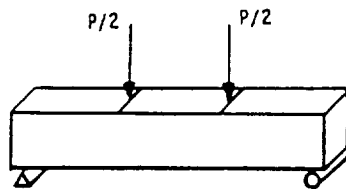
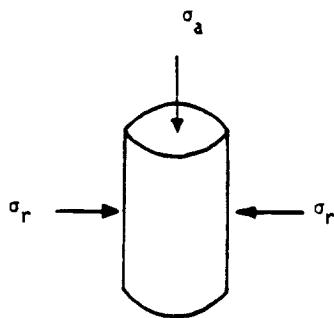


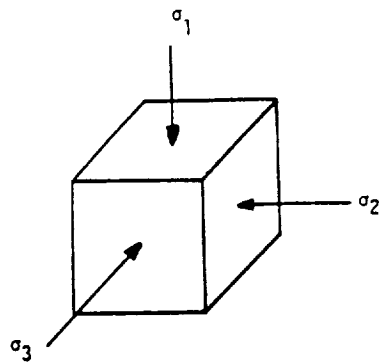
Figure 1. Grain size distribution of actual lunar soil and simulant



a) Beam bending.



b) Cylindrical triaxial.



c) Multiaxial.

Figure 2. Specimens for bending, cylindrical, and cubical tests

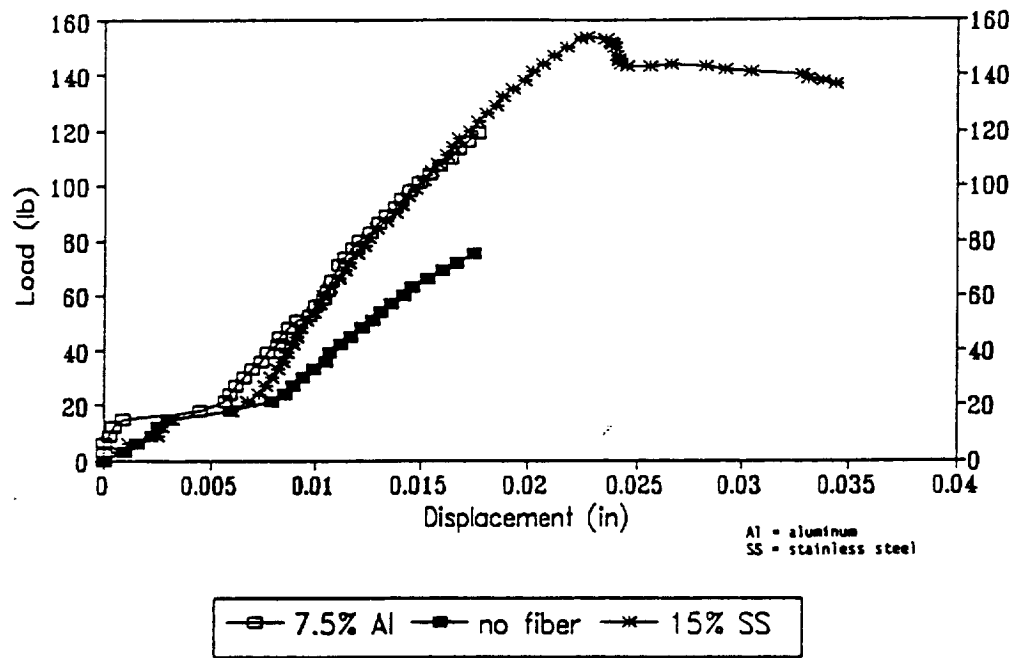


Figure 3. Load-displacement curves for typical simulant-fiber beams

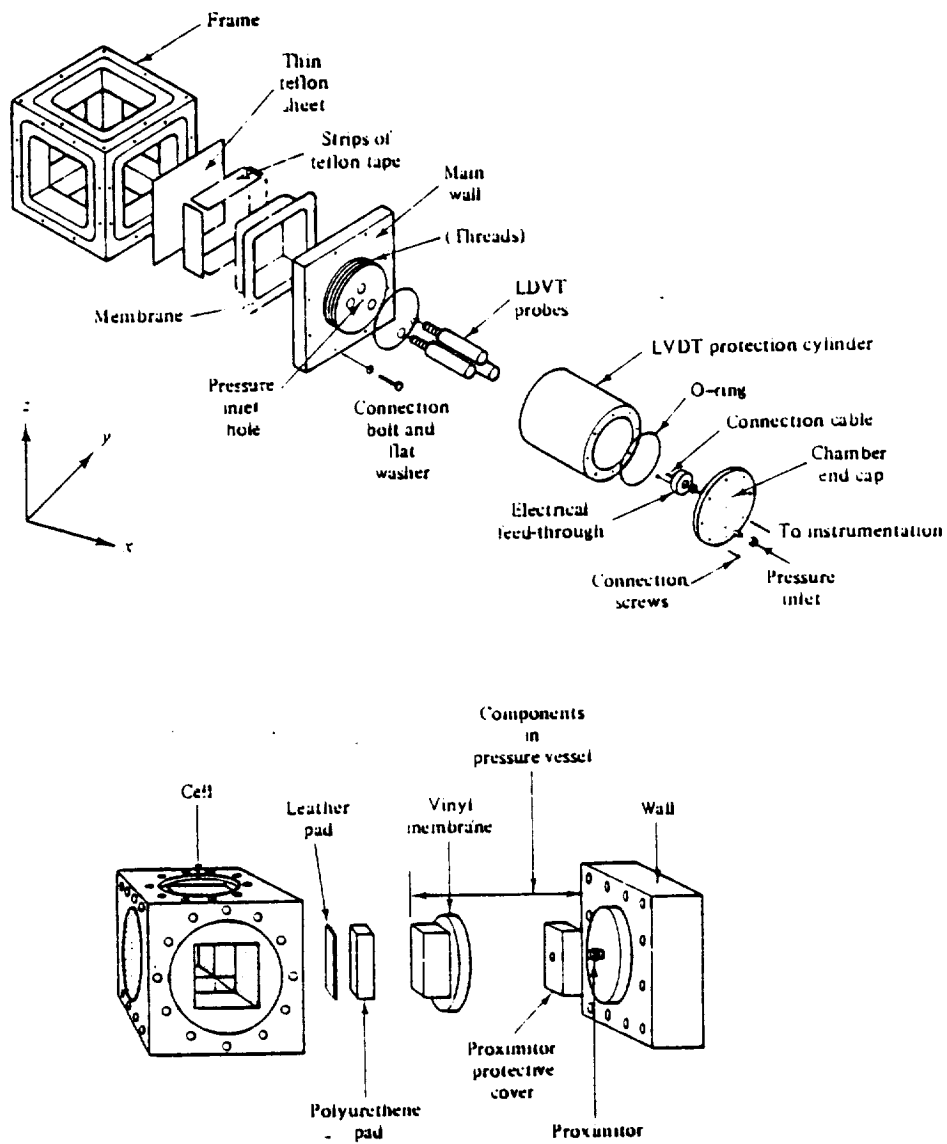


Figure 4. Multi-axial test devices

517-27  
N91-24382-17

HIGH TEMPERATURE SEALS BETWEEN CERAMIC SEPARATION MEMBRANES  
AND SUPER-ALLOY HOUSING

P.B.

G. Honea and K.R. Sridhar  
Department of Aerospace and Mechanical Engineering  
University of Arizona

AY 73295

Abstract

One of the concepts for oxygen production from Martian atmospheric carbon dioxide involves the use of tubular electrochemical membranes for oxygen separation. The tubular configuration offers the advantage of being able to separate the oxygen at pressures of up to 500 psi, thereby eliminating the need for a "pre-liquefaction" oxygen compressor. A key technology that has to be developed in order for the electrochemical separator to combine as a compressor is a high temperature static seal between the ceramic separation cell and the nickel-based super-alloy tube. Equipment has been designed and fabricated to test the seals. Efforts are under way to develop a finite element model to study the thermal stresses at the joints and on the seal, and the optimal shape of the seal. The choice of seal materials and the technique to be used to fabricate the seals are also being investigated.

Problem Statement

Preliminary experiments are being conducted to evaluate the feasibility of concentrating  $O_2$  from the electrochemical decomposition of gaseous  $CO_2$  using a solid oxide electrochemical cell (ECC) leased from Ceramtec, Inc, Salt Lake City, Utah. A schematic of the ECC is shown in figure 1. The separation membrane, composed of an electrolyte sandwiched between electrode coatings, has a tubular structure. The membrane tube is enclosed in a concentric nickel-based super-alloy tube. Since ceramics (electrolyte material is ceramic) have excellent compression strength but are weak under tension, the outside of the ceramic tube (oxygen side) can be subjected to fairly high pressures (up to 500 psi). Hence, if the  $O_2$  produced is liquefied and stored for later use, the configuration shown in figure 1 has the advantage over a disk system in that an  $O_2$  compressor

can be eliminated. The energy required to compress the  $O_2$  is provided to the system by way of the potential applied across the membrane. The minimum voltage required is given by:

$$E_{\text{Nernst}} = \frac{RT}{nF} \ln (P_2/P_1)$$

where  $E_{\text{Nernst}}$  = Pumping Voltage

$R$  = Ideal Gas Constant

$T$  = Absolute Temperature

$n$  = number of electrons per mole of the reactant

$F$  = Faraday Constant

$P_1$  = Partial Pressure of  $O_2$  on the inlet side and

$P_2$  = Partial Pressure of  $O_2$  on the exit side

In figure 1, the inlet stream is  $CO_2$  flowing at room temperature. This gas is heated as it flows through the feed tube by means of clam-shell heaters that wrap around the super-alloy tube. The reason for not preheating the gas is that the seal between the ceramic membrane and super-alloy tube is rated only for a maximum operating temperature of  $150^\circ\text{C}$ . Efficient design of an electrochemical membrane calls for seals between the ceramic cell and the outer metal tube that can withstand the high temperatures. Such seals would permit the design of once-through multi-tube modules that would look similar to a shell and multi-tube heat exchanger in configuration.

#### State-of-the-Art

Ceramic joining and sealing technology is quite well developed for low-temperature applications. However, the technology for joining and sealing ceramics and metals for high-temperature, high stress, and/or corrosive environments is still in its infancy. In the area of brazing with filler metals, efforts have been made to specially formulate filler metals that will wet and adhere to untreated ceramic surfaces (direct brazing). Another approach has been to vapor coat the ceramic surface with a suitable metal layer prior to brazing (indirect brazing). A totally different approach has been

to use specially formulated glasses for brazing. All three techniques have had some success for specific applications. While it is possible to calculate the stresses induced in the joints and the seal due to the differences in coefficients of thermal expansion, no systematic and rigorous analysis has been found in the literature.

### Approach

An experimental facility has been designed and fabricated for testing the seals. Figure 2 shows a schematic of the facility. It has the capability of heating the test seal to temperatures ranging from 600°C to 1300°C. The seal can be pressurized to 600 psi. A Validyne variable reluctance type differential pressure transducer has been calibrated and installed to monitor pressure drops as low as 0.1 psi. The pressure and temperature sensors and controllers are connected to an IBM compatible personal computer via a Data Translation analog-to-digital conversion board. An electrically activated valve shuts the system down and turns off the supply gas when the loss of pressure (due to a leak in the seal) exceeds a predetermined value.

A PC-based finite element code will be developed to analyze the stresses induced in the seals and joints due to the difference in the coefficients of thermal expansion between the metal, ceramic material, and filler material.

The code will permit the selection of the optimum shape and thickness of the seal. Since the specialty filler materials used for brazing are generally expensive, such an optimization would reduce the cost of the seals significantly. Presently, efforts are also under way to identify the appropriate filler materials between the two tubes and the fabrication shops that have the technical expertise to do the brazing.



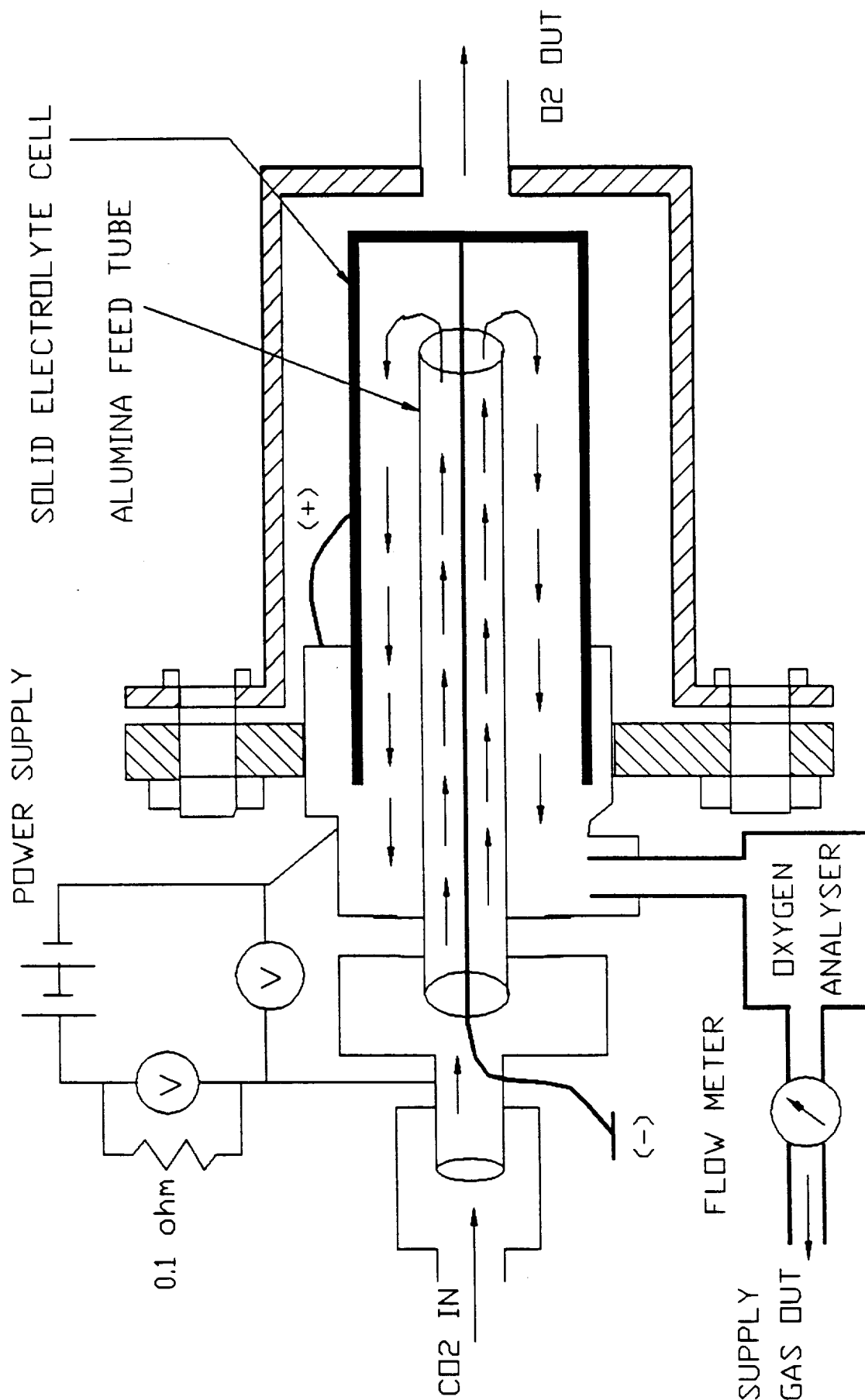


Fig 1: Schematic of The CERAMATEC Tubular Device

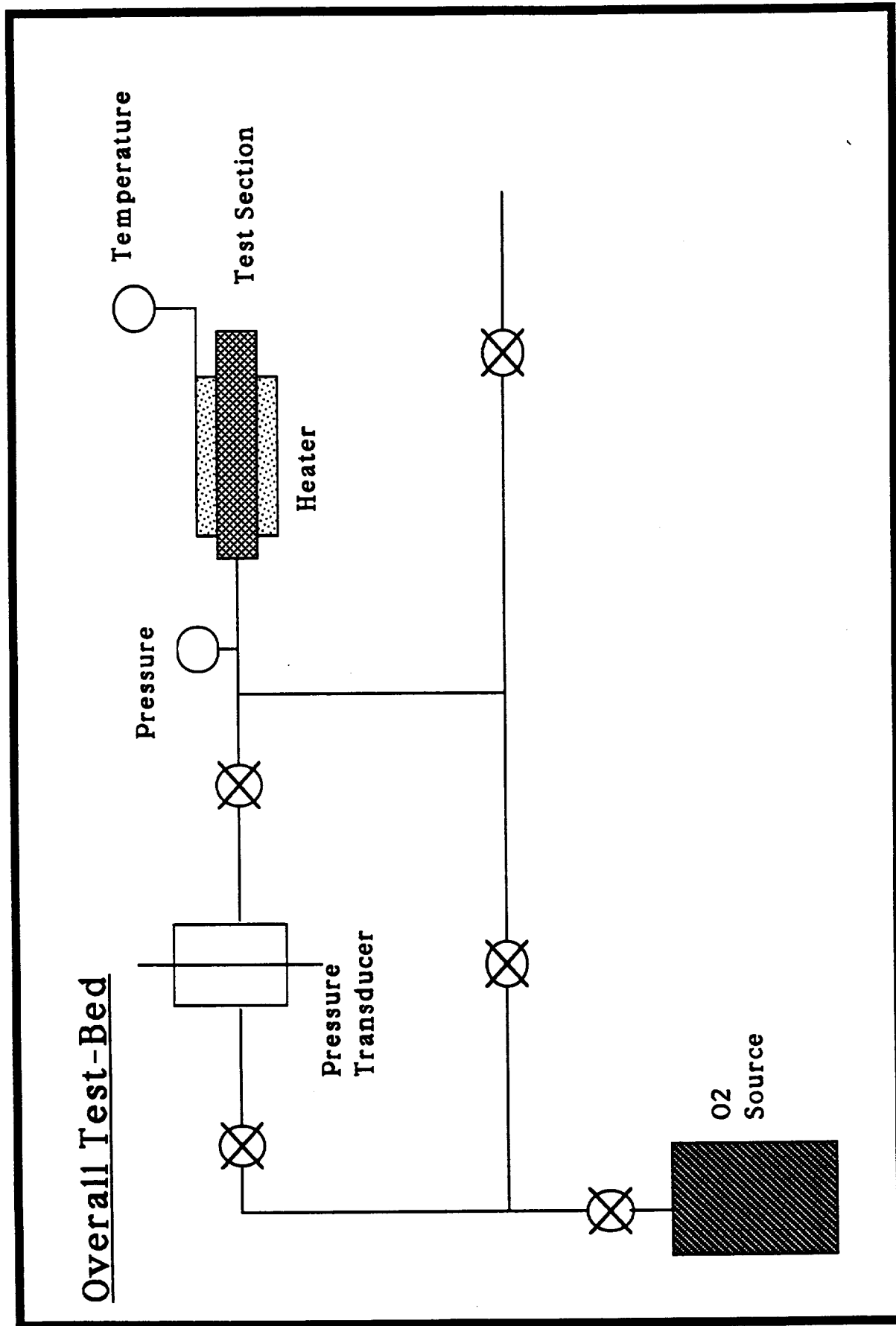


Fig 2: Schematic of The Experimental Facility for Testing High Temperature Seals

---

### **III. RESOURCE DISCOVERY AND CHARACTERIZATION**

ORIGINAL CONTAINS  
SCIENCE ILLUSTRATIONS

518-71  
N91-24383 44678  
p.6

DETERMINATION OF LUNAR ILMENITE ABUNDANCES FROM  
REMOTELY SENSED DATA

Stephen M. Larson, Jeffrey R. Johnson and Robert B. Singer  
Department of Geosciences/Lunar and Planetary laboratory  
University of Arizona

The mineral ilmenite ( $\text{FeTiO}_3$ ) was found in abundance in lunar mare soils returned during the Apollo project. Lunar ilmenite often contains greater than 50 weight-percent titanium dioxide ( $\text{TiO}_2$ ), and is a primary potential resource for oxygen and other raw materials to supply future lunar bases. Chemical and spectroscopic analysis of the returned lunar soils produced an empirical function that relates the spectral reflectance ratio at 400 and 560 nm to the weight percent abundance of  $\text{TiO}_2$  (Charette et al., 1974). This allowed mapping of the lunar  $\text{TiO}_2$  distribution using telescopic vidicon multispectral imaging from the ground (Johnson et al., 1977). However, the time variant photometric response of the vidicon detectors produced abundance uncertainties of at least 2-5%. Since that time, solid-state charge-coupled device (CCD) detector technology capable of much improved photometric response has become available.

We have been carrying out an investigation of the lunar  $\text{TiO}_2$  distribution utilizing groundbased telescopic CCD multispectral imagery and spectroscopy. The work has been approached in phases to develop optimum technique based upon initial results. The goal is to achieve the best possible  $\text{TiO}_2$  abundance maps from the ground as a precursor to lunar orbiter and robotic sample return missions, and to produce a better idea of the peak abundances of  $\text{TiO}_2$  for benefaction studies. These phases and the results thus far are summarized below.

A. Low spatial resolution global survey producing a photometrically homogenous  $\text{TiO}_2$  map of the entire lunar near-side using the traditional 400/560 nm ratio. This involved constructing a Newtonian focus on the Tumamoc Hill 0.5 m telescope to produce an appropriate scale on the CCD, and a filter wheel to facilitate rapid cycling between filters. With this arrangement, the visible lunar disc could be covered with a mosaic of 5 CCD fields with 5.3 km pixels on the moon. The resulting map (fig. 1) shows that the highest  $\text{TiO}_2$  regions are in Mare Tranquillitatis and Oceanus Procellarum. Where they overlap, most of this map is consistent with the Apollo Gamma Ray Spectrometer data, but with much better spatial resolution.

Maps based on 950/560 nm ratios were also made to define the location of mature mare soil for which the spectral  $\text{TiO}_2$  abundance relation is considered valid. In this ratio, fresh craters appear dark because of abundant pyroxene grains which produce strong absorption near 950 nm due to  $\text{Fe}^{2+}$  crystal field transitions. Micrometeoroid impacts over time increases the agglutinate content and a weakening of the 950 nm pyroxene absorption band. We obtained substantial differences from previous 950/560 nm ratio maps which seem to result from inexact correction of scattered light in the silicon vidicon tubes. The silicon substrate becomes transparent at wavelengths longward of 800 nm, and because of the high index of refraction causes "light piping" within the CCD. This scattering can substantially alter the effective modulation transfer function of the detector preferentially for the longer wavelengths. Previous investigators attempted to correct for this by subtracting a constant "DC level" from the 950 nm image. Studies of the lunar limb profiles and laboratory testing of our CCD shows that the thinned silicon substrate does not exhibit significant scattering. Because of this, we feel that we can better identify regions of various relative soil maturity.

B. Medium resolution (1 nm) 330-870 nm spectrophotometry of high TiO<sub>2</sub> regions to investigate a broader spectral range and identify spectral signatures which might alter the interpretation of the image ratio values. Using the all-reflecting Larson IHW CCD spectrograph on the Tumamoc Hill 0.5 m telescope, we adopted a technique of dividing the spectrum of the region of interest by a spectrum of the standard area "MS-2" taken within 10 - 30 seconds to correct for terrestrial atmospheric extinction, instrumental response, solar Fraunhofer absorption lines and the general red spectral slope of the moon. With relative photometric uncertainties of only 0.1%, the resulting spectra can be readily compared and show many new spectral features, especially in the near-ultraviolet region. Figure 2 shows examples of these ratio spectra. Follow-up spectrophotometry has been made with better spatial resolution on the Catalina 1.5 m telescope of all of the Apollo sites (for "ground truth" checks with returned samples), the high TiO<sub>2</sub> areas and other interesting and relevant locations on the moon.

C. Absolute spectral calibration of the standard area MS-2 with respect to flux calibrated solar analog stars is underway with data obtained with the Catalina 1.5 m telescope to convert the ratio spectra to absolute reflectivity for more direct comparison with the laboratory spectra of Apollo samples. The long slit spectra also permitted determination of the spatial extent of the spectrally uniform MS-2 standard area, and what errors are introduced by imprecise pointing of the spectrograph slit aperture.

D. Investigation of laboratory spectra of lunar samples in the Brown University RELAB database to clarify apparent inconsistencies and uncertainties in the empirical abundance relationship. High spatial resolution groundbased spectra of the Apollo landing sites are needed to test the consistency between spectra of returned spectra and groundbased data.

E. As a result of B and D, we have found that the use of 400/730 nm image ratios appear to show the same feature distribution as the 400/560 nm ratios but at higher spectral contrast. The 400/730 nm image ratios may thus yield better TiO<sub>2</sub> abundance accuracy due to 40% greater spectral contrast. This is being studied in more detail, but it promises to provide greater accuracy, especially in the medium TiO<sub>2</sub> regions.

F. To make the best possible TiO<sub>2</sub> abundance maps from the ground, we have applied an experimental 2048 by 2048 pixel CCD built by Photometrics Ltd. of Tucson. A successful observing run on the Catalina 1.5 m telescope on 1990 Dec. 1-2 yielded good images with 240m pixel size of 7 areas on the moon at .36, .40, .56, .73 and .95 nm. These selected areas include all of the Apollo landing sites, MS-2, and the high TiO<sub>2</sub> regions in Mare Tranquillitatis and Oceanus Procellarum. These very large images (16 Mb) are currently being reduced, and some of them appear to be as good as the best full moon photographic images yet obtained from the ground. The resulting ratio images should provide TiO<sub>2</sub> abundance maps to 500 m resolution and help determine the sharpness of composition boundaries and compositional variations in the Apollo landing sites. An example of the effect of increased resolution is shown in figure 3, where TiO<sub>2</sub> abundance maps with 5.3 and 1.2 km pixels are compared. The smaller sample size shows more localized areas of higher TiO<sub>2</sub> abundance.

Many of these results have been included in a major paper submitted to the Journal of Geophysical Research (Johnson et al., 1991), and have been presented at the 21th Lunar and Planetary Science Conference (Johnson et al., 1990a) and the meeting of the Division of Planetary Sciences of the American Astronomical Society (Johnson et al., 1990b). Subsequent papers are in preparation and planned which will cover all aspects of this research. We believe that this work represents a very useful contribution to understanding the potential resource

distribution on the moon as well as developing improved detection techniques that may be applied to future spacecraft experiments.

#### CITED REFERENCES

- Charette, M.P., McCord, T.B., Pieters, C and Adams, J.B. (1974). Application of remote spectral reflectance measurements to lunar geology classification and determination of titanium content of lunar soils. *J. Geophys. Res.*, **79**, 1605.
- Johnson, J.R., Larson, S.M., and Singer, R.B. (1990a). Estimates of lunar mare titanium and ilmenite abundances from CCD imaging and spectroscopy. *Abstracts of the LPSC XXI*, 567-568.
- Johnson, J.R., Larson, S.M., and Singer, R.B. (1990b). Remote compositional mapping of potential lunar resources. *Bull. Am. Astron. Soc.*, **22**, no. 3, 1048.
- Johnson, J.R., Larson, S.M., and Singer, R.B. (1991). Remote sensing of potential lunar resources: I. Global compositional mapping. Submitted to *J. Geophys. Res.*
- Johnson, T.V., Saunders, R.S., Matson, D.L. and Mosher, J.A. (1977). A TiO<sub>2</sub> abundance map for the northern maria. Proc. Lunar Sci. Conf. 8th, 1029-1036.

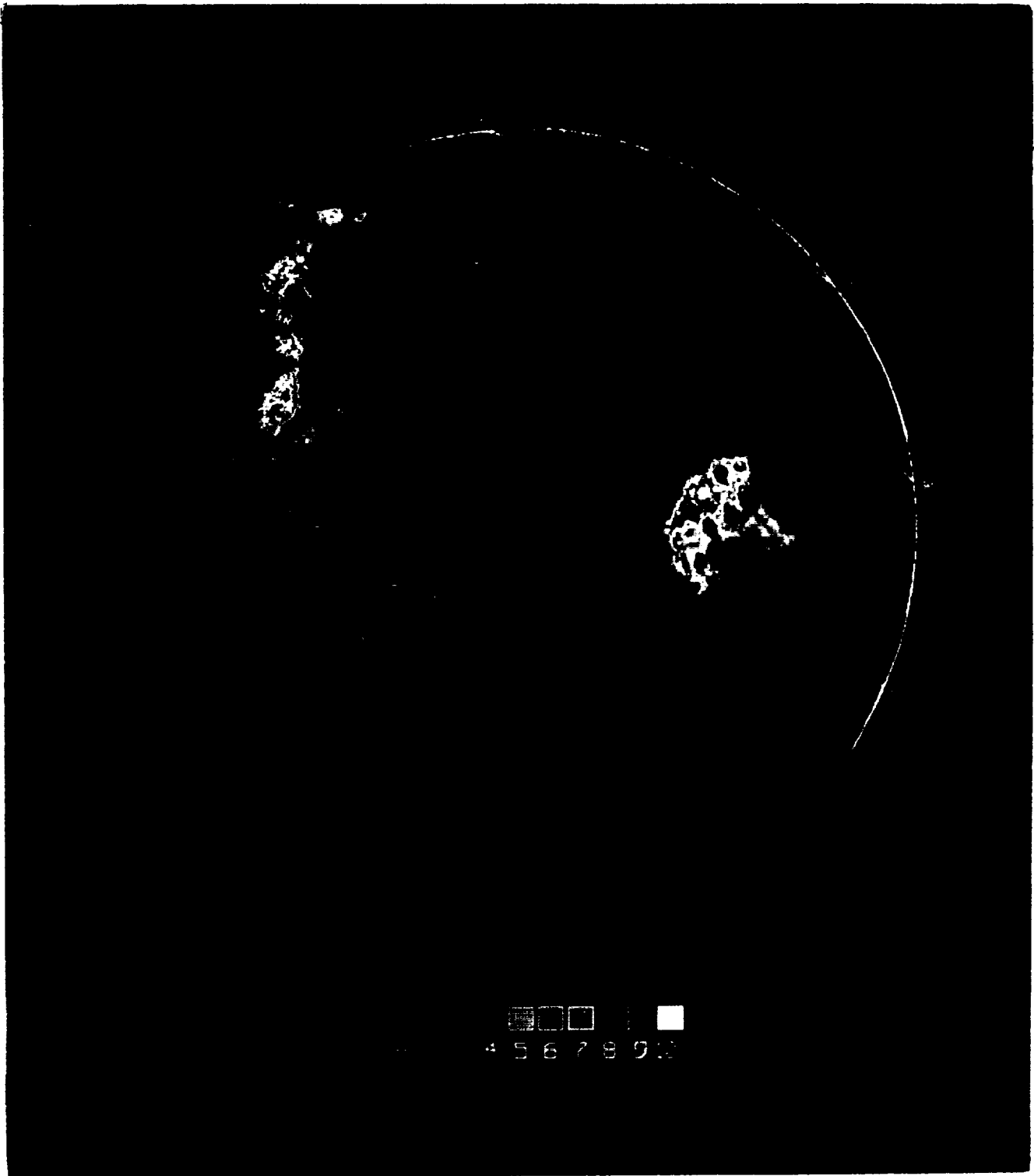


Figure 1. Color encoded  $\text{TiO}_2$  abundance map for the near-side lunar maria with units expressed in weight percent  $\text{TiO}_2$ . The masked areas (unit H) include highland regions and major regions of dark mantle materials where the empirical abundance relation does not apply.

ORIGINAL PAGE  
COLOR PHOTOGRAPH

ORIGINAL PAGE IS  
OF POOR QUALITY

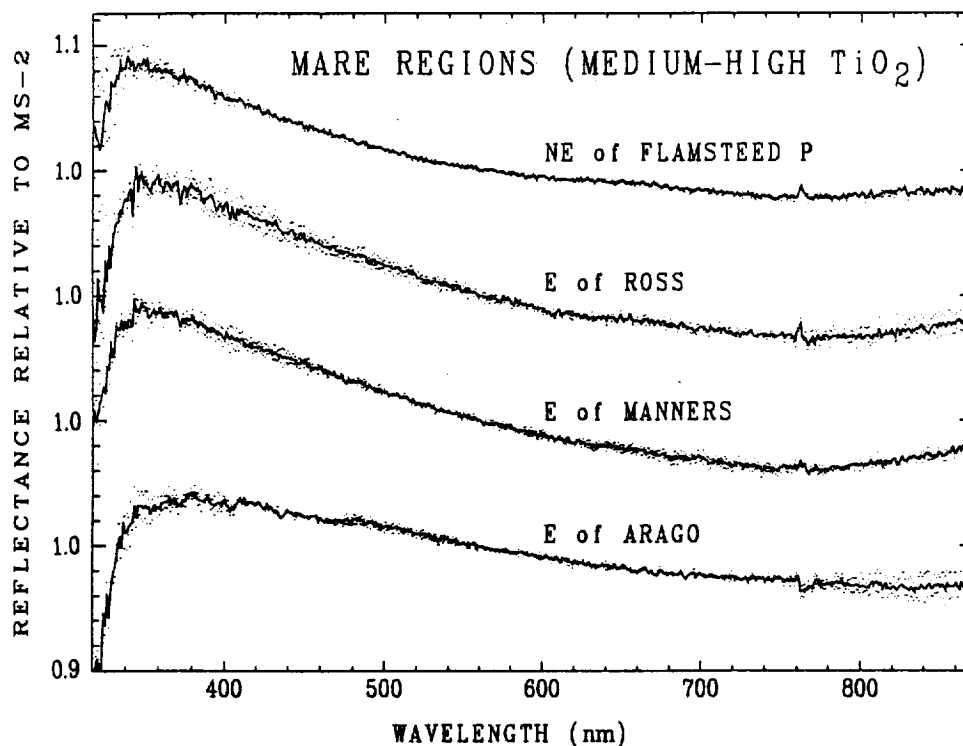
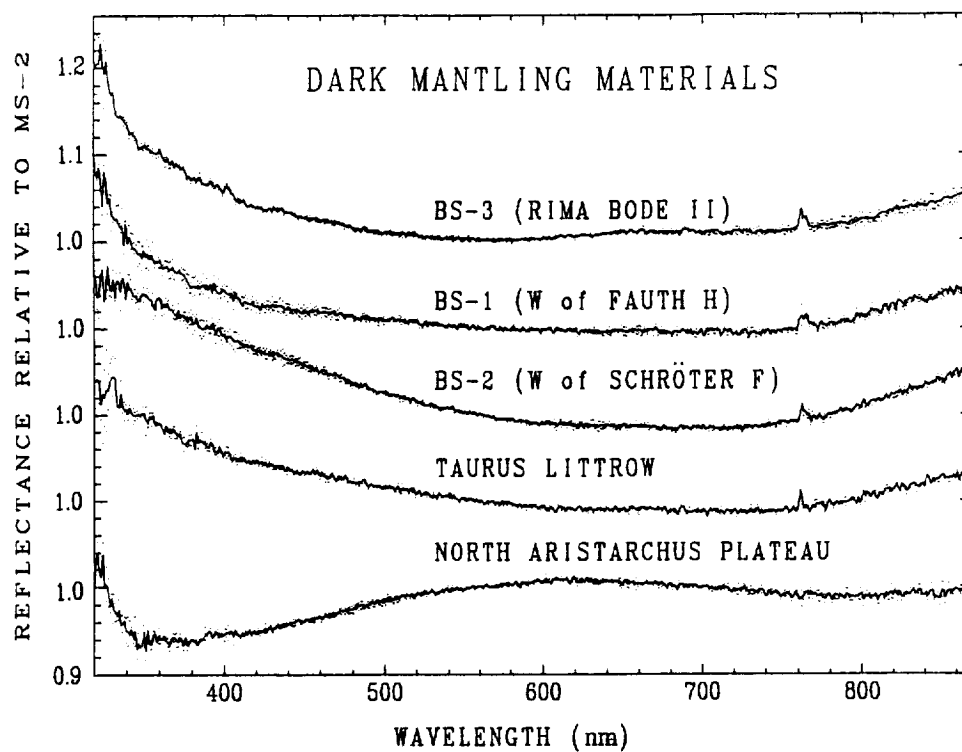


Figure 2. Representative 330-870 nm spectra (all relative to MS-2) of various areas composed of dark mantle materials (top) and maria regions of medium to high  $\text{TiO}_2$  (bottom). Dots are 1 standard deviation between samples along the slit at the same wavelength.



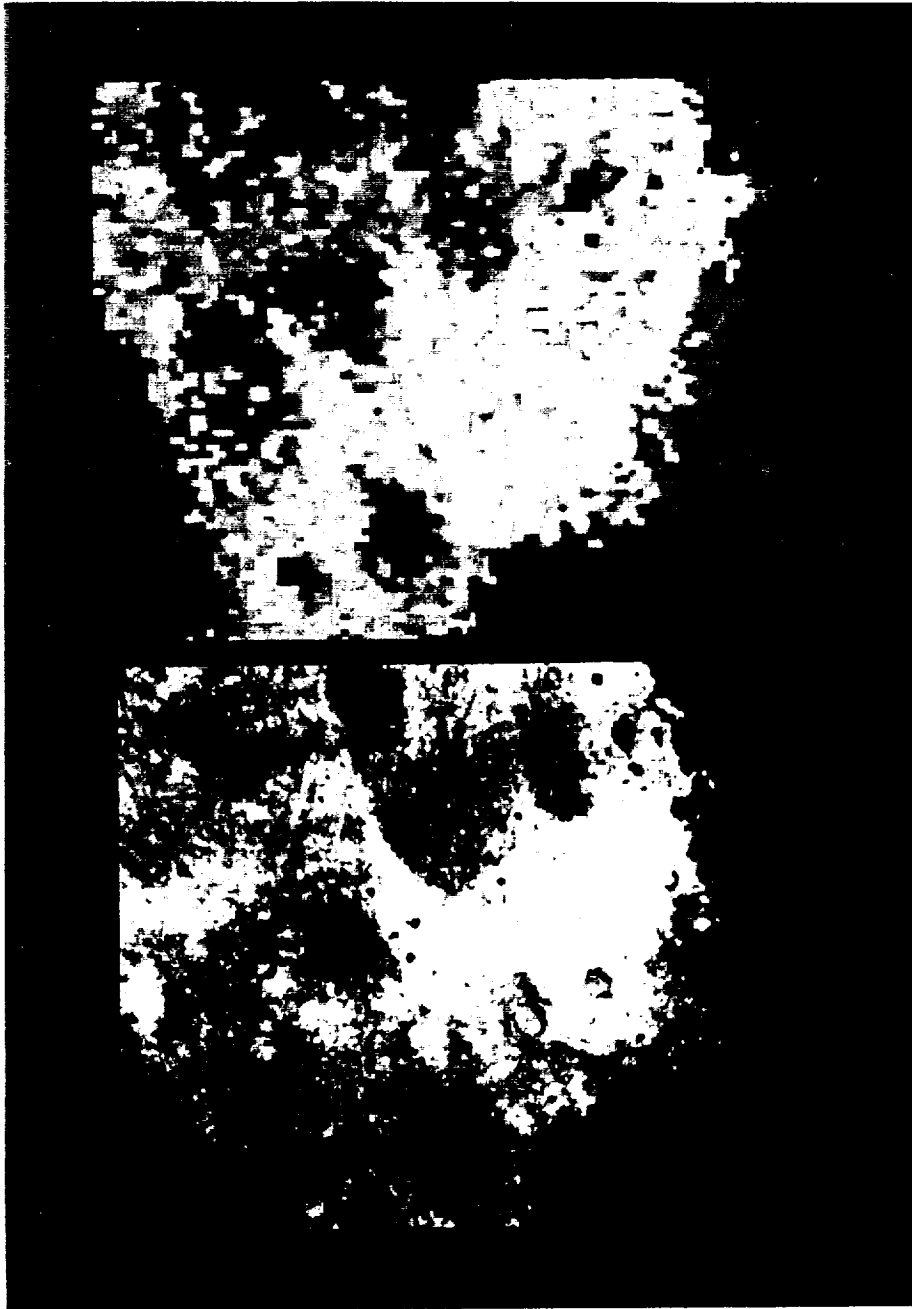


Figure 3. Comparative  $\text{TiO}_2$  abundance maps with resolutions of 5.3 (top) and 1.2 km per pixel (bottom) of the high  $\text{TiO}_2$  region in Mare Tranquillitatis. The general boundaries are consistent, but the smaller pixels may yield locally higher concentrations of  $\text{TiO}_2$ .

Figure 3. Comparative  $\text{TiO}_2$  abundance maps with resolutions of 5.3 (top) and 1.2 km per pixel (bottom) of the high  $\text{TiO}_2$  region in Mare Tranquillitatis. The general boundaries are consistent, but the smaller pixels may yield locally higher concentrations of  $\text{TiO}_2$ .

**ORIGINAL CONTAINS  
COLOR ILLUSTRATIONS**

519-91  
14677  
N91-24384<sup>21</sup>

Continuous Monitoring of the Lunar or Martian Subsurface  
Using On-Board Pattern Recognition and  
Neural Processing of Rover Geophysical Data

Charles E. Glass, Richard V. Boyd, and Ben K. Sternberg

University of Arizona

ASSISTANT  
MON

**ABSTRACT**

The overall aim of this research is to provide base technology for an automated vision system for on-board interpretation of geophysical data. During the first year's work we have demonstrated that geophysical data can be treated as patterns and interpreted using single neural networks. Research underway at this time is developing an integrated vision system comprising neural networks, algorithmic preprocessing and expert knowledge. This system is to be tested incrementally using synthetic geophysical patterns, laboratory generated geophysical patterns and field geophysical patterns.

## SUMMARY OF PREVIOUS WORK

The objectives of the first year funding were threefold. First, develop a continuous profiling EM vision system. Second, develop a continuous profiling sonic system. Third, evaluate pattern recognition and neural network approaches for automated interpretation of continuous profile data. As funding for the first year effort (1989-1990) necessitated a reduction in scope, objectives one and three became the operative objectives for the project.

Combining SERC Funding with funding from several other projects, we purchased a ground penetrating radar (GPR) system for continuous profiling using EM radiation in the 500 MHz and 300 MHz frequency ranges. Extensive experimentation of the GPR system at our geophysical test site and at several sites in Arizona is reported in McGill et al., 1989, McGill et al., 1990, and McGill, 1990.

Research during the first year has also demonstrated that radar signatures can be represented as patterns and interpreted automatically using a single neural network, see Figures 1 and 2. Our increasing experience in the field, however, indicated that GPR signatures can become quite complex, but target shape and aspects of the GPR survey (such as profiling speed) also strongly influence the radar return signatures. Hence, we believe that a single neural network could rapidly become overwhelmed by actual field situations, as we ourselves are at times. This belief has led to this year's project, which has as an objective to develop and incrementally test an integrated vision system comprising neural networks, algorithmic preprocessing and expert knowledge represented by a symbolic paradigm.

## SUMMARY OF CURRENT RESEARCH

The research objective of the current reporting period is to develop and incrementally test an integrated vision system comprising neural networks, algorithmic preprocessing and expert knowledge.

### VISION SYSTEM

During our previous research, we have demonstrated that GPR patterns are amenable to adaptive pattern recognition using a single neural network. In these experiments a continuous output simulated neural network was used to predict the horizontal and vertical location of a buried plate given the radar signal returned from the irradiated plate.

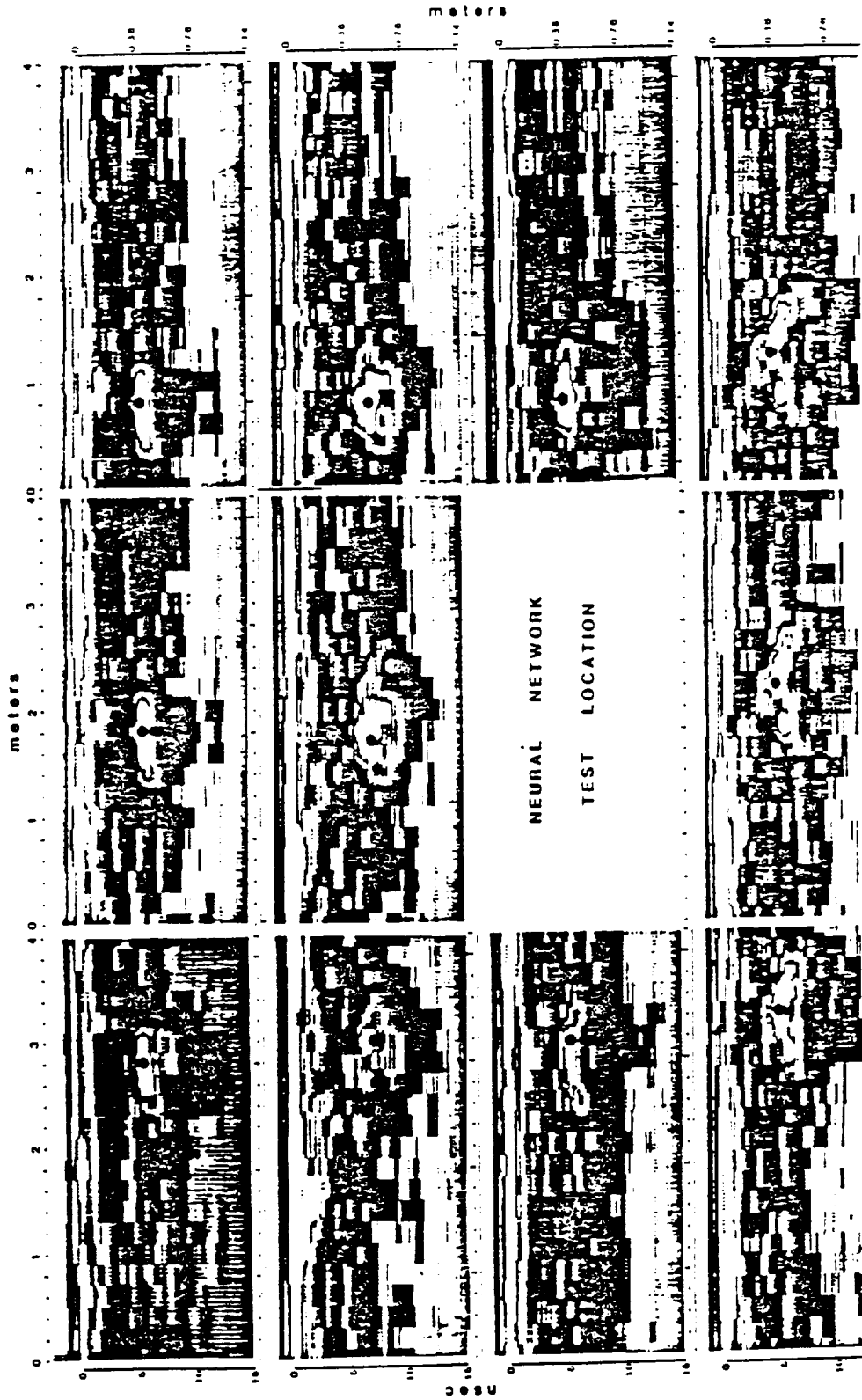


Figure 1. Digital GPR signatures used to train artificial neural networks. The black dot represents the spatial location of the target plate.

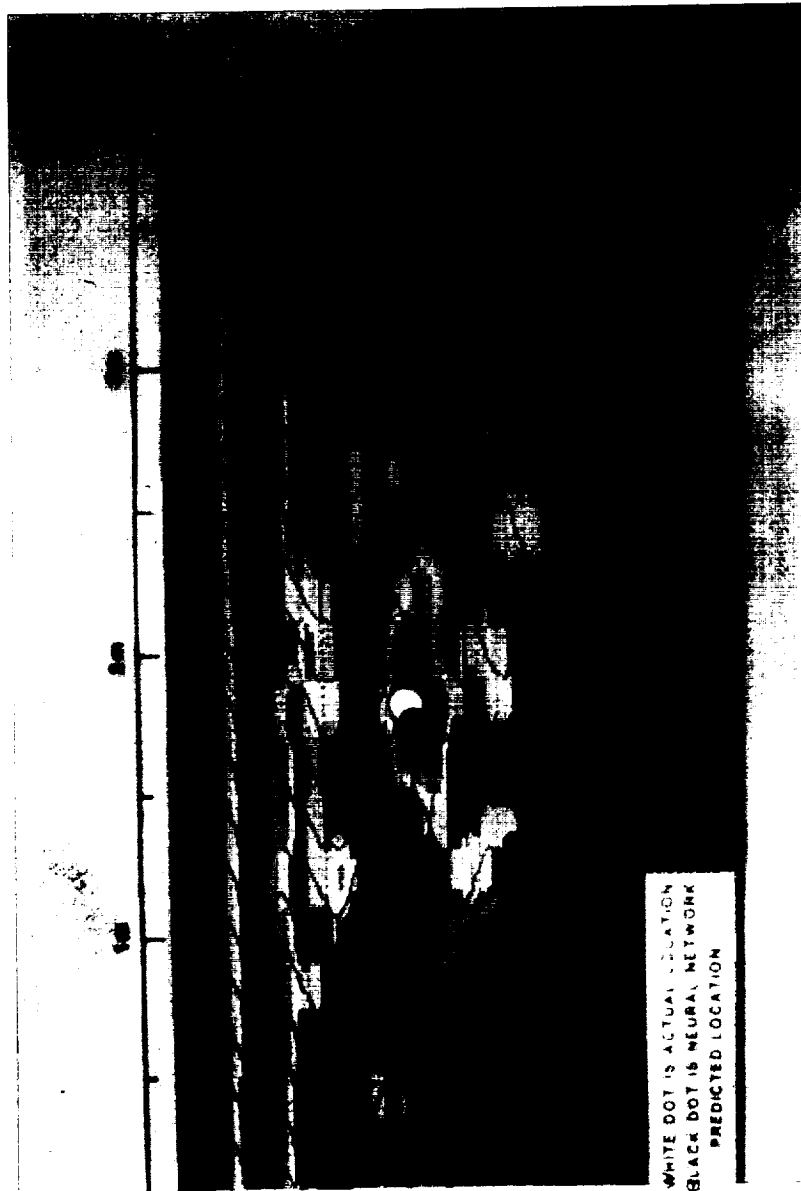


Figure 2. Neural network test profile. The black dot is the target location, the cross is the location predicted by the neural network.

ORIGINAL PAGE  
COLOR PHOTOGRAPH

ORIGINAL PAGE IS  
OF POOR QUALITY

Results from generating synthetic radar signatures over regular geometric shapes, Figures 3 through 7, show that, theoretically at least, far more than the target's spatial location can be derived from the radar pattern. The target shape can be ascertained from the slope of the signature arms, and the vertical and horizontal extent of the target can be calculated from the length and shape of the signature arms. Hence, neural network-based pattern recognition systems should be able to provide more information than our previous experiments have asked of them.

In the field, though, several factors combine to complicate the GPR patterns. First, attenuation in the surrounding soils will limit the radar penetration, thus truncating the anomaly arms. Second, the EM wave velocity of the background soils and the speed of the GPR profile can compress the radar pattern, making shape determination difficult. And third, heterogeneties in the background soils can superimpose noise on the desired GPR patterns.

Because of these difficulties, we have undertaken a program to design a more complex vision system able to incorporate the advantages of neural networks, knowledge base and algorithmic paradigms into a single unit. Neural networks, for example, appear to work best on simple (toy) problems. That is, the simpler the pattern, the more successful neural networks are in recognizing it. Furthermore, the scale of the "toy" (Minsky and Papert, 1968) problem is at a level at which most of the functioning of the human visual system seems to work, i.e., the human visual system appears to be composed of numerous simple neural networks working, for the most part, independently on specific aspects of a pattern.

The complexity of the human visual system seems to reside not as a single huge network, but rather in the complex (and so far little known) way in which the component networks interact or are coordinated. The focus of this effort, then, is on organizing several simple systems into a more effectively complex larger one. Although we are still experimenting with some fundamental uncertainties related to the specifics of how to go about such an organizational task, the following discussion outlines our general approach.

Applying the concept of encapsulation found in object oriented programming, particular domains of the pattern recognition function will be isolated from others to keep the level of inter-model complexity down. We anticipate that higher level objects will be employed to coordinate, or manage, the interaction of simpler objects. Research on the visual system of the horseshoe crab, for example, indicates that the information flow into the crab's visual cortex from its brain exceeds the information flow into its visual cortex from the system of neural networks constituting its optic nerve. Hence, even in simple visual systems there appears to be significant management of image information through knowledge gained from heredity or experience.

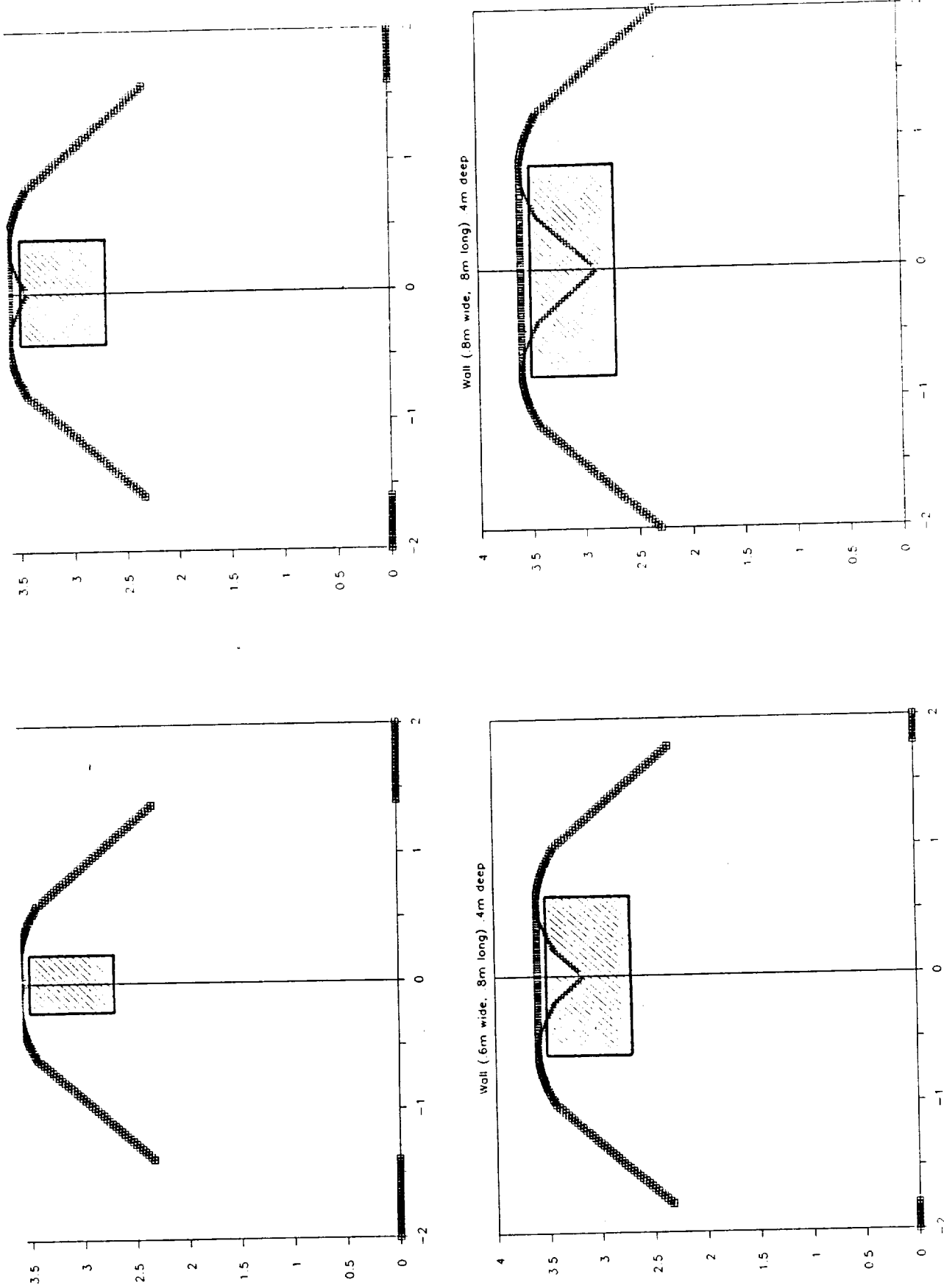


Figure 3. Synthetic GPR profiles over blocks having vertical sides and varying widths, (a) 0.4m, (b) 0.8m, (c) 1.2m, and (d) 1.6m. Reflections from top (squares) and inside surfaces (crosses) are shown.

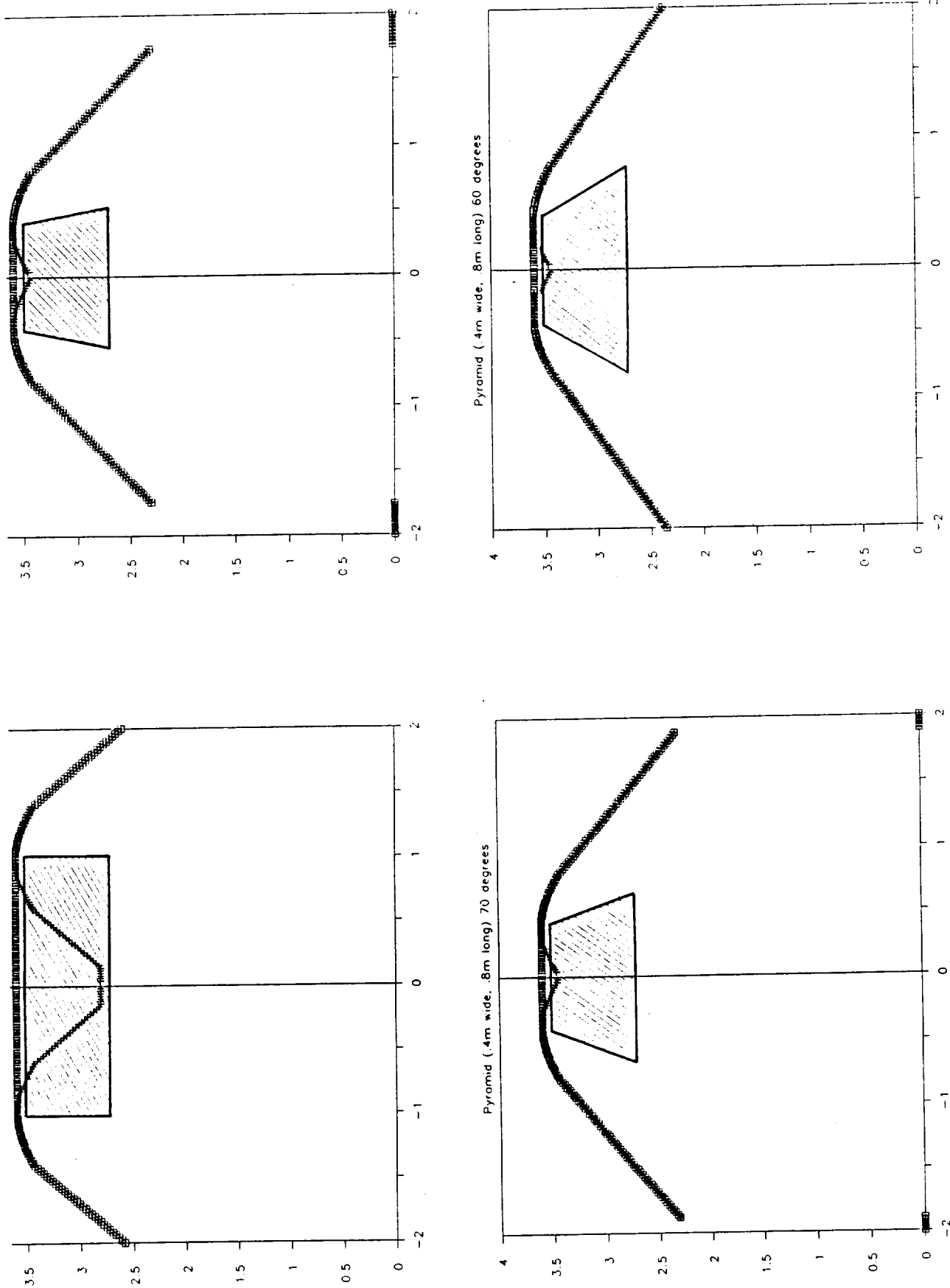


Figure 4. Synthetic GPR profiles over blocks having varying slope angles, (a) 90 degrees, (b) 80 degrees, (c) 70 degrees and (d) 60 degrees. Symbols are described in Figure 3.



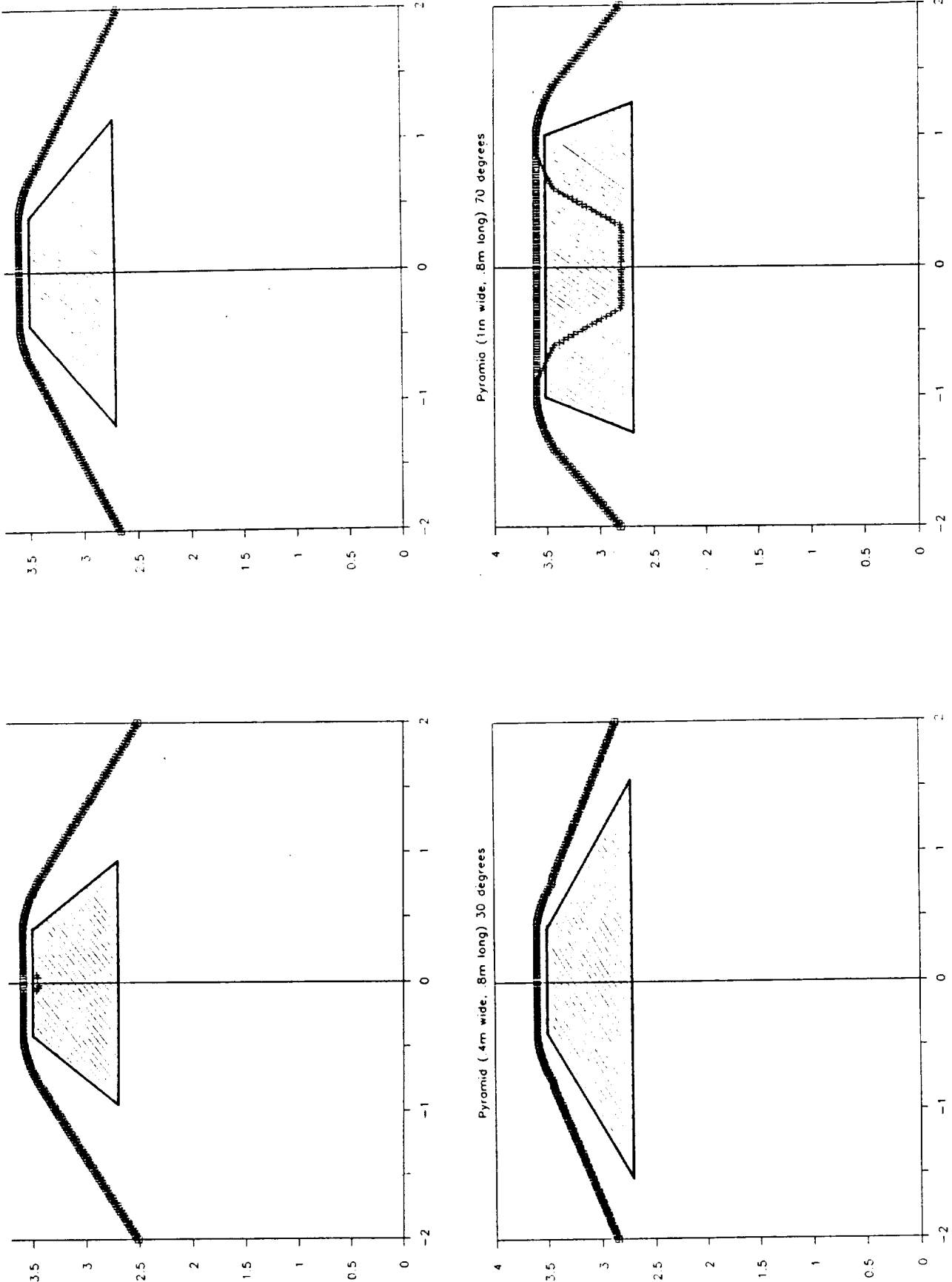


Figure 5. Synthetic GPR profiles over blocks having varying slope angles and widths, (a) 0.8m wide, 50 degrees, (b) 0.8m wide, 40 degrees, (c) 1m wide, 70 degrees and (d) 0.8m wide, 30 degrees. Symbols are described in Figure 3.

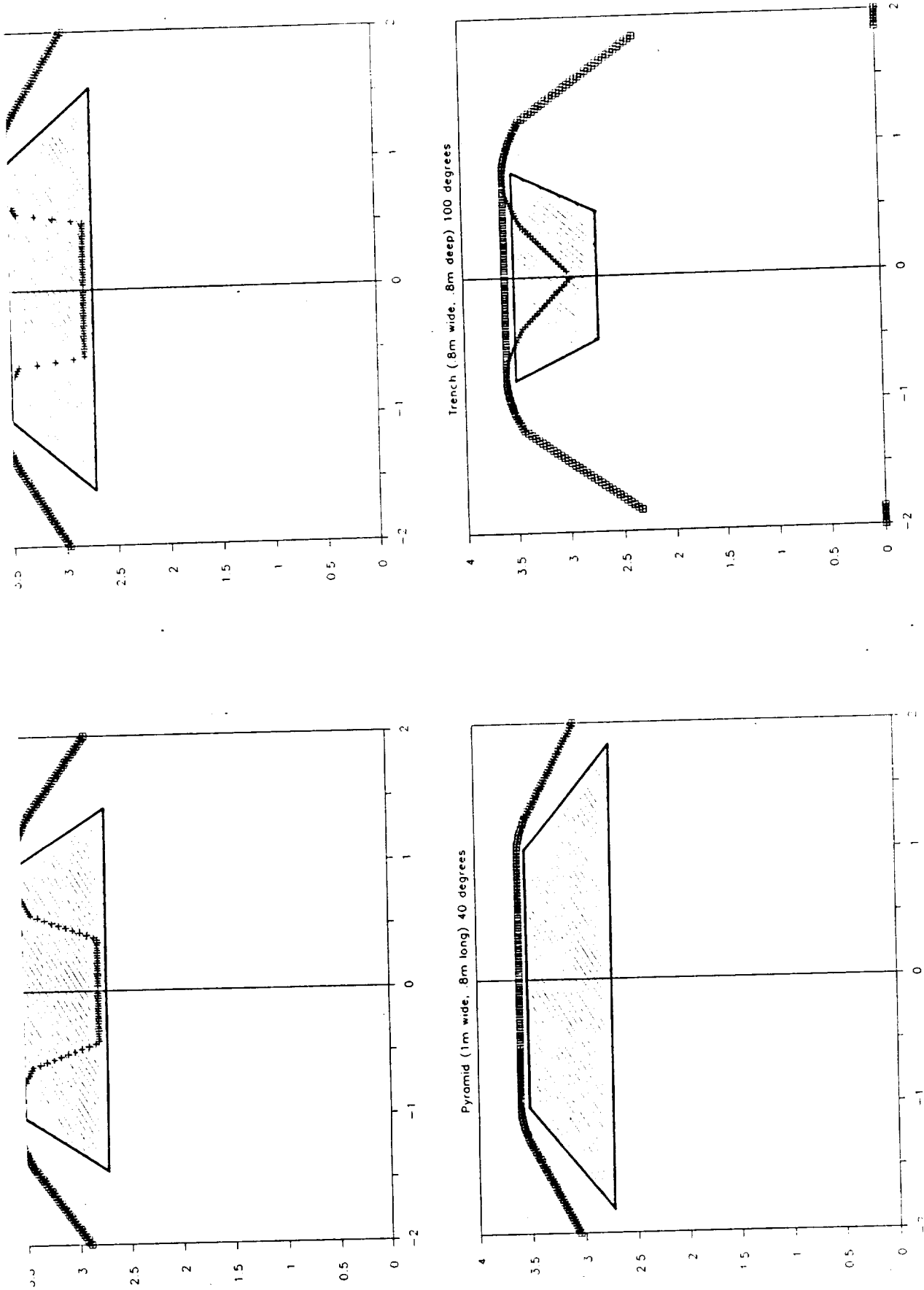


Figure 6. Synthetic GPR profiles over blocks having varying slope angles, (a) 60 degrees, (b) 50 degrees, (c) 40 degrees and (d) 100 degrees. Symbols are described in Figure 3.

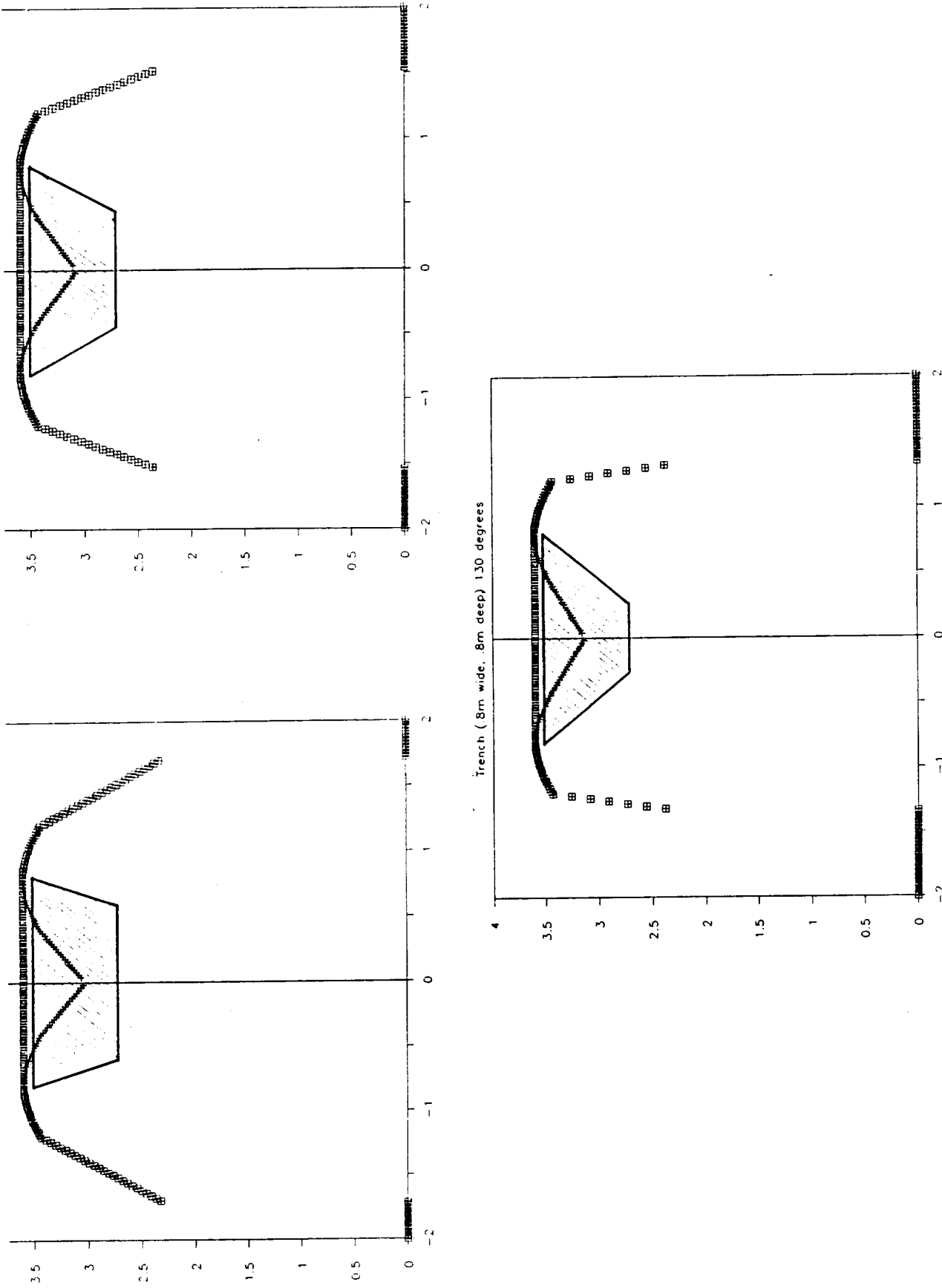


Figure 7. Synthetic GPR profiles over blocks having varying slope angles, (a) 110 degrees, (b) 120 degrees and (c) 130 degrees. Symbols are described in Figure 3.

The basic idea is to use neural network paradigms as separate objects within the object oriented programming environment. Nets for associative memory, nets for self organization and back-propagation nets for discrimination, will ideally be guided and directed in terms of access and activation by expert system modules. At the time of this progress report, a preliminary knowledge base has been assembled, the components (expert system shell, neural network simulation package, and small talk based object oriented programming environment) have been implemented on a Sun Sparcstation, and software to generate synthetic data for neural network training (Figures 3 to 7, for example) has been assembled.

## INCREMENTAL TESTING

### Synthetic Patterns

Testing of the vision system will interact with system development. Tests will first be completed using synthetic data such as those shown in Figures 3 through 7. That actual GPR patterns look like these synthetic data is demonstrated in Figure 8. The vision system will be supervised until it can perform well on the synthetic data.

### Laboratory Test Tank

To test the system in a more natural environment, but still in a well controlled, laboratory situation, we have constructed as part of this project a laboratory GPR test tank shown in Figure 9. The large GPR test tank has been constructed for testing GPR imaging apparatus under well-controlled laboratory conditions.

The test tank consists of a 2.1m high by x 2.1m diameter fiber-glass and polyester mat stock tank. The aqueous, background, solution in the tank has a high permittivity, hence realistic field situations can be scaled within the tank to distances within a few tenths of a meter.

The aqueous solution will serve two purposes: first, to compress the waves enough to present a scaled-down version of an actual field site, and second, to attenuate the waves enough to keep the sides, bottom, and surface reflections small. Because the permittivity of water is generally an order of magnitude greater than that of most rocks. Electromagnetic waves having equal frequencies can be scaled to a third the wavelength. Furthermore, frequencies higher than that in the field can be employed to further decrease wavelength. The medium's skin depth will be adjusted by adding ionic compounds such as HCl to a specified concentration, yielding the necessary conductivity. The model anomalies will be constructed using resin and graphite.

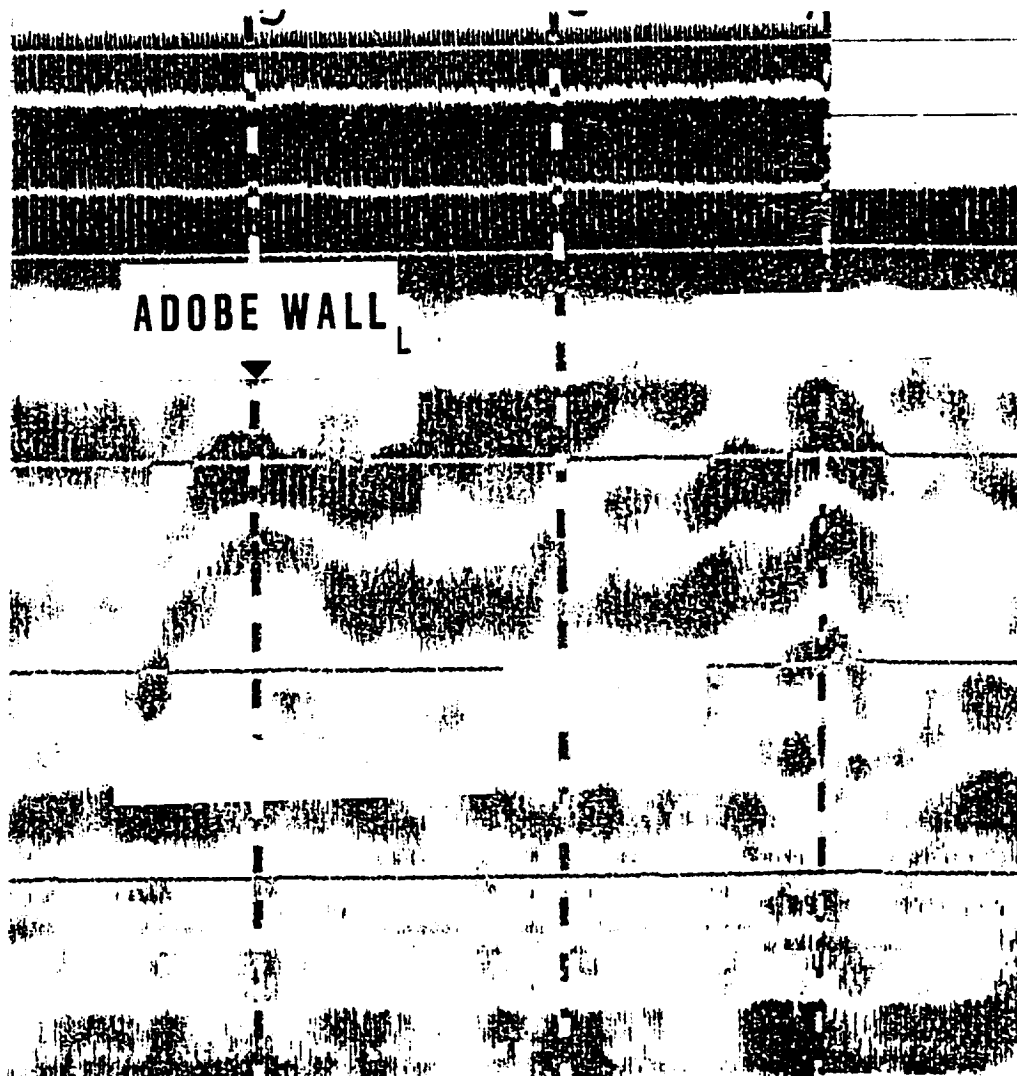


Figure 8. Actual GPR profile from an historical archaeology site at Tubac, Arizona. The adobe wall is similar to the target modeled in Figure 1a.

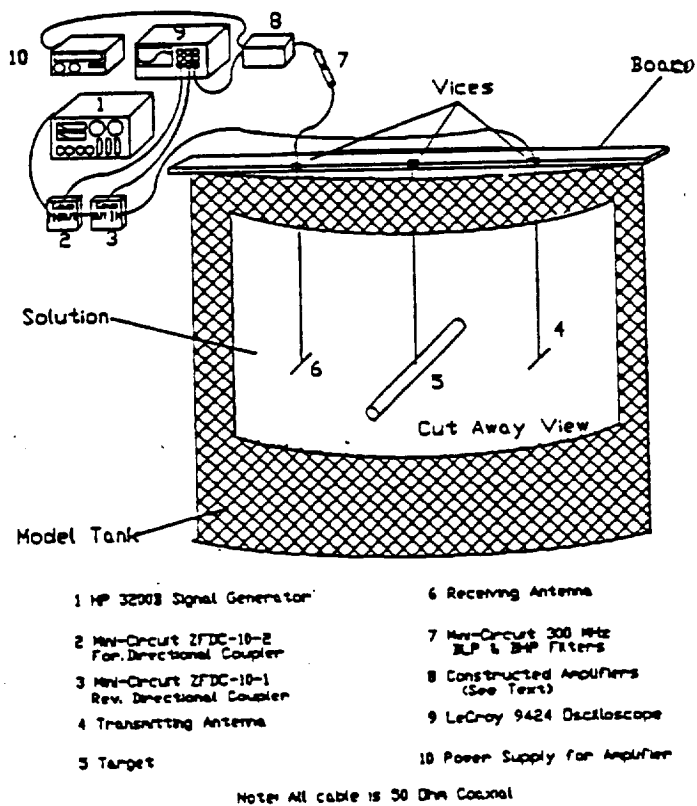


Figure 9. Test tank.

ORIGINAL PAGE IS  
OF POOR QUALITY

The modeling scheme will be chosen to provide an attenuation per wavelength similar to that found in the field. In this way, the same conditions encountered in the field can be modeled in a controlled environment. Using this unique facility, the influence of EM wave velocity, profiling speed and background attenuation on GPR patterns can be assessed while still maintaining homogeneous background conditions. The research during this phase will evaluate the ability of the GPR vision system to extrapolate from synthetic patterns to real, but still ideal, patterns. This phase will also be interactive as the system is adjusted to improve performance.

### FIELD TEST

As a final test, the GPR system will be applied using the GPR test facility at the San Xavier Geophysical Test Site. This test facility has been designed specifically for our SERC GPR work (Figures 10, 11, and 12). Details of this site are provided in McGill, 1990.

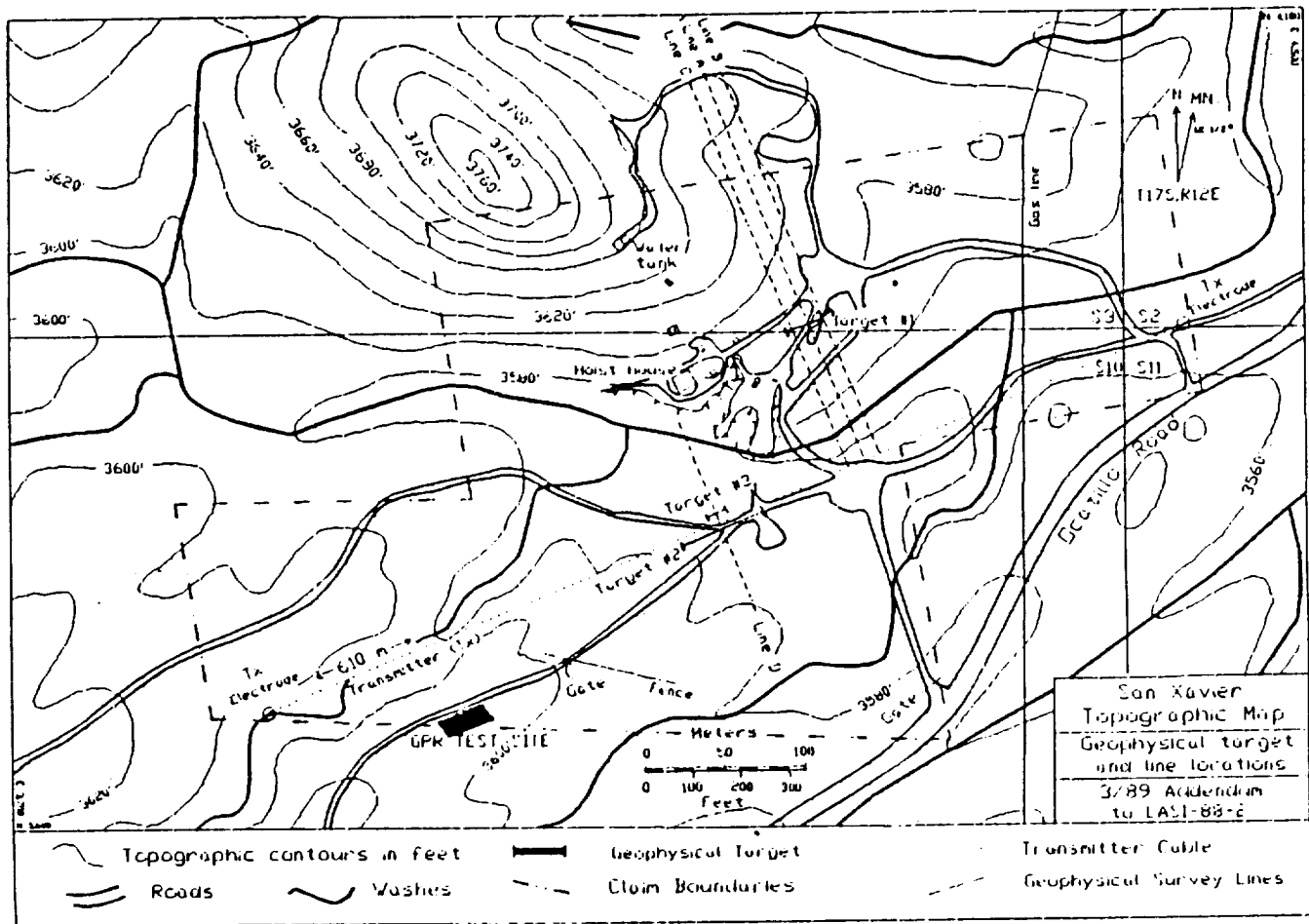


Figure 10. Location of the SERC, GPR test site at the San Xavier Geophysical Test Facility.



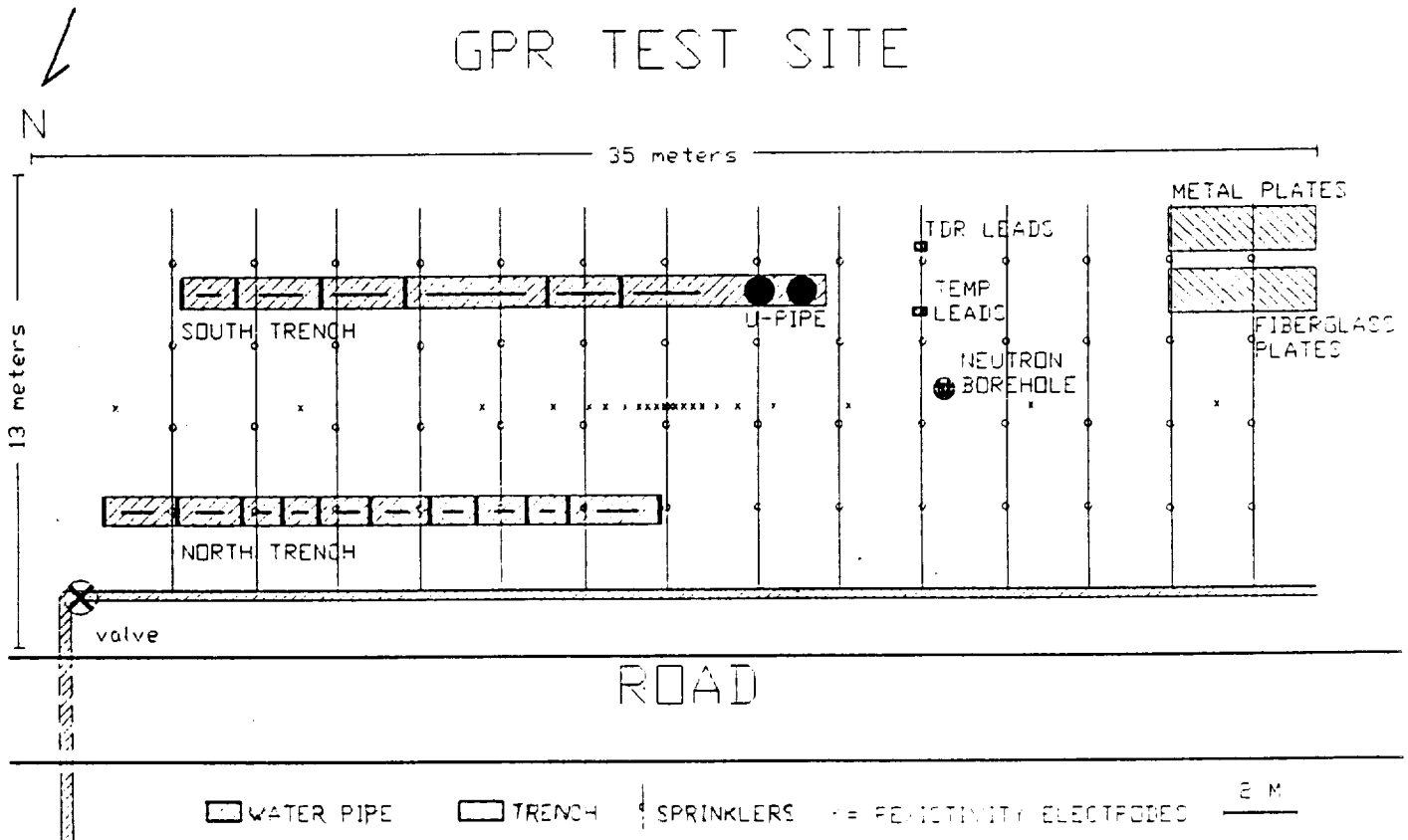
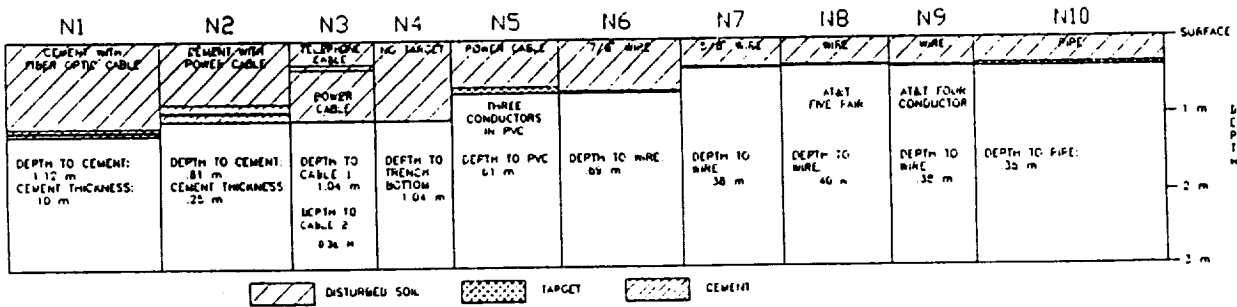


Figure 11. Plan view of the SERC, GPR test site.

# NORTH TRENCH



# SOUTH TRENCH

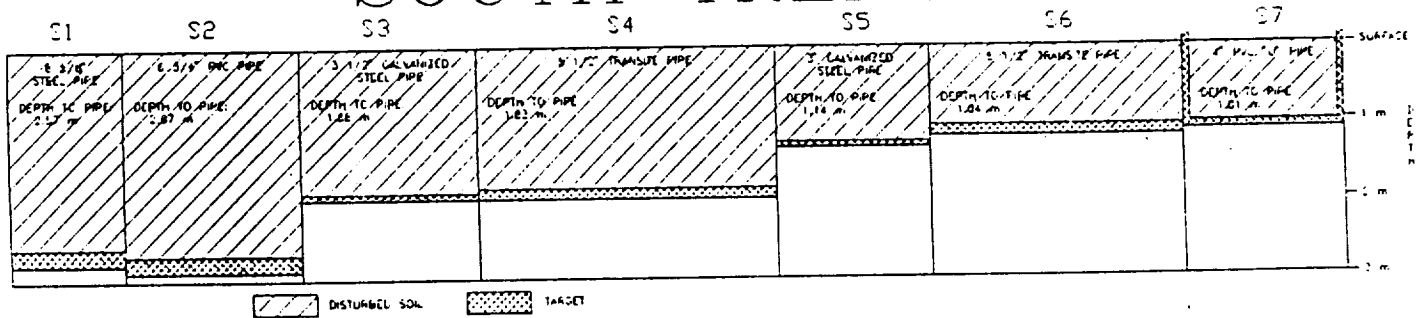


Figure 12. Cross-section of the targets at the SERC, GPR test site.

ORIGINAL PAGE IS  
OF POOR QUALITY

## REFERENCES

McGill, J.W., B.K. Sternberg and C.E. Glass, 1989, "Applications of ground penetrating radar in southern Arizona," Report of the Laboratory for Advanced Subsurface Imaging, LASI-89-2, The University of Arizona, Tucson, Arizona 85721.

McGill, J.W., B.K. Sternberg and C.E. Glass, 1990, "GPR research at the University of Arizona," Third International Conference on Ground Penetrating Radar, Poster Presentation, Lakewood, Co.

McGill, J.W., 1990, "Ground penetrating radar investigations with applications for southern Arizona," M.S. Thesis, The University of Arizona, Tucson, Arizona 85721.

Minsky, M.L. and S. Papert, 1958, Perceptions, MIT Press, Cambridge.

N 9 1 - 2 4 3 8 5 8 9  
14680

## Spacewatch Search for Near-Earth Asteroids

Tom Gehrels  
Lunar and Planetary Laboratory  
The University of Arizona

p. 3

10/7/2

### Abstract

The objective of the Spacewatch program is to develop new techniques for the discovery of near-Earth asteroids and to prove the efficiency of the techniques. We have obtained extensive experience with a dedicated facility, the 0.91-meter Spacewatch Telescope on Kitt Peak, that now has the largest CCD detector in the world, a Tektronix 2048 x 2048 with 27-micron pixel size. During the past year, Research Associate D. L. Rabinowitz joined us in order to help with the installation of software and hardware for optimizing the discovery of near-Earth asteroids. As a result, automatic detection of objects that move with rates between 0.1 and 4 degrees per day has come into routine operation beginning in September 1990.

We appear to be discovering one or two near-Earth asteroids per month, on average. The follow up is with astrometry over as long an arc as the geometry and faintness of the object allow, typically three months following the discovery observations.

During the second half of 1990 we began to consider to increase the discovery rate by replacing the 0.91-m mirror with a larger one. Studies and planning for this switch are proposed for funding during the coming year. We also propose to move the Spacewatch Telescope on the sky, instead of the present mode of having the drive turned off, in order to increase the rate of discoveries by perhaps a factor of 2.

### The Work of this Year

Our main concern during the present year is with the software of the computer system that was newly installed at the Spacewatch Telescope. The Solbourne computer was delivered in October 1989 at about the same time that Dr. David Rabinowitz joined us to do the programming for it, together with J. V. Scotti who had programmed everything for us before. Now, however, the computer routines are much more advanced, with recognition of elongated images and of image motion for moving objects. The fastest of near-Earth asteroids make trails on the CCD frame; during our usual scanning with the drive off the exposure time is about 3 minutes, long enough for a sizeable trail. Rabinowitz had been trained by John Simpson and his group at the University of Chicago in image recognition; he also has an interest and training in physical studies of comets which will be useful in our future. The recognition of asteroid motion had been programmed by J. V. Scotti before and used for quite some time on our 320 x 512 RCA CCD, and now it was adapted and expanded for usage with the new 2048 x 2048 Tektronix CCD. Rabinowitz wrote a paper for the Astronomical Journal describing in detail the software routines for image and motion recognition.

The trail and motion recognition programs have been in operation with the 2048 x 2048 CCD system and the Solbourne computer at the Spacewatch Telescope on Kitt Peak since the middle of April. Since that time, refinements have been programmed on the Solbourne and they were tested night by night during the dark runs of May and June. Further expansion of memory was needed and this was put into operation.

The observing was completely suspended during the months of July and August because of major repair and maintenance to the telescope and also because the monsoon and the short summer nights make the observing less efficient; even in September we still had a lot of cloudy weather.

During the summer Gehrels went again to India where the program of building a 1.27-m Scannerscope has been officially approved for funding by the Indian Government and by the Smithsonian Institution. The first stone was laid for their dome at the Kavalur Observatory in Southern India. They already have a scanning system at their 2.3-m prime-focus reflector at Kavalur, using some of our software that had been made available beforehand during a visit of Indian colleagues to Arizona.

Our Spacewatch system on Kitt Peak began full operation in September of 1990. Its special strength is that it can detect objects when they are far away and slow moving, down to 0.05 deg/day, in addition to fast ones. The observer can decide at a glance whether the object is a Jovian Trojan (or even slower), at various distances in the a main belt, near the inside of the asteroid belt, just barely crossing the Mars orbit, or one that may come even closer to Earth. It is noted, however, that such discrimination works only when

the observations are made near opposition, within a region in ecliptic latitude that is opposite the Sun, where the motion of the object is primarily a reflex of the orbital motion of the Earth.

Since the limiting magnitude of this system is about 20.5 (at 6-sigma detection), we find as many as 400 asteroids per night, which are mostly the ones in the main belt. Because they are so faint, they are nearly all new findings. We let them go, however, because it would take too much time away from discovery scanning to get the astrometric observations that are required for precise orbits. Only the ones that appear to be near-Earth asteroids are followed up with such astrometry in the following weeks and months.

Rabinowitz and Scotti had already in October 1989 discovered our first near-Earth asteroid, 1989 UP. It had been found through visual recognition of a trail on the Solbourne screen, and it was reported in Circular 4887 of the International Astronomical Union (IAU). Its perihelion distance is 0.98 AU, indicating that it is gravitationally controlled by the Earth and may eventually impact. Aphelion is in the middle of the asteroid belt where it probably originated. Its mean diameter is 0.3 km; that is in the lowest 10% of the sizes of near-Earth asteroids that are presently known. W. Wisniewski (personal communication, 1989) observed a lightcurve amplitude of more than a magnitude. It is therefore an elongated object, probably a fragment of a collision in the asteroid belt.

As noted before, automatic operation began in September 1990, which yielded a run with poor weather, but near-Earth asteroid 1990 SS was discovered, an Apollo. October 1990 had exquisite conditions, and four new ones were discovered. In addition, we rediscovered 1865 Cerberus, periodic comet Kopff and our own 1990 UP. The table lists our new objects. The diameters are based on a mean for carbonaceous and silicaceous reflectivity yielding a diameter of 0.075 km for 1990 UN (Bowell, personal communication, 1990). 1990 UN is the smallest natural object observed outside the Earth's atmosphere (IAU Circular 5130); this has drawn attention as far as Hiroshima, Japan! 1990 UP has a peculiar orbit, close to Mars' distance, and a period of rotation of about 16 hours (Wisniewski, personal communication, 1990), possibly slowed by multiple collisions from the usual 2-6 hours for these objects. Or, it may be an extinct cometary core, as it has a high inclination, and its rotation rate was then controlled by outgassing. We still have not learned how to distinguish such cores from fragments of collisions in the asteroid belt.

#### Discoveries of the Second Spacewatch Survey

Identification	Perihelion distance (AU)	Aphelion distance (AU)	Inclination (deg)	Diameter (km)	Date of discovery	Remarks
1989 UP	0.98	2.7	3.9	0.3	89.10.27	elongated
1990 SS	0.87	3.0	25.4	1.0	90.09.25	
1990 TG1	0.78	4.1	8.9	4.3	90.10.14	
1990 UN	0.81	2.6	3.7	0.08	90.10.22	small (H=23.8)
1990 UO	0.31	2.1	27.4	0.3	90.10.22	crosses the Mercury orbit
1990 UP	1.11	1.6	28.7	0.3	90.10.24	slow rotation
1990 VA	0.72	1.2	14.1	2.3	90.11.09	Aten

Perspectives for Next Year

By moving the telescope during the scans the area coverage can be increased so that fast-moving objects have shorter trails, whereby objects are discovered in larger numbers than before. We are beginning to try this, with new software, while the telescope drive also needs improvement. This points in the direction of replacing the 0.91-m mirror with a larger one. We can do this efficiently as a larger telescope, up to 2-m aperture, will fit inside our dome on Kitt Peak. This new plan was further stimulated by T. Triffet by his introduction of the Spacewatch programs to the University of Arizona Foundation for funding.

We propose to prepare more in detail the next configuration of our telescope with a larger mirror. Availability of mirrors, optical designs, CCD parameters, mirror support system and cost estimates will be studied in order to make the program more realistic and specific for fund raising by the University of Arizona Foundation. R. S. McMillan is expert in instrumentation and we are fortunate to have him with some time available for these conceptual designs. For more detailed calculations and drawings we consult with engineer M. Williams.

Steady progress is expected at Kavalur and at Kitt Peak both. With the Spacewatch Telescope we begin to move the telescope so as to increase the area coverage for fast-moving objects, as mentioned. Until now we have obtained the scans by turning off the drive, and the old 36-inch telescope cannot move very fast, but a factor of 2 in area coverage seems possible. We will be observing with the Spacewatch Telescope during all available dark time of about 17 nights per month which already includes about 3 nights more than the half of the month that we had originally negotiated with our partners who search for planets of other stars during the bright half of the month.

In conclusion, we thank the NASA Space Engineering Research Center and its officers for the stimulating support we are receiving.

521-90  
N 91 - 24 386  
/ 4281  
p. 8  
AX 252-003

Compositions of Near-Earth Asteroids

L. A. Lebofsky and M. L. Nelson

Lunar and Planetary Laboratory

The University of Arizona

Abstract

The goal of this study is to determine whether any of the near-earth asteroids contain water-bearing phyllosilicate (clay) minerals. If these minerals are present, they would provide a readily available source of water for propellant generation and use in life support systems. Telescopic detection of water on the near-earth asteroids is complicated because thermal emission from the asteroid itself masks the diagnostic absorption features for objects this close to the sun. Sophisticated thermal models will be necessary to determine whether the absorption features are present. This year, we have continued development of these models and have obtained more telescopic data to test the models.

Introduction

The CI1 and CM2 carbonaceous chondrite meteorites are known to contain clay minerals in their matrix. In fact, the CI1 meteorites contained enough water that it was able to migrate in the parent body, dissolving minerals and redepositing them as evaporite veins. Asteroidal size bodies with these compositions would prove rich sources of water and oxygen, and the resources might be easier to extract from clays than from other oxides. Reflectance spectra of these meteorites are similar to telescopic spectra of some of the C-class asteroids in the main asteroid belt, implying similar mineralogy. Unfortunately, all of these asteroids are extremely dark, which makes it difficult to measure accurate reflectance spectra. The dark components on their surface also mask the presence of other components in their reflectance spectra because the darkest components dominate the reflectance spectra of a mixture of minerals. In addition, the features diagnostic of water occur in the 3-4  $\mu$ m wavelength region. In the main asteroid belt, this wavelength region is still dominated by reflected light, although thermal emission makes a significant enough contribution

that is must be modeled before the reflectance spectrum can be analyzed (Fig. 1). Careful telescopic work has found water absorption features in the telescopic spectra of some of the C-class asteroids, but not all. This makes it impossible to assume that all C-class asteroids will contain hydrated minerals. Recent work by Dan Britt has suggested that some of these asteroids (the ones that do not show the water absorption features) may actually be similar in composition to ordinary chondrites, which do not contain any hydrated phases.

The near-earth asteroids are much more accessible than the main belt asteroids, so it is desirable to determine if any of the C-class objects in the near-earth population contain clays. This is a difficult problem for two reasons. First, the near-earth asteroids are small, and the C-class asteroids are dark, which makes them very difficult to observe telescopically. Second, the near-earth asteroids are much nearer to the sun than the main belt asteroids, which makes them significantly warmer. This shifts the peak in their thermal emission to much shorter wavelengths, thus the thermal component of the asteroids dominates the spectrum in the 3-micron region where the diagnostic water absorption feature is present. Simple thermal models are not accurate enough to remove this thermal contribution.

Hapke has proposed the first model which treats the reflected and emitted radiation simultaneously, which offers the best opportunity for modeling the spectra of the near-earth asteroids. The model is an application of radiative transfer theory to particulate surfaces. It includes terms for the absorption and scattering properties of the component minerals, the photometric geometry, and the physical properties of the surface. Reflectance spectra can be calculated from the model and compared to measured spectra, or the model can be fit to observational data, making appropriate assumptions about the unknown parameters. Parts of this theory have been, and are being tested extensively, but the thermal terms are new and relatively untested.

We have proposed to apply this theory to analyze telescopic spectra of C-class near-earth asteroids to determine their water content. Before this is possible, we must test the theory to



determine its validity and sensitivity in better understood applications. This year, we have done much to advance our understanding of the theory.

#### Results for This Year

*Software Development.* This year Marcia Nelson has ported a major program to the Planetary Image Resource Center computers at the Lunar and Planetary Laboratory. This program calculates many of the terms in the published Hapke theory, and fits the equations to reflectance spectra to determine parameters in the theory of interest, such as the grain size and abundance of component minerals.

*Modeling.* Last year, Marcia Nelson worked on three modeling applications to improve our understanding of the Hapke model. In the first project, she showed that the theory can calculate spectra of mineral mixtures directly from the optical constants of the components, and given the end members, the mineral abundances can be determined fairly accurately from the optical constants. In the second project, she used the theory to determine the modal composition of the surface of Vesta, assuming end members from the pre-existing literature. In the third project, she calculated spectra of some lunar analogue mineral mixtures to study the mixture systematics.

This year, she has been continuing to analyze her previous results. The previous Vesta analysis was adequate, but not as good as had been hoped. Initially, the problems had been attributed entirely to the deficiencies in the mineral chemistry of the end members Nelson was able to obtain from the literature and the lack of information on the grain size. The differences in mineral chemistry definitely contributed to the problems, but on closer examination of the initial failed attempts, she realized that the uncertainty in the grain size was also a major contributor. No information was available on the grain sizes of the minerals chosen as end members. A uniform grain size was assumed for all components which was reasonable for a regolith, assuming asteroid regoliths are similar to that of the Moon. This year, it was realized that the grain size of one of the components was probably much larger than the one assumed, because the laboratory spectrum

was unusually dark for that mineral. This distorted the calculated abundances because the fitting program was forced to add excessive amounts of the brighter components to match the continuum reflectance.

Further analysis showed that in all three of these applications, the grain size had a major effect on the model. This is a parameter which had not really been examined systematically in the theory. We didn't have a laboratory available to create an ideal test set of spectra, so she found ways to learn as much about this problem as possible with the spectra obtained for the other projects.

We had all of the necessary data for a complete analysis of the single grain size fraction used in creating the samples for the first project. Nelson measured the actual grain size of the samples from a number of scanning electron microscope images of the samples and used these to calculate the average grain size. This had been used in the initial calculation of the mineral abundances. She then used the software ported this year to fit the laboratory spectra to determine what grain size provided the best model fit. The grain size determined by the fit differed insignificantly from that determined by direct measurement. She next made histograms of the actual grain size measurements. The theory assumes spherical grains, but the actual measurements of the length and width showed a bimodal distribution. She determined the relative areas under the two peaks and calculated spectra for mixtures of grains of sizes corresponding to the two peaks and abundances proportional to their areas. These spectra were virtually indistinguishable from those calculated using a single average grain size (Figures 2 and 3).

This work has shown several things. First, it has proven that the theory is using the actual average grain size, and not some imaginary grain size determined by the mean optical pathlength of the light in the grains. It has also shown that an average grain size is sufficient to obtain valid results for a narrow grain size fraction. And it has shown that the theory results are extremely sensitive to the grain size. This means that a reasonable range of grain sizes will have to be used to create a series of possible results when the model is applied to real surfaces where the grain size is unknown. Nelson is in the process of doing this with the Vesta model at this time.

*Observing.* This year, we have had four observing runs (two at the MMT and 61" near Tucson and two at the IRTF in Hawaii), which were partially funded through NASA Planetary Astronomy. Useful data were obtained on half of these runs. Telescopic spectra of several asteroids were obtained over 1-3.5  $\mu\text{m}$  wavelength range. These data will be used to test the models we are developing. The Vesta data will be used to test the complete theory next year.

### Publications

- Gaffey, M. J., L. A. Lebofsky, M. H. Nelson, and T. D. Jones. Asteroid surface compositions from earthbased reflectance spectroscopy (submitted for inclusion in conference volume edited by Carle Pieters).
- Howell, E. S. and L. A. Lebofsky. *Bull. Amer. Astron. Soc.*, **22**, 1122-1123, 1990.
- Jones, T. D., L. A. Lebofsky, J. S. Lewis, and M. S. Marley. The composition and origin of the C, P, and D asteroids: Water as a tracer of thermal evolution in the outer belt, *Icarus*, **88**, 172-192, 1990.
- Lebofsky, L. A., W. B. Hubbard, E. Asphaug, D. M. Hunten, R. L. Millis, O. G. Franz, L. H. Wasserman, M. A'Hearn, R. Schnurr, A. R. Klemola, W. Osborn, F. Vilas, A. E. Potter, P. D. Maley, and P. L. Manly. *Bull. Amer. Astron. Soc.*, **22**, 1113, 1990.
- Lebofsky, L. A., T. D. Jones, P. D. Owensby, M. A. Feierberg, and G. J. Consolmagno. The nature of low albedo asteroids from 3- $\mu\text{m}$  spectrophotometry. *Icarus*, **83**, 12-26, 1990.
- Nelson, M. L. Sensitivity of Hapke modeling of mixtures to grain size. Lunar and Planetary Science **XXI**, 869-860, 1990. (Abstract of talk presented at the LPSC XXI Conference 3/90).
- Nelson, M. L. and R. N. Clark. Comparison of different measures of the grain size in Hapke modeling. *Bull. Amer. Astron. Soc.*, **22**, 1033, 1990. (Abstract of talk presented at the Division of Planetary Science Conference 10/90).

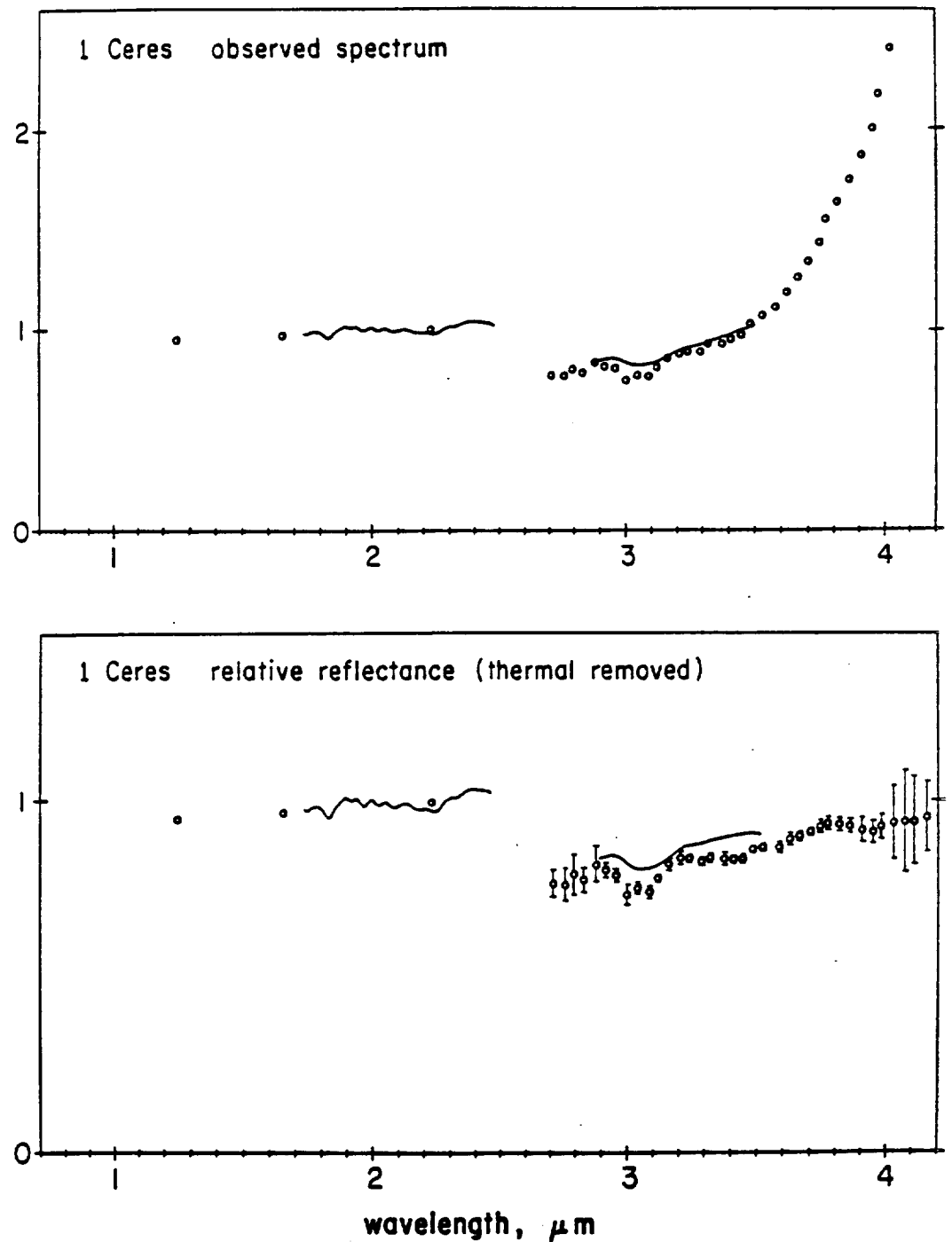


Fig. 1. Observations of the spectral reflectance of Ceres between 1 and 4  $\mu\text{m}$ . The solid lines are high-resolution Fourier spectra and the circles are medium-resolution spectrophotometry. The upper curves are the observed spectra of Ceres, including the thermal emission from the asteroid at longer wavelengths. The bottom curves are the relative reflectance with the thermal emission removed using the "standard thermal model."

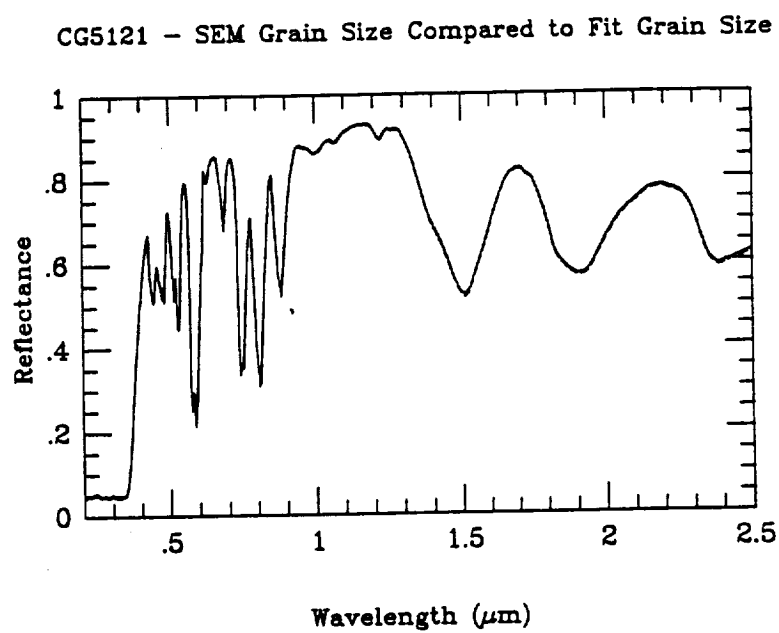


Figure 2. Calculated spectra of corning glass 5121. The solid line is calculated using the measured grain size and the dashed using the model grain size.

CG5121 - Measured Spectrum compared to Spectra Calculated  
From the SEM Grain Size and From a Grain Size Mixture

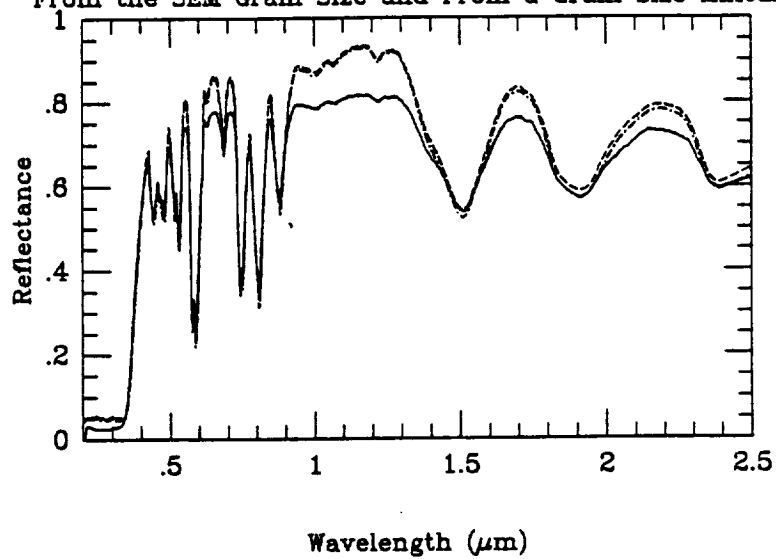


Figure 3. The measured spectrum of coming glass 5121 is plotted as a solid line. Spectra calculated using the measured grain size (dashed) and the grain size mixtures (dash-dot) are plotted as dashed lines. The calculated spectra are virtually identical.

#### **IV. SYSTEM AUTOMATION AND OPTIMIZATION**

N 9 1 - 2 4 3 8 7

Development Of A Figure-of-Merit For Space Missions

Bruce Preiss, Thomas Pan, and Kumar Ramohalli

Aerospace and Mechanical Engineering

University of Arizona

**ABSTRACT**

The concept of a quantitative figure-of-merit (F-o-M) to evaluate different and competing options for space missions, is further developed. Over six hundred individual factors are considered at the time of this report. These range from mission orbital mechanics to In-Situ Resource Utilization (ISRU/ISMU) plants. The program utilizes a commercial software package for synthesis and visual display; the details are completely developed in-house. Historical FoM's are derived for successful space missions such as the Surveyor, Voyager, Apollo,... A cost FoM is also mentioned and will be further developed. The bulk of this work is devoted to one specific example of Mars Sample Return (MSR). The program is flexible enough to accommodate a variety of evolving technologies. Initial results show that the FoM for sample return is a function of the mass returned to LEO, and that missions utilizing ISRU/ISMU are far more cost effective than those that rely on all earth-transported resources.

**INTRODUCTION**

The variables in a space mission are so numerous and their interactions so complex that it is not easy to visualize the overall mission impact of many components. Frequently, we are faced with difficult choices that must consider competing technologies, anticipated advances, expected improvements in reliability, and the overall life-cycle costs that could easily run into hundreds of millions of dollars. For initial screening purposes, it was felt highly desirable to develop an overall figure-of-merit (FoM) for the mission that could be used for ranking these competing candidates. When one recognizes that the parameters vary from orbital mechanics to rocketry, and chemical plant masses to the power source reliability, the difficulty of accurately combining these becomes apparent.

Work was initiated last year on this difficult task. The input parameters were divided into four major categories: the mission, transportation, ISRU/ISMU plants, and the support systems. The feasibility of developing a meaningful FoM was proven. The quantitative examples included various MSR missions that clearly showed the advantages of ISRU/ISMU [reference 1]. It was felt desirable to further develop this highly useful concept. One of the main aims this year was to tie this concept to the current SERC work on the oxygen plant design. In addition, the FoM's of various successful



missions were examined within the framework of the software.

Section II describes the input parameters. Section III describes the software development. Section IV presents the principal results. This report concludes with a brief outline of future work and applications.

#### THE INPUT PARAMETERS

The FoM concept organizes the inputs into four major categories and then integrates the dependent variables through the appropriate governing equations. The four categories are loosely described as mission details, rocket design, in-situ resource utilization (ISRU), and support components. The bulk of the inputs pertain to the joint spacecraft and rocket design. This is where most of the flexibility will occur in any given design. The governing equations have been modified to accurately reflect the dependencies of many detailed spacecraft parameters. The categories have been developed and defined as much as possible, but the technology is constantly changing and innovations are always being introduced. It should be stressed here that the FoM is a dynamic property since it directly reflects even minor changes in the mission planning.

#### SOFTWARE DEVELOPMENT

The FoM itself is calculated within a commercial spreadsheet software package. The spreadsheet option was chosen over a programming language due to its ability to integrate either internal or external data and then present the results in simple color graphics. Ease of use is also a major factor, since no knowledge of any programming language is necessary. Only an understanding of the basic equations is required. The spreadsheet structure was completely reorganized to simplify the input process and take full advantage of the three-dimensional capabilities of the software. The spreadsheet equations and structure have been generalized wherever possible to maximize the flexibility of the approach.

Two key emerging technologies have been included in the spreadsheet program. The ISRU concept and the use of modular engines are options now available for the mission planner. Both technologies are innovations that may provide major improvements in mission capabilities. The quantitative effect of either on mission planning can now be calculated in a relative manner.

The ISRU idea is to use local resources whenever possible to help fulfill the mission goals. Exploration of the Earth has historically utilized local resources to succeed, and the natural and logical progression is to apply this concept to planetary exploration also. A proof-of-concept oxygen production plant is being built at the Center for the Utilization of Local Planetary Resources. It is designed to use an electrocatalytic process to convert gaseous carbon dioxide into molecular oxygen. The available data from the Center has been included in the spreadsheet to provide accurate figures for the masses of each component. The projected production rate and total mass

are, therefore, all based on current research directly related to the manufacture of the plant. As the technology matures, the spreadsheet can easily be updated to reflect the improvements.

The use of modular engines will not reduce the initial total mass of the spacecraft as the use of ISRU will. However, the other direct benefits will have an overall effect of increasing the FoM. The benefits to be gained from modular engines are increased reliability, reduced risks, simpler reparability. There is even the important added benefits of a reduction in both design and production costs. The spreadsheet has been configured for the possible use of modular engines for the return voyage. The size of the engine is dictated by the thrust required for the last staging maneuver. The number of engines needed in a cluster for all previous stages is based on this one engine. All the calculations are done automatically. The current limit imposed on the modular engine design is the restricted use of propellants. Only fuels and oxidizers that do not need refrigeration for the return voyage in space can be utilized.

A propellant database has also been incorporated into the overall scheme for the calculation of the FoM. The database has been constructed in another commercial software package with which the spreadsheet can form a direct link. All of the pertinent performance parameters have been input for a total of twenty-six different propellant combinations. The parameters that have been varied for each database record are the chamber pressure, oxidizer to fuel ratio, and the nozzle area ratio. For each of these various combinations, the chamber temperature, characteristic velocity, specific impulse, pressure ratio, and vacuum specific impulse have also been input. Special thermodynamic data is being included in the spreadsheet for each propellant in the database so the storage parameters can be automatically calculated. Only by knowing the specific volume of both the fuel and oxidizer can the tanks be sized accurately. The database, of course, could be used for other projects, but its sole use until now is for the FoM spreadsheet.

## RESULTS

The FoM definition is allowed flexibility in order to apply to almost any mission architecture. A set of definitions has been devised, and a few of them have been applied to historical U.S. space missions. To date, only technical definitions have been utilized. Cost definitions have been identified and would be very useful, but the difficulty in gathering accurate accounting data has caused many problems. The application to historical missions has identified the usefulness of using different definitions depending on the type of mission. For example, the definition used in a sample return mission is defined as the mass of the payload returned to low-Earth orbit (LEO) divided by the initial spacecraft mass starting in LEO. It was important to factor in the mass of the sample for this type of mission, but of course, this parameter did not apply to previous orbiter missions. In essence, the flexibility of the FoM concept was tested within a historical context and given a certain validity that will hopefully also apply to any future missions. In an effort to quantify all important

aspects of a planned mission, all the definitions factor in a multiplier to account for variations in reliability, reparability, and risk.

The spreadsheet has been developed sufficiently to handle a rigorous analysis of a Mars Sample Return (MSR) mission. The following graphs show some preliminary findings in the analysis. The FoM is defined in both graphs as

$$FoM = \frac{\text{Sample Mass}}{\text{Initial Mass in LEO}} \times [R_{\text{factor}}] \times 10^4$$

where

$$R_{\text{factor}} = (\text{Inverse Risk}) \times (\text{Reliability}) \times (\text{Reparability})$$

The first graph presents the FOM for a range of payload masses to be returned to LEO. The small masses represent a typical sample mission with the larger masses possibly representing an evolution of manned missions. A series of different propellant combinations is shown with some including the use of ISRU. The important thing to note is that the maximum FoM within each mass category is always accomplished by using ISRU. The second plot shows the typical variation in mission strategies for a MSR mission. The relative gains realized through the use of modular engine configurations and with ISRU, both separately and together, are presented. Two propellant combinations are shown for comparison. The benefits attained using both technologies may not seem greatly significant on the surface, but in terms of the sample mass, even small improvements are very important.

#### FUTURE WORK

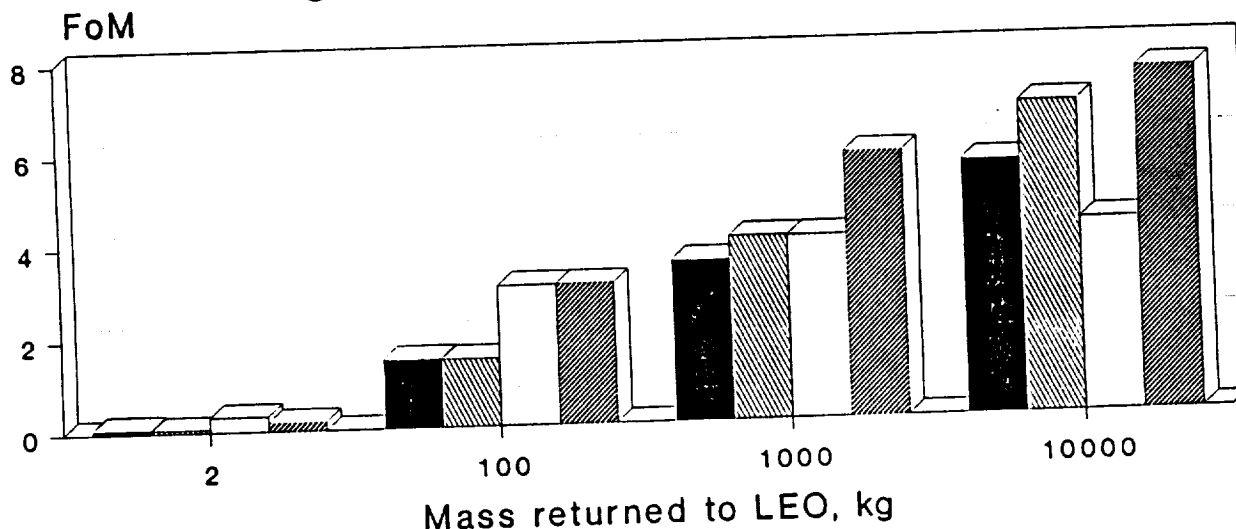
The FoM methodology is fairly unique since it identifies promising mission architecture from the initial planning stages before focusing on more detailed design. The spreadsheet is configured for a MSR mission, and since a mission of this type is only in the planning stages at this point in time, it would be ideal to analyze any preliminary results the FoM can provide. The previous results are interesting in their own right, but a much more detailed analysis is still to be accomplished. All the propellants in the database need to be analyzed to determine possible hidden advantages in an overall framework. In addition, many of the spacecraft design variables should be varied to help focus on a more beneficial design. Both strong and weak correlations need to be identified between related input parameters, and further overall optimization needs to be accomplished.

REFERENCES

1. K.N.R. Ramohalli, B. Preiss, and T. Kirsch, "A Figure-of-Merit Approach to Extraterrestrial Resource Utilization," paper no. IAA 89-716 at 40th Congress of the International Astronautical Federation, 1989, also accepted in AIAA Journal of Propulsion and Power, 1990.

# MARS MISSION VARIATIONS

## Figure-of-Merit vs. Returned Mass

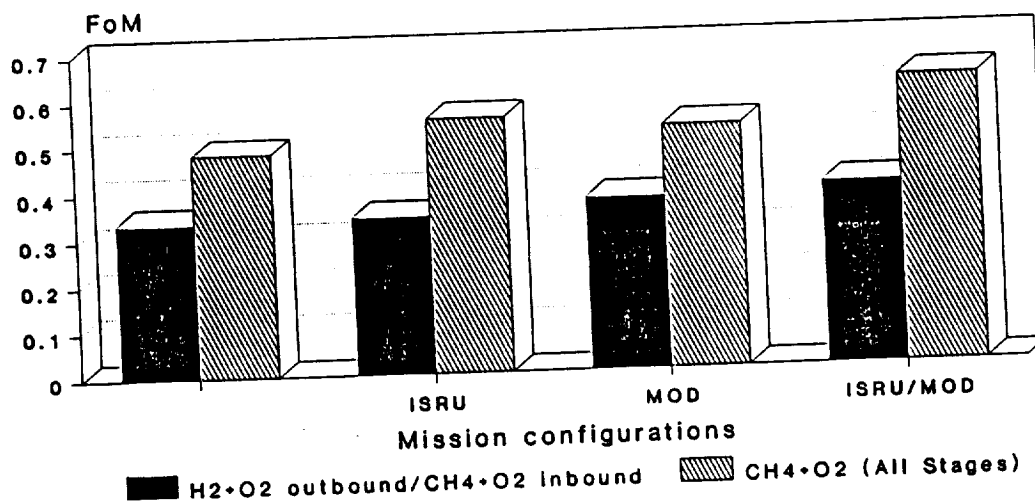


$$\text{FoM} = [(M \text{ sample}) / (M \text{ LEO})] \cdot R \text{ factor} \cdot 10^4$$

$$R \text{ factor} = \text{Inverse Risk} \cdot \text{Reliability} \cdot \text{Reparability}$$

# MARS SAMPLE RETURN VARIATIONS

## Sample Mass = 4 kg



MOD = Modular engine use  
ISRU = In-situ resource utilization

ORIGINAL CONTAINS

COLOR ILLUSTRATIONS

## Abstract

This is a multicomponent, multidisciplinary project whose overall objective is to build an integrated database, simulation, visualization and optimization system for the proposed oxygen manufacturing plant on Mars. Specifically, the system allows users to enter physical description, engineering and connectivity data through a uniform, user-friendly interface and stores the data in formats compatible with other software also developed as part of this project. These latter components include programs to simulate the behavior of various parts of the plant in Martian conditions; an animation program which, in different modes, provides visual feedback to designers and researchers about the location of and temperature distribution among components as well as heat, mass and data flow through the plant as it operates in different scenarios; a control program to investigate the stability and response of the system under different disturbance conditions; and an optimization program to maximize or minimize various criteria as the system evolves into its final design. All components of the system are interconnected so that changes entered through one component are reflected in the others.

## Introduction

The design of complex mechanical systems which are required to operate reliably and autonomously in alien environments is an intricate and iterative process which requires extensive testing in a wide range of hypothetical scenarios. Given the impossibility or the high cost of recreating alien environments on earth, such scenarios have to be generated by computers and applied to simulated versions of the actual mechanical systems. As a result, computer simulation has become an essential and integral part of designing and building mechanical systems to be used in space or extraterrestrial environments.

This specific project was initiated with the aim of providing the essential simulation capability for the oxygen manufacturing plant that the Space Engineering Research Center at the University of Arizona has undertaken to build on Mars. Because of the multidisciplinary nature of the plant's design process, this integrated software project was designed to provide data storage, classification, access and visualization services for all the different groups working on the design and testing of the plant. This project consists of the following principal components

- i) A relational bill of components database;
- ii) A visualization system for animation of the plant's dynamics;
- iii) A control design system associated with data collection equipment connected to an experimental setup;
- iv) An optimization system to maximize specified performance criteria while meeting weight, thermal, cost and other constraints.

The technical features and current status of these principal components are briefly outlined below.

### Relational Bill of Components Database

The purpose of this component of the project is to construct a uniform data entry system which can act as a server of information to other components of the project in the appropriate format after conducting basic checks against physical constraints. In addition, the system serves as a rudimentary expert system which can monitor spatial, thermal, electrical and data compatibilities among different system components. Ultimately, this database will act as the common user

interface for entering every piece of information about the system as the system evolves into its final design.

The FoxPro 1.02 database package has been selected to serve as the basic platform for building the desired relational database system. This package was selected principally because of its sophisticated multiple-window and pull-down menu user interface which can permit users from any background to operate the system with ease. The package was used to design a customized data entry and organization system which is specific to the needs of the overall project. The primary objectives of this design was to build a standard, portable database structure, to provide a uniform graphical user interface and to facilitate data access from other software components in the project.

The basic philosophy underlying the design of the database system is to represent the various components in the plant in terms of their connections to each other rather than their own features and properties. This was accomplished by abstracting each of the components into their various input-output characteristics and representing those characteristics in database entities corresponding to connections. This model of the system is depicted by Fig. 1. where a component *A* is connected to component *B* by a set of connections each of which represents an input-output relationship between *A* and *B*. For example, if *A* is a pump and *B* is a heat exchanger, one connection may represent the mass flow from *A* into *B* (with corresponding inlet and outlet pressures) and another one may be the heat flow from *A* to *B* (with corresponding inlet and outlet temperatures). Consequently, a pipe between *A* and *B* can be abstracted into two different connections: a mass-flow connection and a heat-flow connection. In this abstract model, space is also represented as a connection so that intervening volumes of space connect one component to another (with corresponding spatial coordinates on each sides). A space and thermal connection is assumed (and represented by appropriate connections) to exist between every pair of components in the system.

Each component of the plant and each appropriate connection of each component are entered on data forms which are predesigned with appropriate data fields for each common type of component that is used in the plant (e. g. pump, heat exchanger, thermal, mass-flow, etc.). Sample component and connection data forms are shown in Fig. 2. Both component and connection data forms incorporate data fields which are common to all components and connections as well as fields which are specific to certain types of components and connections. Generic forms have been designed so that users can design new forms for components and connections for which forms have not yet been designed. In addition, users can add data fields to existing predesigned forms if that data is needed for a new software package that is being developed for the overall project.

Once all the components in the plant together with their connections are entered into the database, a program written in the FoxPro database language (compatible with other common database languages such as dBase IV) carries out basic compatibility checks between each pair of components that are connected to each other. Since each component is connected by at least space and thermal connections to each other component in the system, this compatibility check includes physical interference and high and low-temperature proximity checks. Warnings are issued to the user in the event any of the compatibility checks fail. This is an essential function for an iterative design process in which a plant component is typically replaced by another model because of a specific improved feature, but the replacement results in changes in a complete array of characteristics associated with the component and its connections (e. g. a pump may be replaced with one that has better power efficiency but the new pump's outlet pressure may not be compatible with the inlet pressure specifications of the existing heat exchanger). A schematic flow-chart of the operation of the database system is shown in Fig. 3.

The database system has the capability to write the entered data in a format that is usable by the other components of this project. Over the coming months, this capability will be enhanced to generate all the necessary files for the other software components of the project. In addition, the

database software will be modified to accept input generated by changes made in other programs of the integrated system.

### **Visualization/Animation System**

The purpose of this component of the project is to construct an animation and visualization system which can serve both as a design tool (especially for packaging) and a communication tool to convey the status of the plant design to researchers and students working on the overall project. With appropriate hardware, this component may ultimately serve as an interactive graphical user interface for controlling different parts of the plant while it is being tested on earth and a troubleshooting system with "what-if" features when the plant is operational.

In this component of the project, each component of the Martian oxygen manufacturing plant is represented as a geometric object of the appropriate shape and size. These objects are constructed in three dimensions using flat polygons. Each polygon, its color, fill, edge and opaqueness attributes as well as its connectivities to other polygons are entered in a data file. This data file (which will ultimately be generated by the relational database program outlined in the previous section) is then read by GAAP (Graphical Analysis and Animation Program), an in-house package developed at the Computer Aided Engineering Laboratory of the Department of Aerospace and Mechanical Engineering, which can draw and manipulate the objects on the screen. GAAP can be used to program the motion of different objects on the screen as well as the perspective of the viewer by varying "camera" angle and location. Figures 4 and 5 show two snapshots of animation sequence depicting the landing and operation of the oxygen manufacturing plant on Mars. These two images were created in the initial stage of the project on a Silicon Graphics IRIS 3130 using GAAP.

Figures 6 and 7 show the same plant in greater detail and with better texture. These images were created on a Silicon Graphics IRIS 4D using Wavefront, a commercial graphics package. This newer system offers substantially better performance features and capabilities and is expected to be the hardware/software platform for the final version of the animation and visualization system for the Martian oxygen manufacturing plant.

Over the next year, the animation and visualization package will be enhanced so that any changes made from the relational database will be instantly reflected in the images generated by this package and any changes in the position of an object, affected interactively with a pointing device through the animation program, will be reflected in the database. Such a capability would be invaluable for designing and packaging the plant.

### **Control/Data Collection System**

The purpose of this component of the project is to construct a control design and data collection system to investigate the stability, sensitivity and response of the plant system to external disturbances and changes in operating parameters. Progress on this component of the project was limited due to unexpected cuts in funding and subsequent departure of personnel assigned to this task.

Over the next year, this component will be developed to perform data collection and basic control functions and to interact with the relational database and animation and visualization software.

### **Optimization System**

The purpose of this component of the project is to maximize or minimize various design and performance criteria subject to physical and cost constraints. This component has not yet been started. Subject to funding levels, this component will be started over the next year with the initial aim of optimizing the placement of different components of the plant inside a constrained space. The program to be developed will interact with both the animation/visualization and the relational database packages for its input and output.



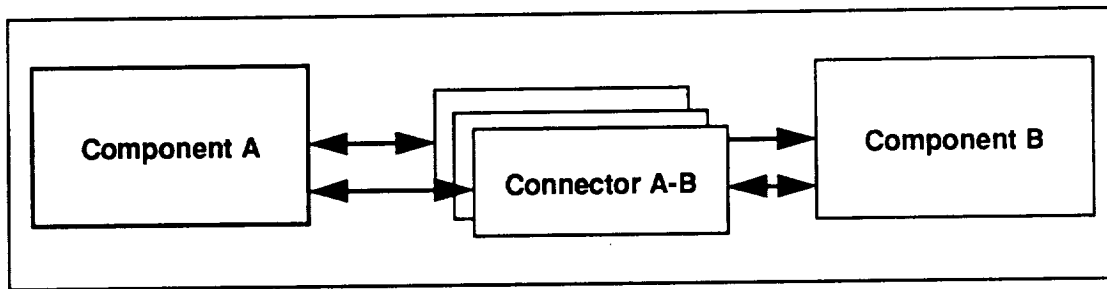


Figure 1. Layered representation of connections

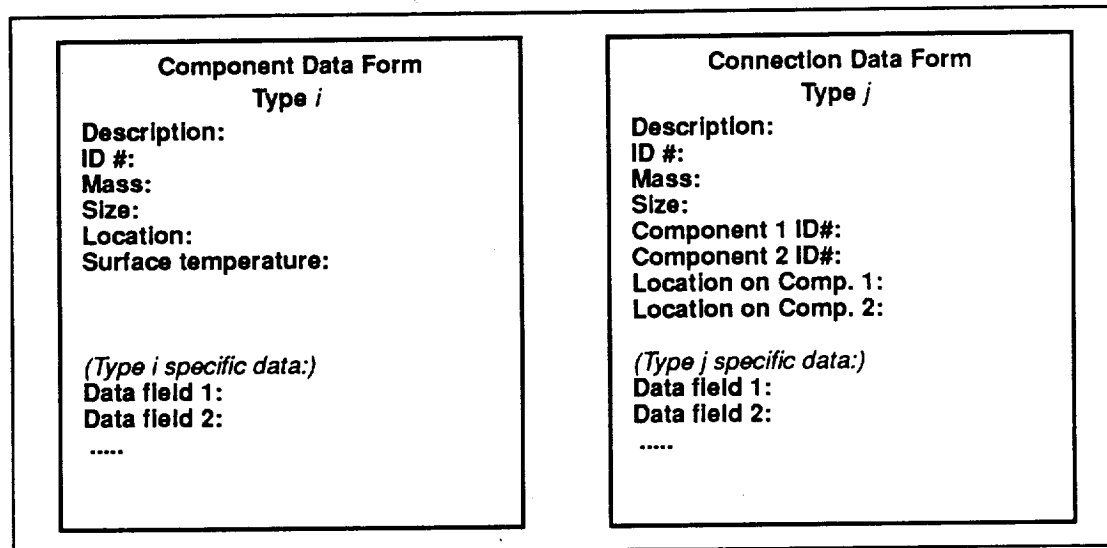


Figure 2. Sample data forms for components and connections

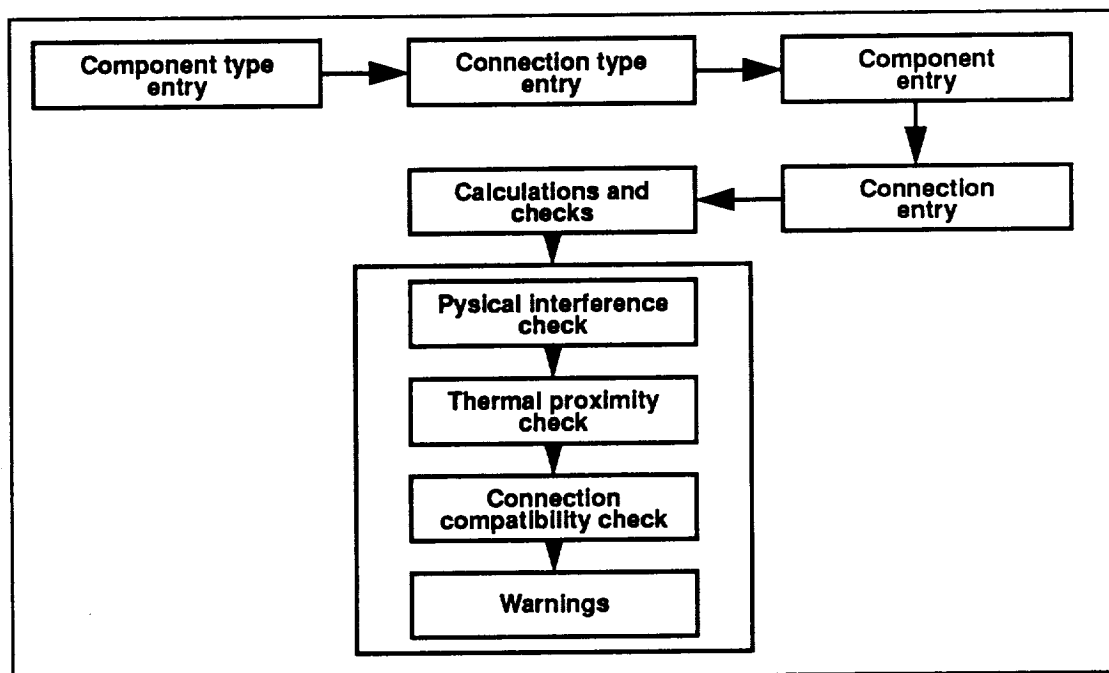


Figure 3. Schematic of database functions

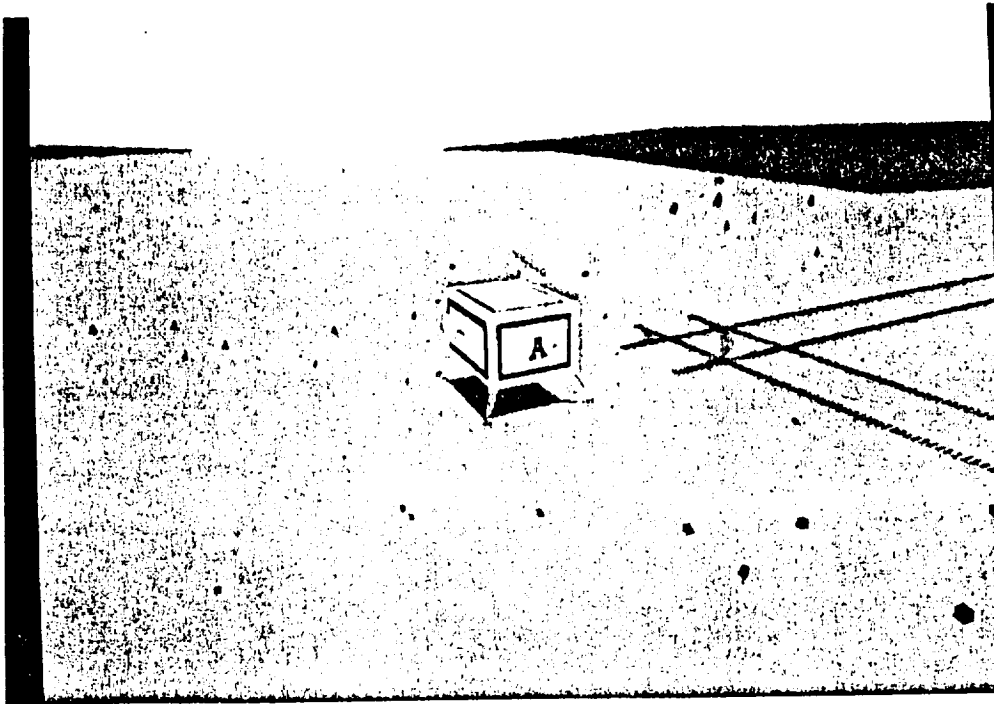


Figure 4. Oxygen manufacturing plant after landing on Martian surface.

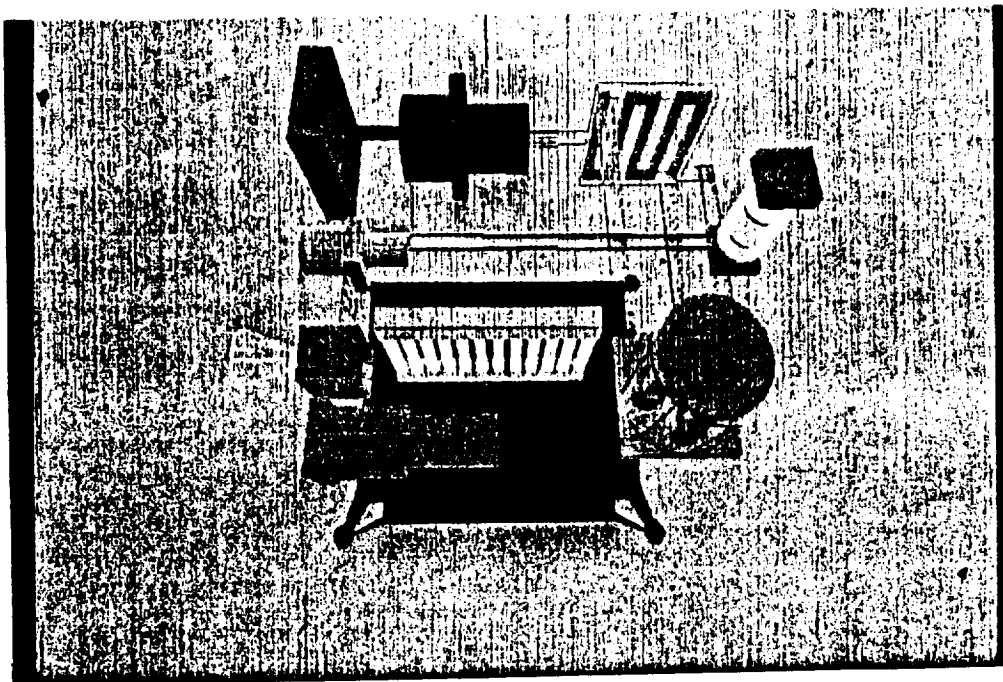


Figure 5. Exploded view of the oxygen manufacturing plant.

ORIGINAL PAGE IS  
OF POOR QUALITY

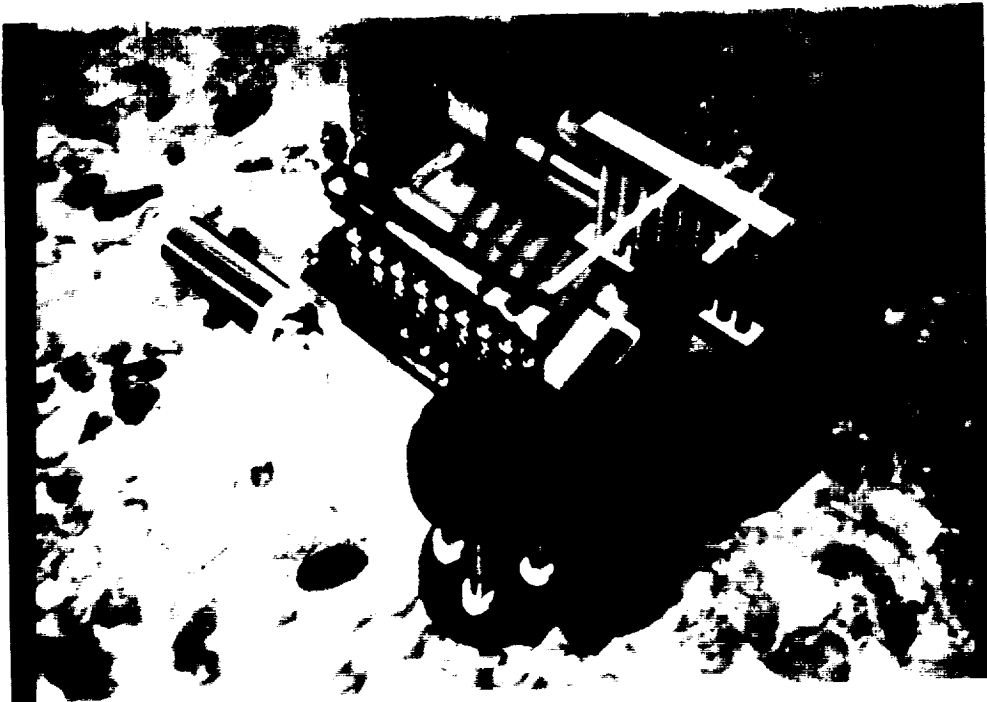


Figure 6. Oxygen manufacturing plant with shading and texture (Earth sunlight).

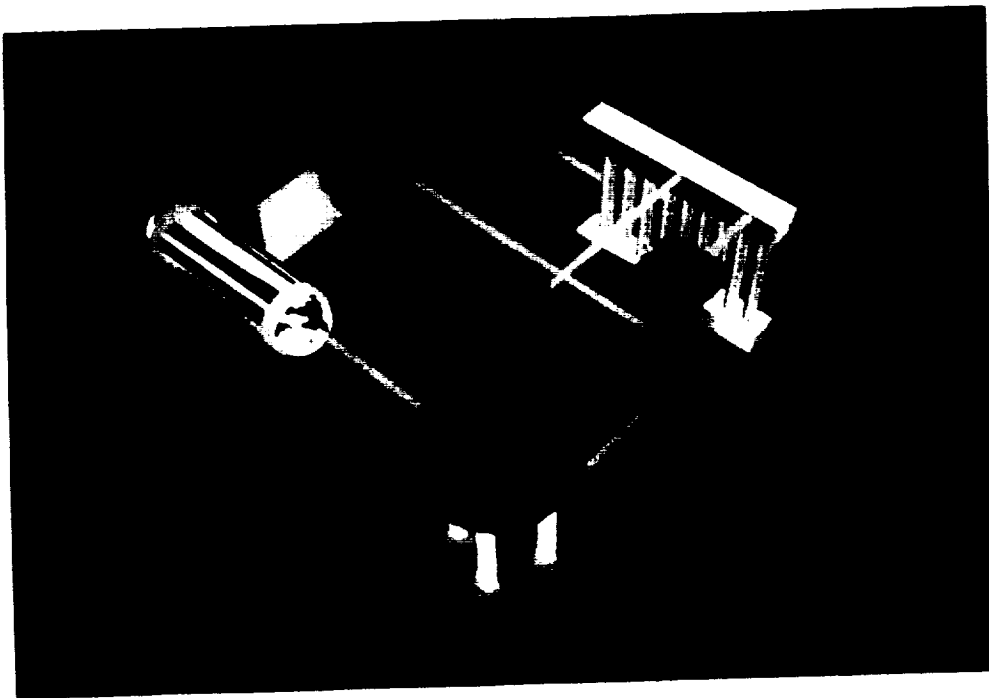


Figure 7. Oxygen manufacturing plant with shading and texture (Martian sunlight).

ORIGINAL PAGE  
COLOR PHOTOGRAPH

ORIGINAL PAGE IS  
OF POOR QUALITY

N 9 1 - 2 4 3 8 9 /

MODELING, SIMULATION, AND CONTROL OF AN EXTRATERRESTRIAL  
OXYGEN PRODUCTION PLANT

L. Schooley, F. Cellier, B. Zeigler, A. Doser, and G. Farrenkopf  
Department of Electrical & Computer Engineering  
The University of Arizona

Abstract

The immediate objective of this project is the development of a new methodology for simulation of process plants used to produce oxygen and/or other useful materials from local planetary resources. Computer communication, artificial intelligence, smart sensors, and distributed control algorithms are being developed and implemented so that the simulation or an actual plant can be controlled from a remote location.

The ultimate result of this research will provide the capability for teleoperation of such process plants which may be located on Mars, Luna, an asteroid, or other objects in space [1,2]. A very useful near-term result will be the creation of an INTERACTIVE DESIGN TOOL, which can be used to create and optimize the process/plant design and the control strategy. This will also provide a vivid, graphic DEMONSTRATION MECHANISM to convey the results of other researchers to the sponsor.

Introduction

In most areas of physical endeavor, the modern computer age has provided the possibility of performing design through modeling and simulation. The meta-laws in areas such as electrical or mechanical engineering are so well established that a plant (process) can be designed on the computer by use of well established modeling and simulation techniques before it is ever built. The design parameters identified in the simulation can then drive the process of implementation, and the resulting plant will, in all likelihood, function as anticipated by the simulation.

Chemical engineers and chemists are not at this stage of design yet. The area of chemical process modeling lags behind most other areas of physical system modeling. Meta-laws have been established, but they are valid only under specific (and often unstated) assumptions such as isothermic and isobaric, or isothermic and isochoric conditions. Furthermore, many of the necessary chemical process parameters have not been determined, and others are known with a very limited accuracy only. Therefore, it is essential that a chemical process design tool provides more than trajectory behavior only. It must be able to investigate the sensitivity of the design to inaccurately known parameter values. To solve these problems, we are utilizing a new methodology (bond graph modeling) which enables us to describe the complete dynamics of a chemical reaction

system and its environment.

In this project, we are working closely with Dr. Ramohalli to develop reasonable process flow diagrams for the testbed for his process for producing oxygen from carbon dioxide [3]. The dynamic parameters (the reaction rate constants) for the reaction kinetics equations that describe the reaction are being identified, as well as the static parameters of the energy equilibrium, such as the enthalpies of formation, the absolute entropies, and the heat capacitance functions of the materials involved. We are using our bond graph methodology to generate dynamic models of the processes, and we shall validate our models using experimental results from the testbed.

We are also creating a control model that allows us to optimally control the overall oxygen production plant, as well as an OASIS application data base and the data communication protocols that will allow us to teleoperate the locally controlled oxygen production plant [4,5]. This includes a preliminary investigation of the influence of smart components (smart sensors and smart controllers) on the degree of autonomy under which the plant can be operated, and a plan for future incorporation of artificial intelligence for increased autonomy.

Progress in the areas of modeling, communication, instrumentation and control, and artificial intelligence is described in the following sections.

### Modeling

A test bed system for extracting oxygen from carbon-dioxide (of which Mars' atmosphere is about 95%) has been designed and constructed at the University of Arizona - NASA Space Engineering Research Center, and is described elsewhere in this report. Development of simulation models of this test bed system is currently underway.

Three simulation models of the oxygen production system are of particular interest. The first involves the static mass flow of  $\text{CO}_2$ ,  $\text{CO}$  and  $\text{O}_2$  within the system, and is based on thermodynamic and conservation of mass principles. From this simulation we can estimate what the production rate of oxygen will be in steady-state, and what various system pressures and temperatures can be expected to be.

The second simulation concerns the static energy flow within the system, and is based on thermodynamic and conservation of energy principles. This simulation allows conditions that were assumed in the first model to be verified, and enables an estimate to be made of the power requirements of the different system components.

The third simulation model will describe the dynamics of the system, and will be based on a modeling and design methodology involving the use of bond graphs. Bond graphs were originally introduced to model mechanical systems, and have since been adapted by Dr. Francois Cellier to model chemical reaction systems. Chemical reaction bond graphs model dynamic chemical reactions through the use of six variables; chemical potential, molar flow, hydraulic/pneumatic

pressure, volume flow, temperature and entropy flow. This will enable temperature and energy to be balanced for each separate subsystem of the entire system. These modular subsystems can then be connected together to form the model for the entire oxygen production plant, and valuable information can be learned about system start up and shut down, and optimal control strategies can be studied both for normal operation as well as for handling emergency situations.

The subsystem which performs the actual separation of the carbon dioxide into oxygen and carbon-monoxide is a zirconia cell. A dynamic model for this cell will be developed based on the chemical reaction and power balance which takes place within the cell. Separate program modules will be developed for each of the system processes, and then the simulation software DYMOLA will be used with DESIRE or ACSL to obtain a hierarchical coupling of these processes. The static simulation models are written in Ada and are currently running on a MicroVAX workstation at the University of Arizona. A remote controlling computer (another MicroVAX) sends input data to the local simulation computer over an Ethernet connection. The simulation executes on the local computer and then sends its results back to be displayed. The local simulation computer will eventually be moved out to the NASA center, which is several miles away from the University. Communication between the local and remote computers will then take place via a microwave link.

As the simulations and actual construction of the oxygen production plant enter their mature stages, model validation will be accomplished and the simulations will be used to give insight into which system configuration will result in optimum performance.

#### Communication

OASIS (Operations and Science Instrument System) is a software package developed by the University of Colorado in 1987. The purpose of OASIS is to allow remote operation of scientific experiments or remote supervisory control of telerobots or automated process plants. With this software, a remote commanding computer (RCC) on Earth would communicate with a local controlling computer (LCC) at some other location (e.g. Mars), which would implement the appropriate local control and monitoring algorithms [1, 2].

An OASIS application has been created to interact with the static mass flow model of the MARS test bed. The implementation of this application uses a MicroVAX II/GPX workstation (node name CACTUS) as the RCC and a second MicroVAX II/GPX workstation (node name PUEBLO) as the LCC. CACTUS prompts the user to enter certain information about the test bed (the flowrate of  $\text{CO}_2$  into the system, the efficiency of the  $\text{ZrO}_2$  cell, and the efficiency of the membrane separator). These data are sent to PUEBLO, where the temperatures, pressures and other mass flow rates of the system are calculated. The calculated values are transmitted back to CACTUS, where they are displayed for the user. The communication protocol presently employed is DECnet over an ethernet link within the same building. The protocol is currently being changed to TCP/IP,

and it will soon be tested over a microwave radio link to the testbed location which is about seven miles away.

Future work will include interfaces with the dynamic simulation and with the testbed itself, as illustrated in Figure 1. An expansion to allow multiple remote observers in addition to the remote commander will also be implemented, as well as a token passing protocol to allow any one of the observers to assume command.

#### Instrumentation and Control

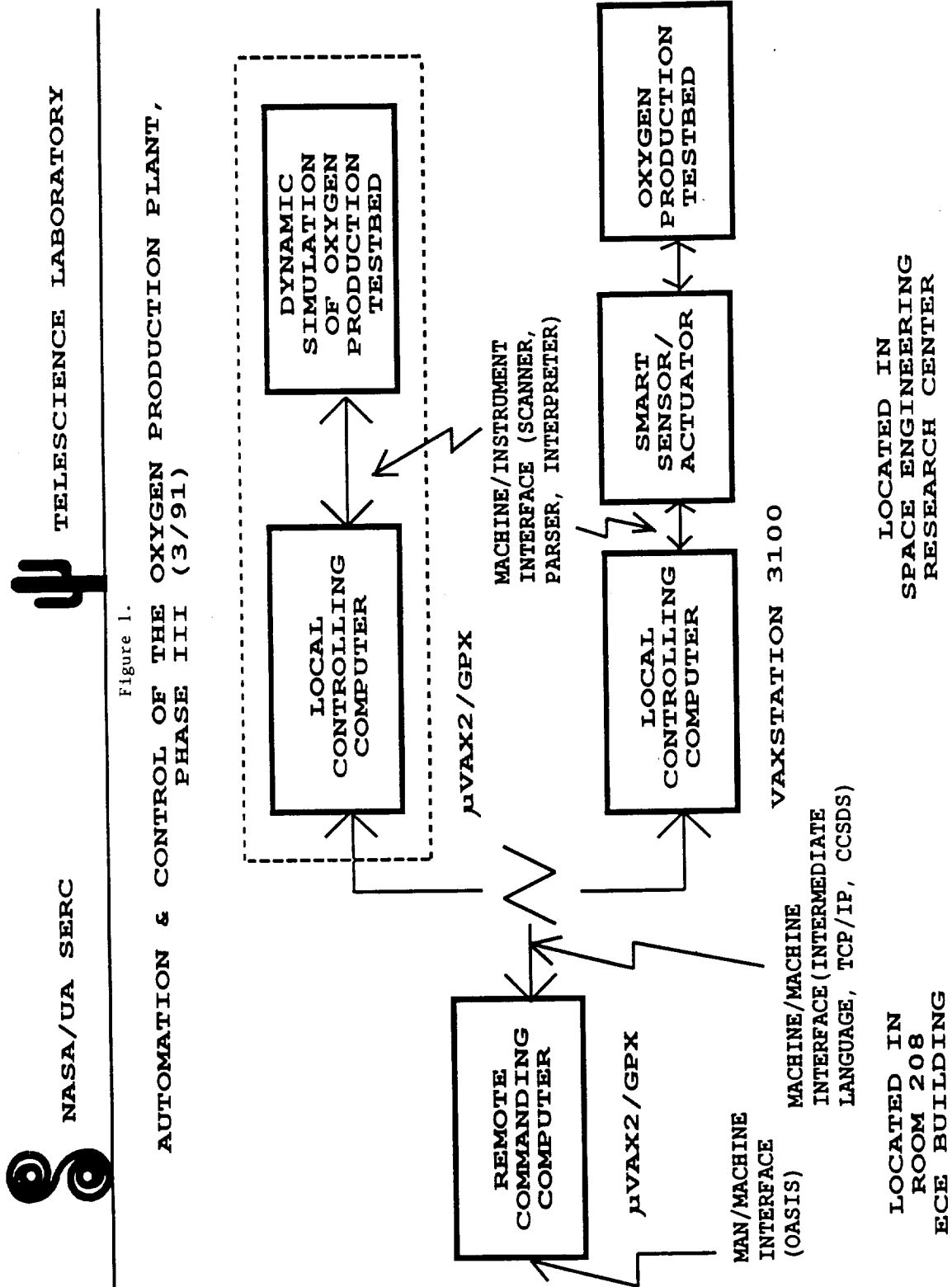
An intelligent controller (smart sensor) which supports a fast local control loop has been used for control of a small testbed which was constructed for investigation of the seals between a section of stainless steel pipe and the zirconia cell. This controller has some simple programmable functions, limited logic functions and scaling capability for each instrumentation channel. It includes thermocouple transducers, a connection card, analog voltage input signal cards (for pressure transducers and flow meters), and a digital output signal card. The controller communicates commands and data with a 386 class personal computer (serving as the LCC) so that it can control a heater according to input commands from the computer.

More recently, the seven transducers of the oxygen production testbed have been connected to the smart sensor. Three thermocouple transducers are sensing temperatures of the input pipe, the  $ZrO_2$  cell pipe, and the output pipe. Two flow-meters and two pressure transducers are also used for monitoring the input and output gas streams. All these data are transferred to the LCC and the higher level control systems will generate appropriate control commands. Details of the high level control strategy are currently under development.

#### Artificial Intelligence

Some preliminary work has been initiated on a diagnostic system and related high autonomy concepts. The diagnostic system can be divided into two subsystems, the local diagnoser and the global diagnoser. The local diagnoser has shallow behavior knowledge of each component, and it will monitor the behavior discrepancies between its model and the real system. If there is any anomaly in readings from a sensor, for example, this will be detected by the local diagnoser, which will activate the global diagnoser to start a fault determination procedure. The fault will then be corrected locally, or further guidance will be requested from the remote commander.

The local fault diagnoser models have been completed for the oxygen production portion, which includes the compressor, heat exchanger, temperature mixer, heater, temperature controller, and  $ZrO_2$  cell. Each component has its own causal effect model, which consists of shallow knowledge about the component, and it allows an experienced user to easily model the whole fault causal structure in a hierarchical manner. Each causal effect model is a rule





based model, and each fault event is associated with one or more rules. The inference of each fault event is different depending on the operational status of the component.

The global diagnoser simulator will run those fault diagnoser models and traverse all the possible causes that effect the fault symptom. The corresponding trajectories of event time for those causes will be generated as output from the simulator. Those trajectories can be used with the history records of sensors just before the anomaly is detected to determine the exact causes. Further development and implementation of these concepts will be proposed for the next contract period.

### Summary

All work on this project is proceeding on schedule. It is anticipated that the dynamic simulation will be completed, and that the dynamic simulation and/or the testbed will be capable of remote supervisory control by the end of the current contract period. Implementation of the higher level automation and control functions will be proposed for the next period.

### References

- [1] Automation of Extraterrestrial Systems for Oxygen Production (AESOP) Workshop, LaJolla, CA, July 13-15, 1989. Report published by University of Arizona/NASA Space Engineering Research Center, 4717 E. Ft. Lowell, Tucson, AZ 85712.
- [2] Schooley, L.C. and F.E. Cellier, "Monitoring and Control Systems for Automated Process Plants," UA/NASA Space Engineering Research Center, Proceedings of Invitational Symposium on Space Mining and Manufacturing, University of Arizona, Tucson, AZ, October 24-26 1989.
- [3] Ramohalli, K., E. Lawton, and R. Ash, "Recent Concepts in Missions to Mars: Extraterrestrial Processes," Journal of Propulsion and Power, Vol. 5, No. 2, March-April 1989, pp. 181-187.
- [4] Davis, R. and E. Hansen, "OASIS Teleoperations Package Makes its Debut," Information Systems Newsletter, March 1986.
- [5] Schooley, L. C. and F. E. Cellier, Telescience Testbed Pilot Program Final Report, Technical Report TSL-021/88, Electrical and Computer Engineering Department, University of Arizona, Tucson AZ, December 1988.

---

## **V. DATABASE DEVELOPMENT**

525-89  
14685  
p.7  
Near-Earth Asteroids:

N 9 1 - 2 4 3 9 0

Observer Alert Network and Database Analysis

Donald R. Davis and Clark R. Chapman

Planetary Science Institute

PI 152893

Abstract

The Planetary Science Institute (PSI) has been funded by SERCulpr to develop a communication network to alert observers of newly discovered near-Earth asteroids (NEAs). This network is intended to encourage observers to obtain physical observations of NEAs, which are needed in order to characterize and assess the resource potential of these bodies. This network was declared operational in October, 1990 via an announcement to the asteroid observing community. PSI is also supported to develop the Near-Earth Asteroid Database (NEAD), a comprehensive database of physical and dynamical data on NEAs. In the past year we updated the database on newly discovered NEAs during 1990 and added new data on radar observations and dynamical classifications.

Introduction

Near-Earth asteroids are being discovered at an increasing rate; however, usually only a preliminary orbit and an estimate of the brightness of the asteroid is obtained during the discovery apparition. This is due to the brief interval (typically days to weeks) that the asteroid is bright enough to be observed by workers at 1-2 meter class telescopes. Unfortunately, it is usually several years before a newly discovered NEA makes another close apparition to Earth; thus little is known about the physical properties of NEAs until long after their discovery. However, as NASA is becoming increasingly interested in NEAs as potential mission targets and as a source of resources for expanded space activities, it is essential to learn more about these bodies as early as possible in order to meet the needs of the space program.

The importance of timely observations during the discovery apparition was recently emphasized by Wisniewski of the Lunar and Planetary Laboratory who found that over the next few years, roughly twice as many newly discovered NEAs will be bright enough for physical observation as there will be "old" NEAs this bright. The Planetary Science Institute established an Observer Alert Network in October, 1990; Appendix A contains the announcement letter that was sent to 111 observatories and individual observers. We have 14 observers on our active list that we communicate with whenever an appropriate NEA is discovered. We also assist in alerting observers of the need to obtain positions of newly discovered fast moving objects, both prior to and following the release of an IAU circular. In the two months following establishment of our network, we have responded to 4 requests to alert observers via the network. We plan to review the operation of the network next May to evaluate its effectiveness.

In addition to developing and operating the Observer Alert Network, we have developed the Near-Earth Asteroid Database (NEAD), which is designed to be a comprehensive catalogue of data on NEAs. NEAD will be a valuable tool in evaluating potential targets for near-Earth asteroid missions and for assessing the resource potential inherent in the NEA population. This database now exists as a dBase IV file, thus the tools of this relational database are available for analysis of data on near-Earth asteroids. In the past year, we expanded NEAD by adding radar data (cross-section and polarization ratio) and the dynamical classification scheme of Milani *et al.* for near-Earth asteroids. This classification is based on long timescale numerical integration of NEA orbits and includes the strong orbital perturbations due to close encounters with the terrestrial planets, which is omitted from the secular perturbation theories used to calculate proper elements. NEA lightcurves from the 2nd Photometric Catalogue (Lagerkvist *et al.* 1988) are scheduled to be added to the database early next year. Program documentation and additional analysis tools are being developed in dBase IV to make the data more usable for scientific users. Examples of the types of output available from NEAD are shown in Fig. 1.

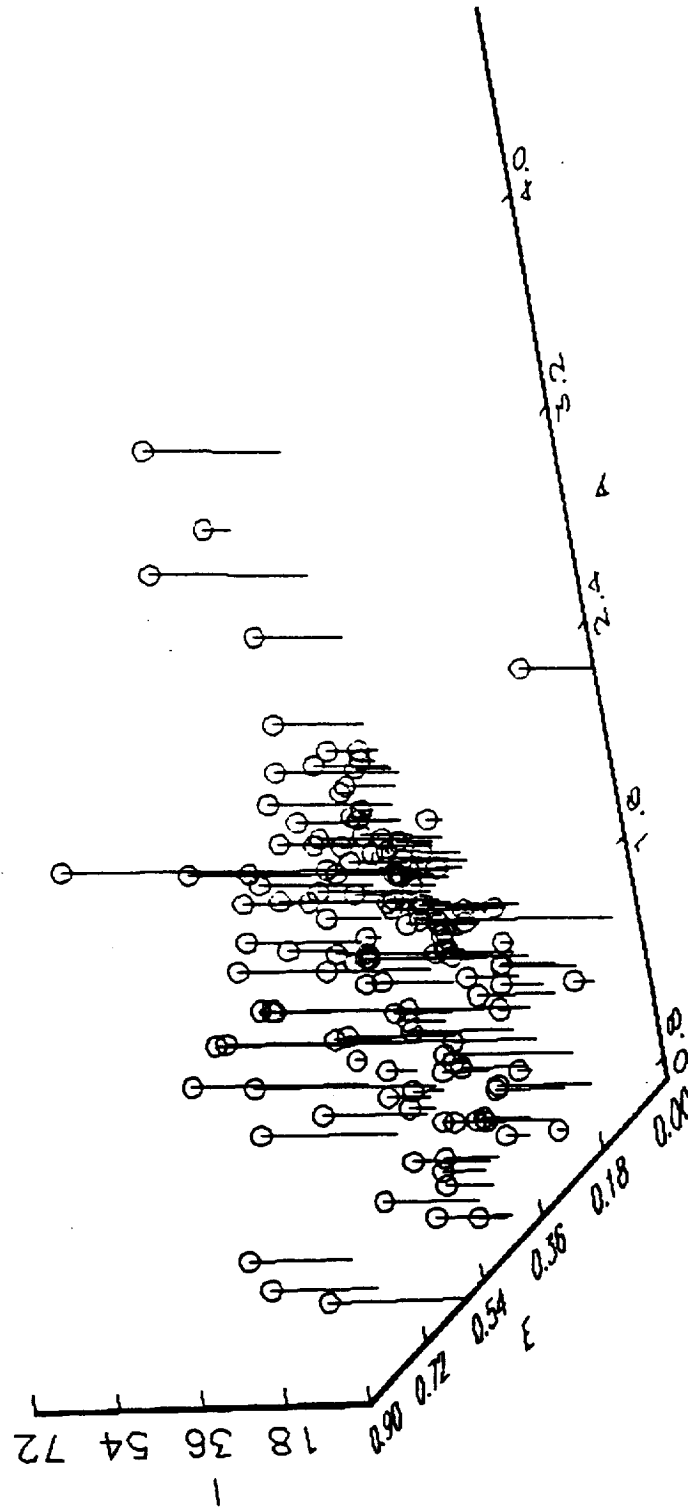


Fig. 1(a). Plot of orbital elements semimajor axis ( $a$ ), eccentricity ( $E$ ), and inclination ( $I$ ) for all Near-Earth Asteroids.

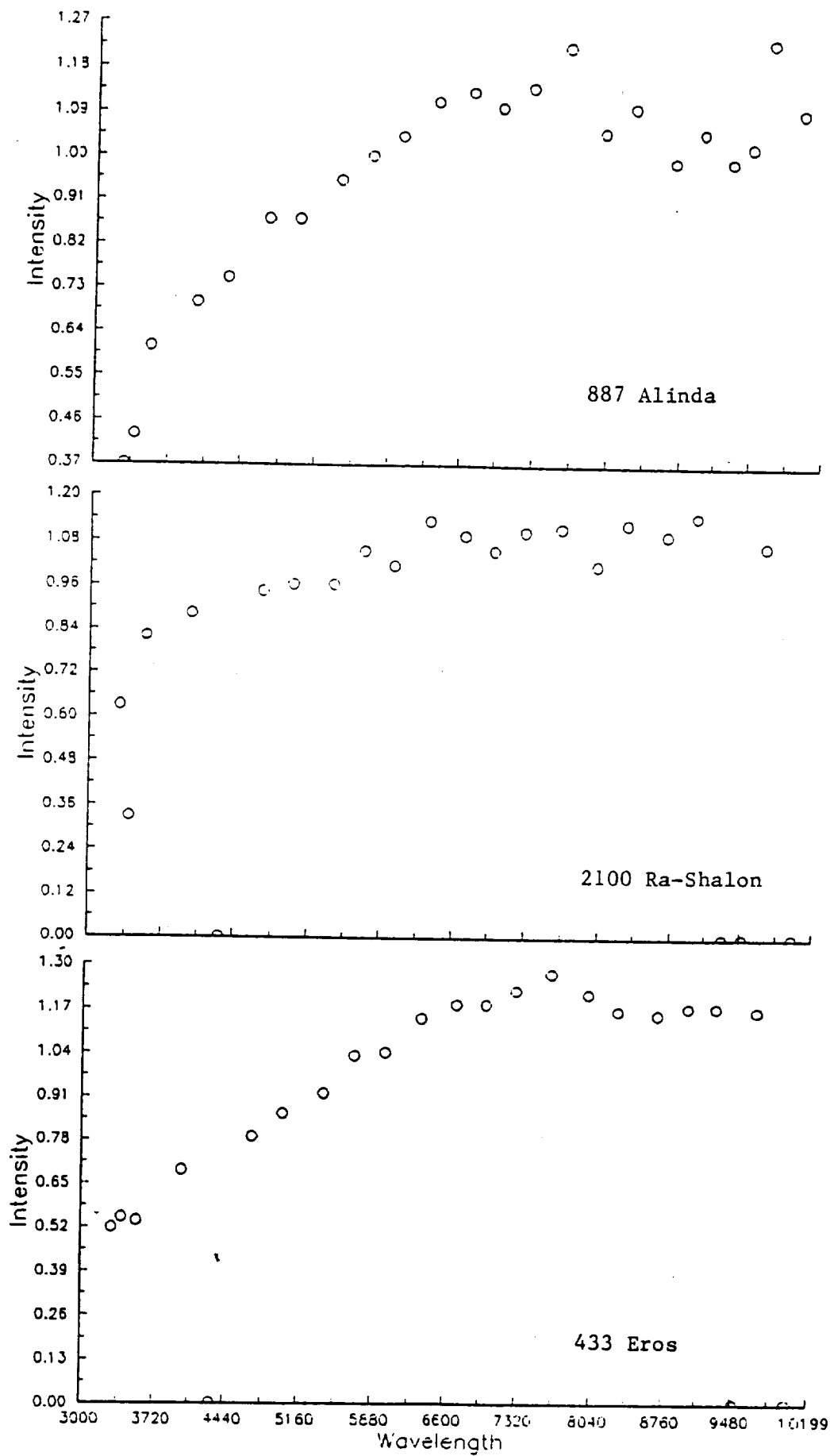


Fig. 1(b). 24-color spectrophotometry data.

REFERENCE

Lagerkvist, C.-I., *et al.* (1988). *Asteroid Photometric Catalogue: First update*. Consiglio Nazionale Delle Ricerche: Rome.

PLANETARY SCIENCE INSTITUTE  
2421 E. 6th Street  
Tucson, AZ 85719  
(602) 881-0032

APPENDIX A

Notification Network for Physical Observations  
of Near-Earth Asteroids

The Planetary Science Institute wishes to announce that, effective 29 October 1990, we will be operating a network designed to alert observers concerning especially interesting near-Earth asteroids for which *physical observations* are desired. The service is supported by the NASA/University of Arizona Space Engineering Research Center for the Utilization of Local Planetary Materials. The effort is headed by Dr. Donald R. Davis, with participation by Dr. Clark R. Chapman and Mr. David H. Levy.

We solicit the names and communications channels for all observers interested in being notified about important near-Earth asteroids. We will be asking them, and major observatories, to provide us with advanced observing schedules so that we will know who to contact when an important object is discovered. We will also ask the individuals who work on discovering Earth-approaching objects to notify us when particularly important objects are discovered, and we will also be regularly checking the *IAU Circulars*.

We will notify observers concerning unusually important objects for which physical observations are desired. We will give priority to those objects that (a) are likely radar targets, (b) have B brighter than 15, (c) will be well-placed for a short but adequate duration to make physical observations possible but timely notification desirable, (d) have sufficiently good orbits/ephemerides to make acquisition fairly reliable, and (e) have other unusual traits of particular interest. We anticipate, based on unofficial, partial operation of this service during the past year, that an object might meet our criteria every month or so.

The service will be an *active* supplement to the normal IAU announcements of discoveries. We encourage observers to subscribe directly to the *IAU Circulars* and to check them regularly. If you hear from us, you will know that the object is deemed to be particularly important and that an "observing campaign" is underway. We thereby hope to enhance the quantity of physical data available for these important objects that often fade so rapidly. We will be coordinating with Dr. Brian Marsden of the IAU Central Bureau to ensure that our alerts are based on sound orbits, in order to minimize wasted time at the telescope. We will be evaluating the effectiveness of the network after seven months of operation.



Our goal is to alert observers within twelve hours of when we receive notice of an important discovery (usually morning, Mountain Standard Time) but certainly within 48 hours; our response may be slower on weekends and holidays than on normal workdays. We will check *IAU Circulars* and our phone messaging service once a day, including weekends. We will send announcements out by electronic mail and telephone. While our primary goal is to alert physical observers, we will also assist when needed to alert astrometric observers about critical needs for positions.

If you have questions or suggestions about the service, or if you wish to sign up, please contact:

Dr. Donald R. Davis  
Planetary Science Institute  
2421 East Sixth Street  
Tucson AZ 85719 USA

Telephone: 602/881-0332 (Logistical details can be handed by Ms. Elaine Owens at this number; during off-hours, a 24-hour message service is in operation for this telephone number.)

E-mail: PSKEY::PSKEY (on SPAN)

Fax: 602/881-0335

19 Oct 1990

526-89  
N91-24394686  
p.8

The Steward Observatory Asteroid Relational Database

Mark V. Sykes and Elizabeth M. Alvarez del Castillo

Steward Observatory

The University of Arizona

ORIGINAL CONTAINS  
COLOR ILLUSTRATIONS

ABSTRACT

A 1000  
MCN

The Steward Observatory Asteroid Relational Database (SOARD) has been created as a flexible tool for undertaking studies of asteroid populations and sub-populations, to probe the biases intrinsic to asteroid databases, to ascertain the completeness of data pertaining to specific problems, to aid in the development of observational programs, and to develop pedagogical materials. To date SOARD has compiled an extensive list of data available on asteroids and made it accessible through a single menu-driven database program. Users may obtain tailored lists of asteroid properties for any subset of asteroids or output files which are suitable for plotting spectral data on individual asteroids. The program has online help as well as user and programmer documentation manuals. Already SOARD has provided data to fulfill requests by members of the astronomical community. SOARD continues to grow as data is added to the database and new features are added to the program.

## INTRODUCTION

Asteroids are characterized by their diversity. We study them using a wide variety of remote sensing techniques in an attempt to determine their composition and physical properties, and relate this information to processes effecting asteroids and other solar system bodies over the age of the solar system. Observations are obtained through groundbased telescopes, spacecraft such as the Infrared Astronomical Satellite (IRAS), and radar, and are focussed on individual objects of particular interest or dedicated surveys. SOARD incorporates the data obtained from these various observations into a single database.

In addition to being objects of scientific investigation, asteroids are potential resources to be utilized in support of the expansion of humans into the solar system. The most accessible of these are the Near Earth Asteroids (NEA's) whose motions around the Sun bring them within reach of low-energy transfer orbits from the Earth. Until recently, the information available on the NEA's has been relatively limited, but with increased rates of discovery and greater numbers of observational programs focussing on these objects, this information is expected to grow rapidly. Since NEA's derive from the main asteroid belt (though some may be extinct comets), knowledge of their source populations provides additional insight into the nature and physical properties of NEA's.

**TABLE 1. SOARD DATA SETS****ASTEROIDS II**

- Proper Orbital Elements
- Taxonomic Classifications
- Family Designations
- Pole Orientations
- Magnitudes, UBV Colors, Albedos, and Diameters

**IRAS**

- Radiometric Diameters and Albedos
- Individual IRAS Observations
- Polarimetry file
- Lightcurve file
- UBV Observations
- 8-Color Spectroscopy
- 24 Color Spectroscopy

**MISCELLANEOUS**

- 52-Color Spectroscopy (J. Bell)
- Osculating Orbital Elements (E. Bowell)
- Preliminary Designations and Discovery Circumstances (MPC)
- Photometric Parameters (MPC)

**TABLE 2. DATA SETS IN THE PROCESS OF BEING ADDED**

- Families (Zappala, et. al.)
- Proper Elements (Milani and Knezevic)
- Radar Observations (S. Ostro)
- CCD Spectroscopy (L. McFadden, F. Vilas)
- Near-IR Spectra (Lebofsky, Bus, et. al.)

SOARD's goal is to incorporate ALL published asteroid data into one generally accessible database for use in research and in expanding our general and specific understanding of asteroid populations.

SOARD is a menu-driven asteroid database management system which utilizes dBase IV software in a fashion transparent to the user. It allows three basic system outputs at this time: (1) files of designations of asteroids satisfying range criteria for parameters or functions of parameters, (2) subsets of database parameters for subsets of asteroids, and (3) files of multiband photometry or spectroscopy for individual asteroids (for plotting).

## SOARD DATA

Table 1 lists the individual data sets which are currently online and accessible through SOARD. It combines ground based observations which were published in ASTEROIDS II, radiometric data collected by IRAS, ancillary IRAS data sets of ground-based polarimetry, lightcurve, and spectroscopic observations, Jeff Bell's 52-color near-IR survey, osculating orbital elements for 16,610 asteroids, and discovery information and photometric parameters published through the Minor Planet Circulars (MPC). As data is incorporated into SOARD, it receives a reference to its source in the literature. This provides online information on the origin of the data and allows maximum understanding of data quality. Data evaluation is critical to its use in an engineering context.

## UPDATING THE DATABASE

SOARD is expanding to include the data sets listed in Table 2. Some of the data such as CCD spectroscopy of certain asteroids has been published. Some data is collected and needs to be reduced and published. Monthly updates to SOARD include data available through literature searches, data sent by individual observers, and data obtained from the Minor Planet Circulars (MPC). Ongoing observations and research promise a continually growing body of data which will be added to SOARD.

## USING SOARD

When running the SOARD program, the user will view first the main menu shown in Fig. 1. The main menu offers currently three options for system output. Option 1 allows the user to select which asteroid parameters, for any subset of asteroids, to output to a separate file. With Option 2 the user creates files of identification numbers of asteroids which satisfy user-defined range criteria of asteroid parameters. This file can be used as input to either of the other two options to identify the subset of asteroids for which a user selects data. Option 3 creates files of multiband photometry or spectroscopy for individual asteroids.

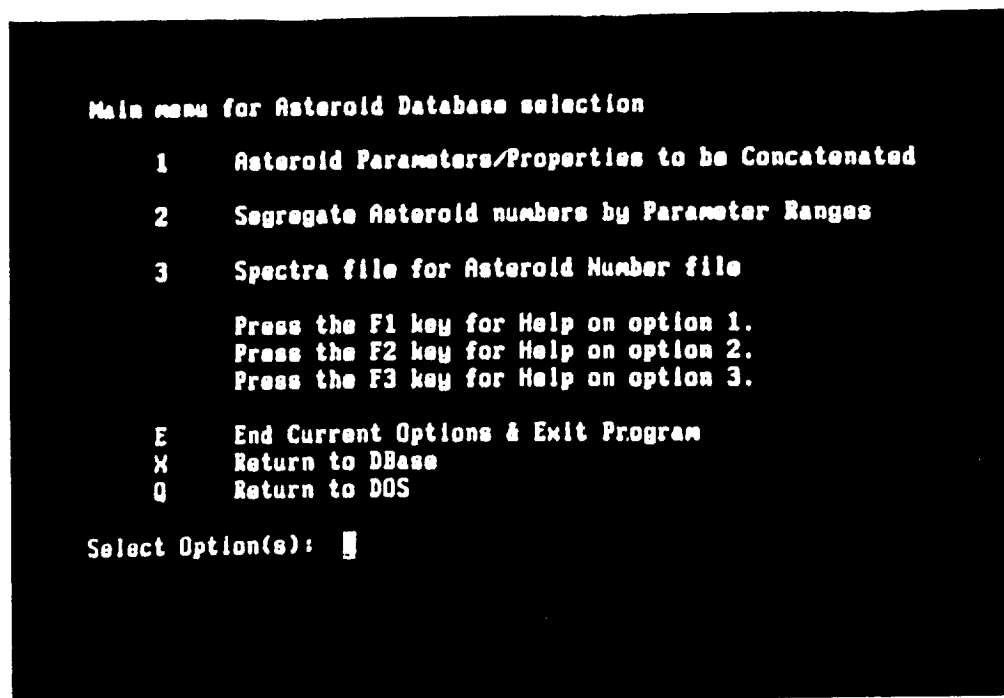


Fig. 1. SOARD main menu.

Under Option 2, SOARD will display the list of parameters within selected data files (e.g. Fig. 2), and the user builds an expression from the parameters (Fig. 3) which specifies the range criteria which the asteroids must satisfy. SOARD prompts the user for the name of the output file. The user may cycle through this process as many times as desired and then take the union or the intersection of any of the created asteroid subsets to write a new subset file.

Option 3 creates individual spectra files for each of the asteroids in the user-specified subset of asteroids. Each spectra file contains four columns: wavelength, reflectance, uncertainty of reflectance, and half width half max.

All output files are dBase format by default and become part of the database which the user can access through SOARD. Output may be written to an ASCII format file as well for access by non-dBase software. Online help is available at various points in the program and can be displayed with a single keystroke.

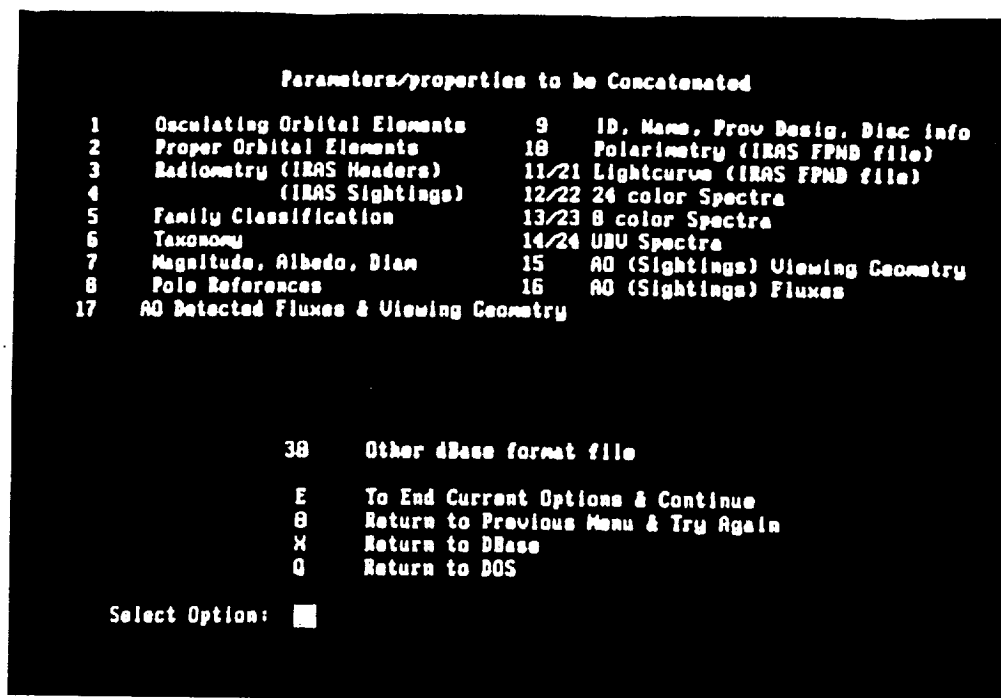


Fig. 2. Second level menu for Option 1. The same choices are available under Option 2.

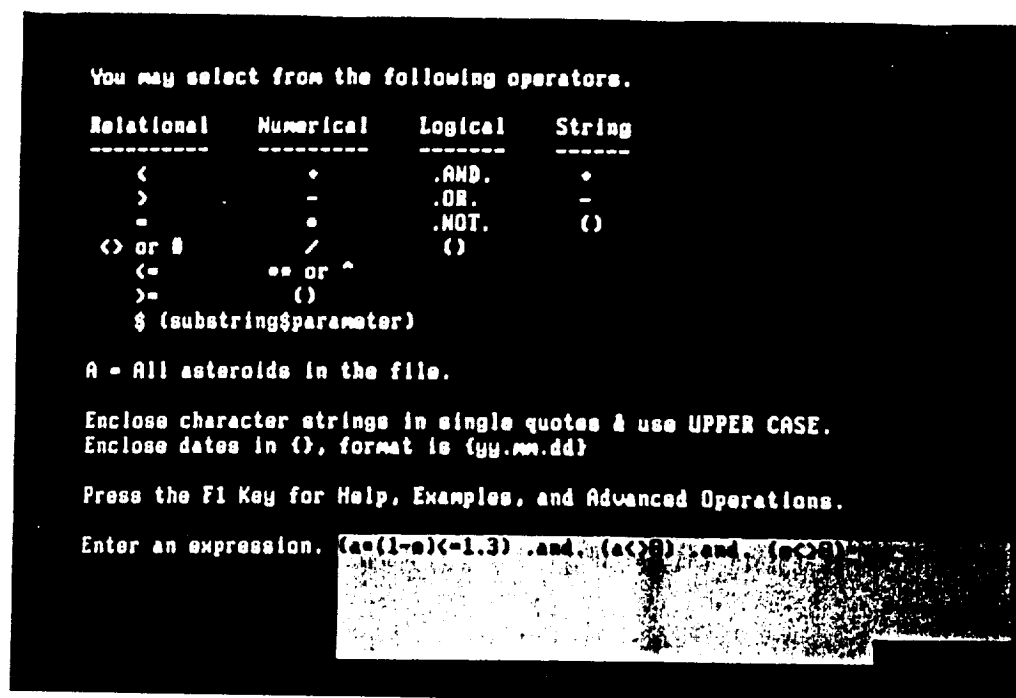


Fig. 3. Sample menu for selecting and building parameter range criteria under Option 2.

## SAMPLE OUTPUT

Graphical and image representations of output files created by SOARD can provide insight into asteroid characteristics and the extent to which they have been explored. In the remaining figures, asteroid populations are shown in semi-major axis/orbital inclination space which is related to their mean physical locations. Figure 4 illustrates the distribution of asteroid geometric albedos determined by IRAS. Geometric albedo clearly decreases with semi-major axis. This has been related to the effects of a heating episode in the early solar system, resulting in greater differentiation of asteroids occurring in the inner belt.

Figure 5 shows the distribution of all 16,610 asteroids in SOARD and identifies the known population of Near Earth Asteroids, which are clustered at low values of semi-major axis. The level of completeness to which these objects have been studied is indicated in Figure 6. Of 140 NEA's in the database, radiometry exists for 5 (from IRAS) and colorimetry (including UBV, 8-, 24-, or 52-color photometry) exists for 31. The sampling of this population is far from exhaustive.

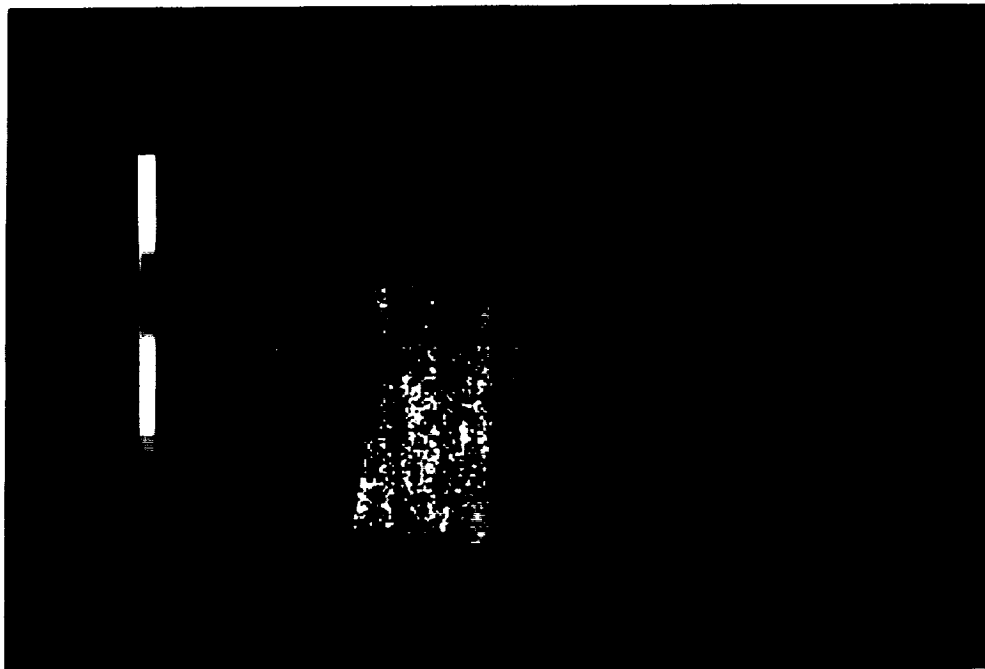


Fig. 4. Distribution of IRAS geometric albedos in the asteroid belt.

ORIGINAL PAGE  
COLOR PHOTOGRAPH

ORIGINAL PAGE IS  
OF POOR QUALITY

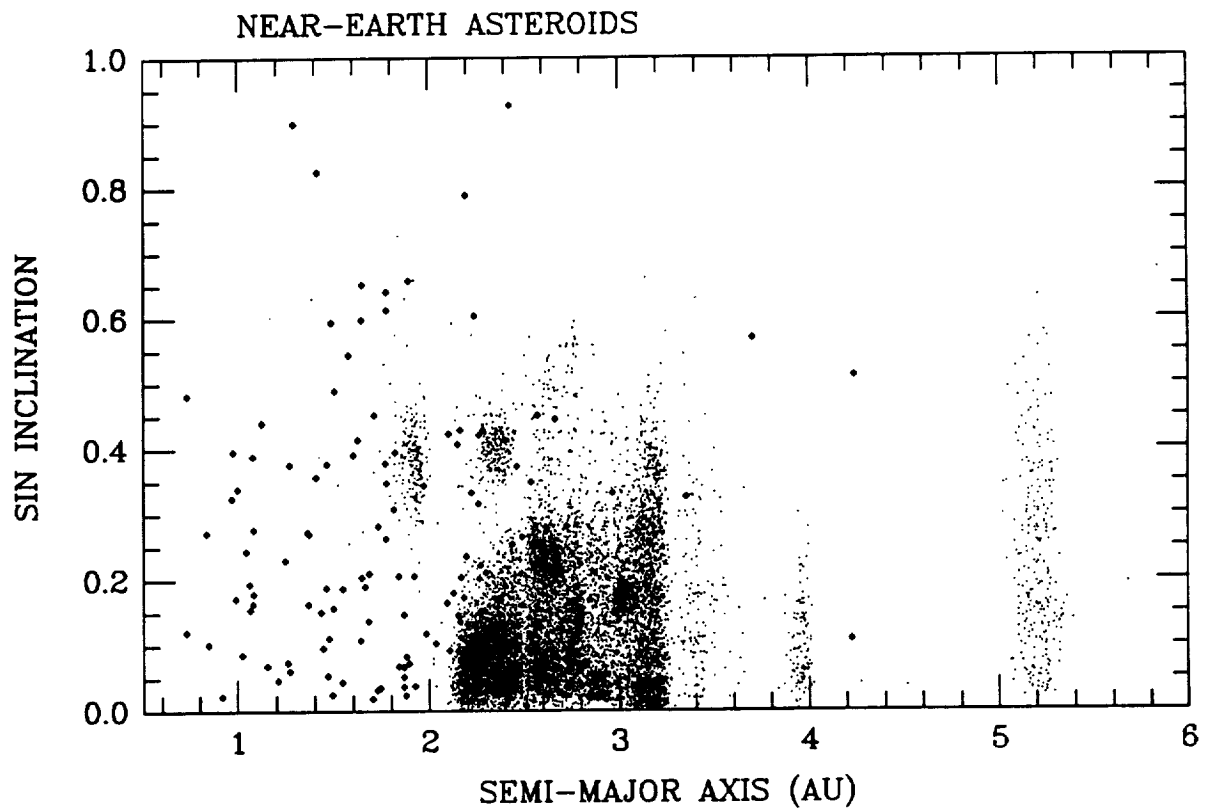


Fig. 5. The distribution of 16,610 asteroids are shown as a function of osculating semi-major axis and the orbital inclination. The Near Earth Asteroids ( $q < 1.3$  AU) are displayed as larger points.

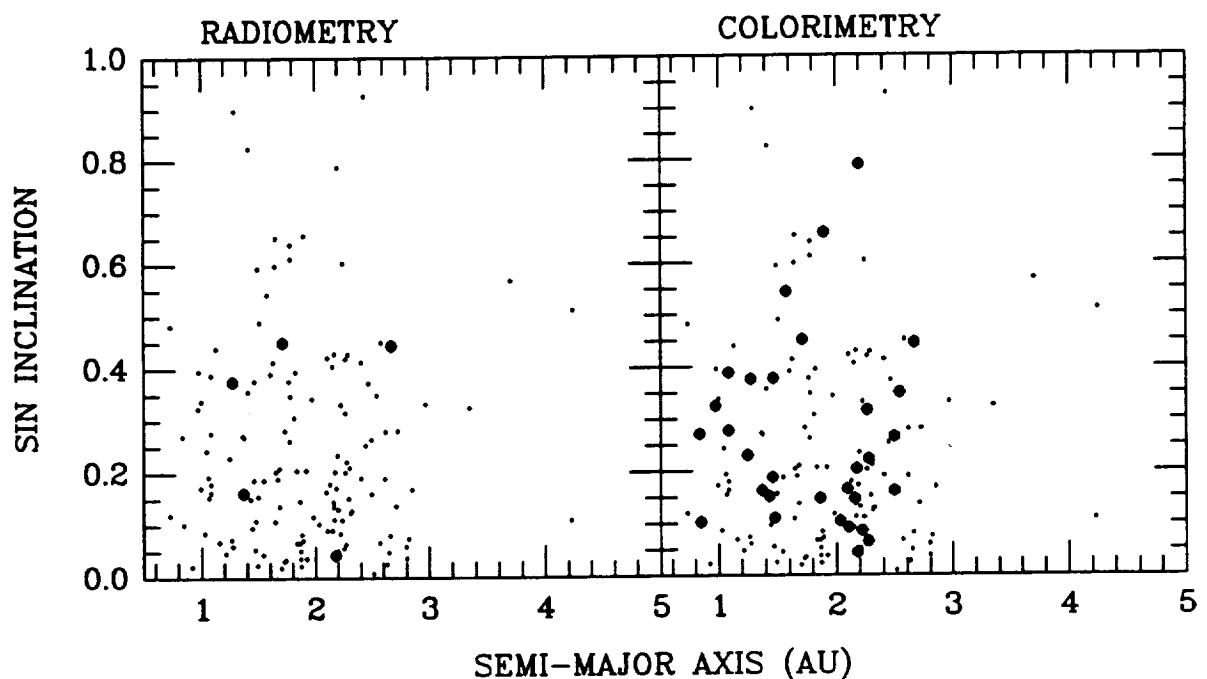


Fig. 6. The distribution of 140 Near Earth Asteroids are shown in both panels. In the left panel, larger points indicate NEA's for which radiometry has been acquired. In the right panel, larger points indicate those for which colorimetry has been acquired.



## EXPANDING SOARD

Additional programming will expand the features available through SOARD. A fourth main menu item will allow the user to concatenate functions of asteroid parameters. If a file contains orbital elements such as semi-major axis and eccentricity, the user may calculate the perihelion distance as an output parameter of specific interest. This feature will minimize data which must be distributed with the system while allowing the user maximum choice for customized output of asteroid parameters.

A fifth main menu item will bring a reference search capability online. The user will be able to search a file with more than 11000 literature references. The search may be by author, title, date, publication, some subset of authors or words in a title, or any combination of these parameters.

Another main menu item being investigated is the ability to run external code. Specific programs such as code to generate ephemerides, to run standard thermal models, or to calculate magnitudes would be accessible without leaving the main SOARD program. Files generated through SOARD would be available for direct input into the external code and the output of the external code would be in a form accessible to SOARD.

Because of the desirability of a straightforward graphics display capability for SOARD output, we tested the dBase APPLAUSE II graphics package but found it inadequate for the scientific applications to which we were applying it. At present, results are displayed by writing SOARD output to an ASCII file which serves as input for external graphics packages such as MONGO.

## TESTBED ACTIVITIES

SOARD has a testbed site at the California Space Institute in La Jolla, California. This is run by Dr. Lucy-Ann McFadden, who is testing a transportable execution version of the relational database. She has helped identify bugs in the program and has offered many suggestions for improving the SOARD environment. Recently one of Dr. McFadden's students wanted to use SOARD to help him address a research question. He had received no prior tutoring, but with the help of online documentation only, he was able to run the program to extract the subset of data he required. Such successes bode well for a future distributable system.

## COMMUNITY SUPPORT

We respond to all moderate requests from the community, and have provided data in support of observing, research, and teaching programs. For instance, the International Space University requested and received information on Near Earth Asteroids. The ISU teaches young professionals from around the world about space activities. The ISU was held in Toronto this year and hosted 130 participants from 30 countries.